

<sup>1</sup> Copyright

<sup>2</sup> by

<sup>3</sup> Ryan Patrick Hannigan

<sup>4</sup> 2023

5 The Dissertation Committee for Ryan Patrick Hannigan certifies that  
6 this is the approved version of the following dissertation:

7 Stranger Things at the LHC

### **Committee:**

**Christina Markert, Supervisor**

---

Peter Onyisi

---

Aaron Zimmerman

---

Chandrajit Bajaj

8

9

**Stranger Things at the LHC**

10

by

11

**Ryan Patrick Hannigan, Ph.D.**

12

**Dissertation**

13

Presented to the Faculty of the Graduate School of

14

The University of Texas at Austin

15

in Partial Fulfillment

16

of the Requirements

17

for the degree of

18

**Doctor of Philosophy**

19

The University of Texas at Austin

20

May, 2023

To Jaynee.

## Acknowledgements

23 As it turns out, completing a dissertation is *a lot* of work. I am eternally grateful to the large  
24 number of people who have helped me along the way, and without whom this work would not  
25 have been possible. I can assure you if I were to properly thank everyone who has helped me, this  
26 acknowledgements section would be longer than the “systematic studies” chapter of this dissertation.  
27 So, I will try to keep it brief, but even by virtue of you reading this sentence, you have my sincerest  
28 thanks.

29 To my advisor, Professor Christina Markert, for her guidance and support throughout my grad-  
30 uate career. I am grateful for the opportunity to have worked with her, and for all of the time and  
31 effort she has put into helping me succeed, both as a graduate student *and* as a scientist. To Amanda  
32 and Josey, who have had to share an office with me for most of their time at UT. I appreciate all  
33 of the conversations and friendship we’ve shared over the years. To Erin and Alex, who welcomed  
34 me into the group and immediately made me feel at home. To Professor Deepa Thomas, who works  
35 harder than anyone I have ever met, and yet *somehow* still managed to find time to answer my  
36 endless questions. To Lanny, who always made me *believe* I’m capable of understanding the theory  
37 of our field. I’m not, but he still made me feel like I could. To Justin, who I’ve spent more time  
38 bugging in his office about random puzzles than I’ve spent writing this document. His seemingly  
39 infinite patience and willingness to help me with my many, many struggles has been invaluable.

40 To all of the friends I made within the UT Counter Strike community. Without them, I would  
41 have finished this dissertation *much* sooner, but all of the memories we’ve made over the years  
42 have been well worth it. To Devanshu and Richard, who would brighten up my day with horrible  
43 puns and surprise visits to my office. To my roommates Travis, Kevin and Luke, whose friendship  
44 has pulled me through some of the most stressful times. To Matteo, Arild, Matthias and Jo, who  
45 converted me from someone who had never heard the acronym “ssh” into a full-fledged computer  
46 nerd. Without their endless support during my times at CERN, I would have been completely lost.

47 To my family, especially my parents and sister, whose love and support during this entire  
48 process (a.k.a. my life) cannot be overstated. Their encouragement and belief in me as I pursue my  
49 passions has been a constant source of strength. To my fianceé Jaynee, who has given me enough  
50 happiness and love to last a lifetime, which is *just* enough to offset the stress and anxiety of writing a  
51 dissertation. I am so very much excited to spend the rest of my life with her. To Jaynee’s family, who  
52 have welcomed me into their family with open arms and given me plenty of indispensable guidance  
53 during these past few years.

54

## Stranger Things at the LHC

55

Publication No. \_\_\_\_\_

56

Ryan Patrick Hannigan, Ph.D.

57

The University of Texas at Austin, 2023

58

Supervisor: Christina Markert

59        Quantum chromodynamics (QCD) is the branch of fundamental particle physics  
60 that studies the strong interaction, which is responsible for binding quarks and gluons  
61 into the familiar protons and neutrons that compose almost all ordinary matter. One  
62 of the most exciting predictions of this theory is the existence of a new state of matter,  
63 known as the quark-gluon plasma (QGP). At extreme temperatures and densities,  
64 protons and neutrons dissolve into their constituent quarks and gluons, forming a  
65 soup-like plasma of deconfined partons. This QGP is thought to have existed in the  
66 early universe, thus studying its formation and properties can help answer questions  
67 about the evolution of the universe and the nature of the strong force. However,  
68 recreating the extreme conditions of the early universe requires smashing together  
69 heavy nuclei at *very* high energies. This can only be done at the world's most powerful  
70 particle accelerators, making the QGP the most expensive soup on the menu.

71        Unfortunately, producing the QGP in these heavy ion collisions has a major draw-  
72 back; it is only created for around  $10^{-23}$  seconds, making it impossible to study di-  
73 rectly with a detector. Instead, there are a few key experimental observables that  
74 are associated with the formation of this plasma which can be studied in a detector.  
75 One such signature of QGP formation is known as strangeness enhancement, where  
76 the production of strange quarks within the QGP is enhanced relative to the stan-  
77 dard up and down quarks that compose protons and neutrons. Previously believed  
78 to be unique to heavy ion collisions, recent measurements have indicated that this  
79 enhancement is also present in high multiplicity proton-proton (pp) and proton-lead  
80 (p-Pb) systems as well. While statistical and phenomenological models are capable of  
81 describing this enhancement in these smaller collision systems, the microscopic origins  
82 of strangeness enhancement are not well understood.

83        Jets, which are streams of hadrons in the detector produced by an initial hard  
84 scattering of the partons within the colliding nuclei, can be used to illuminate the  
85 underlying processes that produce these strange particles. By measuring the angular  
86 correlation between a high-momentum trigger hadron (as a proxy for a jet axis) and  
87 a lower momentum strange hadron, it is possible to differentiate the strangeness-  
88 producing mechanisms between hard (jet-like) and soft (underlying event) processes.  
89 This technique can be used to study the production of strangeness as a function of  
90 multiplicity in these regimes, giving insight into the origins of the observed enhance-  
91 ment.

92        This thesis presents the first measurements of hadron(h)- $\Lambda$  azimuthal angular cor-

93 relations in p–Pb collisions at  $\sqrt{s_{NN}} = 5.02$  TeV using the ALICE detector at the  
94 LHC. These correlation measurements are used to extract the  $\Lambda$  yields in different  
95 kinematic regions, as well as obtain the widths of the jets to provide more context for  
96 the observed jet production. These results are studied as a function of the  $\Lambda p_T$  and  
97 collision multiplicity, which can be used to quantify the strangeness enhancement in  
98 these different kinematic regimes. Comparisons with theoretical predictions are also  
99 made to provide a framework for interpreting the results of this thesis. Moreover,  
100 these measurements are compared with published measurements of the  $\phi(1020)$  me-  
101 son, which utilized similar techniques, to investigate the differences between open  
102 ( $|S| > 1$ ) and hidden ( $|S| = 0$ ) strangeness production. These strange measurements  
103 will hopefully provide new insight into the production of strangeness in smaller col-  
104 lision systems, thus further constraining the microscopic origins of strangeness en-  
105 hancement.

# Contents

107	Acknowledgements . . . . .	v
108	List of Figures . . . . .	xi
109	List of Tables . . . . .	xxv
110	Chapter One: Introduction . . . . .	1
111	1.1 What is fundamental? . . . . .	2
112	1.2 The Standard Model . . . . .	8
113	1.3 Quantum chromodynamics . . . . .	10
114	1.4 Heavy ion collisions . . . . .	19
115	1.5 Experimental signatures of QGP formation . . . . .	23
116	1.6 Theoretical models . . . . .	30
117	Chapter Two: Experimental Apparatus . . . . .	39
118	2.1 The LHC . . . . .	39
119	2.2 The ALICE Detector . . . . .	40
120	2.3 The Inner Tracking System . . . . .	43
121	2.4 The Time Projection Chamber . . . . .	52
122	2.5 The Time of Flight detector . . . . .	56
123	2.6 The Electromagnetic Calorimeter . . . . .	57
124	2.7 The VZERO Detector . . . . .	58
125	Chapter Three: Analysis Motivation and Methodology . . . . .	60
126	3.1 Motivation . . . . .	60
127	3.2 Methodology . . . . .	64
128	Chapter Four: Analysis Details . . . . .	70

129	4.1 Dataset and event selection . . . . .	70
130	4.2 Charged hadron track selection . . . . .	71
131	4.3 $\Lambda$ reconstruction . . . . .	73
132	4.4 Reconstruction efficiency . . . . .	80
133	4.5 Corrections to the correlation distributions . . . . .	83
134	4.6 Systematic uncertainties . . . . .	100
135	4.7 Cross-checks . . . . .	148
136	Chapter Five: Results and Discussion . . . . .	161
137	5.1 Quick recap: motivation and methodology . . . . .	161
138	5.2 Per-trigger $\Delta\varphi$ distributions . . . . .	162
139	5.3 Per-trigger jet-like yields and jet widths . . . . .	164
140	5.4 Model comparisons . . . . .	170
141	5.5 Comparison with the $\phi(1020)$ . . . . .	182
142	Chapter Six: Summary and outlook . . . . .	185
143	6.1 Future outlook . . . . .	188
144	Appendix A: Resonance technique for $\Lambda$ reconstruction . . . . .	189
145	A.1 Introduction . . . . .	189
146	A.2 Combinatorial background estimation . . . . .	189
147	A.3 Signal and sideband regions . . . . .	191
148	A.4 Corrections to the h- $\Lambda$ distributions . . . . .	194
149	A.5 MC closure test . . . . .	195
150	A.6 Some additional results . . . . .	196
151	Bibliography . . . . .	199

## List of Figures

153	1.1	Dimitri Mendeleev’s periodic table of elements from the late 1800s, taken 154      from [4]. The elements are grouped by similar chemical properties, and 155      the gaps in the table are where Mendeleev predicted that new elements 156      would be discovered. . . . .	2
157	1.2	The “Eightfold Way” diagrams of the $J = 1/2$ mesons (left) and $J = 3/2$ 158      baryons (right) plotted against strangeness and electric charge. Under- 159      standing the underlying symmetry group that gives rise to such patterns <sup>1</sup> 160      ultimately led to the development of the quark model. While the original 161      patterns were found using isotopic spin and hypercharge, it is trivial to 162      convert between the two using the Gell-Mann-Nishijima formula [19], [20]. . . . .	4
163	1.3	The energy distribution of electrons scattered off of protons at an initial 164      electron energy of 10 GeV and a scattering angle of 6 degrees. The large 165      spike on the left side of the distribution corresponds to the elastic scat- 166      tering of the electron off the proton, and the “bumps” correspond to the 167      inelastic scattering of the electron off the proton. The “background” un- 168      derneath the bumps and the apparent continuum of events at even lower 169      values of the scattered electron energy correspond to a mess of unknown 170      particles being produced. The behavior of this continuum with respect to 171      the scattering angle and the scattered electron energy ultimately led to 172      the conclusion that the proton was not fundamental. . . . .	6
173	1.4	A schematic of the field lines between two electrically charged particles 174      (left) and two quarks (right). The field lines between the quarks are pulled 175      together due to the self-interaction of the gluons, whereas the electric field 176      lines are not. . . . .	14
177	1.5	The value of the strong coupling constant $\alpha_s$ as a function of momentum 178      transfer $Q$ , which represents the energy scale of the interaction. . . . .	15
179	1.6	A diagram depicting the formation of a jet within the Lund model from 180      an initial hard scattering of partons, adapted from [61]. The vertices rep- 181      resent perturbative QCD processes, the shaded regions represent string 182      fragmentation/hadronization, and the outgoing arrows represent the re- 183      sulting hadrons (which may decay further). . . . .	17

184	1.7	A phase diagram of the QGP, taken from [64]. The axes are temperature 185 and baryon density, and the orange band represents the phase transition 186 from normal hadronic matter to the QGP. . . . .	18
187	1.8	A schematic of the evolution of the universe, taken from [60]. The QGP 188 phase of the universe on this diagram lies roughly between $10^{-10}$ and $10^{-5}$ 189 seconds after the Big Bang. . . . .	18
190	1.9	A schematic of the formation and evolution of the QGP in a heavy ion 191 collision. The QGP is formed in the overlap region of the two colliding 192 nuclei, and then expands and cools very quickly. . . . .	20
193	1.10	A schematic of a heavy ion collision with impact parameter $b$ , taken from [68].	21
194	1.11	The distribution of Pb–Pb collision events as a function of event activity 195 in the ALICE VZERO detector, taken from [70]. . . . .	23
196	1.12	A schematic of the formation of dijets in pp and A–A collisions, taken 197 from [75]. . . . .	25
198	1.13	Hadron yields corresponding to the near-side jet (near $\Delta\varphi = 0$ ) and the 199 away-side jet ( $\Delta\varphi = \pm\pi$ ), taken from [76]. In pp and minimum bias Au– 200 Au collisions, the away-side jet is present. However, at high centrality 201 (0–10%), the away-side jet completely disappears. . . . .	26
202	1.14	A schematic of the formation of elliptic flow in a heavy ion collision. The 203 initial anisotropy in coordinate space results in a pressure gradient that 204 causes a momentum space anisotropy in the final state hadrons. . . . .	27
205	1.15	The four leading-order Feynman diagrams responsible for the production 206 of $s\bar{s}$ pairs in the QGP, adapted from [18]. Diagrams (a), (b) and (c) are 207 the gluon fusion processes, while diagram (d) is the quark-based process.	29
208	1.16	The particle ratios of strange hadrons to pions as a function multiplicity 209 for different collision systems (left) and those same ratios normalized to 210 an inclusive pp sample (right). The ratios appear to only depend on the 211 multiplicity of the collision, and not the collision system. Taken from [87].	30
212	1.17	The Lund string model, with pre-hadrons and leading hadrons labeled. .	32
213	1.18	The effective quark-quark (green), quark-gluon (blue), and gluon-gluon 214 (red) interactions as a function of parton density in DQPM, taken from [92].	34
215	1.19	The cells within PHSD. If the energy density of the cell is greater than 216 the critical energy density, the pre-hadrons dissolve into partons. . . . .	36

217	1.20	A schematic of the elementary interaction in EPOS LHC in which many parton-parton interactions are occurring simultaneously [99]. . . . .	37
219	2.1	A diagram depicting the LHC with its various main detectors shown underground. Illustration by Philippe Mouche, taken from [113] . . . . .	40
221	2.2	A 3-D schematic of the ALICE detector, with labels for all of the sub-detectors, taken from [114]. Note the humans-for-scale in the bottom left of the diagram. . . . .	41
224	2.3	A diagram showing the cylindrical coordinate system used to describe the ALICE detector. . . . .	42
226	2.4	A schematic of the ITS showing the six layers of silicon detectors, taken from [116]. . . . .	44
228	2.5	A schematic of the ITS upgrade, showing the seven layers of silicon detectors. . . . .	47
229	2.6	A diagram showing the basic operating principle of a MAPS pixel. . . . .	48
230	2.7	A block diagram showing the logic embedded on top of a single ALPIDE pixel. . . . .	49
232	2.8	The signal that was read out from the ALPIDE chip after sending an extremely technical digital input pattern. . . . .	50
234	2.9	A schematic of the ITS readout system, showing the various components of the system. . . . .	52
236	2.10	A picture of a readout unit in its (not-so) natural habitat at the University of Texas at Austin. The heat sink and fan are covering the main SRAM FPGA, and to its north-east is the flash FPGA. . . . .	53
239	2.11	A schematic of the TPC field cage, taken from [126] . . . . .	54
240	2.12	The energy loss signal for different particle species using the ALICE TPC gas mixture, taken from [129]. The solid lines represent the expected energy loss signal for each particle species (Equation 2.9). . . . .	55
243	2.13	The time of flight signal $\beta_{\text{TOF}}$ measured in 5.02 TeV Pb–Pb collisions for different particle species as a function of momentum [132]. The curves are labeled with the particle species they correspond to. . . . .	57
246	2.14	A schematic of the EMCal [135], along with the module and supermodule structure [136]. . . . .	58

248	3.1	The enhancement of strange hadrons relative to pions as a function of event multiplicity in pp, p–Pb, and Pb–Pb collisions at ALICE, taken from [87]. . . . .	61
251	3.2	The $p_T$ -integrated $\Lambda$ /pion ratio as a function of event multiplicity in pp, p–Pb, and Pb–Pb collisions at ALICE. . . . .	63
253	3.3	A cartoon of a Pb–Pb (p–Pb) collision that produces particles in the near- and away-side jets, along with the UE. The corresponding regions in the $\Delta\varphi$ distribution are highlighted on the right. . . . .	64
256	3.4	A simple diagram showing the differences between the generation of the raw distribution $S(\Delta\varphi, \Delta\eta)$ (left) and the mixed-event distribution $B(\Delta\varphi, \Delta\eta)$ (right). The yellow tracks are those observed by the detector. The raw distribution is obtained by looking at trigger-associated pairs within the same event, whereas the mixed-event distribution is generated from pairs that come from separate events. Note that both $\Delta\varphi$ and $\Delta\eta$ cannot be easily shown on a 2D plot, but the distributions are filled with both quantities. . . . .	67
264	3.5	Examples of the h– $\Lambda$ same-event distribution $S(\Delta\varphi, \Delta\eta)$ (left), mixed-event distribution $B(\Delta\varphi, \Delta\eta)$ (middle), and fully corrected correlation function $C_{\text{yield}}(\Delta\varphi, \Delta\eta)$ (right). . . . .	68
267	4.1	The $p_T$ (left), $\varphi$ (middle), and $\eta$ (right) distributions for the trigger hadrons in the multiplicity range 0–20%. . . . .	72
269	4.2	The $p_T$ (left), $\varphi$ (middle), and $\eta$ (right) distributions for the associated hadrons in the multiplicity range 0–20%. The dips observed in the $\varphi$ distribution are due to the TPC sector boundaries. . . . .	73
272	4.3	A diagram depicting a typical $V^0$ decay with labels for the most important kinematic variables. The diagram was taken from [145]. . . . .	74
274	4.4	$n\sigma$ for protons (left) and pions (right) in the TPC detector as a function of $p_T$ . . . . .	76
276	4.5	$n\sigma$ for protons (left) and pions (right) in the TOF detector as a function of $p_T$ . . . . .	76
278	4.6	$n\sigma$ in TOF vs $n\sigma$ in TPC for protons (left) and pions (right). No continuation is observed for both of the particle species. . . . .	77

280	4.7	Invariant mass distributions in the 0-20% (top), 20-50% (middle), and 281 50-80% (bottom) multiplicity bins for the $\Lambda$ candidates which pass the 282 selection criteria with $1.5 < p_T < 2.5 \text{ GeV}/c$ (left) and $2.5 < p_T < 4.0 \text{ GeV}/c$ (right). A Voigtian signal + straight-line background fit to the 283 data is shown in blue, with just the background fit shown in red. For 284 these plots, the $\Lambda$ s were only reconstructed in events with a trigger hadron.	79
286	4.8	Efficiency vs. $p_T$ for trigger (left) and associated (right) hadrons. While 287 they may look identical, the associated hadron efficiency is slightly lower 288 due to the stricter selection criteria. . . . .	81
289	4.9	Efficiency vs. $p_T$ (left) and $\eta$ (right) for $\Lambda$ reconstruction in each multi- 290 plicty bin, along with an integrated 0-100% point in red. . . . .	82
291	4.10	2-D non-acceptance corrected h- $\Lambda$ angular correlations for the 0-20% (top), 292 20-50% (middle), and 50-80% (bottom) multiplicity bins for $1.5 < p_T <$ 293 $2.5 \text{ GeV}/c$ (left) and $2.5 < p_T < 4.0 \text{ GeV}/c$ (right). . . . .	85
294	4.11	2-D non-acceptance corrected h-h angular correlations for the 0-20% (top), 295 20-50% (middle), and 50-80% (bottom) multiplicity bins for $1.5 < p_T <$ 296 $2.5 \text{ GeV}/c$ (left) and $2.5 < p_T < 4.0 \text{ GeV}/c$ (right). . . . .	86
297	4.12	2-D mixed-event h- $\Lambda$ angular correlations for the 0-20% (top), 20-50% 298 (middle), and 50-80% (bottom) multiplicity bins for $1.5 < p_T < 2.5 \text{ GeV}/c$ 299 (left) and $2.5 < p_T < 4.0 \text{ GeV}/c$ (right). The $Z_{\text{vtx}}$ bins are merged 300 together for these plots. . . . .	87
301	4.13	2-D mixed-event h-h angular correlations for the 0-20% (top), 20-50% 302 (middle), and 50-80% (bottom) multiplicity bins for $1.5 < p_T < 2.5 \text{ GeV}/c$ 303 (left) and $2.5 < p_T < 4.0 \text{ GeV}/c$ (right). The $Z_{\text{vtx}}$ bins are merged 304 together for these plots. . . . .	88
305	4.14	Invariant mass distribution of $p\pi$ pairs in the 20-50% multiplicity class. 306 The signal region is shown in light green, and the sideband region is shown 307 in light pink. The correlation distribution in the sideband region is used 308 to remove the combinatorial background from the signal region. . . . .	90
309	4.15	The signal (top) and sideband (bottom) distributions $C_{\text{signal}}^{\text{h-p}\pi}$ and $C_{\text{SB}}^{\text{h-p}\pi}$ 310 for the lower (left) and higher (right) associated $p_T$ bins. All plots were 311 generated in the 0-20% multiplicity class. . . . .	91

312	4.16 Demonstration of the track merging effect for h- $\Lambda$ pairs, whereby we see a dip in the reconstructed distribution at small $\Delta\varphi$ and $\Delta\eta$ when compared to the MC ground truth (left). This dip is not present at large $\Delta\eta$ (right), but we also lose nearly the entirety of our near-side peak. . . . .	93
316	4.17 The reconstructed/ground truth ratios of the 2D $C(\Delta\varphi, \Delta\eta)$ distributions for h-(secondary pions) (left) and h-(primary pions) (right). The suppression at smaller $\Delta\varphi, \Delta\eta$ is clearly seen in the secondary case, but is not observable in the primary case, indicating a decay-length dependence. . .	94
320	4.18 The reconstructed and ground truth $\Delta\varphi$ distributions in the $-1.2 < \Delta\eta < 1.2$ region for h-(secondary pions) with $0.15 < p_T < 2$ (left) and $2 < p_T < 4$ (right). The suppression at smaller $\Delta\eta, \Delta\varphi$ is clearly seen in the higher momentum bin, but not present in the lower one. . . . .	95
324	4.19 The $\epsilon_{\text{pair}}(\Delta\varphi, \Delta\eta)$ templates for the track merging correction in the lower ( $1.5 < p_T < 2.5$ GeV/ $c$ , left) and higher ( $2.5 < p_T < 4.0$ GeV/ $c$ , right) associated momentum bins. While it may be difficult to observe, the lower $p_T$ bin has a minimum dip of around 0.84, whereas the higher $p_T$ bin has a minimum dip of around 0.81, reflecting the $p_T$ dependence discussed in this section. . . . .	97
330	4.20 2-D fully-corrected h- $\Lambda$ angular correlations for the 0-20% (top), 20-50% (middle), and 50-80% (bottom) multiplicity bins for $1.5 < p_T < 2.5$ GeV/ $c$ (left) and $2.5 < p_T < 4.0$ GeV/ $c$ (right). . . . .	98
333	4.21 2-D fully-corrected h-h angular correlations for the 0-20% (top), 20-50% (middle), and 50-80% (bottom) multiplicity bins for $1.5 < p_T < 2.5$ GeV/ $c$ (left) and $2.5 < p_T < 4.0$ GeV/ $c$ (right). . . . .	99
336	4.22 The h- $\Lambda$ $\Delta\varphi$ distributions within the 0-20% (top), 20-50% (middle), and 50-80% (bottom) multiplicity bins in the lower associated $p_T$ bin for each of the signal region variations (left) with the ratios to the nominal distribution (right). . . . .	106
340	4.23 The h- $\Lambda$ $\Delta\varphi$ distributions within the 0-20% (top), 20-50% (middle), and 50-80% (bottom) multiplicity bins in the higher associated $p_T$ bin for each of the signal region variations (left) with the ratios to the nominal distribution (right). . . . .	107
344	4.24 The h- $\Lambda$ $\Delta\varphi$ distributions within the 0-20% (top), 20-50% (middle), and 50-80% (bottom) multiplicity bins in the lower associated $p_T$ bin for each of the sideband region variations (left) with the ratios to the nominal distribution (right). . . . .	108

348	4.25 The h- $\Lambda$ $\Delta\varphi$ distributions within the 0-20% (top), 20-50% (middle), and 349 50-80% (bottom) multiplicity bins in the higher associated $p_T$ bin for each 350 of the sideband region variations (left) with the ratios to the nominal 351 distribution (right). . . . .	109
352	4.26 The h- $\Lambda$ $\Delta\varphi$ distributions within the 0-20% (top), 20-50% (middle), and 353 50-80% (bottom) multiplicity bins in the lower associated $p_T$ bin for each 354 of the PID cut variations (left) with the ratios to the nominal distribution 355 (right). . . . .	110
356	4.27 The h- $\Lambda$ $\Delta\varphi$ distributions within the 0-20% (top), 20-50% (middle), and 357 50-80% (bottom) multiplicity bins in the higher associated $p_T$ bin for each 358 of the PID cut variations (left) with the ratios to the nominal distribution 359 (right). . . . .	111
360	4.28 Barlow check for the signal (left), sideband (middle), and PID (right) 361 variations in the 0-20% multiplicity bin. The red lines represent $N\sigma_{RB} =$ 362 $\pm 1$ , and if the majority of the points fall within the red lines (across 363 all $\Delta\varphi$ , multiplicity and $p_T$ bins), they are excluded from the systematic 364 uncertainty calculation. . . . .	112
365	4.29 A visual depiction of the final systematic errors for the h- $\Lambda$ $\Delta\varphi$ distribu- 366 tions for each multiplicity bin in the low (left) and high (right) associated 367 $p_T$ bins. The total systematic error is shown in black. . . . .	114
368	4.30 Visual depiction of the multiplicity-uncorrelated systematic errors for the 369 h- $\Lambda$ $\Delta\varphi$ distributions for each multiplicity bin in the low (left) and hig 370 (right) associated $p_T$ bins, along with the total systematic error shown in 371 black. . . . .	115
372	4.31 The $v_2$ values for identified hadrons as a function of $p_T$ , taken from [158].	118
373	4.32 The published [155] $p_T$ spectra for $\Lambda$ baryons (top) and charged hadrons 374 ( $\approx$ pions) (bottom), used to compute the weighted average of the $v_2$ coef- 375 ficients across the wide momentum bins used in this analysis. . . . .	119
376	4.33 Examples of the underlying event fit using the $v_2$ -based procedure for the 377 h- $\Lambda$ (left) and h-h (right) $\Delta\varphi$ distributions in the 0-20% multiplicity bin 378 in the higher associated $p_T$ bin. . . . .	120
379	4.34 The h- $\Lambda$ (left) and h-h (right) $\Delta\varphi$ distributions in the 0-20% multiplicity 380 bin and higher $p_T$ bin at small and large values of $\Delta\eta$ , with the UE fit using 381 the $v_2$ -based procedure shown in blue. The fits are in good agreement with 382 data in both cases. . . . .	120

383	4.35	The final per-trigger h- $\Lambda$ $\Delta\varphi$ correlation distributions with the full double Gaussian fit for the 0-20% (top), 20-50% (middle), and 50-80% (bottom) multiplicity bins in the lower (left) and higher (right) associated $p_T$ bins. The UE fit is also shown as a dashed line. . . . .	124
387	4.36	The final per-trigger h-h $\Delta\varphi$ correlation distributions with the full double Gaussian fit for the 0-20% (top), 20-50% (middle), and 50-80% (bottom) multiplicity bins in the lower (left) and higher (right) associated $p_T$ bins. The UE fit is also shown as a dashed line. . . . .	125
391	4.37	The final per-trigger h- $\Lambda$ $\Delta\varphi$ correlation distributions with the von Mises fit for the 0-20% (top), 20-50% (middle), and 50-80% (bottom) multiplicity bins in the lower (left) and higher (right) associated $p_T$ bins. The UE fit with $v_2$ contribution is also shown as a dashed line. . . . .	128
395	4.38	The final per-trigger h-h $\Delta\varphi$ correlation distributions with the von Mises fit for the 0-20% (top), 20-50% (middle), and 50-80% (bottom) multiplicity bins in the lower (left) and higher (right) associated $p_T$ bins. The UE fit with $v_2$ contribution is also shown as a dashed line. . . . .	129
399	4.39	The Barlow check for the yield extraction procedure in the 0-20% multiplicity bin for the lower (left) and higher (right) associated $p_T$ bins. The red lines represent $N_{\sigma_{RB}} = \pm 1$ , and if the majority of the points from a given procedure fall within these lines (across all multiplicity and momentum bins), the procedure is excluded from the systematic uncertainty calculation. . . . .	130
405	4.40	The deviation from the nominal h- $\Lambda$ per-trigger yields for each yield extraction procedure variation (post Barlow check) in each kinematic region for the 0-20% (top), 20-50% (middle), and 50-80% (bottom) multiplicity bins in the lower (left) and higher (right) associated $p_T$ bins. The systematic uncertainty for the yield extraction procedure is calculated by taking the RMS of these deviations for each kinematic region. . . . .	133
411	4.41	The deviation from the nominal h-h per-trigger yields for each yield extraction procedure variation (post Barlow check) in each kinematic region for the 0-20% (top), 20-50% (middle), and 50-80% (bottom) multiplicity bins in the lower (left) and higher (right) associated $p_T$ bins. The systematic uncertainty for the yield extraction procedure is calculated by taking the RMS of these deviations for each kinematic region. . . . .	134
417	4.42	The Von Mises (left) and Gaussian (right) dist with $\kappa = 1$ and $\sigma = 1$ . Note that the von Mises distribution does not approach zero at large x, while the Gaussian does. . . . .	136

420	4.43 The $p_T$ distributions of $\Lambda$ candidates with and without the TOF signal requirement. The mean $p_T$ of the $\Lambda$ candidates with daughters that generate a TOF signal is nearly 10% higher than those without this requirement, which indicates that the requiring a TOF signal for the $\Lambda$ daughters introduces a physical bias. . . . .	137
425	4.44 The resulting von Mises fits and extracted jet widths after the signal, sideband and PID cut variations are applied to the h- $\Lambda$ $\Delta\varphi$ distributions. . . . .	140
427	4.45 The resulting h- $\Lambda$ (top) and h-h (bottom) von Mises fits and extracted jet widths in each multiplicity and momentum bin after each variation of the fitting procedure. . . . .	141
430	4.46 Barlow check for the width extraction procedure for the signal (left), sideband (middle), and PID (right) variations in the 20-50% multiplicity bin. The red lines represent $N\sigma_{RB} = \pm 1$ , and if the majority of the points fall within the red lines (across all $p_T$ and multiplicity bins), they are excluded from the width systematic uncertainty calculation. . . . .	143
435	4.47 Final systematic errors for the h- $\Lambda$ $\Delta\varphi$ near-side (top) and away-side (bottom) width extraction for each multiplicity bin in the lower (left) and higher (right) associated $p_T$ bins. . . . .	145
438	4.48 Final systematic errors for the h-h $\Delta\varphi$ near-side (top) and away-side (bottom) width extraction for each multiplicity bin in the lower (left) and higher (right) associated $p_T$ bins. . . . .	146
441	4.49 The resulting h- $\Lambda$ (top) and h-h (bottom) von Mises fits and extracted jet widths in the 20-50% multiplicity bin for each momentum bin after random variations of the individual $\Delta\varphi$ bins within the topological selection (h- $\Lambda$ ) and tracking efficiency (h-h) uncertainties from Table 4.6. . . . .	146
445	4.50 The reconstructed (pink) and ground-truth (blue) h- $\Lambda$ $\Delta\varphi$ distributions in the lower (top) and higher (bottom) associated $p_T$ bins, along with a (reconstructed)/(ground-truth) ratio and straight-line fit with errors shown as dashed lines. The ratio is consistent with unity, and thus the corrections applied to the h- $\Lambda$ distributions are valid. . . . .	150
450	4.51 The reconstructed (pink) and ground-truth (blue) h-h $\Delta\varphi$ distributions in the lower (top) and higher (bottom) associated $p_T$ bins, along with a (reconstructed)/(ground-truth) ratio and straight-line fit with errors shown as dashed lines. Again, the ratio is consistent with unity, and thus the corrections applied to the h-h distributions are valid. . . . .	151

455	4.52	The $p_T$ spectra shape of the $\phi$ (triangles) and $\Lambda$ (squares) in p–Pb collisions at $\sqrt{s_{NN}} = 5.02$ TeV in the 0-5% (red) and 60-80% (green) multiplicity bins. Both spectra in the 0-5% have been normalized to unity, whereas the 60-80% spectra has been normalized to 0.5 for visibility. The $\Lambda$ and $\phi$ spectra shapes are very similar in both multiplicity bins. . . . .	153
460	4.53	The fits to the momentum spectra of the $\phi$ (left) and $\pi$ (right) in the 0-5% (red) and 60-80% (green) multiplicity bins, with fit function given by Equation 4.33. The $2 < p_T < 4$ GeV/ $c$ momentum window is highlighted in blue. . . . .	154
464	4.54	A diagram showing the effect of multiple triggers on the per-trigger pair-wise yield. In the first event, there is a single trigger with three associated particles, so the pair-wise yield is equal to the number of associated particles. In the second event, there are two triggers with three associated particles, so the pair-wise yield is twice the number of associated particles.	155
469	4.55	A log-plot showing the number of triggers per event across the entire data sample. Only a small fraction of events have at least a single trigger, and of those events, only a small fraction have more than one trigger. . . . .	156
472	4.56	The per-trigger h- $\Lambda$ (top) and h-h (middle) $\Delta\varphi$ distribution comparison between using a single trigger (closed points) and all triggers (open points) in a given event, along with the (single trigger)/(all trigger) distribution ratio (bottom), for the 0-20% (left), 20-50% (center), and 50-80% (bottom) multiplicity bins in the associated momentum range $2.0 < p_T < 4.0$ GeV/ $c$ . The distributions are nearly identical up to a $\approx 0.95$ scale factor, which is constant as a function of multiplicity. . . . .	157
479	4.57	Comparison of the dihadron $\Delta\varphi$ correlations between the $\phi$ and $\Lambda$ analyses for the 0-20% (left), 20-50% (middle), and 50-80% (right) multiplicity bins, taken in the $2.0 < p_T < 4.0$ GeV/ $c$ associated momentum range. They are functionally identical for all multiplicity bins. . . . .	159
483	4.58	The final per-trigger h- $\Lambda$ $\Delta\varphi$ correlations for $\Lambda$ s reconstructed using the resonance technique (blue) and the $V^0$ -based technique (red) in the 0-20% (left), 20-50% (middle), and 50-80% (right) multiplicity bins, taken in the associated momentum range $2.0 < p_T < 4.0$ GeV/ $c$ , after the subtraction of the UE. The distributions show good agreement across all multiplicity bins, indicating that the $V^0$ -based reconstruction technique is not introducing a bias in the correlation shape. . . . .	160

490	5.1	A cartoon of a Pb–Pb (p–Pb) collision that produces particles in the near- 491 and away-side jets, along with the UE. The the corresponding regions in 492 the $\Delta\varphi$ distribution are highlighted on the right. . . . .	162
493	5.2	The final per-trigger h- $\Lambda$ $\Delta\varphi$ distributions for the 0-20% (top), 20-50% 494 (middle), and 50-80% (bottom) multiplicity bins for $1.5 < p_T < 2.5 \text{ GeV}/c$ 495 (left) and $2.5 < p_T < 4.0 \text{ GeV}/c$ (right). . . . .	163
496	5.3	The final per-trigger h-h $\Delta\varphi$ distributions for the 0-20% (top), 20-50% 497 (middle), and 50-80% (bottom) multiplicity bins for $1.5 < p_T < 2.5 \text{ GeV}/c$ 498 (left) and $2.5 < p_T < 4.0 \text{ GeV}/c$ (right). . . . .	164
499	5.4	The h- $\Lambda$ (top) and h-h (bottom) $\Delta\varphi$ distributions for each multiplicity 500 class with $1.5 < p_{T,\text{assoc}} < 2.5 \text{ GeV}/c$ , with statistical (systematic) uncer- 501 tainties shown as vertical lines (shaded boxes). The multiplicity classes are 502 plotted from most central (left) to least central (right). The UE estimate 503 is shown as a dashed line, and is taken as the average of the distribution 504 in the regions $[-\frac{\pi}{2}, -\frac{\pi}{4}) \cup [\frac{\pi}{4}, \frac{5\pi}{8}) \cup [\frac{11\pi}{8}, \frac{3\pi}{2})$ . . . . .	165
505	5.5	The h- $\Lambda$ (top) and h-h (bottom) $\Delta\varphi$ distributions for each multiplicity 506 class with $2.5 < p_{T,\text{assoc}} < 4.0 \text{ GeV}/c$ , with statistical (systematic) uncer- 507 tainties shown as vertical lines (shaded boxes). The multiplicity classes are 508 plotted from most central (left) to least central (right). The UE estimate 509 is shown as a dashed line, and is taken as the average of the distribution 510 in the regions $[-\frac{\pi}{2}, -\frac{\pi}{4}) \cup [\frac{\pi}{4}, \frac{5\pi}{8}) \cup [\frac{11\pi}{8}, \frac{3\pi}{2})$ . . . . .	166
511	5.6	The per-trigger pair-wise yields $Y_{\text{near}}$ , $Y_{\text{away}}$ as a function of multiplicity 512 percentile for the h- $\Lambda$ (square markers) and h-h (circle markers) azimuthal 513 correlations in the lower (left) and higher (right) associated $p_T$ ranges. The 514 statistical (systematic) uncertainties are shown as vertical lines (boxes). .	167
515	5.7	The h- $\Lambda$ and h-h near- and away-side peak widths shown as a function of 516 multiplicity for both associated momentum ranges. The statistical (sys- 517 tematic) uncertainties are shown as vertical lines (boxes). . . . .	168
518	5.8	The per-trigger yield ratios $R_i^{\Lambda/h} \equiv Y_i^{h-\Lambda}/Y_i^{h-h}$ ( $i = \text{near-side, away-side,}$ 519 $\text{UE}$ ) as a function of charged particle multiplicity for the lower (left) and 520 higher (right) associated $p_T$ ranges. The statistical (systematic) uncer- 521 tainties are shown as vertical lines (boxes), and a first order polynomial 522 fit to the data is shown as a dashed line. . . . .	169
523	5.9	The multiplicity-integrated per-trigger h-h 2D $\Delta\varphi\Delta\eta$ distributions in data 524 and for each model within the $1.5 < p_T < 2.5 \text{ GeV}/c$ associated momentum 525 bin. . . . .	173

526	5.10 The multiplicity-integrated per-trigger h- $\Lambda$ 2D $\Delta\varphi\Delta\eta$ distributions in data 527 and for each model within the $1.5 < p_T < 2.5 \text{ GeV}/c$ associated momentum 528 bin. . . . .	174
529	5.11 The fraction of events that pass various selection criteria for PHSD (left) 530 and data (right). The right-most bin in both distributions represents the 531 fraction of events that contribute to the h- $\Lambda$ yield, which is 10 times lower 532 in PHSD than it is in data. . . . .	175
533	5.12 The multiplicity-integrated per-trigger h-h $\Delta\varphi$ distributions in data and 534 for each model within the $1.5 < p_T < 2.5 \text{ GeV}/c$ associated momentum bin. 176	
535	5.13 The multiplicity-integrated per-trigger h- $\Lambda$ $\Delta\varphi$ distributions in data and 536 for each model within the $1.5 < p_T < 2.5 \text{ GeV}/c$ associated momentum bin. 177	
537	5.14 The per-trigger pair-wise yields $Y_{\text{near}}$ , $Y_{\text{away}}$ as a function of charged parti- 538 cle multiplicity for the h- $\Lambda$ (square markers) and h-h (circle markers) cor- 539 relations in the lower (left) and higher (right) associated $p_T$ ranges. The 540 statistical (systematic) uncertainties are shown as vertical lines (boxes), 541 and a first order polynomial fit to the data is shown as a dashed line. 542 The same yields predicted by DPMJET are also shown as shaded bands, 543 with the width of the band representing the systematic uncertainty on the 544 model. The ratio of the model to the data is shown in the bottom panel, 545 along with a dashed line drawn at unity. . . . .	179
546	5.15 The h- $\Lambda$ and h-h near- and away-side peak widths shown as a function of 547 multiplicity for both associated momentum ranges, along with a straight- 548 line fit to the data. The statistical (systematic) uncertainties are shown as 549 vertical lines (boxes). The ratios predicted by DPMJET are also presented 550 as shaded bands, with the width of the band represending the systematic 551 uncertainty on the model. The ratio of the model to the data is presented 552 in the bottom panel, along with a dashed line drawn at unity. . . . .	180
553	5.16 The per-trigger pair-wise yield ratios $R_i^{\Lambda/h} \equiv Y_i^{h-\Lambda}/Y_i^{h-h}$ ( $i = \text{near-side}$ , 554 $\text{away-side}$ , UE) as a function of multiplicity in the lower (left) and higher 555 (right) associated momentum ranges. The statistical (systematic) uncer- 556 tainties are shown as vertical lines (boxes). The ratios predicted by DP- 557 MJET are also presented as shaded bands, with the width of the band 558 represending the systematic uncertainty on the model. The ratio of the 559 model to the data is presented in the bottom panel. . . . .	181
560	5.17 Previously published results for the per-trigger pair-wise yield ratios $R_i^{\phi/h} \equiv$ 561 $Y_i^{h-\phi}/Y_i^{h-h}$ ( $i = \text{near-side}$ , $\text{away-side}$ , UE, total) as a function of charged 562 particle multiplicity for lower (left) and higher (right) associated $p_T$ ranges. 182	

563	5.18 The per-trigger pair-wise yield ratios $R_i^{\Lambda/\phi} \equiv Y_i^{h-\Lambda}/Y_i^{h-\phi}$ ( $i = \text{near-side,}$	183
564	$\text{away-side, UE}$ ) as a function of multiplicity in the lower (left) and higher	
565	(right) associated momentum ranges. The statistical (systematic) uncer-	
566	tainties are shown as vertical lines (boxes). The ratios predicted by DP-	
567	MJET are also presented as shaded bands, with the width of the band	
568	representing the systematic uncertainty on the model. The ratio of the	
569	model to the data is presented in the bottom panel. . . . .	
570	A.1 Left: Invariant mass distribution with corresponding Voigt + Polynomial	190
571	fit in the 20-50% multiplicity bin (data). Right: The signal and back-	
572	ground shapes in MonteCarlo (MC). Note that even though MC appears	
573	to have a completely different S/B, the signal shapes should be similar.	
574	The fit in data appears to be massively underestimating the $\Lambda$ signal, as	
575	the MC sample indicates there is $\Lambda$ signal where the total data fit converges	
576	with the BG fit. . . . .	
577	A.2 Left: Invariant mass distribution for reconstructed unlike-sign $p\pi$ pairs	191
578	(black) in the MonteCarlo sample. The like-sign $p\pi$ pair mass distribu-	
579	tion (purple) and unlike-sign rotated $p\pi$ distributions are scaled to match	
580	the unlike-sign distribution outside of the $\Lambda$ signal range. The true com-	
581	binatorial background (red) matches most closely with the like-sign pairs.	
582	Right: The actual $\Lambda$ signal (magenta) compared with the result of sub-	
583	tracting the like-sign from the total unlike-sign $p\pi$ distribution (green).	
584	The two distributions show good agreement. . . . .	
585	A.3 Left: Invariant Mass distribution for unlike-sign $p\pi$ pairs (black) along	192
586	with the like-sign $p\pi$ background (purple) and the sideband region (red) in	
587	the 0-20% multiplicity bin. Right: The extracted signal (green) compared	
588	with the resonance-technique reconstructed signal shape in MonteCarlo	
589	(magenta). The sideband region was chosen to minimize the differences	
590	between these distributions. . . . .	
591	A.4 Efficiency vs. $p_T$ for $\Lambda$ reconstruction using resonance technique for each	193
592	multiplicity bin, along with an integrated 0-100% point in red. There does	
593	not appear to be any significant dependence on multiplicity. Also worth	
594	nothing that the efficiency is higher for this technique when compared to	
595	the V0 technique, as expected (all AOD tracks from V0 finder daughters	
596	are also in total AOD track list). . . . .	
597	A.5 The projected $\Delta\varphi$ distributions for different choices of sideband, taken	194
598	within the $-1.2 < \Delta\eta < 1.2$ region. The correlation shapes are identical	
599	within the statistical errors. . . . .	

600	A.6 The reconstructed (red) and ground-truth (blue) $h\text{-}\Lambda_{\text{res}}$ $\Delta\varphi$ distributions along with a (reconstructed)/(ground-truth) ratio and straight-line fit. The fit is technically consistent with unity, but the statistical fluctuations are quite large. . . . .	195
604	A.7 The reconstructed (red) and ground-truth (blue) $h\text{-}\Lambda_{\text{res}}$ $\Delta\varphi$ distributions along with a (reconstructed)/(ground-truth) ratio and straight-line fit, but instead requiring the reconstructed $\Lambda$ to have a corresponding particle at the generator level to make sideband subtraction unnecessary. The result is no longer consistent with unity at small $\Delta\varphi$ due to the track merging effect, but the non-closure is much smaller than the V0 technique. . . . .	196
610	A.8 The final per-trigger $h\text{-}\Lambda$ $\Delta\varphi$ correlations for $\Lambda$ s reconstructed using the resonance technique (blue) and the $V^0$ -based technique (red) in the 0-20% (left), 20-50% (middle) and 50-80% (right) multiplicity bins, taken in the associated momentum range $2.0 < p_T < 4.0 \text{ GeV}/c$ , after the subtraction of the UE. The distributions show good agreement across all multiplicity bins, indicating that the $V^0$ -based reconstruction technique is not introducing a bias in the correlation shape. . . . .	197
617	A.9 The final $h\text{-}\Lambda$ and $h\text{-}h$ per-trigger pairwise jet yields (top) and $(h\text{-}\Lambda)/(h\text{-}h)$ yield ratios (bottom) vs. multiplicity in the associated momentum range $2.0 < p_T < 4.0 \text{ GeV}/c$ for $\Lambda$ s reconstructed using the resonance technique. The general trends are similar to the nominal $V^0$ technique-based procedure, with larger statistical uncertainties. . . . .	198

## List of Tables

623	1.1	The fermions of the Standard Model for each generation and their corresponding multiplets. The Standard Model does not allow for fermions to leave their respective multiplets. . . . .	10
626	2.1	A summary of the medial system used to determine where a particular chip should be installed. Note that while 99% <i>seems</i> strict, it corresponds to over 5000 misbehaving pixels. . . . .	51
629	4.1	Number of events passing our criteria for each multiplicity bin considered. Here $Z_{vtx}$ refers to the position of the PV along the beam (z) axis. . . . .	71
631	4.2	The track quality cuts applied to the trigger hadrons in this analysis. . . . .	72
632	4.3	The ALICE standard track quality cuts for primary charged hadrons, used for the selection of the associated hadrons in this analysis. . . . .	73
634	4.4	The track quality cuts applied to both the daughter proton and pion tracks used to reconstruct $\Lambda$ candidates. These cuts are intentionally less strict than those applied to the trigger and associated hadrons as the daughter tracks are reconstructed from secondary particles. . . . .	75
638	4.5	Topological selection criteria applied to $\Lambda$ candidates. . . . .	77
639	4.6	The systematic uncertainties for the $\Delta\varphi$ distributions which are not directly calculated in this thesis, instead taken from previous analyses using the same particle species and collision system [151], [154]–[156]. Each source of uncertainty is verified to be independent of multiplicity, but the $\Lambda$ material budget and topological selection uncertainties exhibit a small dependence on $p_T$ . . . . .	102
645	4.7	The variations of the $\Lambda$ invariant mass signal region considered for this analysis. . . . .	103
647	4.8	The variations of the $\Lambda$ invariant mass sideband region considered for this analysis. Note that the “shifted left” sideband falls on the opposite (left) side of the signal region. . . . .	104
650	4.9	The variations of the $\Lambda$ daughter PID cuts considered for this analysis. The “require TOF” variation requires a TOF hit for both the proton and pion, but maintains the nominal values for $ n\sigma_{\text{TPC, TOF}} $ . . . . .	105

653	4.10	The final systematic uncertainties (in percentages) from the h- $\Lambda$ $\Delta\varphi$ distribution generation for each multiplicity and associated $p_T$ bin. . . . .	113
655	4.11	$v_2$ values used in this analysis for each associated $p_T$ bin. The values were calculated as the weighted average of published $p_T$ -differential $v_2$ measurements with the published $p_T$ spectra, taken across the entire associated $p_T$ range. . . . .	117
659	4.12	Final systematic errors (in %) for the per-trigger h- $\Lambda$ yields in each kinematic region, multiplicity, and momentum bin. . . . .	131
661	4.13	Final systematic errors (in %) for the h-h per-trigger yields in each kinematic region, multiplicity, and momentum bin. . . . .	131
663	4.14	Final multiplicity-uncorrelated systematic errors (in %) for the per-trigger h- $\Lambda$ yields in each kinematic region, multiplicity, and momentum bin, used for calculating errors associated with quantities describing trends versus multiplicity (slopes and percent changes). . . . .	132
667	4.15	Final multiplicity-uncorrelated systematic errors (in %) for the h-h per-trigger yields in each kinematic region, multiplicity and momentum bin, used for calculated errors associated with quantities describing trends versus multiplicity (slopes and percent changes). . . . .	132
671	4.16	The final systematic errors from the h- $\Lambda$ $\Delta\varphi$ near-side (NS) and away-side (AS) width extraction for each multiplicity bin in the lower (top) and higher (bottom) associated $p_T$ bins. The total systematic error is calculated by adding each systematic error in quadrature. . . . .	144
675	4.17	The final systematic errors from the h-h $\Delta\varphi$ near-side (NS) and away-side (AS) width extraction for each multiplicity bin in the lower (top) and higher (bottom) associated $p_T$ bins. The total systematic error is calculated by adding each systematic error in quadrature. . . . .	144
679	4.18	The final systematic uncertainties for the h- $\Lambda$ $\Delta\varphi$ distributions, the per-trigger jet and UE yields, and the jet widths in all multiplicity and associated momentum bins. The fraction of the systematic uncertainty which is uncorrelated with multiplicity is reported separately in parentheses for the extracted yields. The low (high) momentum bin is such that $1.5 < p_T^{\text{assoc.}} < 2.5 \text{ GeV}/c$ ( $2.5 < p_T^{\text{assoc.}} < 4.0 \text{ GeV}/c$ ). . . . .	147

685	4.19	The final systematic uncertainties for the h-h $\Delta\varphi$ distributions, the per-trigger jet and UE yields, and the jet widths in all multiplicity and associated momentum bins. The fraction of the systematic uncertainty which is uncorrelated with multiplicity is reported separately in parentheses for the extracted yields. The low (high) momentum bin is such that $1.5 < p_T^{\text{assoc.}} < 2.5 \text{ GeV}/c$ ( $2.5 < p_T^{\text{assoc.}} < 4.0 \text{ GeV}/c$ ). . . . .	147
691	5.1	The percent change in the per-trigger yields from the lowest to highest multiplicity class in the lower and higher associated momentum ranges. The errors reported are obtained using the systematic and statistical uncertainties summed in quadrature. The reported significance is the number of standard deviations away from zero percent change. . . . .	167
696	5.2	The slopes obtained from the straight-line fits to the per-trigger pair-wise $(h-\Lambda)/(h-h)$ yield ratios as a function of multiplicity in both associated momentum ranges. The fits are made using the statistical and systematic errors summed in quadrature. All fits are such that $\chi^2/\text{ndf} < 1$ . . . . .	170
700	5.3	The values of $\langle dN_{\text{ch}}/d\eta \rangle_{ \eta_{\text{lab}} <0.5}$ for each multiplicity class in min bias events (non-triggered) and events with a trigger hadron (triggered events). . . . .	170
702	5.4	The total systematic uncertainties associated with the various width and yield extraction procedures in DPMJet for the $h-\Lambda$ distributions. . . . .	178
704	5.5	The total systematic uncertainties associated with the various width and yield extraction procedures in DPMJet for the $h-h$ distributions. . . . .	178
706	5.6	The slopes obtained from the straight-line fits to the per-trigger pair-wise $(h-\Lambda)/(h-\phi)$ yield ratios as a function of multiplicity in both associated momentum ranges. The fits are made using the statistical and systematic errors summed in quadrature. All fits are such that $\chi^2/\text{ndf} < 1$ . . . . .	184

## Chapter One: Introduction

711 The initial section of this chapter will mostly serve as a historical overview of the  
712 field of particle physics, leading to the development of the **Standard Model**—the  
713 theory that describes all of the fundamental<sup>1</sup> particles and the way in which they  
714 interact with each other. An emphasis will be made on the discovery of quarks, as  
715 the research presented in this thesis is centered around these particles.

716 The second section will more thoroughly introduce the Standard Model, providing  
717 an overview of its three distinct sectors. Words like “fundamental representation”  
718 and “gauge symmetry” will be thrown around, but the goal is to provide a high-level  
719 mathematical overview of the theory without getting bogged down in the details.

720 As this thesis is focused nearly entirely on the strong nuclear force, the remain-  
721 ing sections of the chapter will delve into the details of Quantum ChromoDynamics  
722 (QCD), which is the component of the Standard Model that describes the interactions  
723 between **quarks** and **gluons**—the constituent particles of the more familiar protons  
724 and neutrons. Unfortunately, QCD is enormously complicated and many components  
725 of the theory are not yet fully understood. While this may be disheartening for the-  
726 orists, it is a boon for experimentalists as it provides a wealth of opportunities to  
727 probe the theory in regimes where it is both well- and poorly-understood.

728 To that end, the remainder of the chapter will focus on the ways in which QCD can  
729 be investigated using heavy-ion collisions, with an emphasis on the **Quark-Gluon**  
730 **Plasma** (QGP)—a novel state of nuclear matter that QCD predicts should exist at the  
731 extreme temperatures and densities that are achieved in these collisions. The exper-  
732 imental signatures of QGP formation will also be discussed, with a particular focus  
733 on **strangeness enhancement**—the phenomenon where the production of strange  
734 quarks is enhanced in heavy-ion collisions relative to proton-proton collisions.

---

<sup>1</sup>As of the year 2023, but reading this chapter will hopefully illustrate why this may be subject to change in the (likely very distant) future.

## 735 1.1 What is fundamental?

736 The answer to the question

737 What are the fundamental building blocks of our universe?

738 has changed drastically over the course of human history. The idea that all matter  
739 is composed of smaller, uncuttable pieces has been around since 5th century BCE  
740 when Greek philosophers Democritus and Leucippus first introduced the concept of  
741 an atom [1]. While this idea was mostly motivated by philosophical reasoning, it was  
742 later adopted by the English scientist John Dalton in the 19th century to explain the  
743 results of his chemical experiments, where he found that chemical elements always  
744 combined with each other by discrete units of mass [2]. As scientists discovered more  
745 and more of these elements, the number of “fundamental” building blocks grew as  
746 well. By the late 1800s, over 70 unique chemical elements had been discovered, though  
747 they would often be grouped together due to similar chemical properties using what  
748 chemist Dimitri Mendeleev dubbed the *periodic table of elements* [3]. An example of  
749 the periodic table from the time of Mendeleev can be seen in Figure 1.1. While this  
750 grouping was useful for chemists, it also served as a hint to physicists that perhaps  
751 these elements were not actually fundamental, but rather composed of even smaller  
752 pieces.

		Ti = 50	Zr = 90	? = 180
		V = 51	Nb = 94	Ta = 182
		Cr = 52	Mo = 96	W = 186
		Mn = 55	Rh = 104,4	Pt = 197,4
		Fe = 56	Ru = 104,4	Ir = 198
		Ni = Co = 59	Pd = 106,6	Os = 199
H = 1		Cu = 63,4	Ag = 108	Hg = 200
	Be = 9,4	Zn = 65,2	Cd = 112	
	B = 11	Al = 27,4	? = 68	Uu = 197?
	C = 12	Si = 28	? = 70	Sn = 118
	N = 14	P = 31	As = 75	Sb = 122
	O = 16	S = 32	Se = 79,4	Te = 128?
	F = 19	Cl = 35,5	Br = 80	J = 127
Li = 7	Na = 23	K = 39	Rb = 85,4	Cs = 133
		Ca = 40	Sr = 87,6	Ba = 137
		? = 45	Ce = 92	Tl = 204
		?Er = 56	La = 94	Pb = 207
		?Yt = 60	Di = 95	
		?In = 75,6	Th = 118?	

Figure 1.1: Dimitri Mendeleev’s periodic table of elements from the late 1800s, taken from [4]. The elements are grouped by similar chemical properties, and the gaps in the table are where Mendeleev predicted that new elements would be discovered.

753        Things changed quite a bit around the turn of the 20th century, with scientists  
754 like Rutherford and Chadwick determining that the supposedly indivisible atom was  
755 composed of even smaller sub-atomic particles, eventually named electrons, protons,  
756 and neutrons [5]–[7]. Thus the number of fundamental blocks of matter had decreased  
757 substantially from nearly 100 to just three, but only very briefly. Only months after  
758 the discovery of the neutron, the fundamental anti-particle of the electron—known as  
759 the positron—was discovered in 1932 by Carl Anderson [8]. In the next two decades,  
760 the number of known fundamental particles would skyrocket. In 1947, the muon was  
761 discovered [9], followed by the discovery of a laundry list of particles [10]–[12] that  
762 participate in the same interaction that holds the positively charged protons together  
763 in the nucleus of an atom—the so-called **strong nuclear force**. These “fundamental”  
764 particles were collectively called **hadrons**, which were further separated into lighter  
765 and heavier categories, dubbed **mesons** and **baryons**, respectively [13]. By the late  
766 1960s, the number of known hadrons had grown to well over 100 [14], which is a far  
767 cry from the number of “fundamental” chemical elements that were known to exist  
768 in the 1800s.

769        In the same way that Mendeleev tried to group the elements by their similar  
770 chemical properties, physicists attempted to group the hadrons together based on  
771 their known sub-atomic properties at the time. The first successful attempt at such  
772 a grouping was the **Eightfold Way**, which was independently proposed by Mur-  
773 ray Gell-Mann and Yuval Ne’eman in 1961 [15], [16]. This grouping was found by  
774 examining the following properties of the hadrons:

- 775        1. **Isotopic spin**: a quantum number introduced by Werner Heisenberg in 1932  
776           to try to explain the apparent symmetries between the proton and neutron with  
777           respect to the strong nuclear force [17] (i.e. although the proton and neutron  
778           have different electric charges, the strong interaction does not seem to distinguish  
779           between the two)
- 780        2. **Strangeness**: another quantum number introduced by Gell-Mann and Nishi-  
781           jima in 1953 to explain why some hadrons decayed much more slowly than  
782           expected, but such particles appeared to be created in pairs [18]. In other  
783           words, the strong interaction responsible for the creation of these particles ap-  
784           peared to conserve strangeness, but the weak interaction responsible for the

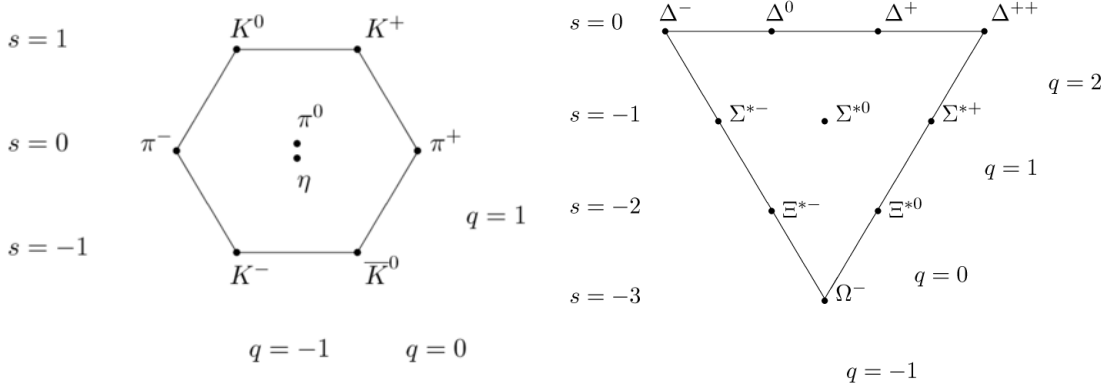


Figure 1.2: The ‘‘Eightfold Way’’ diagrams of the  $J = 1/2$  mesons (left) and  $J = 3/2$  baryons (right) plotted against strangeness and electric charge. Understanding the underlying symmetry group that gives rise to such patterns<sup>3</sup> ultimately led to the development of the quark model. While the original patterns were found using isotopic spin and hypercharge, it is trivial to convert between the two using the Gell-Mann-Nishijima formula [19], [20].

slower decay of these particles did not. This<sup>2</sup> quantity is of utmost importance to this thesis, and will be discussed in more detail in the coming chapters.

Plotting the baryons and mesons in a two-dimensional space based on these two properties revealed striking patterns, as shown in Figure 1.2. Similar to Mendeleev, GellMann also left a blank space<sup>4</sup> where he believed a new particle—the  $\Omega^-$ —would be discovered. The patterns in these diagrams hinted at an underlying symmetry governing the strong nuclear force, and ultimately led to the invention of the very first quark model by Gell-Mann and Zweig in 1964 [21]. This model proposed that all of the hadrons were actually composed of even smaller particles, which Gell-Mann dubbed ‘‘quarks’’. The quark model was able to explain the patterns seen in Figure 1.2 by introducing three different types of fermionic quarks—up, down and strange—along with their corresponding anti-quarks. Baryons would then be composed of three such

---

<sup>2</sup>Strangeness was introduced a few years before the very first quark model, but it now has the modern interpretation which is directly related to the number of strange and anti-strange quarks within a hadron.

<sup>3</sup>Namely  $SU(3)$ , but this is a history lesson. Also the path from  $SU(3)$  to patterns of this type is long and arduous, involving a thorough understanding of representation theory.

<sup>4</sup>The original paper on the Eightfold Way does not contain any of these diagrams, but there are discussions about the properties of particles that should exist if the theory were correct, but had not been observed [15].

797 quarks, whereas mesons would be composed of quark and anti-quark pairs. If the  
798 quark model were correct, the number of fundamental building blocks of matter would  
799 again decrease from over 100 to just 14: electrons, muons, electron neutrinos, muon  
800 neutrinos, up quarks, down quarks, strange quarks, and all of their corresponding  
801 anti-particles.

802 Initially, many physicists believed that the quarks from this model were just a  
803 mathematical abstraction [22]. This possibility did not stop Sheldon Glashow and  
804 James Bjorken from extending the quark model in less than a year after its inception  
805 by introducing a fourth quark: the charm [23]. This new quark was primarily intro-  
806 duced to equalize the number of leptons (four at the time: electron, muon, and their  
807 respective neutrinos) with the number of quarks. The theory was mostly aesthetic [24]  
808 in that the charm quark was not explicitly required by any known mechanisms. It  
809 was only after the Glashow-Iliopoulos-Maiani (GIM) mechanism was introduced in  
810 1970 [25] that the existence of the charm quark became necessary. This mechanism  
811 helped explain why neutral kaons decayed into two muons at a much lower rate than  
812 expected, but it required the existence of a quark with the same charge as the up  
813 quark but with a much larger mass.

814 On the experimental side of things, the notion that protons and neutrons were  
815 fundamental particles was also being challenged. The deep inelastic scattering ex-  
816 periments at the Stanford Linear Accelerator Center (SLAC) performed by Kendall,  
817 Friedman, and Taylor in 1968 [26]–[28] revealed unexpected<sup>5</sup> behavior when probing  
818 the structure of the proton: it appeared to be composed of point-like particles. These  
819 experiments were performed by firing electrons at stationary protons and measuring  
820 the energy distributions of the scattered electrons at different scattering angles. An  
821 example of such a distribution for electrons with initial energies of 10 GeV scattered  
822 at 6 degrees can be seen in Figure 1.3. The large spike on the left side of the dis-  
823 tribution corresponds to the elastic scattering of the electron off the proton, which  
824 was well understood at the time [29]. The “bumps” observed at lower values of the  
825 scattered electron energy were also well understood [30], and they correspond to the  
826 “shallow” inelastic scattering of the electron off the proton, where the proton gets  
827 excited into a so-called *resonance* state (like the  $\Delta$  baryon). However, the “back-  
828 ground” underneath the bumps and the apparent continuum of events at even lower

---

<sup>5</sup>Depending on who you asked at the time, both the three and four quark models were not universally accepted.

values of the scattered electron energy correspond to a mess of unknown particles being produced. This mess of particles appeared to grow with increasing scattering angle and decreasing scattered electron energy, which ultimately led to the conclusion that the proton was composed of point-like particles that were being “knocked out” of the proton by the incoming electron [26], [31].

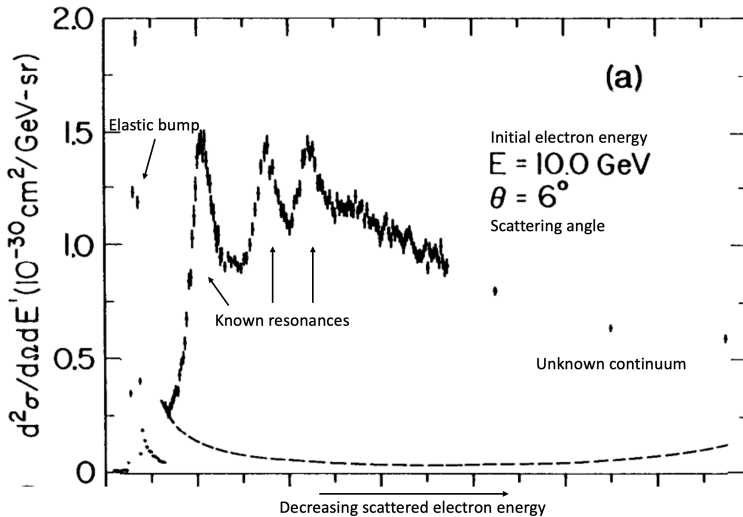


Figure 1.3: The energy distribution of electrons scattered off of protons at an initial electron energy of 10 GeV and a scattering angle of 6 degrees. The large spike on the left side of the distribution corresponds to the elastic scattering of the electron off the proton, and the “bumps” correspond to the inelastic scattering of the electron off the proton. The “background” underneath the bumps and the apparent continuum of events at even lower values of the scattered electron energy correspond to a mess of unknown particles being produced. The behavior of this continuum with respect to the scattering angle and the scattered electron energy ultimately led to the conclusion that the proton was not fundamental.

While many physicists were perfectly happy to interpret these point-like particles as the very same quarks from the aforementioned quark model(s), they received the much more noncommittal name **partons** after Richard Feynman’s parton model of hadrons [32]. The association of these partons with quarks was not universally accepted<sup>6</sup> until the discovery of the  $J/\psi$  meson in 1974 [33]. In the meantime, the theoretical description of the strong nuclear force was closing in on its final form.

<sup>6</sup>No acceptance of any model is a step function, but the discovery of  $J/\psi$  seems to be a turning point in literature.

840 The formulation of Quantum ChromoDynamics (QCD) in the early 1970s by Gell-  
841 Mann, Fritzsch, and Leutwyler [34] resolved many of the issues that were present in  
842 the initial quark models<sup>7</sup>. QCD introduced the concept of color charge, which all of  
843 the quarks would carry. The mediating bosons of the strong interaction—known as  
844 **gluons**—were also introduced, carrying color charge as well.

845 While QCD gave a solid mathematical description of the strong interaction, it  
846 wasn’t until the discovery of **asymptotic freedom** [35], [36] by Gross, Wilczek, and  
847 Politzer in 1973 that the theory became experimentally testable. Asymptotic freedom  
848 is the notion that the strong interaction becomes weaker at higher energies, allowing  
849 for QCD calculations to be performed using perturbative techniques. This discovery  
850 allowed theorists to use QCD to make predictions of the results of very high energy  
851 particle collision experiments. The first QCD prediction to be experimentally verified  
852 came from the Positron-Electron Tandem Ring Accelerator (PETRA) in 1979 [37],  
853 which experimentally confirmed the existence of gluons [38]. With experimental ver-  
854 ification of QCD, it became clear that the association of partons with quarks was  
855 indeed incorrect: they are both quarks *and* gluons.

856 While not of particular import to this thesis<sup>8</sup>, the theory of electroweak in-  
857 teractions was also being developed during the 1960s by Glashow, Weinberg, and  
858 Salam [39], [40]. With this new theory came the prediction of four<sup>9</sup> new bosons:  
859 the Higgs boson, the charged  $W^\pm$  bosons, and the neutral  $Z^0$  boson. With the com-  
860 bined theories of the electroweak and strong interaction, the **Standard Model** of  
861 particle physics—which describes the now 61<sup>10</sup> fundamental particles and how they  
862 interact—was complete.

---

<sup>7</sup>For example, the wavefunction of the  $\Delta^{++}$  baryon under the first quark model was not anti-symmetric, which is a requirement for fermions.

<sup>8</sup>Though extremely interesting in its own right.

<sup>9</sup>The Higgs mechanism (which predicts the existence of the Higgs boson) came before electroweak unification [41], but it was a requirement for the theory.

<sup>10</sup>There are many ways to count fundamental particles, but this particular number is obtained by: 6 leptons ( $\times 2$  for anti-leptons), 6 quarks ( $\times 3$  for each color,  $\times 2$  for anti-quarks), 1 gluon ( $\times 8$  for color), 1 photon, the  $W$  and  $Z$  bosons, and the Higgs boson.

863 **1.2 The Standard Model**

864 The Standard Model of particle physics is a **quantum field theory** (QFT) that  
865 describes the interactions between all<sup>11</sup> of the fundamental particles. QFTs describe  
866 the dynamics of a quantum system in terms of fields, which are functions of space and  
867 time. The fields are the fundamental objects of QFT, and their excitations correspond  
868 to the particles that are observed in nature. The Standard Model fields can be broken  
869 down into three sectors, which will be discussed in the following sections.

870 **1.2.1 The gauge sector**

871 The gauge sector of the Standard Model corresponds to the spin-one bosons that  
872 mediate the strong and electroweak interactions. In a general sense, this sector corre-  
873 sponds to the mediating particles for three of the four fundamental forces: the strong  
874 nuclear force, the weak nuclear force, and the electromagnetic force. The fourth  
875 fundamental force—gravity—is not included in the Standard Model, as it is not yet  
876 understood from a quantum perspective [44].

877 The symmetry group of the gauge sector is given by

$$\text{SU}(3)_c \times [\text{SU}(2)_L \times \text{U}(1)_Y]. \quad (1.1)$$

878  $\text{SU}(3)_c$  is the symmetry group of the strong interaction, which is described by the QFT  
879 known as Quantum ChromoDynamics (QCD). The subscript  $c$  stands for “color”,  
880 indicating that the gauge fields in QCD (gluons) only couple to colored objects. As  
881 QCD is the theory that mostly describes the research presented in this thesis, it  
882 will be discussed in much greater detail in Section 1.3. The symmetry group of the  
883 electroweak interaction is  $\text{SU}(2)_L \times \text{U}(1)_Y$ , where the subscript  $L$  stands for “left-  
884 handed” and the subscript  $Y$  stands for “weak hypercharge”. Again, these subscripts  
885 indicate the types of objects to which the corresponding gauge fields couple. For  
886 example, the gauge fields of  $\text{SU}(2)_L$  only couple to left-handed objects, and the gauge  
887 fields of  $\text{U}(1)_Y$  only couple to weakly hypercharged objects. Initially, there are four  
888 massless gauge fields in the theory<sup>12</sup>. After the spontaneous symmetry breaking of the  
889 Higgs mechanism [41], these fields mix to give rise to three massive gauge fields and

---

<sup>11</sup>Ignoring potential gravitons [42] or dark matter candidates [43]

<sup>12</sup>Three corresponding to the generators of  $\text{SU}(2)$ , one corresponding to the generator of  $\text{U}(1)$ .

890 one massless gauge field. The three massive gauge fields correspond to the familiar  
891  $W^\pm$  and  $Z^0$  bosons, which are the mediating bosons of the weak interaction. The  
892 massless gauge field corresponds to the photon, which mediates the electromagnetic  
893 interaction.

894 **1.2.2 The scalar sector**

895 The scalar sector of the Standard Model is quite lonely, and only corresponds to  
896 one spin-zero field: the Higgs [41]. As mentioned in the previous section, the Higgs  
897 mechanism that corresponds to this field is responsible for the acquisition of mass  
898 by the  $W^\pm$  and  $Z^0$  bosons. The Higgs field also couples to all of the fermions in  
899 the Standard Model, but the mass acquisition procedure is *slightly* different<sup>13</sup>. The  
900 associated Higgs boson was discovered by the A Toroidal LHC Apparatus (ATLAS)  
901 and Compact Muon Solenoid (CMS) collaborations in 2012 [45], [46], and was the  
902 last major piece of the Standard Model to be experimentally verified.

903 **1.2.3 The fermionic sector**

904 The fermionic sector contains all of the spin one-half particles (quarks and leptons) in  
905 the Standard Model. It is often convenient to group these particles into three genera-  
906 tions, where each generation is identical except for the masses of the particles. It is  
907 even *more* convenient to group the fermions within each family into multiplets, where  
908 the members of the multiplet are related to each other by transformations within the  
909 gauge group of the Standard Model (Equation 1.1). In other words, the fermions  
910 within a particular multiplet can only be transformed to fermions within the same  
911 multiplet. A table of the fermions in the Standard Model and their corresponding  
912 multiplets can be seen in Table 1.2.3. The indices  $L$  and  $R$  correspond to the chirality  
913 of the fields, and the indices  $r$ ,  $g$ , and  $b$  represent to the color charge of the fields.  
914 The color charges are only non-zero for the quarks, making them a key component  
915 of quantum chromodynamics.

---

<sup>13</sup>It's still spontaneous symmetry breaking, but within the Yukawa part of the electroweak La-  
grangian.

Table 1.1: The fermions of the Standard Model for each generation and their corresponding multiplets. The Standard Model does not allow for fermions to leave their respective multiplets.

Gen.	Left-handed quarks	Right-handed up quarks	Right-handed down quarks	Left- handed leptons	Right- handed leptons
1 <sup>st</sup> gen.	$\begin{pmatrix} u_L^r & u_L^g & u_L^b \\ d_L^r & d_L^g & d_L^b \end{pmatrix}$	$(u_R^r \ u_R^g \ u_R^b)$	$(d_R^r \ d_R^g \ d_R^b)$	$\begin{pmatrix} \nu_{eL} \\ e_L \end{pmatrix}$	$(e_R)$
2 <sup>nd</sup> gen.	$\begin{pmatrix} c_L^r & c_L^g & c_L^b \\ s_L^r & s_L^g & s_L^b \end{pmatrix}$	$(c_R^r \ c_R^g \ c_R^b)$	$(s_R^r \ s_R^g \ s_R^b)$	$\begin{pmatrix} \nu_{\mu L} \\ \mu_L \end{pmatrix}$	$(\mu_R)$
3 <sup>rd</sup> gen.	$\begin{pmatrix} t_L^r & t_L^g & t_L^b \\ b_L^r & b_L^g & b_L^b \end{pmatrix}$	$(t_R^r \ t_R^g \ t_R^b)$	$(b_R^r \ b_R^g \ b_R^b)$	$\begin{pmatrix} \nu_{\tau L} \\ \tau_L \end{pmatrix}$	$(\tau_R)$

## 916 1.3 Quantum chromodynamics

917 This section serves as a turning point for this thesis: while the discussions above have  
918 been *mostly* general, the novel research presented in this thesis is centered around  
919 the strong nuclear force. As such, the remainder of this chapter will delve into the  
920 details of this mysterious force, and how it can be studied using high-energy particle  
921 collisions.

### 922 1.3.1 The QCD Lagrangian

The dynamics of these fields and how they interact are completely encoded within the Lagrangian of the theory, which can be used to calculate experimental observables like cross sections and decay rates. However, the Lagrangian of the Standard Model is fairly long [47], and often not particularly insightful when trying to study a specific aspect of the theory. As such, when studying QCD, it is often useful to throw away the electroweak gauge fields, leptons, and scalars to give only the QCD Lagrangian [48],

$$\mathcal{L}_{QCD} = -\frac{1}{4}F_{\mu\nu}^A F^{A\mu\nu} + i\bar{q}\gamma^\mu \left( \partial_\mu + ig_s \frac{1}{2} \lambda^A \mathcal{A}_\mu^A \right) q - \bar{q}_R \mathcal{M} q_L - \bar{q}_L \mathcal{M}^\dagger q_R - \theta\omega,$$

923 where all repeated indices are summed over.

924 The gluons are described by the vector gauge field  $\mathcal{A}_\mu^A$ , with index  $A$  representing  
925 one of the eight color labels. These eight components belong to the color group  
926  $SU_c(3)$ , which is the gauge group of QCD. The corresponding coupling constant is

927  $g_s$ , and the field strength tensor  $F_{\mu\nu}^A$  is given by

$$F_{\mu\nu}^A = \partial_\mu A_\nu^A - \partial_\nu A_\mu^A + g_s f^{ABC} A_\mu^B A_\nu^C, \quad (1.2)$$

928 where  $f^{ABC}$  are the structure constants [49] of  $SU_c(3)$ . Note that while this field  
929 strength tensor shares the same letters as the electromagnetic field strength tensor  
930  $F_{\mu\nu}$ , the additional term  $g_s f^{ABC} A_\mu^B A_\nu^C$  in Equation 1.2 separates QCD and QED in  
931 a very fundamental way: the gluons are allowed to self-interact. This self-interaction  
932 is a direct result of the non-vanishing structure constants of  $SU_c(3)$ <sup>14</sup>, and causes a  
933 lot of headaches for theorists.

934 The quarks are represented by the field  $q$ , which is a bit misleading as the color,  
935 flavor and spin indices have been suppressed. In reality, the quark field  $q$  has:

- 936 • six flavor indices  $\{u, d, s, c, b, t\}$ ,
- 937 • four spin indices  $\{0, 1, 2, 3\}$ , and
- 938 • three color indices  $\{r, g, b\}$ ,

939 where all of these indices are being implicitly summed over in  $\mathcal{L}_{QCD}$ . Luckily all of  
940 the matrices  $(A_\mu^A, \lambda^A, \mathcal{M}, \gamma^\mu)$  act on separate sets of indices<sup>15</sup>. For example, the  $\gamma^\mu$ s  
941 only operate on the spin indices, whereas both the gluon fields  $A_\mu^A$  and Gell-Mann  
942 matrices [15]  $\lambda^A$  operate on the color indices. These Gell-Mann matrices are the  
943 generators of  $SU_c(3)$  and satisfy the commutation relation

$$[\lambda^A, \lambda^B] = 2i f^{ABC} \lambda^C. \quad (1.3)$$

944 The chiral quark fields  $q_L$  and  $q_R$  are defined as  $\frac{1}{2}(1-\gamma_5)q$  and  $\frac{1}{2}(1+\gamma_5)q$ , respectively.  
945 The mass matrix  $\mathcal{M}$  operates on the flavor indices, and its form depends on the choice  
946 of basis for the quark fields [48]. It is often convenient to choose a basis where the  
947 mass matrix is diagonal, which can be done by independent rotations of  $q_L$  and  $q_R$  in  
948  $SU(6)$ . Doing so gives the more familiar term

$$-\bar{q}_R \mathcal{M} q_L - \bar{q}_L \mathcal{M}^\dagger q_R = - \sum_{f=1}^6 \bar{q}_f m_f q_f, \quad (1.4)$$

---

<sup>14</sup>Structure constants of Abelian gauge groups like  $U(1)$  are trivially zero.

<sup>15</sup>Really the components of the field corresponding to those indices.

949 where  $m_f$  is the mass of the quark with flavor  $f$ , and  $q_f$  is the flavor component of  
 950 the quark field. Note that this term completely violates the  $SU(2) \times U(1)$  electroweak  
 951 symmetry, indicating that the given  $\mathcal{L}_{QCD}$  is determined *after* the spontaneous sym-  
 952 metry breaking described in the previous section. These quark masses are also subject  
 953 to renormalization [50], which results in the running of the quark mass with respect  
 954 to the energy scale of the interaction<sup>16</sup>. More simply, the quark masses are inversely  
 955 dependent on this energy scale: at large energies, the quark masses are small, and at  
 956 low energies, the quark masses are large.

957 The final term, known as the  $\theta$ -term [52], is a bit of a mystery. It is a scalar term  
 958 that violates CP symmetry [53], and is often set to zero as there is no experimental  
 959 evidence for its existence. However, it is not clear why this term is zero, as there is  
 960 no symmetry that forbids it. This is known as the **strong CP problem**, and is one  
 961 of the biggest open questions in particle physics [54].

### 962 1.3.1.1 Brief aside: Why eight gluons?

963 The gluon field  $\mathcal{A}^A$  transforms under the adjoint representation of  $SU(3)$ , which  
 964 is a representation of  $SU(3)$  on the vector space of its Lie algebra  $\mathfrak{su}(3)$ . As  $\mathfrak{su}(3)$   
 965 has eight basis elements (for instance, the Gell-Mann matrices  $\lambda^A$  from above), the  
 966 adjoint representation of  $SU(3)$  is eight-dimensional. Thus the gluon field has eight  
 967 independent components, or there are eight gluons. In principle, QCD could have  
 968 been built on top of a  $U(3)$  gauge group, which would give rise to nine gluons (as the  
 969 dimension of  $U(n)$  is  $n^2$ ). However, the singlet state in  $U(3)$  must not be interacting; if  
 970 it were, color neutral baryons would interact with each other via the strong interaction  
 971 at a much longer range [55]. Such interactions have not been observed [56]. As there  
 972 is no physical difference between  $U(3)$  with a non-interacting singlet and  $SU(3)$ , the  
 973 simpler gauge group was chosen.

As an aside to the current aside, a lot of fun can be had with the adjoint representation of  $SU(3)$ . For example, the term  $g_s f^{ABC} \mathcal{A}^B \mathcal{A}^C$  can be thought of as boring  $3 \times 3$  matrix multiplication, but it can also be thought of as an inner product between two eight-dimensional row/column vectors. Unfortunately, the fun breaks down at some point, as terms like  $i\bar{q}\gamma^\mu(i g_s \frac{1}{2} \lambda^A \mathcal{A}_\mu^A) q$  can only be interpreted as  $\mathcal{A}$  transforming

---

<sup>16</sup>They also depend on the *choice* of renormalization scheme, with the most commonly implemented one being minimal subtraction or MS [51].

$q$  under the fundamental representation of  $SU(3)$  (i.e.  $3 \times 3$  matrix acting on  $3 \times 1$  vector). Furthermore, writing  $\lambda^A$  as an  $8 \times 8$  matrix is not particularly enlightening—though it can be done. For example,  $\lambda^1$  in the adjoint representation is given by

$$\lambda^{1,\text{adjoint}} = \begin{pmatrix} 0 & 0 & 0 & 0 & 0 & 0 & 0 & 0 \\ 0 & 0 & -2i & 0 & 0 & 0 & 0 & 0 \\ 0 & 2i & 0 & 0 & 0 & 0 & 0 & 0 \\ 0 & 0 & 0 & 0 & 0 & 0 & -i & 0 \\ 0 & 0 & 0 & 0 & 0 & i & 0 & 0 \\ 0 & 0 & 0 & 0 & -i & 0 & 0 & 0 \\ 0 & 0 & 0 & i & 0 & 0 & 0 & 0 \\ 0 & 0 & 0 & 0 & 0 & 0 & 0 & 0 \end{pmatrix},$$

which is found by interpreting the commutation relation  $[\lambda^{1,\text{adjoint}}, \lambda^A] = 2if_{1AB}\lambda^B$  as the action of  $\lambda^{1,\text{adjoint}}$  on  $\lambda^A$ , where each  $\lambda^A$  is assigned to a trivial column vector with a 1 and the  $A^{\text{th}}$  index and zeroes everywhere else.

### 1.3.2 Properties of QCD

This section details some of the many interesting properties of QCD.

#### 1.3.2.1 Confinement

The first property of QCD to be discussed is **confinement**, which is simply the observation that quarks and gluons are never seen in isolation. Instead, they are *confined* inside of the color neutral bound states known as hadrons. This property is mostly understood in terms of the coupling constant  $g_s$ . The renormalization [57] of QCD gives rise to a  $g_s$  that varies with energy scale or distance. As the distance between two quarks increases, so too does  $g_s$ . At some point, the coupling becomes so strong that the energy required to separate the quarks is enough to create a quark-antiquark pair from the vacuum. Thus any attempts to pluck a quark from a hadron will always result in the creation of a new hadron, making it impossible to observe single quarks in isolation.

The large coupling constant makes it impossible to describe this phenomenon using perturbative techniques, so the exact mechanism of confinement is still not fully understood. However, it is often described using the phenomenological Lund

993 string model [58]. In this model, the field lines of two quarks are pulled together due  
 994 to the self-interaction of the gluons. This creates a string-like structure between the  
 995 two quarks, with a potential given by

$$V(r) \approx -\frac{4}{3} \frac{\alpha_s}{r} + \kappa r, \quad (1.5)$$

996 where  $r$  is the distance between the two quarks,  $\alpha_s = \frac{g_s^2}{4\pi}$  and  $\kappa$  is the string tension.  
 997 This is in contrast to the potential between two electrically charged particles, where  
 998 the field lines are not pulled together and become less dense as the distance between  
 999 the two particles increases. As such, the potential decreases with increasing distance,  
 1000 opposite to that of the Lund model. A schematic of these differences can be seen in  
 1001 Figure 1.4.

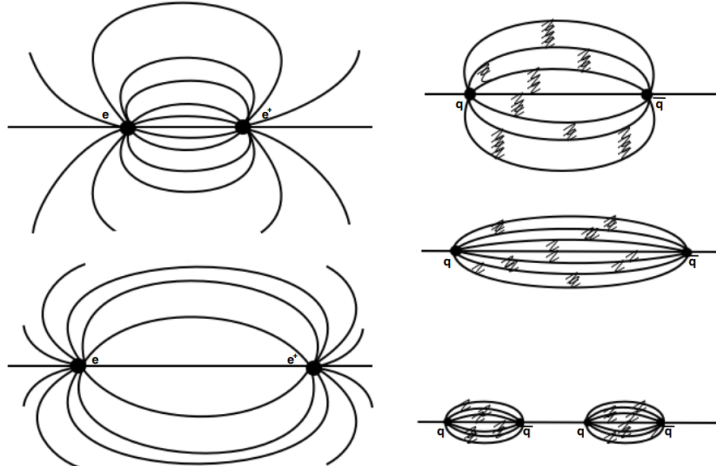


Figure 1.4: A schematic of the field lines between two electrically charged particles (left) and two quarks (right). The field lines between the quarks are pulled together due to the self-interaction of the gluons, whereas the electric field lines are not.

### 1002 1.3.2.2 Asymptotic freedom

1003 Just as the coupling constant becomes large at low energies and large distances, it  
 1004 also becomes small at high energies and small distances. This property is known  
 1005 as **asymptotic freedom**: at high enough energies, the quarks and gluons can be  
 1006 thought of as “free”, and their interactions can be modeled using perturbative QCD  
 1007 (pQCD). As discussed in Section 1.1, the discovery of asymptotic freedom in QCD was

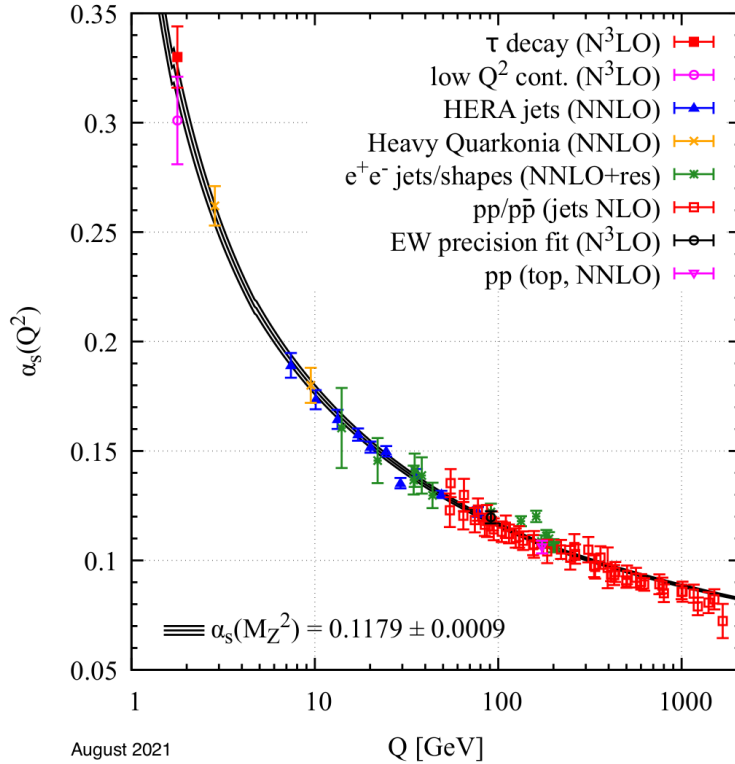


Figure 1.5: The value of the strong coupling constant  $\alpha_s$  as a function of momentum transfer  $Q$ , which represents the energy scale of the interaction.

1008 what allowed for the accurate predictions of the results of high energy particle collision  
 1009 experiments like SLAC [59] and PETRA [37]. The results of such experiments have  
 1010 also been used to calculate the value of the coupling constant itself at different energy  
 1011 scales, as shown in Figure 1.5. The value of  $\alpha_s$  at the  $Z^0$  mass is also given in the  
 1012 figure, which is the most accurate measurement of  $\alpha_s$  to date [60].

### 1013 1.3.2.3 Jets

1014 During high energy particle collisions (between two protons, for example), the con-  
 1015 sistuent partons of the protons will sometimes scatter off each other in a way that  
 1016 converts most of their initial longitudinal momentum (along the collision axis) into  
 1017 transverse momentum. Such a scattering is often referred to as a **hard scatter-**  
 1018 **ing**. Because the momentum transfer is large, the cross section of the parton-parton  
 1019 scattering is calculable using pQCD. Furthermore, branching processes of the high

1020 momentum partons—like gluon radiation—can also be calculated perturbatively. Even-  
1021 tually, however, the partons will lose enough energy such that their behavior can no  
1022 longer be described using perturbative techniques.

1023 Luckily, the aforementioned Lund model is well equipped to deal with lower energy  
1024 partons. Under the Lund model, as these colored partons move away from each  
1025 other, the force between them increases until there is enough energy to produce a  
1026 quark-antiquark pair (as discussed in Section 1.3.2.1). This process—known as string  
1027 fragmentation—continues until the partons are no longer energetic enough to move  
1028 away from each other, at which point they hadronize into a large number of color  
1029 neutral bound states. These hadrons are roughly collimated in the direction(s) of the  
1030 initial hard scattering, forming sprays of particles that may end up being seen by a  
1031 detector. These hadronic showers are known as **jets**. and they are one of the first  
1032 experimentally observed predictions of QCD. A diagram depicting the formation of  
1033 a jet from an initial hard scattering of partons can be seen in Figure 1.6.

1034 Jets serve as a useful experimental probe to study the strong interaction: they  
1035 combine the perturbative and non-perturbative regimes of QCD, and they are rela-  
1036 tively easy to identify in a detector.

### 1037 1.3.3 The Quark-Gluon Plasma

1038 One of the most exciting consequences of the asymptotic freedom of QCD is the  
1039 existence of a new state of matter at extreme temperatures and densities: the **quark-**  
1040 **gluon plasma** (QGP) [62], [63]. In this plasma, the quarks and gluons are not  
1041 confined inside hadrons, and instead behave as quasi-free particles. This is analagous  
1042 to an electromagnetic plasma, where electrons and protons are dissociated from their  
1043 atoms. A phase diagram of this plasma can be seen in Figure 1.7. This diagram  
1044 has two axes: temperature and baryon density. Increasing *either* of these quantities  
1045 beyond a certain threshold will cause a phase transition from normal hadronic matter  
1046 to the QGP. Similarities can be drawn between this phase diagram and that of a  
1047 snowball: heating *or* squeezing a snowball will cause it to melt into a liquid<sup>17</sup>.

1048 Studying the QGP and its formation is interesting for a number of reasons, but  
1049 those reasons often get lost in the cosmological hype: the universe is thought to have

---

<sup>17</sup>Be careful: if you continue to heat up the snowball enough, or squeeze hard enough, it will undergo another phase transition into the QGP.

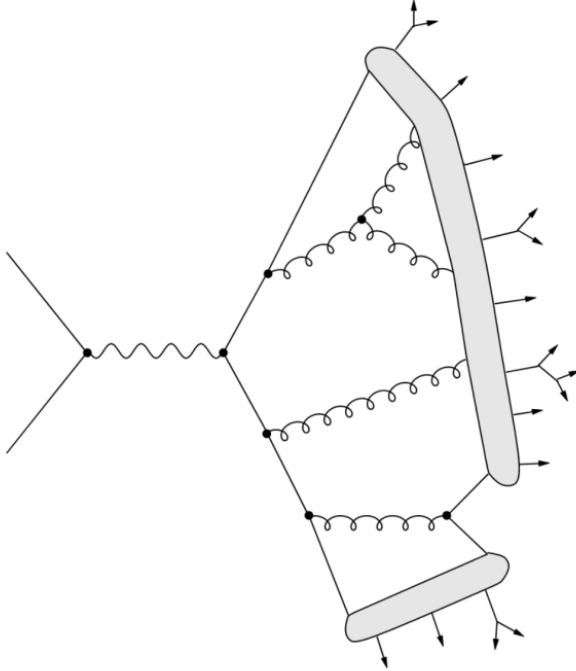


Figure 1.6: A diagram depicting the formation of a jet within the Lund model from an initial hard scattering of partons, adapted from [61]. The vertices represent perturbative QCD processes, the shaded regions represent string fragmentation/hadronization, and the outgoing arrows represent the resulting hadrons (which may decay further).

1050 been composed of this plasma in the first few microseconds after the Big Bang [65].  
 1051 Thus studying the QGP *can* give insight to the early universe and its expansion,  
 1052 which is schematically represented in Figure 1.8. It is also postulated that QGP  
 1053 formation occurs in the cores of neutron stars [66], giving another avenue of interest  
 1054 for astrophysicists.

1055 However, the QGP is also very interesting from a purely particle physics per-  
 1056 spective; it is a highly non-perturbative QCD system that can be generated in a  
 1057 laboratory setting. Studying this plasma and its properties can help illuminate the  
 1058 dark, confounding corners of QCD that are not yet understood—like confinement. Un-  
 1059 fortunately producing this plasma in a laboratory setting is not a trivial task, and  
 1060 requires<sup>18</sup> colliding heavy ions at very high energies.

---

<sup>18</sup>There are hints of QGP formation in proton-proton collisions, which will be discussed in Section 1.5

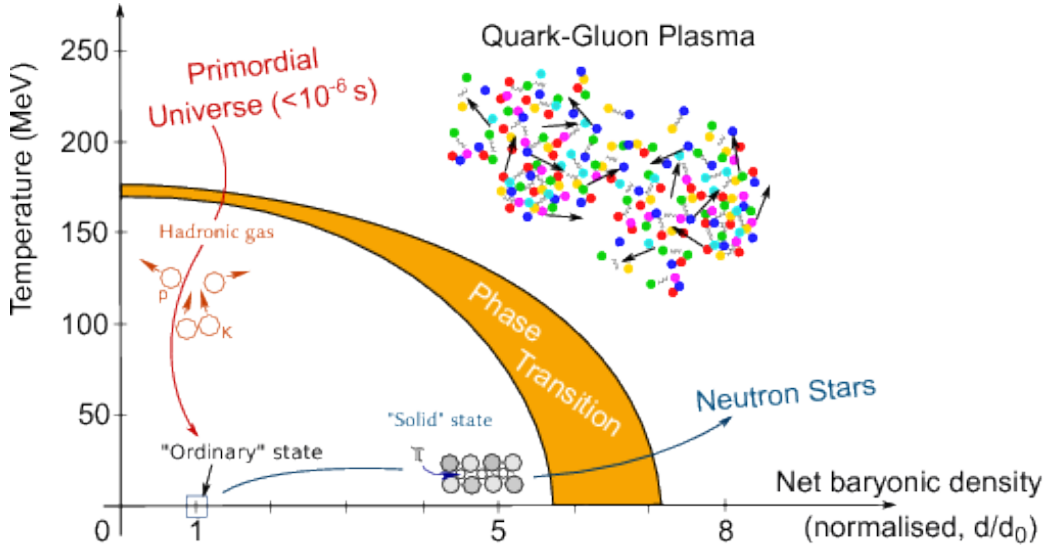


Figure 1.7: A phase diagram of the QGP, taken from [64]. The axes are temperature and baryon density, and the orange band represents the phase transition from normal hadronic matter to the QGP.

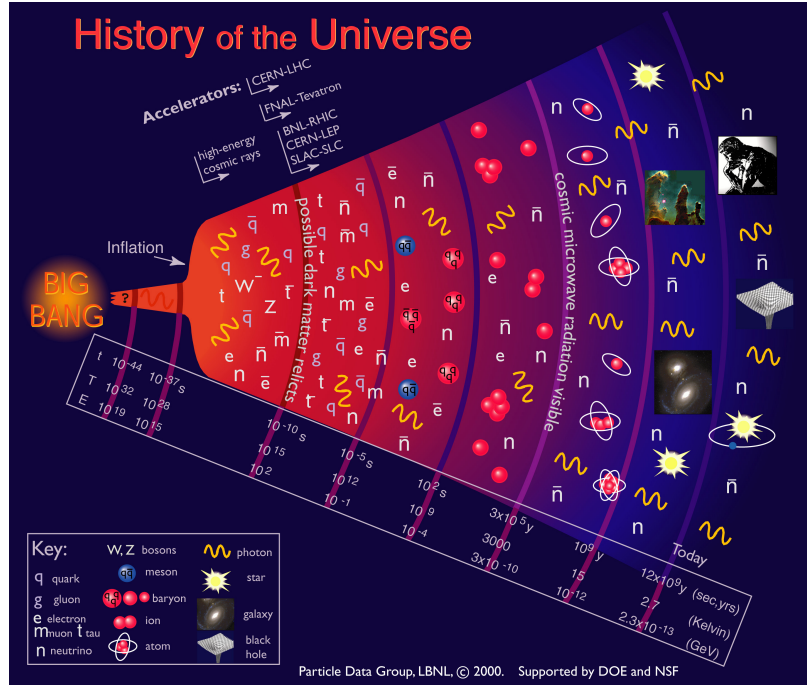


Figure 1.8: A schematic of the evolution of the universe, taken from [60]. The QGP phase of the universe on this diagram lies roughly between  $10^{-10}$  and  $10^{-5}$  seconds after the Big Bang.

1061 **1.4 Heavy ion collisions**

1062 The QGP phase diagram in Figure 1.7 shows two methods for producing the QGP:  
1063 increasing the system's temperature or increasing its baryon density. Luckily these  
1064 two methods are not mutually exclusive:

- 1065 • Baryon density can be increased by looking at systems with a lot of baryons  
1066 packed together (like the nucleus of a lead atom)
- 1067 • Temperature can be increased by smashing the aforementioned systems together  
1068 at higher energies (like in a particle accelerator)

1069 Thus one of the best (and only) ways to study the QGP in a laboratory setting is  
1070 through relativistic **heavy ion collisions**: the smashing together of two heavy nuclei  
1071 at very high energies using a particle accelerator.

1072 Unfortunately, producing the QGP in this manner has a major drawback; while  
1073 it is possible to heat up the system beyond the critical temperature required for  
1074 QGP formation, the system expands and cools *very* quickly. For example, the QGP  
1075 produced by colliding lead ions with center-of-mass energy  $\sqrt{s_{NN}} = 2.76$  TeV at the  
1076 Large Hadron Collider (LHC) only lasts for around  $3 \text{ fm}/c$  [67], or  $10^{-23}$  seconds. A  
1077 diagram depicting the formation and evolution of the QGP in a heavy ion collision  
1078 can be seen in Figure 1.9. This diagram can be split up into the following stages:

- 1079 1. The Lorentz-contracted nuclei approach each other at very high energies, and  
1080 the partons within the nuclei scatter off each other ( $t = 0 \text{ fm}/c$ ).
- 1081 2. As new partons are created from the initial scatterings, the energy density of  
1082 the system increases. Eventually this energy density is high enough to create  
1083 the QGP ( $t \approx 1 \text{ fm}/c$ ).
- 1084 3. Once the QGP is formed, it expands and cools in a hydrodynamic manner.
- 1085 4. After the QGP cools below the critical temperature, the partons begin to  
1086 hadronize, resulting in the formation of a hadron gas ( $t \approx 3 \text{ fm}/c$ ).
- 1087 5. The hadron gas will continue to expand until the hadrons within the gas are no  
1088 longer strongly interacting with each other ( $t \approx 10 \text{ fm}/c$ ). This is often broken  
1089 up into two stages:

- 1090     • The hadrons cease to interact *inelastically*, called **chemical freeze-out**.  
 1091     • The hadrons cease to interact *elastically*, called **kinetic freeze-out**.

1092     6. If a detector is built within a few meters around the collision point, the final  
 1093        state hadrons can be observed ( $t \approx 10^{15} \text{ fm}/c$ ).

1094     The last stage of this diagram is perhaps the most frustrating: it is only possible  
 1095     to study the QGP by observing the final state hadrons. Luckily, there are some  
 1096     key observables associated with those final state hadrons that can shed light on the  
 1097     formation and evolution of this exciting plasma. Before those observables can be  
 1098     discussed, however, it is necessary to introduce a key concept in heavy ion collisions:  
 1099     the centrality of the collision.

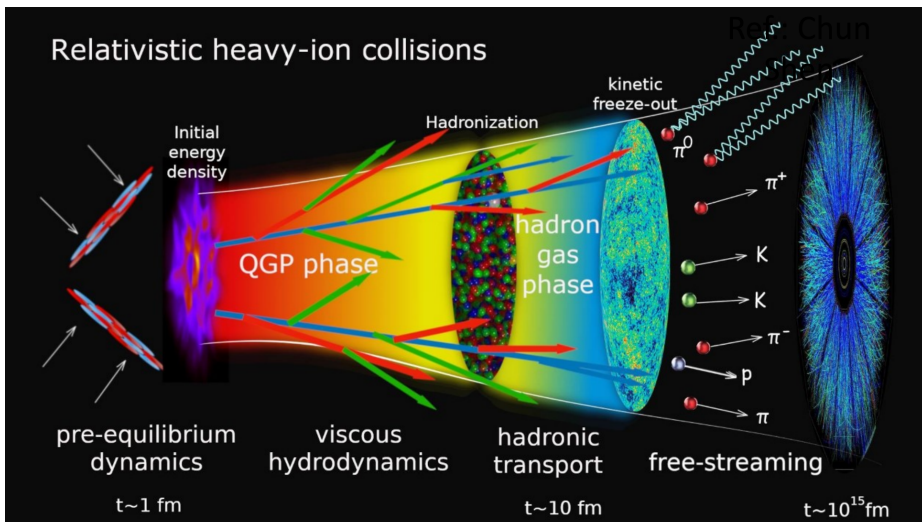


Figure 1.9: A schematic of the formation and evolution of the QGP in a heavy ion collision. The QGP is formed in the overlap region of the two colliding nuclei, and then expands and cools very quickly.

### 1100 1.4.1 Collision centrality

1101     The very first step of the heavy ion collision process involves the scattering of the  
 1102     partons within the two nuclei. However, these nuclei are not point-like objects: they  
 1103     have a finite size, and therefore need not collide “head-on”. Instead, the nuclei  
 1104     can collide at different **impact parameters** (commonly denoted as  $b$ ), as shown in

1105 Figure 1.10. The impact parameter is defined as the distance between the centers  
 1106 of the two nuclei, measured in the transverse plane (the plane perpendicular to the  
 1107 initial directions of the nuclei). Collisions with a large impact parameter give rise to  
 1108 *spectator* nucleons, which do not participate in the collision and continue traveling  
 1109 as they please.

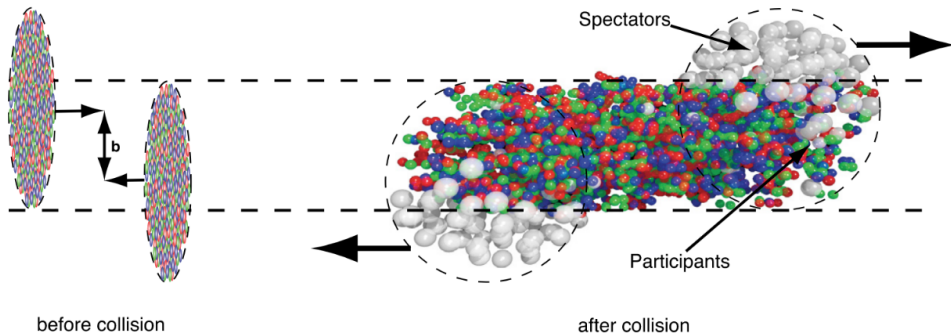


Figure 1.10: A schematic of a heavy ion collision with impact parameter  $b$ , taken from [68].

1100 The impact parameter is very important when studying the QGP for a fairly  
 1101 straightforward reason: as the impact parameter decreases, the number of partonic  
 1102 scatterings increases, which in turn increases the energy density of the system. In  
 1103 some sense, the size of the impact parameter determines whether or not the QGP is  
 1104 formed in the subsequent stages of the collision. As such, characterizing heavy ion  
 1105 collisions by their impact parameter is quite useful. Unfortunately, much like the  
 1106 QGP, the impact parameter is not directly measurable and must be inferred from  
 1107 the final state hadrons.

1108 Instead of classifying collisions based off their unobtainable impact parameter,  
 1109 they are instead classified by their **collision centrality**. The collision centrality is  
 1110 defined as

$$c = \frac{\int_0^b d\sigma / db' db'}{\int_0^\infty d\sigma / db' db'} = \frac{1}{\sigma_{AA}} \int_0^b \frac{d\sigma}{db'} db', \quad (1.6)$$

1121 where  $\sigma_{AA}$  is the total cross section of the nucleus-nucleus (A-A) collision. As this  
 1122 number is strictly between 0 and 1, it is often expressed as a percentile: 0% corre-  
 1123 sponds to the most central collisions (lowest impact parameters), and 100% corre-  
 1124 sponds to the most peripheral collisions (highest impact parameters). If a monotonic

relationship between  $b$  and the number of final state particles seen in the detector is assumed, the collision centrality can be experimentally determined [69]. The number of final state particles from a collision is called the **multiplicity** of the collision, and is often denoted as  $N_{\text{ch}}$ . The subscript  $\text{ch}$  indicates that only charged particles are counted, as neutral particles are not seen by most detectors.

In practice, the collision centrality percentiles are usually determined by looking at the distribution of events as a function of the signal (effectively  $N_{\text{ch}}$ ) as measured by a particular detector. The percentile for a specific event can then be determined by integration:

$$c \approx \frac{1}{\sigma_{AA}} \int_{N_{\text{ch}}}^{\infty} \frac{d\sigma}{dN'_{\text{ch}}} dN'_{\text{ch}}, \quad (1.7)$$

where  $N_{\text{ch}}$  is the multiplicity of the event in question. An example of separating events into centrality percentiles using this method can be seen in Figure 1.11. In this plot, Pb–Pb collisions are characterized by their event activity in the ALICE VZERO detector (which will be discussed in more detail in the next chapter). The red points correspond to fits obtained using Monte Carlo simulations based off of the Glauber model [69], [70]. The Glauber model [71] is a geometric model that treats the nuclei as a collection of nucleons, and models the collisions as a superposition of binary nucleon-nucleon collisions. This model gives a relationship between the impact parameter  $b$ , the number of participating nucleons  $N_{\text{part}}$ , and the number of binary nucleon-nucleon collisions  $N_{\text{coll}}$ . While not of particular import to this thesis, fitting the Glauber model to the data actually allows for the determination of the impact parameter corresponding to a given multiplicity percentile. The fact that the model describes the data well also serves as a sanity check for the experimental estimation of the collision centrality. In this thesis, the terms “multiplicity percentile” and “collision centrality” will be used interchangeably.

The approximation given by Equation 1.7 has an additional benefit: it allows for the determination of centrality without a clearly defined impact parameter. This is useful for proton-proton and proton-lead collisions, where the impact parameter is ill-defined.

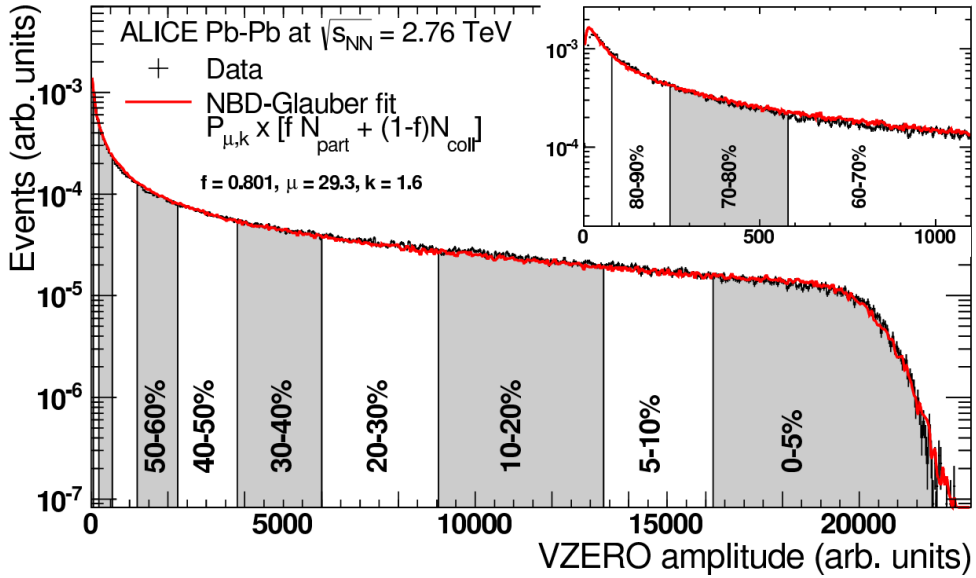


Figure 1.11: The distribution of Pb–Pb collision events as a function of event activity in the ALICE VZERO detector, taken from [70].

## 1153 1.5 Experimental signatures of QGP formation

1154 As mentioned in Section 1.4, the QGP produced within a heavy ion collision is *very*  
 1155 short lived. As such, any attempt to study the QGP and its formation must be  
 1156 done using the detector-accessible final state hadrons. Luckily there are a number of  
 1157 signatures that can be used to study the QGP in experiment, including

- 1158 • **jet quenching** [72], where the energy of a jet is heavily reduced due to its  
 1159 interactions with the QGP,
- 1160 • **collective flow** [73], where the motion of the partons within the QGP is heavily  
 1161 influenced by the overall fluid-like medium, and
- 1162 • **strangeness enhancement** [18], where the QGP exhibits an increase in the  
 1163 production of strange quarks relative to up and down quarks.

1164 These signatures are discussed in more detail in the following sections.

1165 **1.5.1 Jet quenching**

1166 The high momentum partons produced in the initial hard scatterings of heavy ion  
1167 collisions often traverse the QGP medium. Much like electron tomography, where the  
1168 passage of electrons through an atomic medium can give insight to the structure of the  
1169 atoms within, these high momentum partons can be used to probe the QGP. These  
1170 colored partons interact with the colored medium, losing energy in the process. As  
1171 discussed in Section 1.3.2.3, these partons are never observed individually; instead,  
1172 they hadronize into a spray of particles known as a jet. Thus the energy lost by  
1173 the parton is not observed directly, but rather as a reduction in the energy of the  
1174 resulting jet. This phenomenon is known as **jet quenching**, and is one of the most  
1175 well studied signatures of QGP formation.

1176 Experimentally, this quenching is observed by studying *dijets*. While the term  
1177 “jet” refers to a single spray of particles observed in the detector, the initial hard  
1178 scattering responsible for the formation of the jet corresponds to the production of  
1179 *two* high momentum partons. Traveling in opposite directions in the transverse plane,  
1180 these partons often produce two jets that are back-to-back in  $\varphi$  (the azimuthal angle  
1181 in the transverse plane). These two jets are collectively referred to as a dijet. In pp  
1182 collisions, the energy of the two jets is roughly equal as the corresponding partons  
1183 don’t lose energy to a medium. In heavy ion collisions, however, the partons lose  
1184 energy to the QGP due to gluon radiation and elastic scattering with the medium’s  
1185 constituents [74]. If one of the two partons has a larger path length through the  
1186 QGP, it will lose more energy than the other parton, resulting in an imbalance in the  
1187 energy of the two jets. A schematic of this process for pp and A–A collisions can be  
1188 seen in Figure 1.12.

1189 However, the path length within the QGP of the dijet-forming partons should be  
1190 roughly uniform, washing out this assymetry over a large event sample. As such, jet  
1191 quenching is experimentally observed by selecting high momentum “trigger” hadrons,  
1192 which most likely originated from the parton with the smaller QGP path length. The  
1193 jet corresponding to this higher momentum trigger—referred to as the “near-side” jet—  
1194 is then compared with its partner jet, which would be  $180^\circ$  away in azimuth—called  
1195 the “away-side” jet. The first collaboration to observe this jet quenching was the  
1196 STAR collaboration at the Relativistic Heavy Ion Collider (RHIC) [76]. By looking  
1197 at high transverse momentum hadrons produced in Au–Au collisions, they found that

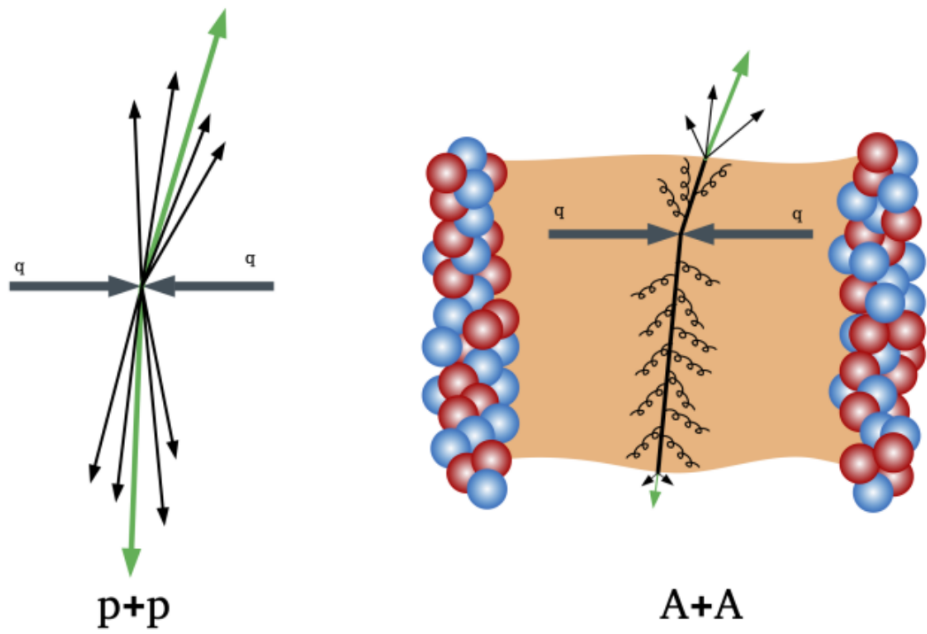


Figure 1.12: A schematic of the formation of dijets in  $p+p$  and  $A-A$  collisions, taken from [75].

1198 the away-side jet began to “disappear” as the centrality of the collision increased, as  
 1199 shown in Figure 1.13. This disappearance is due to the away-side jet losing energy  
 1200 to the QGP, such that the corresponding hadrons in the away-side fall below the  
 1201 momentum cutoff.

### 1202 1.5.2 Collective flow

1203 The QGP is a strongly interacting medium, whose constituent partons are heavily  
 1204 coupled to their surroundings. Just as the pebbles within a river get swept up in  
 1205 the flow of the water, the partons within the QGP are influenced by the flow of this  
 1206 medium. This flow manifests itself by the presence of collective effects in the final  
 1207 state hadrons, which are often quantified using **collective flow** components. These  
 1208 flow components are obtained by expanding the final state hadron distribution in a  
 1209 Fourier series with respect to the azimuthal angle  $\phi$  [77],

$$E \frac{d^3 N}{d^3 p} = \frac{1}{2\pi} \frac{d^2 N}{p_t dp_t dy} \left( 1 + \sum_{n=1}^{\infty} 2v_n \cos[n(\phi - \Psi_R)] \right), \quad (1.8)$$

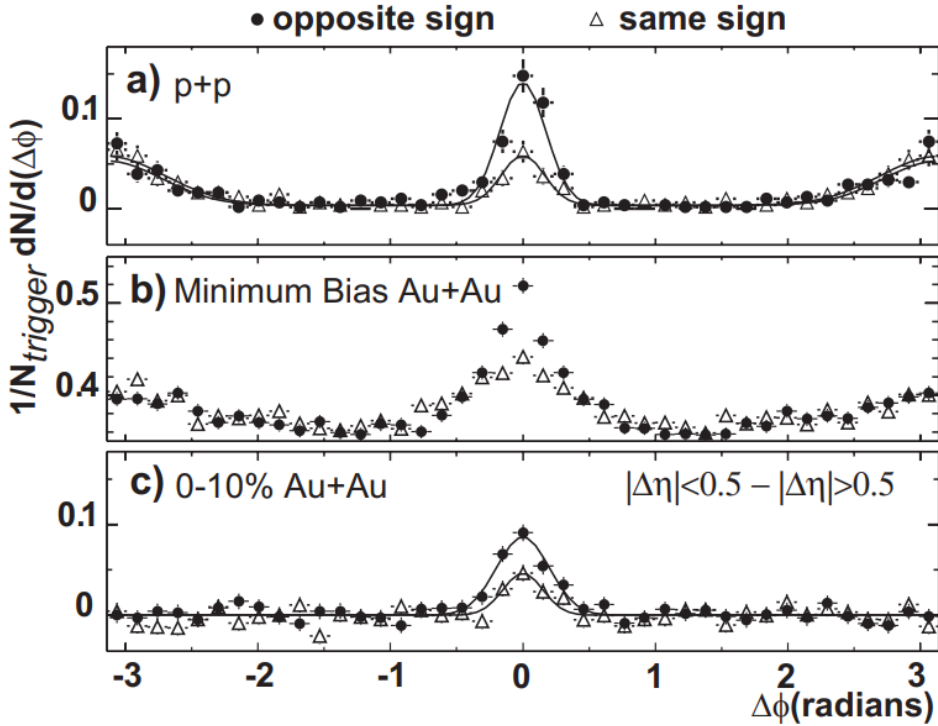


Figure 1.13: Hadron yields corresponding to the near-side jet (near  $\Delta\varphi = 0$ ) and the away-side jet ( $\Delta\varphi = \pm\pi$ ), taken from [76]. In pp and minimum bias Au–Au collisions, the away-side jet is present. However, at high centrality (0–10%), the away-side jet completely disappears.

where  $E$  is the energy of the particle,  $p$  is its momentum,  $p_T$  is the momentum component in the plane transverse to the beam axis,  $y$  is the particle's rapidity, and  $\Psi_R$  is the reaction plane angle. This reaction plane angle is defined by the beam axis and the impact parameter vector. The Fourier coefficients

$$v_n = \langle \cos[n(\phi - \Psi_R)] \rangle \quad (1.9)$$

determine the “strength” of the corresponding flow component. The first two coefficients,  $v_1$  and  $v_2$ , are referred to as **directed (radial) flow** and **elliptic flow**, respectively. A non-zero directed flow originates from the space-momentum correlations in particle production from a longitudinally slanted source [78]. Directed flow is often much smaller than elliptic flow (by over an order of magnitude) [79], but it can still effect some of the measurements presented in this thesis (see Section 4.7.2 for more details).

1221 Elliptic flow characterizes the anisotropy of the particle production in the trans-  
 1222 verse plane. This anisotropy is believed to be caused by the initial anisotropy of the  
 1223 collision geometry, where the overlap region of the colliding nuclei forms an “almond”  
 1224 shape. This almond is where the initial QGP is formed, which then hydrodynamically  
 1225 expands and thermalizes nearly instantaneously. The initial spacial anisotropy results  
 1226 in unequal QGP path lengths for the constituent partons, which ultimately results in  
 1227 an anisotropic momentum distribution for the corresponding hadrons (i.e. partons  
 1228 which travel through more medium lose more energy, as discussed in Section 1.5.1).  
 1229 A diagram depicting this process can be seen in Figure 1.14.

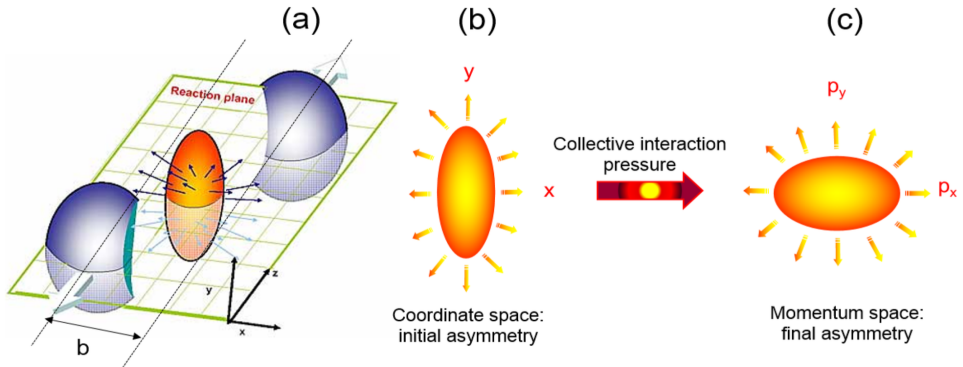


Figure 1.14: A schematic of the formation of elliptic flow in a heavy ion collision. The initial anisotropy in coordinate space results in a pressure gradient that causes a momentum space anisotropy in the final state hadrons.

### 1230 1.5.2.1 Avoiding $\Psi_R$

1231 Reconstructing the reaction plane angle  $\Psi_R$  is difficult as it must be done on an event-  
 1232 by-event basis [77]. As such, it is often more convenient to measure the collective  
 1233 flow components by looking at two-particle correlations in the azimuthal angle  $\phi$ . In  
 1234 other words, the flow components can be obtained by looking at the distribution of  
 1235 pairs of particles as a function of  $\Delta\phi = \phi_1 - \phi_2$ , where  $\phi_1$  and  $\phi_2$  are the azimuthal  
 1236 angles of two (non-identical) particles. This distribution can be decomposed into a  
 1237 Fourier series similar to Equation 1.8 [80],

$$\frac{dN^{\text{pair}}}{d\Delta\varphi} = a_0 + 2a_1 \cos \Delta\varphi + 2a_2 \cos 2\Delta\varphi + \dots, \quad (1.10)$$

1238 where  $v_n \equiv a_n/a_0$  are the very same flow coefficients from before. This bypasses the  
1239 need to reconstruct the reaction plane angle  $\Psi_R$ , but it also makes clear that any  
1240 analyses involving two-particle angular correlations (like the one presented in this  
1241 thesis) must be mindful of the presence of these coefficients (see Chapter 3 for more  
1242 details).

### 1243 1.5.3 Strangeness enhancement

1244 The earliest predicted signature of QGP formation was an increase in the production  
1245 of strange quarks relative to the production of up and down quarks [18]. Discovered  
1246 in 1981 by Johann Rafelski and Rolf Hagedorn, this *enhancement* in the produc-  
1247 tion of strange quarks in the QGP is referred to as **strangeness enhancement**.  
1248 As strangeness is conserved during strong interactions, the production of  $s\bar{s}$  pairs  
1249 can only come from four Feynman diagrams (to lowest order in pQCD), shown in  
1250 Figure 1.15. The key insight by Rafelski and Hagedorn was that in the QGP, the  
1251 higher temperatures allow for the thermal production of  $s\bar{s}$  pairs through gluon fusion  
1252 ( $gg \rightarrow s\bar{s}$  or diagrams (a) (b) and (c) in Figure 1.15). This gluon fusion occurs much  
1253 faster than the quark-based production ( $q\bar{q} \rightarrow s\bar{s}$  or diagram (d) in Figure 1.15),  
1254 and allows for the full chemical equilibration of strangeness in the QGP [81]. Such  
1255 an equilibration is not possible with only a hadronic gas phase [82] due to the much  
1256 slower interaction rates of hadrons.

1257 Experimentally, strangeness production is measured by looking at the abundance  
1258 of strange hadrons relative to non-strange hadrons, like pions. For central heavy  
1259 ion collisions—both at the LHC and RHIC—these strange/non-strange particle ratios  
1260 are found to be consistent with a hadron gas in both thermal *and* chemical equilib-  
1261 rium [83], [84]. As mentioned previously, this is a strong indication that the QGP  
1262 is formed in these collisions. Furthermore, these particle ratios as measured in lower  
1263 multiplicity pp collisions at the LHC are found to be consistent with statistical mod-  
1264 els *without* chemical equilibration [85], [86]. Under the strangeness enhancement  
1265 picture, this indicates that QGP formation does *not* occur in these lower multiplicity  
1266 pp collisions.

1267 However, filling in the gaps between low multiplicity pp collisions and high multi-  
1268 plicity Pb–Pb collisions reveals a more complicated picture, as shown in Figure 1.16.  
1269 The particle ratios seem to be consistent with a smooth transition between the two

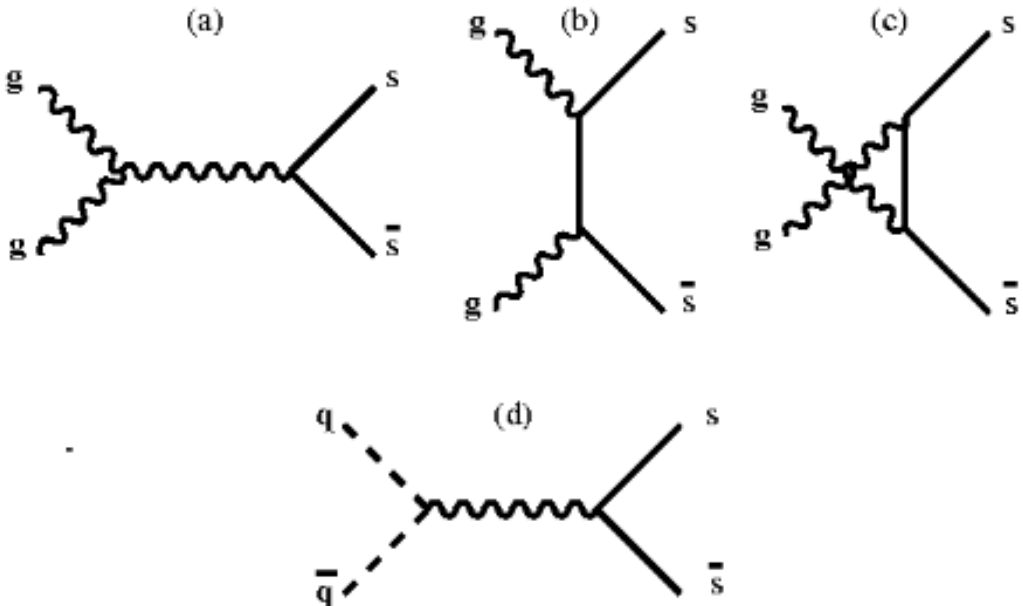


Figure 1.15: The four leading-order Feynman diagrams responsible for the production of  $s\bar{s}$  pairs in the QGP, adapted from [18]. Diagrams (a), (b) and (c) are the gluon fusion processes, while diagram (d) is the quark-based process.

regimes, independent of collision system. In other words, the ratios in higher multiplicity pp and p–Pb collisions match up nicely with the ratios in lower multiplicity Pb–Pb collisions. This indicates that the enhanced production of strange quarks is not exclusive to heavy ion collisions; there is an “onset” of strangeness enhancement occurring in lower multiplicity pp and p–Pb collisions. Furthermore, this enhancement is seen to scale with the number of strange quarks in the hadron: the  $\Omega$  baryon ( $sss$ ) exhibits the largest enhancement, while the proton ( $uud$ ) sees virtually no increase. This provides even stronger evidence for the formation of a chemically equilibrated QGP, which no longer appears exclusive to heavy ion collisions.

While extensions to the aforementioned statistical models can describe these multiplicity-dependent particle ratios in a phenomenological manner [88], the microscopic origins of this enhancement are not well understood. By investigating the production of strange hadrons in p–Pb collisions (where the onset is greatest), this thesis aims to shed light on the origins of this strange enhancement. However, it is necessary to first introduce some theoretical models to help interpret the results of this thesis.

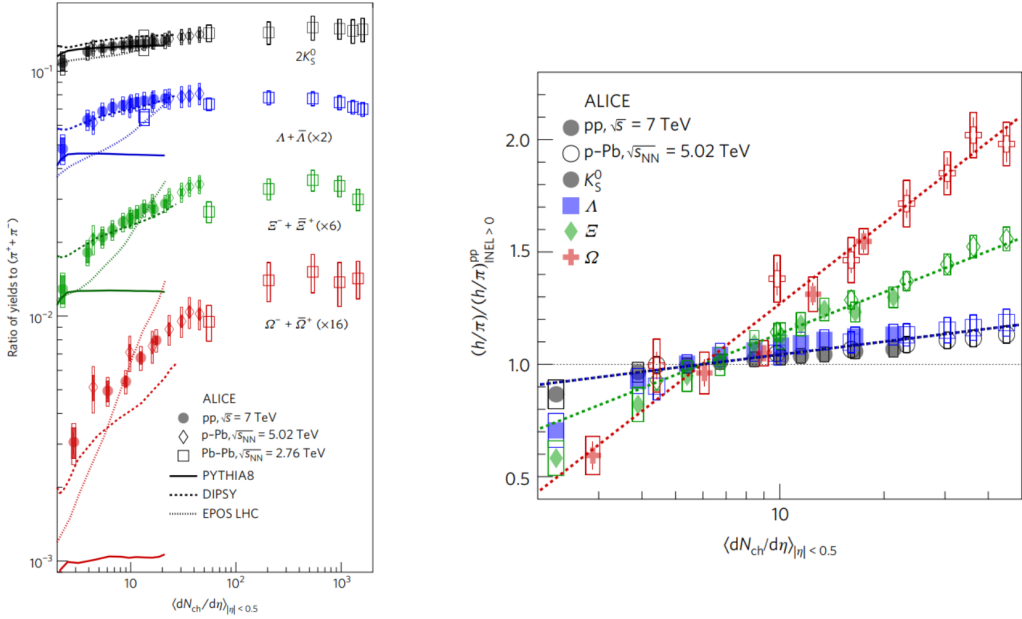


Figure 1.16: The particle ratios of strange hadrons to pions as a function multiplicity for different collision systems (left) and those same ratios normalized to an inclusive pp sample (right). The ratios appear to only depend on the multiplicity of the collision, and not the collision system. Taken from [87].

## 1.6 Theoretical models

Theoretical models of heavy ion collisions are pertinent to the understanding of QCD and the QGP. Without them, there would be no framework for interpreting the results from the very expensive experiments dedicated to studying this strongly interacting plasma. Unfortunately, due to the complexity of these heavy ion collision systems, there is no *single* model that can describe the entire collision evolution. Instead, the choice of model to compare a particular observable to depends very heavily on the observable in question. For example, some models treat the QGP phase of the collision as a hydrodynamic system, washing out information about the initial partonic scatterings [89]. This can be useful when trying to study bulk properties of the QGP (like the  $v_2$  from Section 1.5), but not-so-useful when studying jets and their constituents. Other models focus more on the individual partonic scatterings and subsequent hadronization, but do not include an explicit QGP phase [90], [91]. Such models are powerful tools for analyzing smaller collision systems (pp and lower multiplicity p-Pb), but fail to capture many of the features observed in heavy ion

1301 collision data. In this section, the models used to help interpret the results of this  
1302 thesis will be discussed. All of these models are capable of simulating pp, p–Pb, and  
1303 Pb–Pb events.

1304 **1.6.1 PHSD**

1305 Parton-Hadron-String-Dynamics (PHSD) [92], [93] is the only model explored in this  
1306 thesis that utilizes a **microscopic transport approach**: it simulates the full space-  
1307 time evolution of a heavy-ion collision by modeling the interactions of individual  
1308 particles. Here “particles” refers to different quantities (strings, partons, hadrons)  
1309 which are all evolved in different ways. The transport equations of the partons and  
1310 hadrons are derived from the Kadanoff-Baym (KB) equations [94], which describe  
1311 the non-perturbative transport of particles in a strongly interacting system. The  
1312 evolution of a collision within PHSD is as follows.

1313 **1.6.1.1 Initial stages**

1314 Prior to the collision, the simulation is broken up into a 3D-grid of size 56 in each  
1315 of the x, y, and z directions. The total size of the grid increases with each time step  
1316 such that the number of particles within a given cell evolves smoothly with time. The  
1317 initial momentum distribution and abundances of partons within the nuclei (prior to  
1318 any collision) are given by the thermal distributions

$$f(\omega, \vec{p}) = C_i p^2 \omega \rho_i(\omega, \vec{p}) n_{F/B}(\omega/\tau), \quad (1.11)$$

1319 where  $\rho_i$  are the spectral functions of the quarks and gluons ( $i = q, \bar{q}, g$ ) and  $n_{F/B}$  are  
1320 the Fermi-Dirac (for quarks) and Bose-Einstein (for gluons) distributions. Once the  
1321 nuclei collide, the partons interact with each other under the Lund string model to  
1322 form *leading hadrons* (at large rapidity) and *pre-hadrons* (at midrapidity), as shown  
1323 in Figure 1.17. The leading hadrons are immune to dissociation within the QGP,  
1324 while the pre-hadrons are not.

1325 **1.6.1.2 QGP phase**

1326 If the energy density  $\epsilon$  of a given cell increases beyond the critical energy density  
1327  $\epsilon_c = 0.5 \text{ GeV/fm}^3$ , the pre-hadrons within that cell are dissolved into partons. The

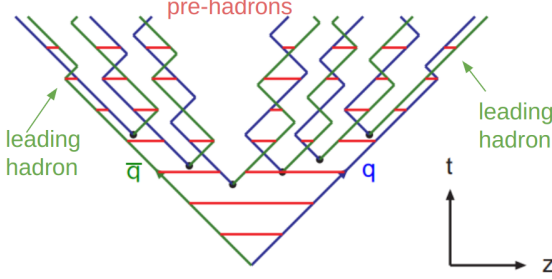


Figure 1.17: The Lund string model, with pre-hadrons and leading hadrons labeled.

1328 partons are then treated as interacting quasi-particles under the DQPM [95] model,  
1329 with Lorentzian spectral functions given by

$$\rho_j(\omega) = \frac{\gamma_j}{E_j} \left( \frac{1}{(\omega - E_j)^2 + \gamma_j^2} - \frac{1}{(\omega + E_j)^2 + \gamma_j^2} \right) \quad (1.12)$$

1330 where  $i$  is one of  $(q, \bar{q}, g)$  and the width  $\gamma_i$  is given by

$$\gamma_g(T) = N_c \frac{g^2 T}{8\pi} \ln \frac{2c}{g^2}, \quad \gamma_q(T) = \frac{N_c^2 - 1}{2N_c} \frac{g^2 T}{8\pi} \ln \frac{2c}{g^2}, \quad (1.13)$$

1331 where  $T$  is the temperature (calculated from the energy density within a given cell).  
1332 This is the key difference between DQPM and other transport models—the quarks and  
1333 gluons have non-zero temperature-dependent widths in the medium! The coupling  
1334 constant  $g$  is also temperature dependent, and is of the form

$$g^2(T/T_c) = \frac{48\pi^2}{(11N_c - 2N_f) \ln (\lambda^2 (T/T_c - T_s/T_c)^2)}. \quad (1.14)$$

1335 The parameters  $T_s$  and  $\lambda$  are fit to lattice QCD (lQCD) results [93]. The spectral  
1336 functions are enough to describe the propagation of the mean-fields of the partons  
1337 (effectively their Greens functions) via the aforementioned KB equations. The col-  
1338 lisional terms in these equations are determined by the modified scattering cross  
1339 sections of the partons. These cross sections are calculated using the leading order  
1340 Feynman diagrams, with the DQPM-modified quark and gluon propagators given by

$$i\delta_{ij} \frac{q + M_q}{q^2 - M_q^2 + 2i\gamma_q q_0} \quad (1.15)$$

1341 and

$$-i\delta_{ab} \frac{g^{\mu\nu} - q^\mu q^\nu / M_g^2}{q^2 - M_g^2 + 2i\gamma_g q_0}, \quad (1.16)$$

1342 respectively. Due to the large masses of the gluons,  $q + \bar{q} \rightarrow g + g$  and  $g \rightarrow g + g$  are  
 1343 suppressed and thus not included in the model.

1344 **1.6.1.3 Hadronization**

1345 Whenever the energy density of a given cell falls below the aforementioned critical  
 1346 energy density ( $\epsilon_c = 0.5$  GeV/fm $^3$ ), the partons within begin to hadronize. The  
 1347 dynamical hadronization of partons into hadrons is modeled by the equations

$$\frac{dN_m(x, p)}{d^4x d^4p} = \text{Tr}_q \text{Tr}_{\bar{q}} \delta^4(p - p_q - p_{\bar{q}}) \delta^4\left(\frac{x_q + x_{\bar{q}}}{2} - x\right) \\ \times \omega_q \rho_q(p_q) \omega_{\bar{q}} \rho_{\bar{q}}(p_{\bar{q}}) |v_{q\bar{q}}|^2 W_m(x_q - x_{\bar{q}}, (p_q - p_{\bar{q}})/2) \\ \times N_q(x_q, p_q) N_{\bar{q}}(x_{\bar{q}}, p_{\bar{q}}) \delta(\text{ flavor, color }). \quad (1.17)$$

1348 for mesons and

$$\frac{dN_B(x, p)}{d^4x d^4p} = \text{Tr}_{q_1} \text{Tr}_{q_2} \text{Tr}_{q_3} \delta^4(p - p_{\xi_3}) \delta^4(x - \xi_3) \delta\left(\sqrt{(\tau_1 - \tau_2)^2}\right) \\ \times \omega_{q_1} \rho_{q_1}(p_1) \omega_{q_2} \rho_{q_2}(p_2) \omega_{q_3} \rho_{q_3}(p_3) \\ \times |M_{qqq}|^2 W_B(\xi_1, \xi_2, p_{\xi_1}, p_{\xi_2}) \\ \times N_{q_1}(x_1, p_1) N_{q_2}(x_2, p_2) N_{q_3}(x_3, p_3) \delta(\text{ flavor, color }). \quad (1.18)$$

1349 for baryons. The terms for the meson case are described as follows:

1350 •  $\text{Tr}_q$  is shorthand notation for  $\text{Tr}_q = \sum_q \int d^4x_q \int \frac{d^4p_q}{(2\pi)^4}$ , where  $q$  is summed over  
 1351 all spin, color, and flavor degrees of freedom.

1352 •  $\delta^4(p - p_q - p_{\bar{q}})$  forces conservation of four-momentum. Note that the quarks  
 1353 and anti-quarks are allowed to be off-shell (due to their non-zero widths), thus  
 1354 this can result in off-shell mesons.

1355 •  $\delta^4\left(\frac{x_q + x_{\bar{q}}}{2} - x\right)$  puts the resulting meson in-between the quark and anti-quark  
 1356 pair.

1357 •  $\omega_q$  and  $\omega_{\bar{q}}$  are the energies of the quark and anti-quark, respectively.

1358 •  $\rho_q(p_q)$  and  $\rho_{\bar{q}}(p_{\bar{q}})$  are the aforementioned spectral functions of the quark and  
 1359 anti-quark, respectively.

- $|v_{q\bar{q}}|^2$  is the DQPM-determined *effective quark-anti-quark interaction*, which is shown as the green dashed line in Figure 1.18. Note that this value is very small for large quark (energy) densities, and thus this entire equation is effectively zero. However, for low quark densities this value blows up, which “turns on” the hadronization (and also guarantees that all partons will hadronize *eventually*).
- $W_m(x_q - x_{\bar{q}}, (p_q - p_{\bar{q}})/2)$  is the phase-space distribution of the resulting (pre-meson)
- $N_q(x_q, p_q)$  and  $N_{\bar{q}}(x_{\bar{q}}, p_{\bar{q}})$  are the phase-space densities of the quark and anti-quark, respectively.
- $\delta(\text{ flavor, color })$  is shorthand for “make sure flavor quantum numbers are conserved and that the resulting meson is color-neutral”.

The terms for the baryon case are similar.

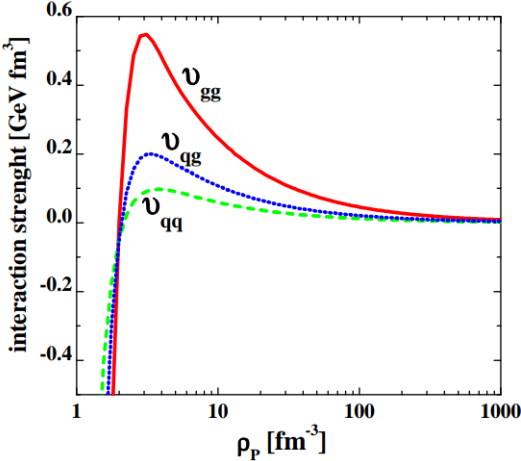


Figure 1.18: The effective quark-quark (green), quark-gluon (blue), and gluon-gluon (red) interactions as a function of parton density in DQPM, taken from [92].

The numerical integrations of equations 1.17 and 1.18 for a fixed test parton ultimately give the probability for a hadronization event to occur. From there, events are randomly selected using Monte Carlo techniques, which give a color neutral state with definite  $x$ ,  $p$  and flavor. However, this is *still* not enough to specify a hadron completely: many hadronic states of the same flavor have large widths. Thus to

1377 determine the identity of the final hadron, the weight of each possible<sup>19</sup> hadronic  
 1378 spectral function is computed. The hadron is then randomly assigned an identity  
 1379 based on these weights using Monte Carlo.

#### 1380 1.6.1.4 Hadronic phase

1381 All of the hadrons produced in the previous steps are transported using Hadron-  
 1382 String-Dynamics [97] (PHSD without the P). The phase-space distributions of the  
 1383 hadrons in HSD are transported using the equation

$$\begin{aligned} & \left\{ \left( \Pi_\mu - \Pi_\nu \partial_\mu^p U_h^\nu - M_h^* \partial_\mu^p U_h^S \right) \partial_x^\mu + \left( \Pi_\nu \partial_\mu^x U_h^\nu + M_h^* \partial_\mu^x U_h^S \right) \partial_p^\mu \right\} f_h(x, p) \\ &= \sum_{h_2 h_3 h_4 \dots} \int d2d3d4 \dots [G^\dagger G]_{12 \rightarrow 34 \dots} \delta_\Gamma^4(\Pi + \Pi_2 - \Pi_3 - \Pi_4 \dots) \\ & \quad \times \left\{ f_{h_3}(x, p_3) f_{h_4}(x, p_4) \bar{f}_h(x, p) \bar{f}_{h_2}(x, p_2) \right. \\ & \quad \left. - f_h(x, p) f_{h_2}(x, p_2) \bar{f}_{h_3}(x, p_3) \bar{f}_{h_4}(x, p_4) \right\} \dots, \end{aligned} \tag{1.19}$$

1384 where  $U_h^S$  and  $U_h^\mu$  are the scalar and vector hadron self-energies, respectively. The  
 1385 effective mass of the hadron  $M_h^*$  is given by

$$M_h^* = M_h + U_h^S, \tag{1.20}$$

1386 and its effective momentum is given by

$$\Pi^\mu = p^\mu - U_h^\mu. \tag{1.21}$$

1387 The “collisional” term  $[G^\dagger G]_{12 \rightarrow 34 \dots}$  is the transition rate for the process  $1 + 2 \rightarrow$   
 1388  $3 + 4 + \dots$ , which is modeled using Lund string fragmentation. The self-energies  $U_h^S$   
 1389 and  $U_h^\mu$  are evaluated on the basis of a Nambu-Jona-Lasinio (NJL)-type model [98]  
 1390 for the QCD Lagrangian. Once these self-energies (and  $[G^\dagger G]_{12 \rightarrow 34 \dots}$ ) are specified,  
 1391 the transport equation (Equation 1.19) can be solved.

#### 1392 1.6.1.5 A simple overview

1393 While the equations that govern PHSD are quite complicated, the overall picture is  
 1394 relatively simple. It can be summarized as follows:

---

<sup>19</sup>PHSD only includes the baryon octet/decouplet, the spin 0 and spin 1 meson nonets, and a few higher resonance states. Furthermore, if the invariant mass of the color neutral state is above 1.3 GeV (for mesons) or 1.5 GeV (for baryons), the state is treated as a Lund string with further decay handled by the JETSET algorithm [96]

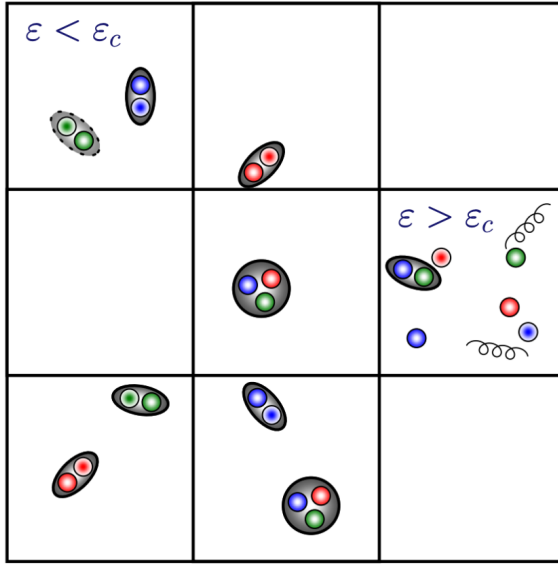


Figure 1.19: The cells within PHSD. If the energy density of the cell is greater than the critical energy density, the pre-hadrons dissolve into partons.

- 1395     • First, the simulation is split up into cells whose sizes evolve with time, as shown
- 1396        in Figure 1.19.
- 1397     • As the initial nuclei collide, and the interacting partons form pre-hadrons and
- 1398        leading hadrons.
- 1399     • If the energy density of a cell is too high, the pre-hadrons dissolve into partons,
- 1400        which are handled by the DQPM model.
- 1401     • If a cell with partons in it cools off, the partons dynamically hadronize.
- 1402     • The resulting hadrons (and any hadrons present in a particular cell) are trans-
- 1403        ported using HSD.

### 1404 1.6.2 EPOS LHC

1405 In the EPOS LHC [99] model, the initial colliding nuclei results in many parton-

1406 parton scatterings happening in parallel, as shown in Figure 1.20. These simultaneous

1407 scatterings form a parton ladder, which are modeled as relativistic Lund strings. Long

1408 before hadronization, the model separates into two distinct parts: the *core* and the

1409 *corona*. This designation is based on the string density (i.e. the number of string  
 1410 segments per unit volume). If the string density exceeds a critical density  $\rho_c$ , the  
 1411 string segments are considered to be in the core. Otherwise, they are in the corona.

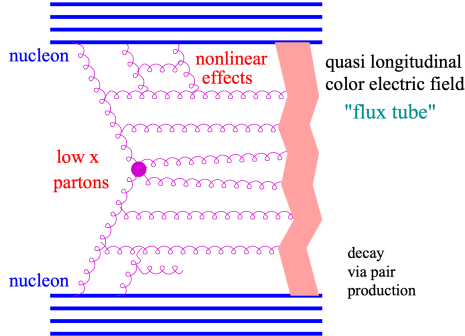


Figure 1.20: A schematic of the elementary interaction in EPOS LHC in which many parton-parton interactions are occurring simultaneously [99].

1412 The core is evolved in a hydrodynamic manner, which loses all information about  
 1413 the initial string segments and their interactions. Hadronization in the core is handled  
 1414 by a microcanonical procedure known as Cooper-Frye freeze-out, which is described  
 1415 in detail in [100]. The core is associated with the QGP medium, and dominates  
 1416 particle production at higher multiplicities. The corona, however, corresponds to  
 1417 unmodified Lund string fragmentation, which dominates at large rapidity and in  
 1418 lower multiplicity events.

### 1419 1.6.3 DPMJET

1420 Perhaps the most simple<sup>20</sup> event generator explored in this thesis is the DPMJET [101]  
 1421 model. DPMJET combines the Dual Parton Model (DPM) [102] with the Lund string  
 1422 model [58] to describe proton-proton, proton-nucleus, and nucleus-nucleus collisions  
 1423 across a large range of energies. The DPM describes all of the soft, non-perturbative  
 1424 multi-particle events that occur within a heavy ion collision using various large  $N_c$   
 1425 and  $N_f$  limits of QCD. This is the only model explored in this thesis that does  
 1426 not have an explicit QGP phase, as the collision constituents<sup>21</sup> are always treated

---

<sup>20</sup>Still *extremely* complicated from a theoretical perspective, but has the least moving parts.

<sup>21</sup>Strings. It's always strings.

1427 independently. Thus DPMJET serves as a good baseline for vacuum fragmentation,  
1428 and can be compared with other models (and data) to help quantify the effects of the  
1429 explicit QGP phase.

## Chapter Two: Experimental Apparatus

1431 As this thesis is focused on the physics of heavy-ion collisions, it stands to reason that  
1432 the data analyzed in this thesis was gathered using the only detector along the LHC  
1433 dedicated to studying such collisions: the ALICE detector. In this chapter, a brief  
1434 synopsis of the LHC will be provided, followed by a much more detailed overview of  
1435 the ALICE detector and its sub-detectors most relevant to this thesis.

1436 **2.1 The LHC**

1437 Located along the Swiss-French border near Geneva, Switzerland, the Large Hadron  
1438 Collider (LHC) [103], [104] is the largest particle accelerator on the planet. At a  
1439 circumference of 27 kilometers, its tunnels lie almost 200 meters beneath the surface of  
1440 the earth. Inside the tunnels are two high-energy particle beams pointing in opposite  
1441 directions, with the beam pipes being kept inside of an ultra-high vacuum. The  
1442 particles inside the beam are guided by a multitude of superconducting magnets:  
1443 393 quadrupole magnets keep the beam focused, while 1232 dipole magnets bend  
1444 the particles along the circular path. The beams are designed to collide at four  
1445 intersection points along the LHC, each with a corresponding detector surrounding  
1446 the collision points:

- 1447 1. ALICE [105], designed for investigating heavy-ion collisions
- 1448 2. ATLAS [106], designed for studying high- $p_T$  particles produced in pp collisions
- 1449 3. CMS [107], designed for precise detection of muons
- 1450 4. LHCb [108], designed for studying CP violations through measurements of B  
1451 mesons at forward rapidity

1452 Note that “designed for” does not mean that these detectors are incapable of investi-  
1453 gating other facets of particle collisions. For example, the ALICE detector is plenty  
1454 capable for studying pp collisions[109], [110], and the ATLAS and CMS detectors

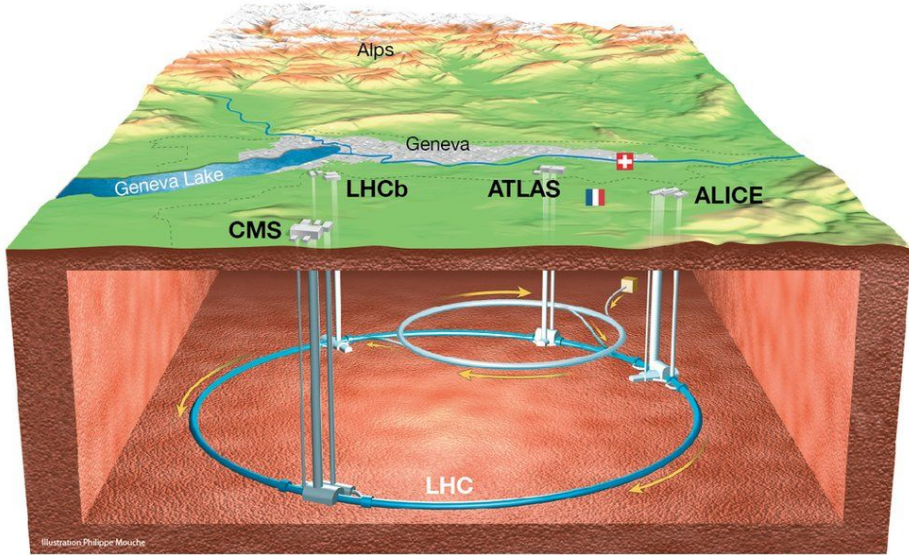


Figure 2.1: A diagram depicting the LHC with its various main detectors shown underground. Illustration by Philippe Mouche, taken from [113]

1455 have been used to publish exciting results for heavy-ion collisions [111], [112]. A di-  
 1456 agram of the LHC with these four intersection points can be seen in Figure 2.1. As  
 1457 of 2023, the highest center of mass energies achieved for each of the main collision  
 1458 systems ( $\text{pp}$ ,  $\text{p-Pb}$ ,  $\text{Pb-Pb}$ ) are  $\sqrt{s} = 13.6 \text{ TeV}$  for  $\text{pp}$ ,  $\sqrt{s} = 7 \text{ TeV}$  for  $\text{p-Pb}$  and  $\sqrt{s}$   
 1459 =  $5.36 \text{ TeV}$  for  $\text{Pb-Pb}$ .

## 1460 2.2 The ALICE Detector

1461 The detector used by the A Large Ion Collider Experiment (ALICE) collaboration,  
 1462 unsurprisingly known as the ALICE detector, has the primary focus of investigating  
 1463 the physical properties of the strongly interacting quark-gluon plasma created during  
 1464 heavy-ion collisions. Building the detector was a massive effort, requiring the help  
 1465 from over 1000 people from 105 institutes in 30 different countries. The detector itself  
 1466 is also massive, weighing in at around 10,000 tons, and spanning 26 meters in length  
 1467 with a 16-meter height and width. It is composed of 18 sub-detector systems, all of  
 1468 which work together to help reconstruct the event. A diagram of the detector with  
 1469 its corresponding sub-detector systems can be seen in Figure 2.2. As the primary  
 1470 focus of the ALICE detector is to study heavy-ion collisions, all of its components

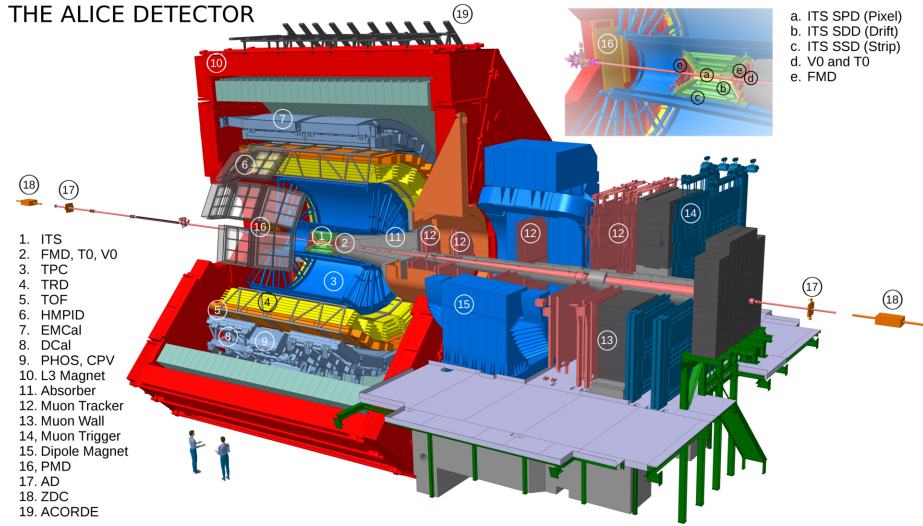


Figure 2.2: A 3-D schematic of the ALICE detector, with labels for all of the sub-detectors, taken from [114]. Note the humans-for-scale in the bottom left of the diagram.

1471 must work together to reconstruct very high multiplicity events. The components  
 1472 most relevant to this thesis will be discussed in the following sections.

### 1473 2.2.1 Detector coordinates

1474 Before discussing the components of the ALICE detector, it is important to first  
 1475 define a coordinate system suitable for describing the geometry of the detector and  
 1476 the collisions within. As the ALICE detector is a giant cylinder, the most pragmatic  
 1477 choice is cylindrical coordinates, with the  $z$ -axis pointing along the beam line. An  
 1478 example of this cylindrical coordinate system is shown in Figure 2.3. The plane  
 1479 defined by the  $x$ - and  $y$ -axes is often referred to as the **transverse plane**, with the  
 1480 angle  $\varphi$  referred to as the **azimuthal angle**.

1481 Unfortunately, collisions within the ALICE detector involve particles moving at  
 1482 relativistic speeds in the beam ( $z$ ) direction. Thus the polar angle  $\theta$  is not particularly  
 1483 useful, as it is not Lorentz invariant. Instead, a more useful quantity is the rapidity  
 1484  $y$ , which can be defined as

$$y = \frac{1}{2} \ln \left( \frac{E + p_z}{E - p_z} \right), \quad (2.1)$$

1485 where  $E$  is the energy of the thing being measured and  $p_z$  is the momentum in the  $z$ -

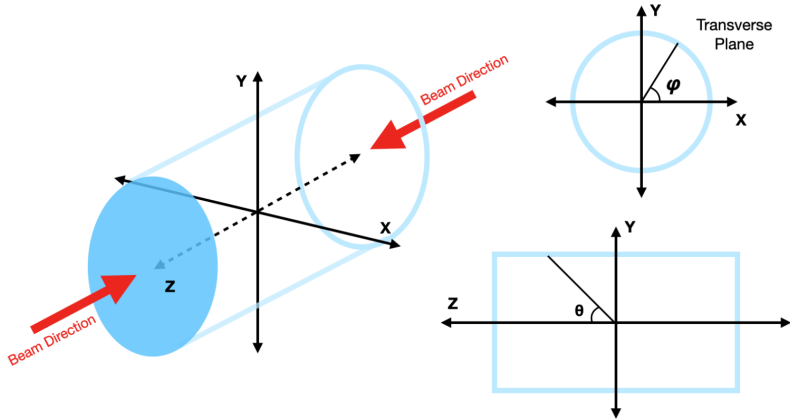


Figure 2.3: A diagram showing the cylindrical coordinate system used to describe the ALICE detector.

1486 direction. This quantity is preferable to  $\theta$  as differences in rapidity are invariant under  
 1487 Lorentz boosts along the z-axis. This follows directly from the fact that rapidity is  
 1488 often defined in terms of such boosts,

$$\begin{pmatrix} ct' \\ z' \end{pmatrix} = \begin{pmatrix} \cosh y & -\sinh y \\ -\sinh y & \cosh y \end{pmatrix} \begin{pmatrix} ct \\ z \end{pmatrix} \equiv \Lambda(y) \begin{pmatrix} ct \\ z \end{pmatrix}. \quad (2.2)$$

1489 It can be shown<sup>1</sup> that  $\Lambda(y)$  obeys

$$\Lambda(y_1 + y_2) = \Lambda(y_1)\Lambda(y_2), \quad (2.3)$$

1490 which in turn gives a rapidity addition rule for reference frames A, B and C moving  
 1491 along the z-axis,

$$y_{AC} = y_{AB} + y_{BC}. \quad (2.4)$$

1492 Now suppose reference frame A is the lab (stationary) frame, and reference frames B  
 1493 and C correspond to two different particles. The above equation can then be written  
 1494 as

$$y_{AC} - y_{AB} = y_{BC} = y_{A'B} - y_{A'C}, \quad (2.5)$$

1495 where  $A'$  can be *any* reference frame. In other words, the difference in rapidity  
 1496 between any two particles does not depend on the reference frame the measurement

---

<sup>1</sup>Using various properties of the hyperbolic trigonometric functions.

1497 is made in. Another consequence of this property is that rapidity distributions of  
1498 particles do not change shape in different reference frames: they only get shifted  
1499 along the rapidity axis.

1500 However, the total energy of a given particle is often not known, and thus rapidity  
1501 is replaced by the more experiment-friendly **pseudorapidity**,

$$\eta = \frac{1}{2} \ln \left( \frac{|\vec{p}| + p_z}{|\vec{p}| - p_z} \right) = -\ln \left( \tan \frac{\theta}{2} \right), \quad (2.6)$$

1502 where  $\theta$  is the aforementioned polar angle. This quantity can be directly measured by  
1503 experiment, at the expense of losing a small amount of Lorentz invariance: the *pseudo*  
1504 part of pseudorapidity comes from the idea that at very high momentum ( $p \gg m$ ),  
1505 the rapidity and pseudorapidity are approximately equal.

## 1506 2.3 The Inner Tracking System

1507 The Inner Tracking System (ITS) [115] is the inner most component of the ALICE  
1508 detector, lying closest to the beam pipe. It is composed of six cylindrical layers of  
1509 silicon detectors that are coaxial with the beam pipe and cover the pseudorapidity  
1510 range  $|\eta| \leq 0.9$ . The distance from the beam line varies from 3.9 cm for the first layer  
1511 to 43 cm for the sixth layer. A diagram of the ITS can be seen in Figure 2.4. Because  
1512 of its proximity to the interaction point, the ITS is invaluable for reconstructing both  
1513 primary and secondary vertices and enhancing the tracking capabilities of the ALICE  
1514 detector near the interaction point. Moreover, the ITS can also track particles that are  
1515 not detected or missed by the external barrel detector due to acceptance limitations  
1516 and momentum cutoff.

1517 The ITS uses different types of silicon detectors for each layer, which will be briefly  
1518 discussed in the following sections.

### 1519 2.3.1 Layers 1 and 2

1520 The first and second layers of the ITS are composed of **Silicon Pixel Detectors**  
1521 (SPD) [117]. The SPD inner and outer barrel layers have radii of 3.9 cm and 7.6  
1522 cm, respectively. The pseudorapidity coverage is  $|\eta| < 1.95$ , the highest of all the  
1523 ITS detectors. The SPD is segmented into 10 sectors which each cover 36 degrees in

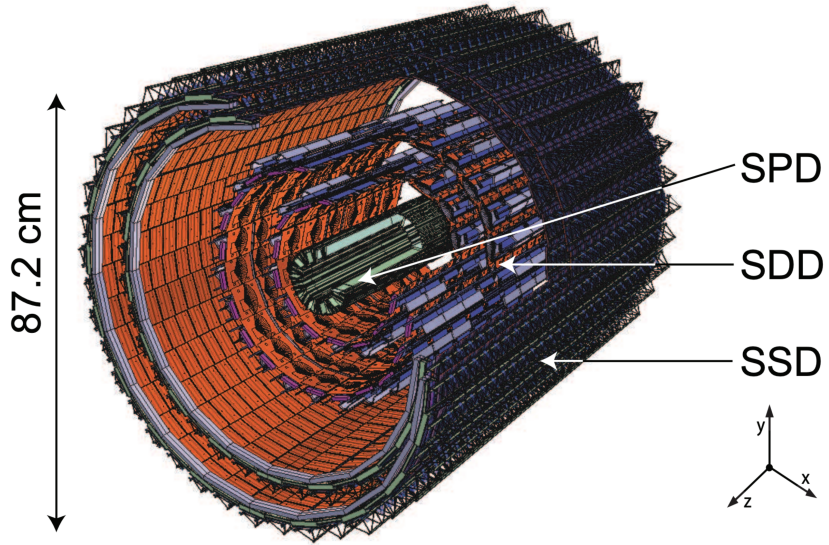


Figure 2.4: A schematic of the ITS showing the six layers of silicon detectors, taken from [116].

azimuth. Each of these sectors contains 12 modules—called half-staves—which themselves consist of 10 silicon pixel chips. These chips are  $13.68 \text{ mm} \times 15.58 \text{ mm}$  in size and contain 8192 pixels each, corresponding to a pixel size of  $425 \mu\text{m} \times 50 \mu\text{m}$ . This small pixel size gives rise to a very low occupancy (< 2%) for even the most central Pb–Pb collisions. As the track densities in the innermost layers are very high (up to 100 tracks/cm<sup>2</sup> for central Pb–Pb collisions), the SPD has a very high granularity in order to keep the occupancy low. The SPD is also used to generate the L0 trigger signal, which is used to trigger the readout of the TPC and TRD.

### 2.3.2 Layers 3 and 4

The middle two layers of the ITS are made up of **Silicon Drift Detectors** (SDD)[118]. These layers extend from an inner radius of 14 cm to an outer radius of 24 cm, and cover the pseudorapidity range  $|\eta| < 0.9$ . There are 260 large area ( $7.02 \times 7.53 \text{ cm}^2$ ) SSD modules in total, which are split into two drift regions. As an ionizing particle passes through the drift regions, the resulting electrons *drift* into the collection anodes, which are at the ends of the drift regions and are connected to the frontend readout electronics. This separates the SPD and the SDD in a fundamental way—the

1540 data from the SDD is analog, and depends very much on how many electrons were  
1541 “knocked loose” during ionization. The SPD, on the other hand, is digital, and only  
1542 registers a hit (1) if a charged particle passes through the pixel. This analog informa-  
1543 tion can be used to help identify the ionizing particle species using the Bethe-Bloch  
1544 formula, which will be discussed in more detail in Section 2.4. Furthermore, there  
1545 are MOS charge injectors [119] connected to the cathodes in the drift region, which  
1546 provide precise timing information to compute the electron drift velocity. This ve-  
1547 locity is needed to precisely measure the location of the initial ionizing particle along  
1548 the direction of the applied electric field. As the track density in the middle layers is  
1549 lower than in the innermost layers, the SSD has a coarser granularity than the SPD.

### 1550 2.3.3 Layers 5 and 6

1551 The last two layers of the ITS are **Silicon Strip Detectors** (SSD) [120], which have  
1552 an inner radius of 38 cm and an outer radius of 43 cm. The SSD covers the pseudora-  
1553 pidity range  $|\eta| < 0.9$ , and is composed of 1698 modules in total. These modules are  
1554 a 1536-strip double-sided silicon sensor, with each strip connected to the front-end  
1555 readout electronics. Similar to the SDD, the SSD collects electrons generated when  
1556 the ionizing particle travels through the silicon—though the drift distance is *much*  
1557 smaller (300 microns for the SSD vs. 70.2 mm for the SDD). The SSD provides two  
1558 dimensional measurements of the ionizing particle’s position with a 20 micron reso-  
1559 lution in the  $r\varphi$  direction. The SSD also captures an analog signal, and is therefore  
1560 used to help identify the ionizing particle species.

### 1561 2.3.4 ITS Upgrade

1562 During the long shutdown (LS2) from December 2018 to June 2022, the LHC under-  
1563 went a fairly substantial upgrade to allow for higher beam energies and luminosities.  
1564 The luminosity increase from Run 2 (before LS2) to Run 3 (after LS2) was substantial,  
1565 from 12 inverse femtobarns before the shutdown to well over 200 inverse femtobarns  
1566 after starting up again [121]. As such, the ALICE detector needed to undergo quite a  
1567 few upgrades to keep up with the increased collision rates. In terms of pure hardware  
1568 upgrades, only three detectors were affected, namely

- 1569 • the Time Projection Chamber (TPC) [122],

1570 • the Muon Forward Tracker (MFT) [123], and

1571 • the ITS [124].

1572 The TPC and MFT upgrades will not be summarized in this thesis<sup>2</sup>, but some key  
1573 features of the ITS upgrade will be discussed in the following sections.

#### 1574 2.3.4.1 Motivation for the ITS upgrade

1575 As mentioned previously, the increased collision rates associated with the higher  
1576 luminosity LHC beam necessitated an upgrade to the ITS. Previously, the readout  
1577 rate for the ITS was 1 kHz for both pp and Pb–Pb collisions. The upgraded ITS, on  
1578 the other hand, is able to readout at 100 kHz for Pb–Pb and 200 kHz for pp collisions,  
1579 drastically increasing the amount of possible data to be taken over the course of Run  
1580 3. The upgraded ITS also has a much finer impact parameter resolution than the  
1581 previous ITS, improving by a factor of 3 in the  $r\phi$  coordinate and by a factor of 5 in  
1582 the  $z$  coordinate. This improved resolution is crucial for the ALICE physics program,  
1583 as it allows for the reconstruction of more secondary vertices—like those from the decay  
1584 of a B meson; this was previously not possible with the old detector. The tracking  
1585 efficiency at lower  $p_T$  was also improved, thanks to a strong reduction in the material  
1586 budget (from 1.14%  $X_0$  to 0.35%  $X_0$ ).

#### 1587 2.3.4.2 Hardware overview

1588 The upgraded ITS consists of seven layers of silicon detectors, as shown in Figure 2.5.  
1589 There are a total of 192 *staves*—rows of silicon chips—which cover a total area of 10  
1590 square meters. Each chip is of the same technology, which will be discussed in more  
1591 detail in the next section. The first three layers form the Inner Barrel (IB), and  
1592 contain 48 staves of 27 cm length. The remaining layers are referred to as the Outer  
1593 Barrel (OB). The OB is further separated into the Middle Layers (MLs) and Outer  
1594 Layers (OLs), which correspond to the 4–5th and 6–7th layers, respectively. The MLs  
1595 each have 54 staves of length 84 cm, and the OLs have 90 staves of 150 cm. The  
1596 grouping of the layers into the IB and OB has ramifications for the hardware testing  
1597 procedure, which is described in Section 2.3.4.4.

---

<sup>2</sup>The author of this thesis was intimately involved with the ITS upgrade, and thus would be unable to provide a fair and unbiased description of the TPC and MFT upgrades.

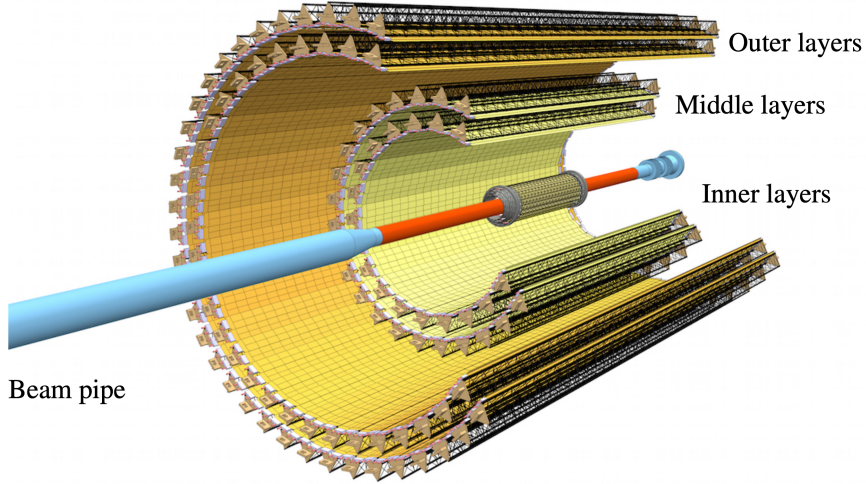


Figure 2.5: A schematic of the ITS upgrade, showing the seven layers of silicon detectors.

#### 1598 2.3.4.3 The ALPIDE chip

1599 The star of the show for the ITS upgrade is the introduction of a new silicon pixel  
 1600 chip: the ALPIDE [125]. The ALPIDE chip is a CMOS Monolithic Active Pixel  
 1601 Sensor (MAPS) that has a few advantages over its predecessors (e.g. the SPD):

- 1602 • Thanks to a deep p-well, complex logic at the pixel level can be employed. This  
 1603 deeper p-well prevents the n-well PMOS part of the CMOS transistor from  
 1604 collecting unwanted electrons (which are intended for the collection electrodes)
- 1605 • These CMOS transistors allow for complicated in-pixel circuitry, which (when  
 1606 coupled with the priority encoder) *drastically* reduces the data rate by only  
 1607 sending the addresses of “hit” pixels to the frontend electronics

1608 Each chip is  $15 \times 30 \text{ mm}^2$ , and contains over half a million pixels (512 rows, 1024  
 1609 columns). This corresponds to a spatial resolution of 5 microns, which is much better  
 1610 than the SPD of the old ITS (around 50 microns in  $r\varphi$ ). A diagram of the cross  
 1611 section of an ALPIDE (or more generally a MAPS) pixel can be seen in Figure 2.6.  
 1612 In this diagram, a charged hadron flies through the chip, generating many electron-  
 1613 hole pairs. The electrons are guided to the n-well diode, which ultimately collects

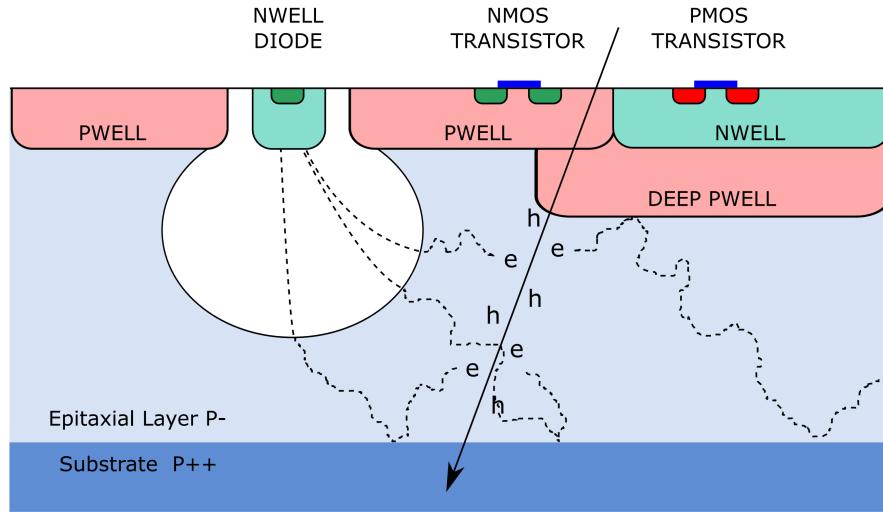


Figure 2.6: A diagram showing the basic operating principle of a MAPS pixel.

1614 the electrons and generates a signal. The CMOS transistors (NMOS and PMOS  
 1615 transistors) are vitally important for the pixel-level logic. Without the deep p-well to  
 1616 protect the PMOS's n-well from wandering electrons, the PMOS (and therefore the  
 1617 CMOS) transistors would be rendered useless.

1618 These CMOS transistors work together to form the logic within the pixel, shown  
 1619 as a block diagram in Figure 2.7. First, the collection diode sends a signal *SUB*,  
 1620 which comes in the form of a large voltage drop in a very short ( $\approx 10$  ns) time,  
 1621 followed by a slow reequilibration. The *VPULSE* signal is used for testing purposes,  
 1622 where a “fake” charge can be sent to the capacitor, generating a similar signal to the  
 1623 collection diode. The resulting *PIX\_IN* signal is sent to an amplifier + signal shaper,  
 1624 and then to a discriminator with threshold *THR*. If the amplified signal is less than  
 1625 the threshold, no *OUT\_D* signal is generated. The digital *OUT\_D* signal is then  
 1626 sent into a simple AND gate, where the other input signal is the digital *STROBE*.  
 1627 This strobing window is ultimately initialized by a trigger signal, and its width is  
 1628 configurable. If the *OUT\_D* signal is high during the strobing window, then one of  
 1629 the three hit storage registers is “latched” (i.e. set to one). Also included in the pixel  
 1630 logic is a masking register, which masks the pixel during readout when hot.

1631 The priority encoder (which physically lies between two columns of pixels) sequen-  
 1632 tially provides the addresses of the latched pixels to the frontend electronics on the

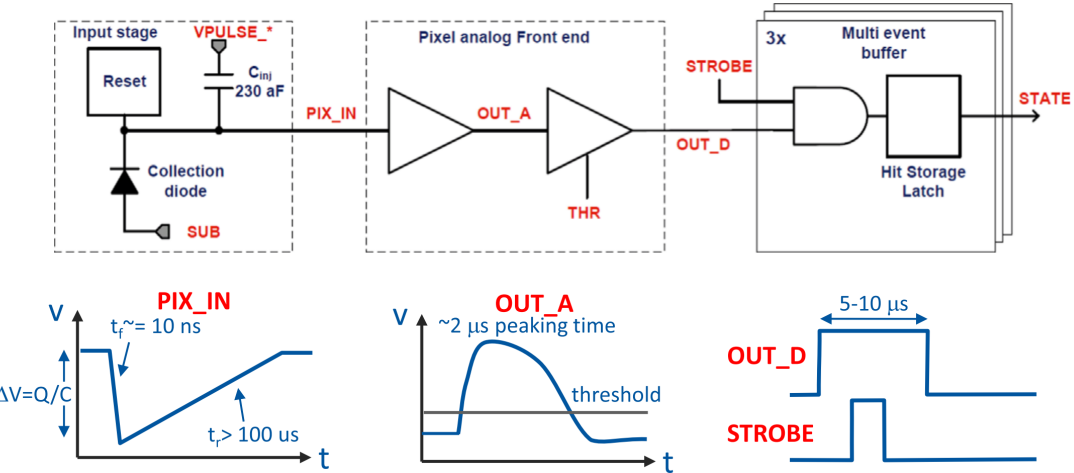


Figure 2.7: A block diagram showing the logic embedded on top of a single ALPIDE pixel.

chip. An important feature of the on-pixel electronics and priority encoder is the lack of a clock: this means that there is no activity if there are no hits. In other words, the ALPIDE chip is not sending a bunch of useless 0's to the readout electronics, saving precious bandwidth.

#### 2.3.4.4 Characterizing the chips for commissioning

Each ALPIDE chip has over 500,000 pixels, each with their own circuit logic. Excluding issues with the frontend electronics on the chip, that is still *over* 500,000 possible points of failure. As such, the chips were thoroughly tested to determine if they are worthy of being installed in the ITS. There are three main tests that were performed on each chip:

1. **Fake hit rate:** All pixels are unmasked, and a *STROBE* signal is repeatedly sent to each pixel. As the *THR* signal should prevent any hits from being registered, any latched pixels are considered “fake hits”.
2. **Threshold scan:** A predetermined amount of charge is injected into each pixel via the *VPULSE* signal, and the *THR* signal is varied. There should be a clear threshold where every pixel registers a hit, and vice-versa.

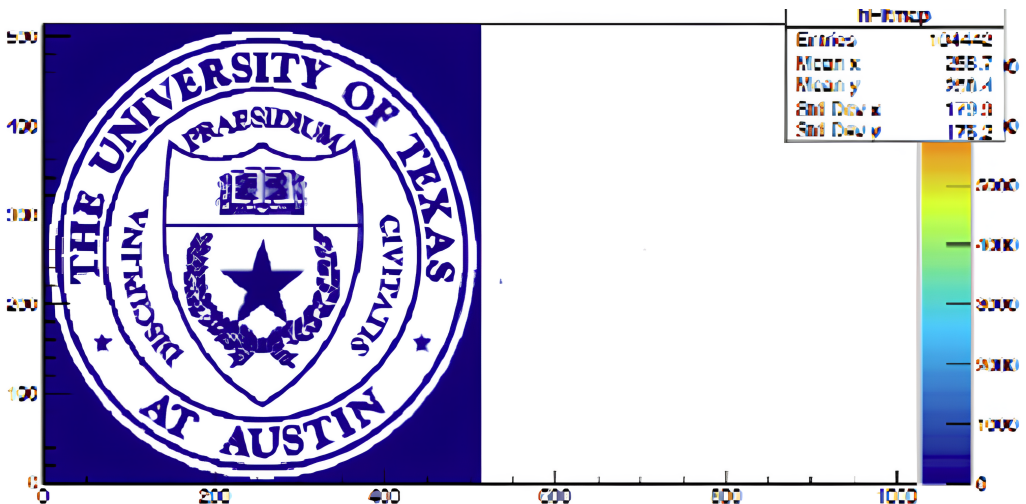


Figure 2.8: The signal that was read out from the ALPIDE chip after sending an extremely technical digital input pattern.

1649     3. **Readout tests:** Either a digital signal (by writing the hit storage register)  
 1650       or an analog signal (by injecting charge into the capacitor) pattern is sent to  
 1651       the entire chip, and then the corresponding output is read out. The resulting  
 1652       output should be the same as the input, like the example shown in Figure 2.8.

1653     These tests were run on the ALPIDE software, which is a graphical user interface  
 1654     (GUI) that allows for easy communication with the chips. The resulting output of  
 1655     the tests was simply one of four options, which are summarized in Table 2.1. This  
 1656     medal system was used to determine where the chip should be installed within the  
 1657     detector. If a chip was GOLD, it was reserved for the IB. If the chip was SILVER, it  
 1658     could be installed in either the MLs or the OLs. If the chip was BRONZE, it could  
 1659     only be installed in the OLs. Finally, if the chip FAILED the tests, it was discarded<sup>3</sup>.  
 1660     Further characterization was done at the stave level to determine where within the  
 1661     IB or OB a particular stave should be installed.

1662     2.3.4.5   The readout unit

1663     Another large overhaul for the ITS upgrade was a complete redesign of the readout  
 1664     system, from chip to DAQ. A schematic of the new readout system can be seen in

---

<sup>3</sup>Sent to the poor souls developing the ALPIDE software.

Table 2.1: A summary of the medal system used to determine where a particular chip should be installed. Note that while 99% *seems* strict, it corresponds to over 5000 misbehaving pixels.

Medal	% of good pixels
GOLD	99.99%
SILVER	99.67%
BRONZE	99.00%
FAIL	< 99.00%

1665    Figure 2.9. Each detector stave is connected to a **readout unit** (RU) via a relatively  
 1666    long copper data cable. A single RU has a lot of responsibilities, including

- 1667       • communicating with the power board so it can properly power the chips,
- 1668       • receiving the trigger information from the Central Trigger Processor (CTP) and  
                 sending it to the chips (which generates the *STROBE* signal discussed above),
- 1670       • receiving *all* of the data from the chips on the stave, which each have their own  
                 1.2 Gbps link (for the IB chips, the OB chips share a 400 Mbps link in groups  
                 of seven), and
- 1672       • sending the readout data from the chips to the Common Readout Unit (CRU),
- 1674       all while being in a highly radiative environment (only 6-8 meters away from the  
                 detector).

1676       These responsibilities are mostly handled by two on-board field-programmable  
 1677       gate arrays (FPGAs): an SRAM FPGA for actually handling all of the aforemen-  
 1678       tioned data transfer between the various components, and a flash FPGA for ensuring  
 1679       that the SRAM FPGA does not misbehave in the radiative environment. The SRAM  
 1680       FPGA continuously scrubs the flash FPGA to ensure that it has not been misconfig-  
 1681       ured due to a radiation upset. If it has, the SRAM FPGA will reconfigure it using  
 1682       the “golden image” of the SRAM firmware stored in the flash memory of the flash  
 1683       FPGA (hence the name). Even still, the important modules of the SRAM FPGA are  
 1684       triplicated, meaning that if one module is subject to a radiation upset, the other two  
 1685       can outvote it. An image of the RU at the University of Texas at Austin can be seen  
 1686       in Figure 2.10.

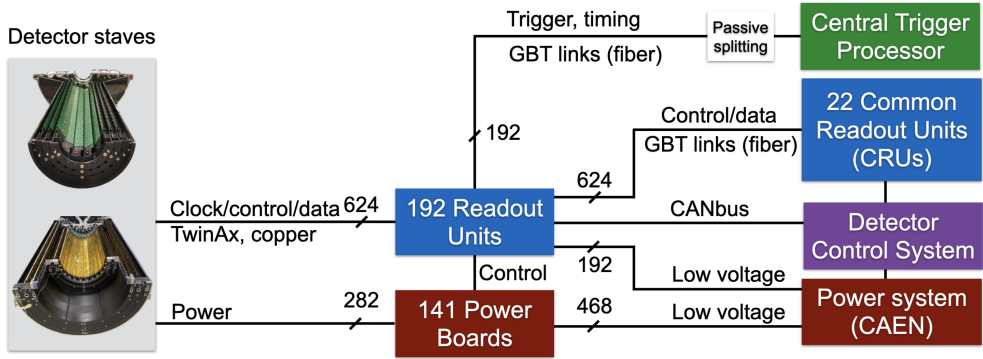


Figure 2.9: A schematic of the ITS readout system, showing the various components of the system.

## 2.4 The Time Projection Chamber

The largest component of the ALICE detector is known as the Time Projection Chamber (TPC) [126], [127]. The TPC is a gas-filled volume with an 85 cm inner radius, a 250 cm outer radius, and a five meter length along the beam axis. This corresponds to an active volume of around 90 cubic meters, all of which is filled with a Ne-CO<sub>2</sub>-N<sub>2</sub> (90-10-5) gas mixture. The TPC has an ionizing drift detector: charged particles moving through the detector ionize the gas, and the resulting electrons drift towards the endplates of the detector<sup>4</sup>—heavily coerced by the presence of a strong 400 V/cm electric field along the z-axis. This electric field is generated by a central cathode that is kept at a potential of 100 kV. A schematic of the TPC field cage can be seen in Figure 2.11.

Readout chambers with design based off of the Multi-Wire Proportional Chamber (MWPC) technique are installed at both endplates. In short, these chambers contain an array of wires held at a high voltage are placed in front of a plane of pads held at ground. The electrons that drift towards the endplate pass through this region, which causes a localized cascade of ionization<sup>5</sup> that is ultimately collected by the pads. The inner readout chamber has 5504 total pads, while the outer readout chamber (i.e.

<sup>4</sup>A very similar mechanism to the SDD, on a much larger scale.

<sup>5</sup>Often called a Townsend avalanche, where the ionizing electrons from the initial ionization of the ionizable gas ionize the ionizable gas, creating more ionizing electrons to ionize more ionizable gas...

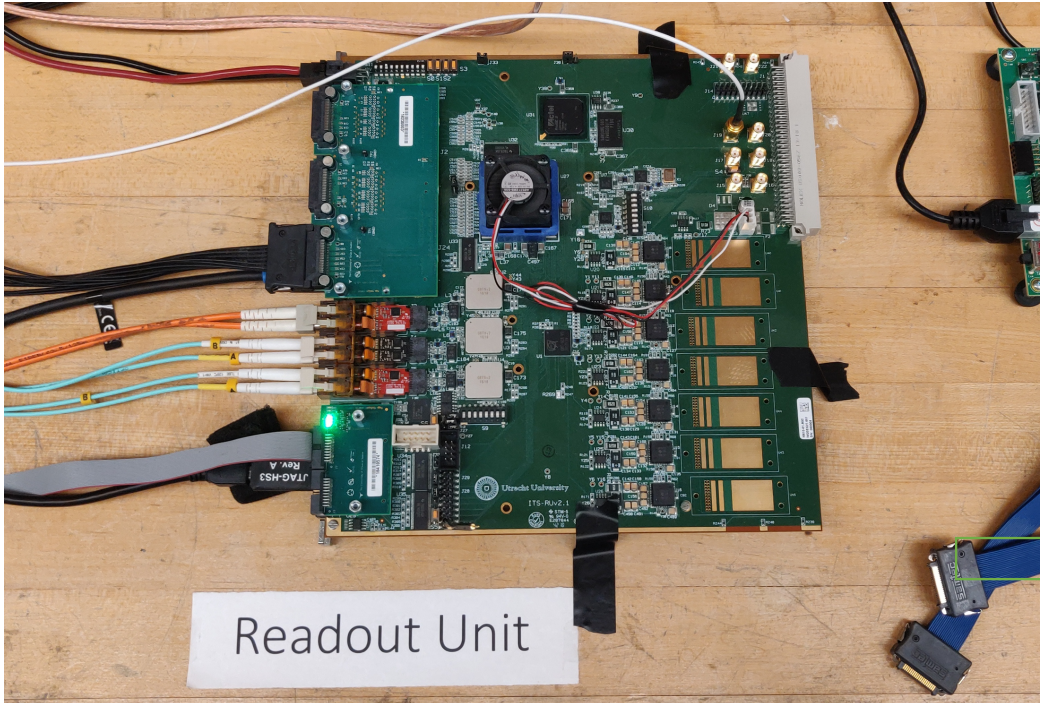


Figure 2.10: A picture of a readout unit in its (not-so) natural habitat at the University of Texas at Austin. The heat sink and fan are covering the main SRAM FPGA, and to its north-east is the flash FPGA.

1704 the one actually visible in Figure 2.11) has nearly 10000. The pads are grouped  
 1705 into 18 trapezoidal sectors, each of which covers  $20^\circ$  in azimuth. Unfortunately the  
 1706 boundaries of these sectors don't contain any pads, resulting in very narrow "dead  
 1707 zones" within the azimuthal acceptance of the TPC. Using information from both  
 1708 the ITS and TPC, it is possible to reconstruct particle tracks with a resolution of 1  
 1709 mm in the transverse plane and 2 mm in the longitudinal direction. The momentum  
 1710 resolution in the transverse plane is also very good, staying below 5% from zero to  
 1711 well over 100 GeV/c.

1712 The TPC is also capable of providing information that can be used to identify  
 1713 particles. As a charged particle travels through the active volume of the TPC, it loses  
 1714 energy as it ionizes the gas in a way that only depends on the particle's velocity. This  
 1715 energy loss is often described by the Bethe-Bloch formula [128]

$$\left\langle -\frac{dE}{dx} \right\rangle = K z^2 \frac{Z}{A} \frac{1}{\beta^2} \left[ \ln \frac{2m_e c^2 \beta^2 \gamma^2}{I} - \beta^2 - \frac{\delta(\beta\gamma)}{2} \right] \quad (2.7)$$

1716 where  $K$  is a constant coefficient ( $\approx 0.31$  MeV mol $^{-1}$  cm $^2$ ),  $z$  is the charge of the

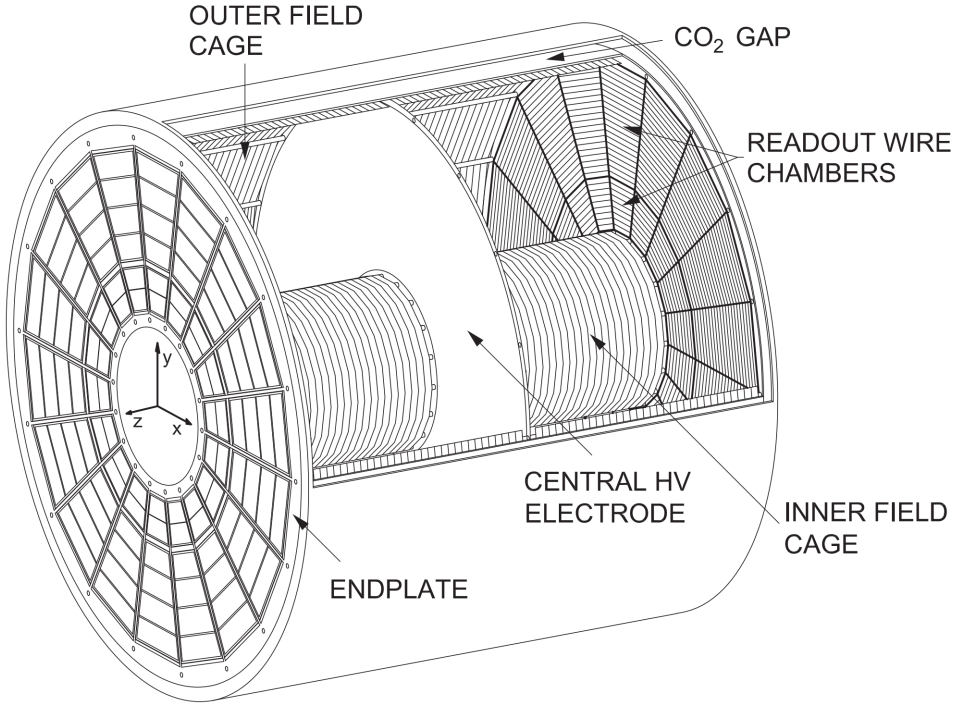


Figure 2.11: A schematic of the TPC field cage, taken from [126]

1717 particle,  $Z$  and  $A$  are the atomic and mass numbers of the gas,  $\beta$  is the velocity of  
 1718 the particle in units of the speed of light,  $\gamma$  is the Lorentz factor,  $m_e$  is the mass  
 1719 of the electron,  $c$  is the speed of light, and  $I$  is the mean excitation energy of the  
 1720 gas. An important feature of this equation is that most of the parameters depend on  
 1721 the gas mixture and the mass of the electron. For a fixed gas mixture, this equation  
 1722 gives a relationship between the energy (loss) and the velocity of the particle. As the  
 1723 momentum of the particle is known, the mass (and therefore the particle species) can  
 1724 be determined. To see this explicitly, it is useful to look at a common parameterization  
 1725 of the Bethe-Bloch formula [129],

$$f(\beta\gamma) = \frac{P_1}{\beta^{P_4}} \left( P_2 - \beta^{P_4} - \ln \left( P_3 + \frac{1}{(\beta\gamma)^{P_5}} \right) \right), \quad (2.8)$$

1726 where parameters  $P_i$  only depend on the gas mixture. Rewriting this equation in  
 1727 terms of the momentum  $p$  of the particle gives a curve for each particle species with

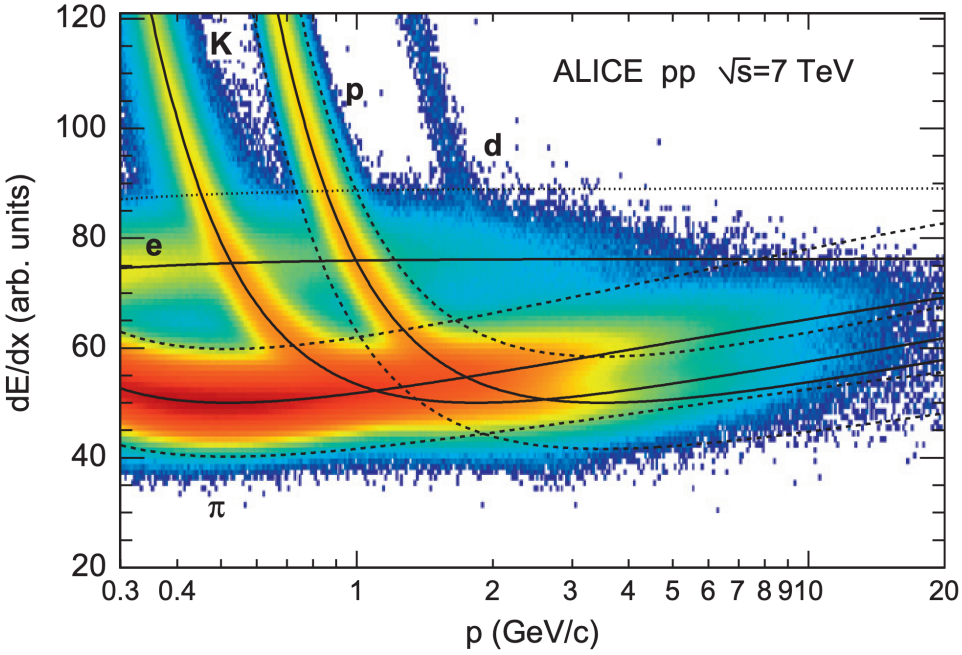


Figure 2.12: The energy loss signal for different particle species using the ALICE TPC gas mixture, taken from [129]. The solid lines represent the expected energy loss signal for each particle species (Equation 2.9).

1728 mass  $m_i$ ,

$$f(p, m_i) = P_1 \left( \frac{\sqrt{m_i^2 + p^2}}{p} \right)^{P_4} \left( P_2 - \left( \frac{p}{\sqrt{m_i^2 + p^2}} \right)^{P_4} - \ln \left( P_3 + \frac{m_i^{P_5}}{p^{P_5}} \right) \right). \quad (2.9)$$

1729 Examples of the energy loss signal for different particle species using the ALICE  
 1730 TPC gas mixture can be seen in Figure 2.12. Note that while there are clearly  
 1731 defined lines for each particle species from Equation 2.9, the actual signal is spread  
 1732 out around these lines due to the energy loss and momentum resolution of the TPC.  
 1733 Furthermore, many of the curves intersect at higher momentum. As such, it is useful  
 1734 to define the quantity

$$n\sigma_{\text{TPC}} = \frac{\langle dE/dx \rangle_{\text{meas}} - \langle dE/dx \rangle_{\text{exp}}}{\sigma_{\text{TPC}}}, \quad (2.10)$$

1735 which is the number of standard deviations away from the expected energy loss signal  
 1736 for a given particle species. If an unidentified particle has an  $n\sigma_{\text{TPC}}$  value close to

1737 zero, it is likely that the particle is of that species. However, when investigating  
1738 a specific particle species, compromises must be made—requiring a low  $n\sigma_{\text{TPC}}$  value  
1739 may result in less contamination from other particle species, but also yields lower  
1740 statistics.

## 1741 2.5 The Time of Flight detector

1742 The Time of Flight (TOF) detector [130] is a large array of Multi-gap Resistive  
1743 Plate Chambers (MRPCs) [131] that is used to measure the time of flight of charged  
1744 particles from the nominal interaction point. The TOF is located directly outside  
1745 of the TPC at a radius of around 3.7 meters, and covers the pseudorapidity range  
1746  $|\eta| < 0.9$ . It consists of 1593 MRPC strips, arranged in 18 sectors along the azimuthal  
1747 direction. Each MRPC strip has two rows of 48 pickup pads with area  $3.5 \times 2.5 \text{ cm}^2$ ,  
1748 to ensure low occupancy even in the most crowded events. This gives a total of 96 pads  
1749 per strip and 152928 readout channels in total. The TOF MRPC has a double-stack  
1750 structure; each of the two stacks has five gas gaps each. The resistive plates are made  
1751 of standard soda-lime glass sheets. The gap (250  $\mu\text{m}$ ) is created by commercial fishing  
1752 line stretched over the glass sheets. The average MRPC time resolution, including  
1753 the effects of the full front-end and readout electronics, was measured to be better  
1754 than 50 ps in a beam test setup.

1755 The primary goal of the TOF detector is particle identification: the time of flight  
1756 of a particle is directly related to its velocity (as the TOF is a fixed length away from  
1757 the interaction point), which can be used with the particle’s momentum to determine  
1758 its mass. More explicitly, the velocity  $\beta$  of a particle is given by (in natural units)

$$\beta_{\text{TOF}} = \frac{L}{t_{\text{TOF}}}, \quad (2.11)$$

1759 where  $L$  is the distance from the interaction point to the TOF (3.7 meters) and  $t_{\text{TOF}}$   
1760 is the time of flight of the particle. Using  $p = m\frac{\beta}{\sqrt{1-\beta^2}}$ ,  $\beta_{\text{TOF}}$  can be written as a  
1761 function of  $p$  for a particle of mass  $m_i$ ,

$$\beta_{\text{TOF}}(p, m_i) = \frac{p}{\sqrt{p^2 + m_i^2}}. \quad (2.12)$$

1762 Much like the TPC, plotting the TOF signal versus momentum provides a unique  
1763 curve for each particle species, as shown in Figure 2.13. Also much like the TPC, the

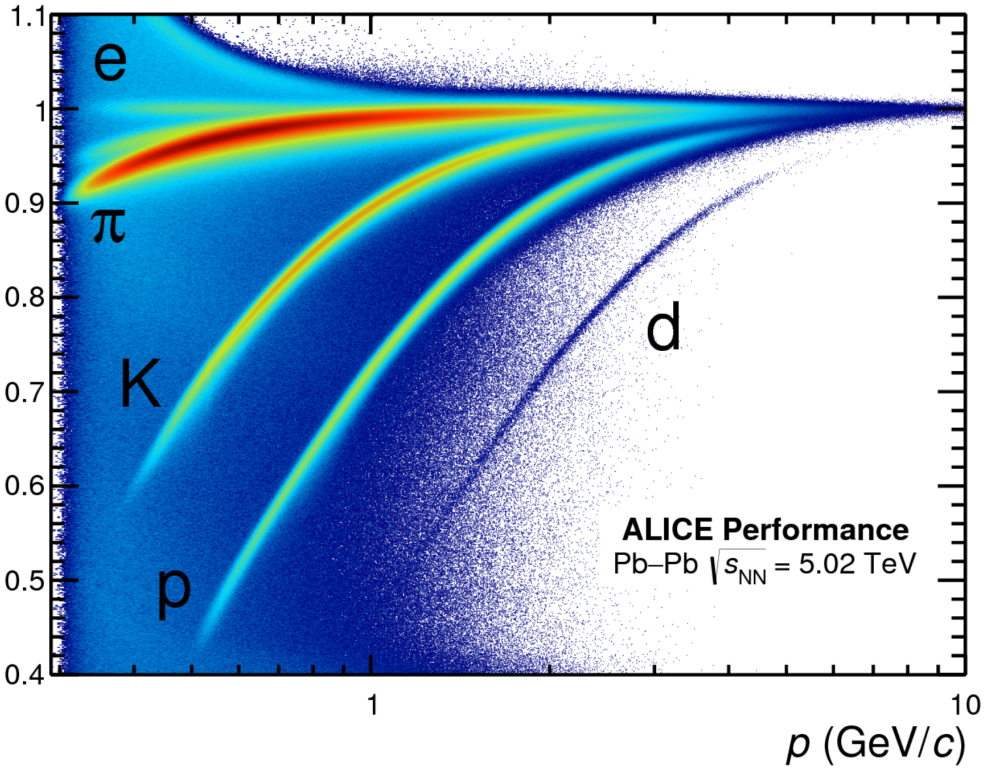


Figure 2.13: The time of flight signal  $\beta_{\text{TOF}}$  measured in 5.02 TeV Pb–Pb collisions for different particle species as a function of momentum [132]. The curves are labeled with the particle species they correspond to.

1764 signal is spread out around the expected curve due to the timing resolution of the  
 1765 TOF and momentum resolution of the TPC + ITS. As such, the quantity

$$n\sigma_{\text{TOF}} = \frac{\beta_{\text{meas}} - \beta_{\text{exp}}}{\sigma_{\text{TOF}}}, \quad (2.13)$$

1766 is defined, which serves a similar purpose to  $n\sigma_{\text{TPC}}$ .

## 1767 2.6 The Electromagnetic Calorimeter

1768 The Electromagnetic Calorimeter (EMCal) [133], [134] is a sampling calorimeter that  
 1769 consists of lead and polystyrene scintillator layers. The EMCal is made of towers,  
 1770 which are stacks of 76 lead layers (1.44 mm thick) and 77 polystyrene layers (1.76 mm  
 1771 thick). Each tower has a size of about  $6.0 \times 6.0 \times 24.6 \text{ cm}^3$  and has an individual

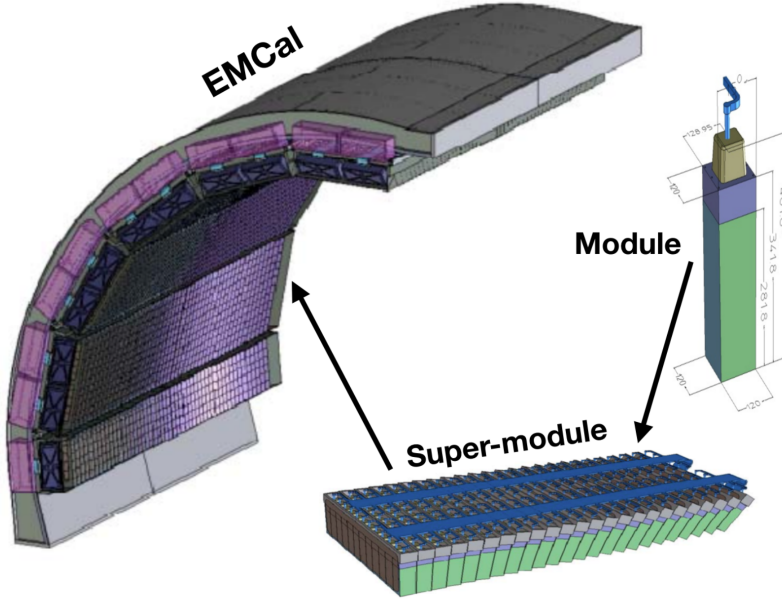


Figure 2.14: A schematic of the EMCAL [135], along with the module and supermodule structure [136].

1772 readout. The towers are arranged into  $2 \times 2$  groups called modules, which are the  
 1773 smallest units of the detector. The modules are further assembled into larger super-  
 1774 modules ( $12 \times 24$  modules), each weighing about 7.7 metric tons. The EMCAL has a  
 1775 total of 10 full-size supermodules and 2 one-third size supermodules, corresponding  
 1776 to 3072 modules and 12,288 towers. It covers a pseudorapidity range of  $|\eta| < 0.7$   
 1777 and an azimuthal angle range of  $\Delta\varphi = 107^\circ$ . It is positioned around 4.5 meters from  
 1778 the beam line, between the space-frame support structure and the L3 magnet coils.  
 1779 Schematics of the detector components can be seen in Figure 2.14. While not used  
 1780 in this thesis, the University of Texas at Austin was involved in the commissioning  
 1781 of the EMCAL, and thus it is worth mentioning for historical purposes.

## 1782 2.7 The VZERO Detector

1783 The VZERO detector [137] consists of two end-cap scintillators: the V0A, located  
 1784 in the forward pseudorapidity region ( $2.8 < \eta < 5.1$ ); and the V0C, located in the  
 1785 backward region ( $-3.7 < \eta < -1.7$ ). While most of the interesting physics lies

1786 at midrapidity, these detectors are vital for estimating the collision centrality (as  
1787 discussed in Section 1.4.1). The VZERO detectors also provide a trigger for the  
1788 other detectors: whenever a coincident signal occurs in the V0A and V0C, a collision  
1789 event must have occurred between the two detectors. The VZERO system is also used  
1790 to monitor LHC beam conditions and reject beam-gas and beam-halo events. As  
1791 the data analyzed in this thesis is from p–Pb collisions, only information from the  
1792 V0A detector—which faces the lead ion beam—is used for determining the multiplicity  
1793 percentile of the collision events.

1794

## Chapter Three: Analysis Motivation and Methodology

1795

1796 This chapter will provide the underlying motivation for the main topic of this thesis,  
 1797 along with a high-level overview of the methodology used to perform the analysis.  
 1798 First, the motivation for this analysis will be given in detail, emphasizing the impor-  
 1799 tance of the  $\Lambda$  baryon and why it was chosen for this study. Next, the main technique  
 1800 used to perform the analysis will be introduced, along with a brief overview of the  
 1801 analysis procedure. Finally, the main observables of interest will be mathematically  
 1802 defined to avoid any ambiguity in the following chapters.

1803

### 3.1 Motivation

1804 As mentioned in Section 1.5.3, the enhancement of strange quarks relative to non-  
 1805 strange ( $u$  and  $d$ ) quarks in heavy ion collisions is a key indicator of the production  
 1806 of a QGP. Experimentally, this enhancement is seen by measuring the production of  
 1807 strange hadrons ( $\Lambda$ ,  $K^0$ ,  $\phi$ ,  $\Xi$ ,  $\Omega$ ) relative to the production of pions as a function of  
 1808 event multiplicity. The results of such measurements from the ALICE is shown again  
 1809 in Figure 3.1 for reference.

1810 This figure shows a clear indication of an *onset* of strangeness enhancement, which  
 1811 transitions smoothly from low multiplicity pp to high multiplicity Pb–Pb in a way that  
 1812 is independent of collision system. While statistical models are able to well-describe  
 1813 these particle ratios in low multiplicity pp (in the form of a canonical ensemble without  
 1814 chemical equilibration [85], [86]) and high multiplicity Pb–Pb (in the form of a grand  
 1815 canonical ensemble [83], [84]), such models cannot describe the transition region.  
 1816 Phenomenological extensions to these models are able to produce a smooth transition  
 1817 between the two regimes [88], [138], but the microscopic origins of this observed  
 1818 enhancement are still unknown.

1819 This thesis aims to shed light on these origins by investigating this enhancement  
 1820 in different kinematic regimes. In particular, the production of strangeness within

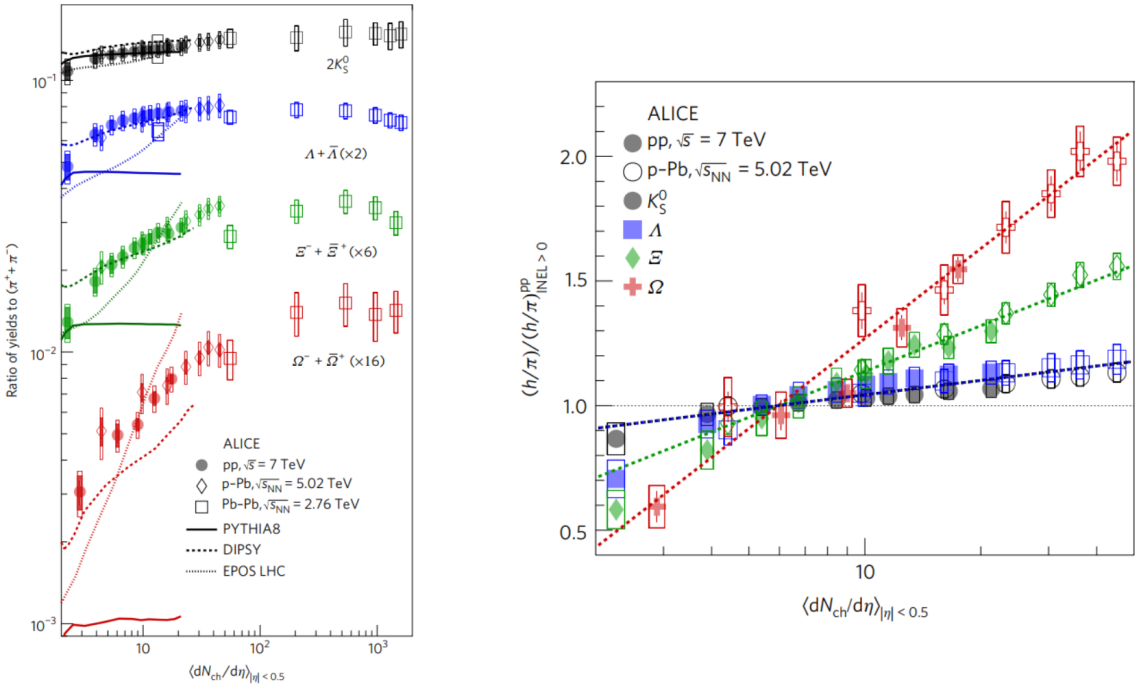


Figure 3.1: The enhancement of strange hadrons relative to pions as a function of event multiplicity in pp, p–Pb, and Pb–Pb collisions at ALICE, taken from [87].

the near-side and away-side components of dijets<sup>1</sup> will be studied and compared with the strangeness production outside of the dijet system. The production in the near-side component of the dijet corresponds to unmodified strange quark production in a jet, whereas the away-side production corresponds to strangeness production in a jet whose initial partons traversed through the QGP medium. The production outside of the dijet system is meant to represent the production of strangeness in the QGP medium itself, and serves as a baseline for “soft” quark production. Measuring the strangeness production in these regions can be used to determine their relative contributions to the overall observed enhancement, in turn illuminating some of its origins at a fundamental level.

The p–Pb collision system is ideal for this study for two major reasons. The first is that the p–Pb system captures the *entirety* of the observed onset of strangeness enhancement, as seen in Figure 3.1. Thus when trying to *study* this onset, p–Pb collisions are the most natural choice. The second reason is that pp collisions give

---

<sup>1</sup>For more details see Section 1.5.1 in the introduction.

rise to a large amount of jet-like production, with very little medium-like production. Pb–Pb collisions, on the other hand, are dominated by medium-like production with very little jet-like contributions. The p–Pb system produces a healthy blend of both jet- and medium-like production, making it the ideal candidate for analyzing the production of strangeness in these two regimes.

### 3.1.1 The $\Lambda$ baryon

When studying strange quark production in experiment, a choice of strange hadron must be made. In this thesis, the strange hadron of choice is the **lambda baryon** ( $\Lambda$ ). The  $\Lambda$  is a neutral hadron with mass  $1.116 \text{ GeV}/c^2$ , consisting of one up, one down, and one strange quark ( $uds$ ). The reasons for choosing the  $\Lambda$  baryon for this analysis are as follows.

Firstly, it is the lightest baryon containing a strange quark, and is thus the most abundantly produced strange baryon in high energy particle collisions. This makes it an ideal candidate for differential studies—like the one presented in this thesis—as correlation measurements require a *lot* of statistics. Second, the  $\Lambda$  has a very long lifetime—relative to the collision evolution—as it can only decay weakly. This has two effects:

1.  $\Lambda$  baryons produced early on in the collision survive until the end of the collision, keeping their decay products in-tact. This is not the case for strongly decaying resonance states like the  $K^*$ , which often decay within the hadronic gas phase of the collision. This can result in their decay products “rescattering” off other hadrons within the gas [139], making it impossible to reconstruct the original resonance.

2. The  $\Lambda$  often travels a significant distance before decaying, which allows for the reconstruction of its decay vertex in the detector. This substantially reduces the background contribution to the  $\Lambda$  signal, which is discussed in more detail in Section 4.3.1

Furthermore, the integrated production of  $\Lambda$  baryons relative to pions has been studied extensively in pp, p–Pb and Pb–Pb collisions at ALICE, as shown in Figure 3.1.1. Due to its strange quark content, the  $\Lambda/\pi$  ratio exhibits a large enhancement,

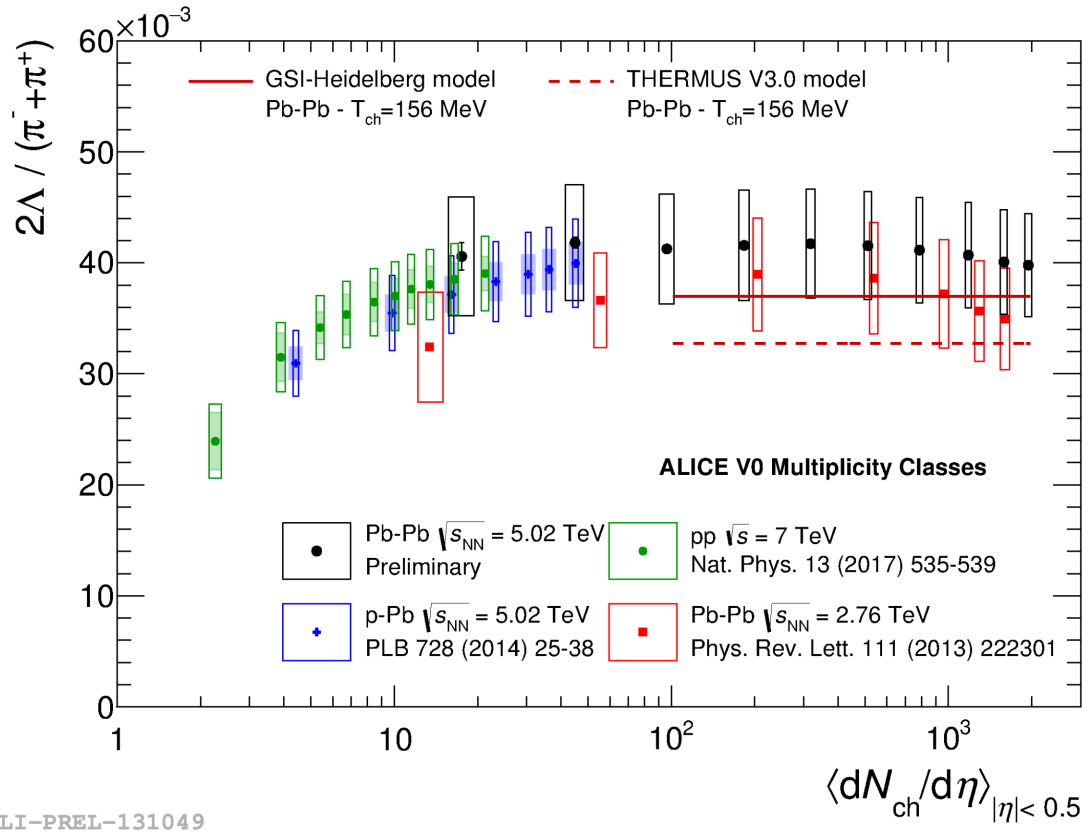


Figure 3.2: The  $p_T$ -integrated  $\Lambda/\pi$  ratio as a function of event multiplicity in pp, p–Pb, and Pb–Pb collisions at ALICE.

especially in the p–Pb region. The measurements in Figure 3.1.1 serve as a baseline for the differential studies presented in this thesis.

Finally, the  $\Lambda$  baryon, with a net strangeness of one, shares a similar mass with the  $\phi(1020)$  resonance ( $s\bar{s}$ ), which has a net strangeness of zero. Thus the differences between “open” strangeness ( $|S| > 0$ ) and “hidden” strangeness ( $|S| = 0$ ) can be studied by comparing the production of  $\Lambda$  baryons with the production of  $\phi$  resonances. Due to their similar masses, any changes in the production of these two hadrons due to differing masses would be negligible.

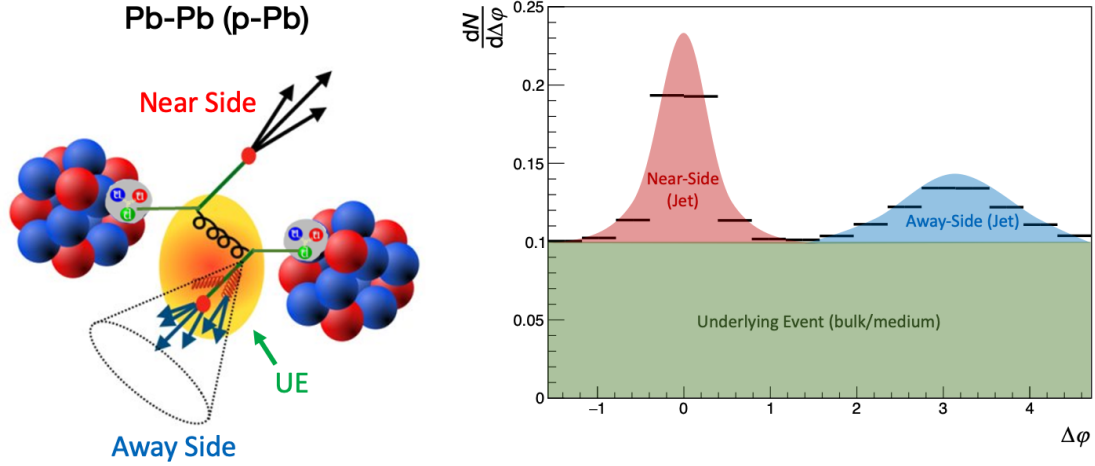


Figure 3.3: A cartoon of a Pb–Pb (p–Pb) collision that produces particles in the near- and away-side jets, along with the UE. The corresponding regions in the  $\Delta\varphi$  distribution are highlighted on the right.

## 3.2 Methodology

### 3.2.1 The main technique

To separate the production of  $\Lambda$  baryons into the jet and non-jet regions, **two-particle angular correlations** are used. By looking at the relative azimuthal angles  $\Delta\varphi = \varphi_{\text{trigger}} - \varphi_{\text{associated}}$  between a high momentum **trigger** particle and a lower momentum **associated** particle, the resulting distribution can be used to separate the production of the associated particles into distinct regions. These regions can be seen in Figure 3.3, and will be referred to as

- the **near-side region** shown in red, corresponding to near-side jet production with no medium interactions,
- the **away-side region** shown in blue, corresponding to away-side jet production with possible medium interaction, and
- the **underlying event (UE) region** shown in green, corresponding to the uncorrelated production within the medium.

1887     The clear separation between these regions in the  $\Delta\varphi$  distribution can be under-  
1888    stood from the following argument. If the trigger momentum is high enough ( $> 4$   
1889    GeV/c), it must be closely aligned with the near-side jet axis [140]. As such, the  
1890    associated particles that are produced in the near-side of the jet will have a small  
1891    relative angle to the trigger, near  $\Delta\varphi = 0$ . The associated particle production in the  
1892    away-side jet would then be  $180^\circ$  away from the trigger, near  $\Delta\varphi = \pi$ . Finally, the  
1893    uncorrelated<sup>2</sup> associated particle production within the medium would be randomly  
1894    distributed across  $\Delta\varphi$ , manifesting as a (mostly) flat background for which the near-  
1895    and away-side peaks sit on top of.

1896    **3.2.2 The end goal**

1897    In this thesis, the h- $\Lambda$   $\Delta\varphi$  distributions in p-Pb collisions at the ALICE detector  
1898    will be measured across a wide range of multiplicities. The resulting distributions  
1899    will be used to extract the associated  $\Lambda$  yields in each of the near-side, away-side  
1900    and UE regions. Moreover, the correlation distributions will be used to extract the  
1901    widths of the near- and away-side jet peaks, which aid in the study of the effects of  
1902    jet-medium interactions on the production of strange hadrons [141]. Each of these  
1903    observables will be compared with those of a h-h (dihadron) sample, which serves  
1904    as a proxy for non-strange quark (pion) production. These measurements will be  
1905    compared with theoretical model predictions from the event generators detailed in  
1906    Section 1.6. The differences between open and hidden strangeness production will also  
1907    be explored using previously published h- $\phi(1020)$  angular correlation measurements  
1908    in p-Pb collisions [142].

1909    Because the analysis procedure is dense with technical details, the remainder of  
1910    this chapter will be dedicated to providing a high-level overview of the analysis. The  
1911    specifics of the analysis procedure will be discussed in Chapter 4.

1912    **3.2.3 A brief overview of the analysis**

1913    To get to the final h- $\Lambda$  and h-h  $\Delta\varphi$  distributions of interest, a correlation function  
1914    must be specified. There are a multitude of ways to define such correlation func-

---

<sup>2</sup>Elliptic flow ( $v_2$ ) gives rise to a small correlation across  $\Delta\varphi$ , see Section 1.5.2.

1915 tions [143], but this thesis uses the per-trigger normalized associated particle yield,

$$C_{\text{yield}}(\Delta\varphi, \Delta\eta) = \frac{1}{N_{\text{trig}}} \frac{d^2 N_{\text{pair}}}{d\Delta\varphi d\Delta\eta}. \quad (3.1)$$

1916 Note that this is a 2D distribution, which has information about the angular separation  
1917 in both  $\Delta\varphi$  and  $\Delta\eta$ . Due to the finite acceptance of the detector along  $\eta$ , naïvely  
1918 integrating over  $\Delta\eta$  (in other words, just looking at the angular separation in  $\Delta\varphi$ )  
1919 would introduce a bias in the jet components, which will be discussed in Section 4.5.2.  
1920 As mentioned previously, the angular separations  $\Delta\varphi$  and  $\Delta\eta$  are measured between  
1921 a high momentum trigger hadron ( $h$ )—which serves as a proxy for the jet axis—and a  
1922 lower momentum associated hadron ( $\Lambda$  or  $h$ ).

1923 **3.2.3.1 Raw distribution corrections**

1924 Unfortunately, the correlation function given by Equation 3.1 cannot be obtained  
1925 without a series of corrections to the raw distribution for various detector effects. The  
1926 **raw distribution** is defined as the distribution obtained by counting the number of  
1927 observed trigger-associated pairs within a given event, summed up over the entire  
1928 event sample. The corrected distribution is then given by

$$C_{\text{yield}}(\Delta\varphi, \Delta\eta) = \frac{1}{N_{\text{trig}}^{\text{corr}}} \frac{1}{\epsilon_{\text{trig}} \times \epsilon_{\text{assoc}}} B(0, 0) \frac{S(\Delta\varphi, \Delta\eta)}{B(\Delta\varphi, \Delta\eta)} \frac{1}{\epsilon_{\text{pair}}(\Delta\varphi, \Delta\eta)}, \quad (3.2)$$

1929 where  $S(\Delta\varphi, \Delta\eta)$  is the aforementioned raw distribution.  $N_{\text{trig}}$  is the total number  
1930 of trigger hadrons across the event sample, corrected for trigger efficiency. Each of  
1931  $\epsilon_{\text{trig}}$ ,  $\epsilon_{\text{assoc}}$  and  $\epsilon_{\text{pair}}$  are efficiency correction factors that are discussed in more detail  
1932 within Section 4.5.1.  $B(\Delta\varphi, \Delta\eta)$  is the distribution generated by combining trigger  
1933 and associated particles that are produced in *separate* events, called the “mixed-  
1934 event” distribution. A simple diagram showing the differences between the generation  
1935 of  $S(\Delta\varphi, \Delta\eta)$  and  $B(\Delta\varphi, \Delta\eta)$  is shown in Figure 3.4. This distribution is used to  
1936 correct for the finite acceptance of the detector, and is detailed in Section 4.5.2.

1937 Examples of  $S(\Delta\varphi, \Delta\eta)$ ,  $B(\Delta\varphi, \Delta\eta)$  and  $C_{\text{yield}}(\Delta\varphi, \Delta\eta)$  for  $h-\Lambda$  pairs can be  
1938 found in Figure 3.5. The peaks observed around  $\Delta\varphi = 0$  and  $\Delta\varphi = \pi$  in the fully  
1939 corrected correlation function define the aforementioned near- and away-side regions,  
1940 respectively, which lie on top of the uncorrelated UE.

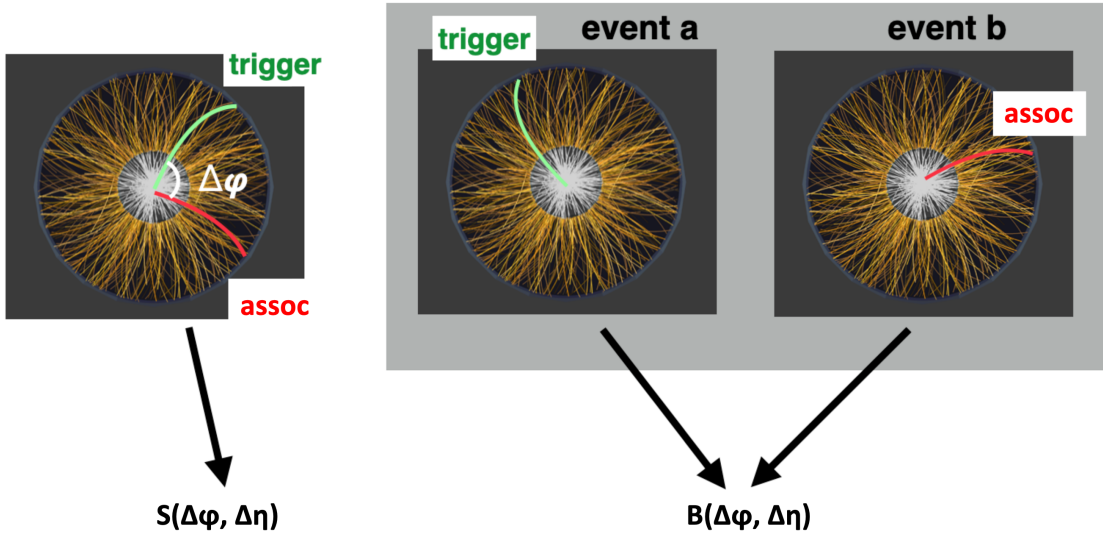


Figure 3.4: A simple diagram showing the differences between the generation of the raw distribution  $S(\Delta\varphi, \Delta\eta)$  (left) and the mixed-event distribution  $B(\Delta\varphi, \Delta\eta)$  (right). The yellow tracks are those observed by the detector. The raw distribution is obtained by looking at trigger-associated pairs within the same event, whereas the mixed-event distribution is generated from pairs that come from separate events. Note that both  $\Delta\varphi$  and  $\Delta\eta$  cannot be easily shown on a 2D plot, but the distributions are filled with both quantities.

### 1941 3.2.3.2 Underlying event fit

1942 Once all of the corrections have been applied to the raw distributions, the resulting  
 1943 correlation function  $C_{\text{yield}}(\Delta\varphi, \Delta\eta)$  can be projected onto  $\Delta\varphi$  to obtain the 1D distri-  
 1944 bution  $dN/d\Delta\varphi$ . To extract the near- and away-side widths and the per-trigger yields  
 1945 in each kinematic region from these distributions, the underlying event contribution  
 1946  $U(\Delta\varphi)$  must be quantified. While there are multiple ways to do this, the nominal  
 1947 procedure is simply to fix  $U(\Delta\varphi)$  to the average of the  $\Delta\varphi$  distribution in the regions  
 1948 where there is little-to-no jet contribution. Explicitly, these regions are

1949     •  $(-\frac{\pi}{2}, -\frac{\pi}{4})$ ,

1950     •  $(\frac{\pi}{4}, \frac{5\pi}{8})$ , and

1951     •  $(\frac{11\pi}{8}, \frac{3\pi}{2})$ .

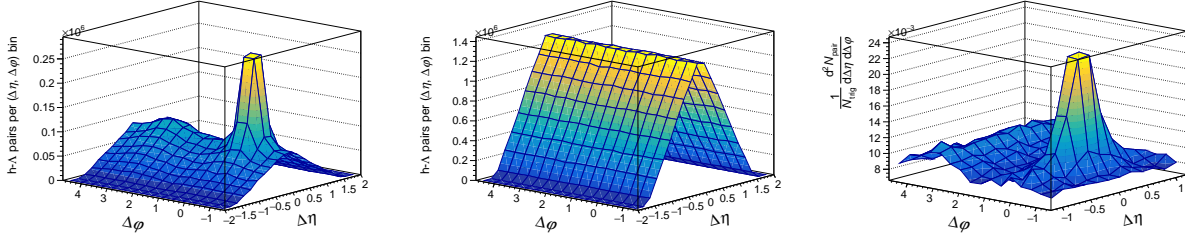


Figure 3.5: Examples of the h- $\Lambda$  same-event distribution  $S(\Delta\varphi, \Delta\eta)$  (left), mixed-event distribution  $B(\Delta\varphi, \Delta\eta)$  (middle), and fully corrected correlation function  $C_{\text{yield}}(\Delta\varphi, \Delta\eta)$  (right).

1952 The effects of varying these regions, along with other assumptions of the form of  
 1953  $U(\Delta\varphi)$ , are explored within Chapter 4.5.3.4.

### 1954 3.2.3.3 Yield and width extraction

1955 After obtaining the underlying event fit  $U(\Delta\varphi)$ , the associated particle yields in the  
 1956 jet-like and UE regions are extracted using

$$Y_{\text{near}} = \int_{-\pi/2}^{\pi/2} \left( \frac{dN}{d\Delta\varphi} - U(\Delta\varphi) \right) d\Delta\varphi, \quad Y_{\text{away}} = \int_{\pi/2}^{3\pi/2} \left( \frac{dN}{d\Delta\varphi} - U(\Delta\varphi) \right) d\Delta\varphi \quad (3.3)$$

$$Y_{\text{UE}} = \int_{-\pi/2}^{3\pi/2} U(\Delta\varphi) d\Delta\varphi, \quad (3.4)$$

1957 where the subscripts near, away and UE refer to the near-side, away-side, and under-  
 1958 lying event regions, respectively.

1959 In order to quantify the widths of the near- and away-side peak regions, the  $\Delta\varphi$   
 1960 distributions are fit using the function

$$F(\Delta\varphi) = U(\Delta\varphi) + \frac{e^{\kappa_{\text{near}} \cos(\Delta\varphi - \mu_{\text{near}})}}{2\pi I_0(\kappa_{\text{near}})} + \frac{e^{\kappa_{\text{away}} \cos(\Delta\varphi - \mu_{\text{away}})}}{2\pi I_0(\kappa_{\text{away}})}, \quad (3.5)$$

1961 which is composed of two von Mises functions describing the near- and away-side  
 1962 peaks. Von Mises functions [141], [144] are the circular analogs of Gaussian distri-  
 1963 butions and provide the best fit to the  $2\pi$ -periodic  $\Delta\varphi$  distributions. The  $\kappa_{\text{near}}$  and  
 1964  $\kappa_{\text{away}}$  terms are the measure of the collimation of the near- and away-side peaks, re-  
 1965 spectively, and  $I_0$  is the zeroth-order modified Bessel function. The underlying event  
 1966 fit  $U(\Delta\varphi)$  is fixed to the function obtained from the previous section during fitting.

1967 Due to symmetry considerations, the means  $\mu_{\text{near}}$  and  $\mu_{\text{away}}$  are also fixed to 0 and  $\pi$ ,  
1968 respectively. The width of the peaks is then quantified via [144]

$$\sigma_{\text{near,away}} = \sqrt{-2 \log \frac{I_1(\kappa_{\text{near,away}})}{I_0(\kappa_{\text{near,away}})}}, \quad (3.6)$$

1969 where  $I_1$  is the first-order modified Bessel function and  $\log(x)$  is the natural loga-  
1970 rithm of  $x$ . As before, the effects of different choices for  $F(\Delta\varphi)$  will be detailed in  
1971 Chapter 4.5.3.4.

## Chapter Four: Analysis Details

1973 This chapter builds upon the analysis overview presented in the previous chapter by  
 1974 providing a much more detailed description of each component of the analysis. These  
 1975 components can be summarized as follows. First, a high-quality data sample of p–Pb  
 1976 collisions is selected, with events further differentiated by their multiplicity. Then,  
 1977 quality tracks are selected for the trigger and associated charged hadrons, and the  $\Lambda$   
 1978 baryons are reconstructed from lower quality tracks using their characteristic decay  
 1979 topology. These  $\Lambda$  daughter tracks are identified as protons or pions using information  
 1980 from the TPC and TOF detectors. Within a given event, the trigger hadrons are then  
 1981 combined with either the associated charged hadrons or the  $\Lambda$  candidates to form  
 1982 pairs, where a distribution of their relative azimuthal angle ( $\Delta\varphi \equiv \varphi_{trig.} - \varphi_{assoc.}$ )  
 1983 and pseudorapidity ( $\Delta\eta \equiv \eta_{trig.} - \eta_{assoc.}$ ) is filled for each pair. These h– $\Lambda$  and h–  
 1984 h angular distributions are then corrected for a laundry list of detector effects using  
 1985 both data- and MonteCaro-driven methods. Further corrections are applied to the h– $\Lambda$   
 1986 distributions to account for effects like the combinatorial background associated with  
 1987 the  $\Lambda$  reconstruction and the two-track merging effect, whereby one of the daughter  
 1988 tracks gets merged with the trigger hadron track, causing a h– $\Lambda$  pair deficit at small  
 1989 angles. Once all corrections are applied, the h– $\Lambda$  and h–h distributions are finalized  
 1990 and ready for the extracting of the many observables discussed at the end of the  
 1991 previous chapter.

1992 **4.1 Dataset and event selection**

1993 **4.1.1 Dataset**

1994 Every event in this analysis was a p–Pb collision at  $\sqrt{s_{NN}} = 5.02$  TeV with data  
 1995 collected by the ALICE detector during the 2016 LHC run. This analysis uses the  
 1996 data from these runs with the “FAST” reconstruction, meaning the data was taken  
 1997 without the ITS’s SDD subdetector due to issues with readout during this period.  
 1998 The total number of events (prior to any selection) is roughly 400 million. For the  
 1999 efficiency studies, the analysis was performed using a standard purpose MC-generated

2000 production anchored to the dataset using the DPMJET [101] event generator. This  
2001 production consists of around 400 million minimum bias events, which is roughly  
2002 equivalent to data.

2003 **4.1.2 Event Selection**

2004 Events are selected by requiring the location of the primary collision interaction point  
2005 (called the “primary vertex” or PV) to be no more than 10 cm from the center of the  
2006 detector along the beam axis or “z”-direction. Furthermore, every event is required  
2007 to have at least three reconstructed tracks that contributed to the reconstruction of  
2008 the PV. This reduces the total number of events considered to approximately 350  
2009 million events, and a summary of the effects of these selection criteria can be seen in  
2010 Table 4.1. The events are further separated into three charged particle multiplicity  
2011 classes (0-20%, 20-50% and 50-80%) based off event activity in the forward-rapidity  
2012 V0A detector.

Table 4.1: Number of events passing our criteria for each multiplicity bin considered.  
Here  $Z_{vtx}$  refers to the position of the PV along the beam (z) axis.

Multiplicity	Total evts.	Has 3 tracks	$ Z_{vtx}  < 10\text{cm} + 3 \text{ tracks}$	% Pass
0-20%	1.0E08	1.0E08	0.8E08	87%
20-50%	1.6E08	1.6E08	1.3E08	86%
50-80%	1.6E08	1.6E08	1.3E08	86%

2013 **4.2 Charged hadron track selection**

2014 **4.2.1 Trigger track cuts**

2015 For any two-particle correlation analysis, the selection criteria of the trigger hadron  
2016 is of utmost importance as any geometric biases introduced by the trigger selection  
2017 could be reflected in the final correlation distributions. However, correlation anal-  
2018 yses generally require large statistics, thus the selection criteria shown in Table 4.2  
2019 are applied to ensure the quality of the trigger hadron track while maximizing the  
2020 statistics of the analysis. Furthermore, the trigger hadron tracks are required to be

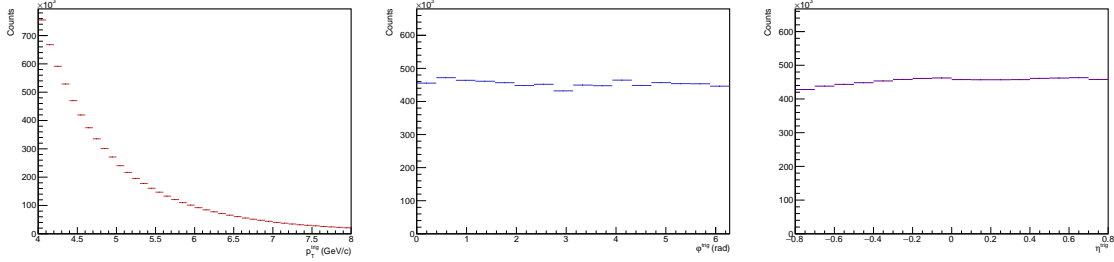


Figure 4.1: The  $p_T$  (left),  $\varphi$  (middle), and  $\eta$  (right) distributions for the trigger hadrons in the multiplicity range 0-20%.

at midrapidity ( $|\eta| < 0.8$ ) and have high<sup>1</sup> momentum with  $4.0 < p_T^{\text{trig.}} < 8.0 \text{ GeV}/c$ , as the trigger is meant to serve as a proxy for a jet axis. Plots of the  $p_T$ ,  $\varphi$ , and  $\eta$  distributions for the trigger hadrons that pass these cuts in the 0-20% multiplicity bin can be seen in Figure 4.1.

Table 4.2: The track quality cuts applied to the trigger hadrons in this analysis.

Selection criterion	Value
TPC clusters	$\geq 50$
$\chi^2$ per TPC cluster	< 4
Fraction of shared TPC clusters	< 0.4
DCA <sub>xy</sub>	< 2.4 cm
DCA <sub>z</sub>	< 3.2 cm
Accept kink daughters	No

## 4.2.2 Associated hadron track cuts

To keep the results of this analysis more comparable to previous measurements of the  $\Lambda/\pi \approx \Lambda/h$  ratio, the selection criteria for the associated hadrons are more strict than those for the trigger hadrons as the associated hadrons are meant to be “primary”, meaning they did not originate from a weak decay. All associated hadrons are required to meet the ALICE standard track quality cuts for primary charged hadrons described in Table 4.3. Furthermore, the associated hadrons are selected only at midrapidity ( $|\eta| < 0.8$ ) in the momentum region  $1.0 < p_T < 4.0 \text{ GeV}/c$ .

<sup>1</sup>“High” in this case means high enough to guarantee the hadron is produced close (in  $\Delta\varphi\Delta\eta$ -space) to a jet axis.

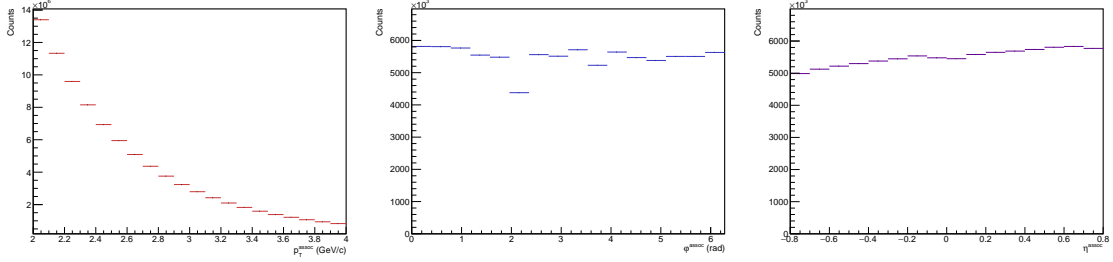


Figure 4.2: The  $p_T$  (left),  $\varphi$  (middle), and  $\eta$  (right) distributions for the associated hadrons in the multiplicity range 0-20%. The dips observed in the  $\varphi$  distribution are due to the TPC sector boundaries.

2033 The  $p_T$ ,  $\varphi$  and  $\eta$  distributions for the associated hadrons that pass these cuts in the  
 2034 0-20% multiplicity bin can be seen in Figure 4.2.

Table 4.3: The ALICE standard track quality cuts for primary charged hadrons, used for the selection of the associated hadrons in this analysis.

Selection criterion	Value
Crossed rows in TPC	$\geq 80$
Crossed rows/findable clusters in TPC	$> 0.8$
TPC clusters	$\geq 80$
ITS clusters	$\geq 3$
$\chi^2$ per TPC cluster	$< 4$
$\chi^2$ per ITS cluster	$< 36$
TPC and ITS refit required	Yes
DCA <sub>xy</sub>	$< 0.0105 + 0.0350/p_T^{1.1}$ cm
DCA <sub>z</sub>	$< 2$ cm

### 2035 4.3 $\Lambda$ reconstruction

#### 2036 4.3.1 Characteristic V<sup>0</sup> decay topology

2037 The  $\Lambda$  candidates in this analysis are reconstructed using their characteristic “V”-  
 2038 shaped decay topology, which is seen in the detector as two oppositely charged tracks  
 2039 originating from a common vertex which is sufficiently displaced from the PV (called  
 2040 the “secondary vertex” or SV). Such particles capable of being reconstructed via this  
 2041 topology are called “V<sup>0</sup>’s: the V describing the decay shape and the 0 indicating that

2042 the particle is neutral. A diagram depicting a typical  $V^0$  decay is shown in Figure 4.3,  
2043 with labels given for the most relevant kinematic variables.

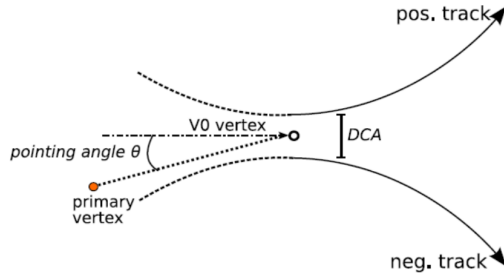


Figure 4.3: A diagram depicting a typical  $V^0$  decay with labels for the most important kinematic variables. The diagram was taken from [145].

2044 The first and most important of these variables is the distance of closest approach  
2045 (DCA) between the two tracks. This DCA needs to be small enough (relative to  
2046 the tracking resolution) to ensure that the tracks originated from a common vertex.  
2047 Another important variable is the transverse decay length of the  $V^0$ , which is the  
2048 distance between the PV and the SV measured in the  $xy$ -plane. The importance of  
2049 this variable is twofold: if the decay length is too small, then it may not even be  
2050 possible to resolve the SV from the PV, plus it allows for the distinction between  $V^0$ s  
2051 of differing decay lengths. The final relevant variable is the cosine of the pointing  
2052 angle, which is the angle between the momentum vector of the  $V^0$  and the vector  
2053 pointing from the PV to the SV. As  $V^0$  candidates are generally required to be  
2054 sufficiently collimated to ensure that the  $V^0$  originated from the PV, the cosine of  
2055 the pointing angle is usually close to unity.

2056 Using these variables, a list of likely  $V^0$  candidates is generated for each event,  
2057 from which further cuts are applied to maximize the likelihood of the candidate  
2058 being a true  $\Lambda$  baryon. These cuts are summarized in the following section. There is  
2059 also another technique for  $\Lambda$  reconstruction whereby all oppositely charged proton-  
2060 pion pairs are combined to form  $\Lambda$  candidates, which is explored in more detail in  
2061 Chapter 4.5.3.4. However, due to the large combinatorial background associated with  
2062 this technique, the  $V^0$  method described above is nominal for this analysis.

2063 **4.3.2  $\Lambda$  daughter proton and pion track cuts**

2064 Because of the longer decay length of the  $\Lambda$  ( $c\tau \approx 10$  cm), the corresponding daughter  
 2065 proton and pion tracks generally have fewer hits in both the ITS and TPC, resulting  
 2066 in “lower quality” track parameters. Because of this, the cuts applied to the daughter  
 2067 tracks used to reconstruct  $\Lambda$  candidates are the least strict of all the track quality  
 2068 cuts in this analysis and are summarized in Table 4.4. The daughter proton and pion  
 2069 are also required to be at midrapidity ( $|\eta| < 0.8$ ) and have a minimum  $p_T$  of  $p_T >$   
 2070  $0.15$  GeV/ $c$ .

Table 4.4: The track quality cuts applied to both the daughter proton and pion tracks used to reconstruct  $\Lambda$  candidates. These cuts are intentionally less strict than those applied to the trigger and associated hadrons as the daughter tracks are reconstructed from secondary particles.

Selection criterion	Value
TPC refit required	Yes
Crossed rows in TPC	$\geq 70$
Crossed rows/findable clusters in TPC	$> 0.8$

2071 Following the particle identification procedure outlined in Sections 2.4 and 2.5,  
 2072 the daughter proton and pion tracks are required to pass the following PID cuts using  
 2073 both the TPC and TOF detectors:

- 2074 •  $|n\sigma_{\text{TPC},p}| < 2$
- 2075 •  $|n\sigma_{\text{TPC},\pi}| < 3$
- 2076 •  $|n\sigma_{\text{TOF},p}| < 2$  (if signal exists)
- 2077 •  $|n\sigma_{\text{TOF},\pi}| < 3$  (if signal exists)

2078 The values of these cuts were chosen to maximize the  $\Lambda$  signal while avoiding  
 2079 contamination from other particle species. The parenthetical “if signal exists” means  
 2080 that the TOF PID cut is only applied if the track has a TOF signal. Due to the  
 2081 large distance between the TOF detector and the PV, many lower momentum tracks  
 2082 are deflected by the magnetic field before reaching the TOF detector, resulting in no  
 2083 signal. Excluding such tracks results in a more pure sample of protons and pions,  
 2084 at the cost of a much lower number of  $\Lambda$  candidates. While such a cost is not

acceptable for the nominal analysis, the effect of excluding these tracks is investigated in Chapter 4.5.3.4. The  $n\sigma$  distributions for both the TPC and TOF detectors of the daughter proton and pion tracks that pass the aforementioned quality cuts are shown in Figure 4.4 and Figure 4.5, respectively. To check for contamination from other particle species, the TOF and TPC information is combined to form a  $n\sigma_{\text{TOF}}$  vs  $n\sigma_{\text{TPC}}$  plot, which is shown for both the protons and pions in Figure 4.6. No contamination is observed for either the proton or pion tracks.

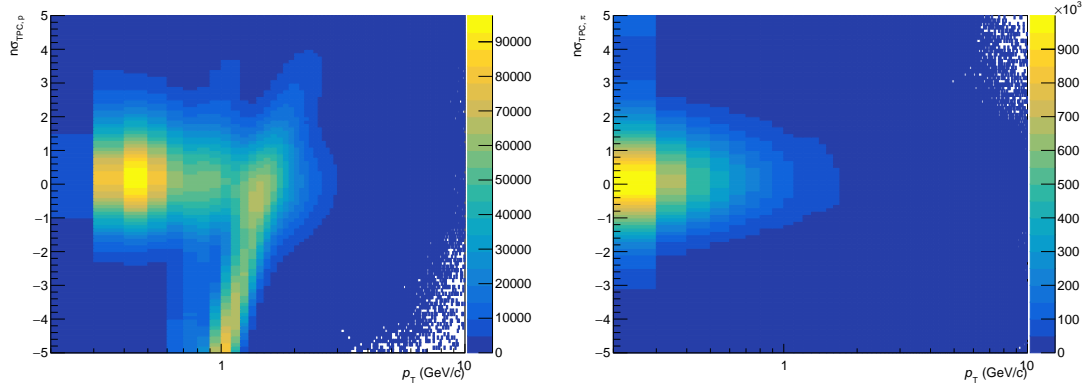


Figure 4.4:  $n\sigma$  for protons (left) and pions (right) in the TPC detector as a function of  $p_T$ .

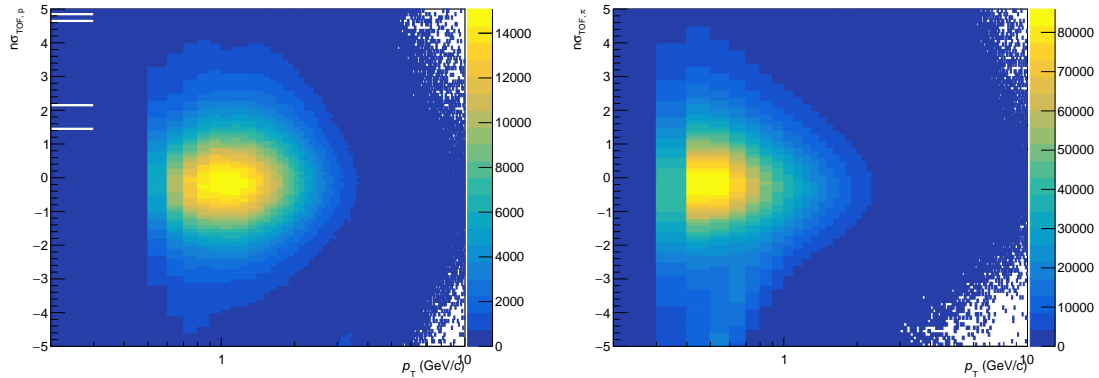


Figure 4.5:  $n\sigma$  for protons (left) and pions (right) in the TOF detector as a function of  $p_T$ .

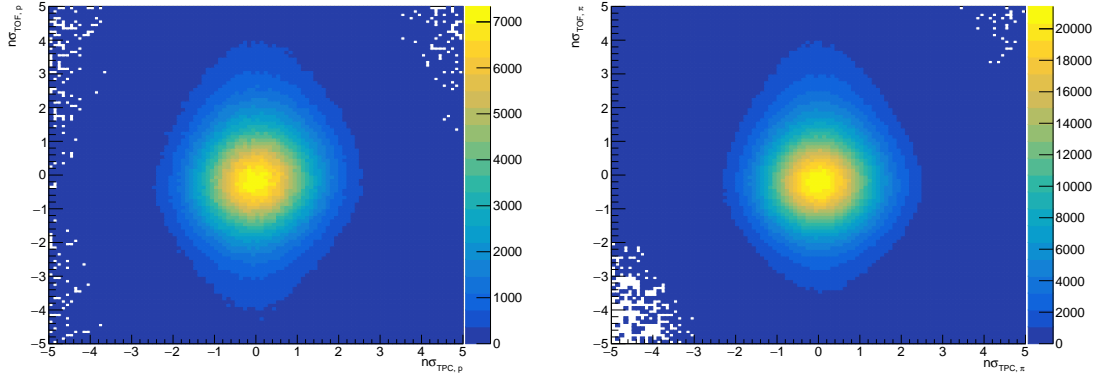


Figure 4.6:  $n\sigma$  in TOF vs  $n\sigma$  in TPC for protons (left) and pions (right). No contamination is observed for both of the particle species.

### 2092 4.3.3 $\Lambda$ candidate selection

2093 With the daughter proton and pion tracks selected, the  $\Lambda$  candidates are generated  
 2094 by combining all oppositely charged proton-pion pairs into  $V^0$ s which meet the topo-  
 2095 logical selection criteria described in Table 4.5.

Table 4.5: Topological selection criteria applied to  $\Lambda$  candidates.

Selection criterion	Value
$ \eta $	$< 0.8$
Decay radius (cm)	$> 0.2$
$DCA_{xy}$ of pion track to PV (cm)	$> 0.06$
$DCA_{xy}$ of proton track to PV (cm)	$> 0.06$
$DCA_{xy}$ between daughter tracks ( $n\sigma$ )	$< 1.5$
$\cos(\theta_{\text{pointing}})$	$> 0.9$
Invariant mass ( $\text{GeV}/c^2$ )	$1.102 < M_{p\pi} < 1.130$

2096 The invariant mass  $M_{p\pi}$  is calculated using

$$M_{p\pi} = \sqrt{(E_p + E_\pi)^2 - (\vec{p}_p + \vec{p}_\pi)^2}, \quad (4.1)$$

2097 where  $E_x = \sqrt{m_x^2 + p_x^2}$  is the energy of the particle of species  $x$ . The  $M_{p\pi}$  distributions  
 2098 for the  $\Lambda$  candidates for all multiplicity and momentum bins are shown in Figure 4.7.  
 2099 The distributions are also fit with a Voigtian function (convolution of Breit-Wigner  
 2100 and Gaussian [146]) plus a straight line to describe the background. Note that despite

2101 the selection criteria, there is still a non-negligible background due to the presence  
2102 of misidentified  $\Lambda$  candidates. As this background inevitably makes its way into the  
2103 final  $h\text{-}\Lambda$  correlation distributions, it is removed using the technique described in  
2104 Section 4.5.3.1.

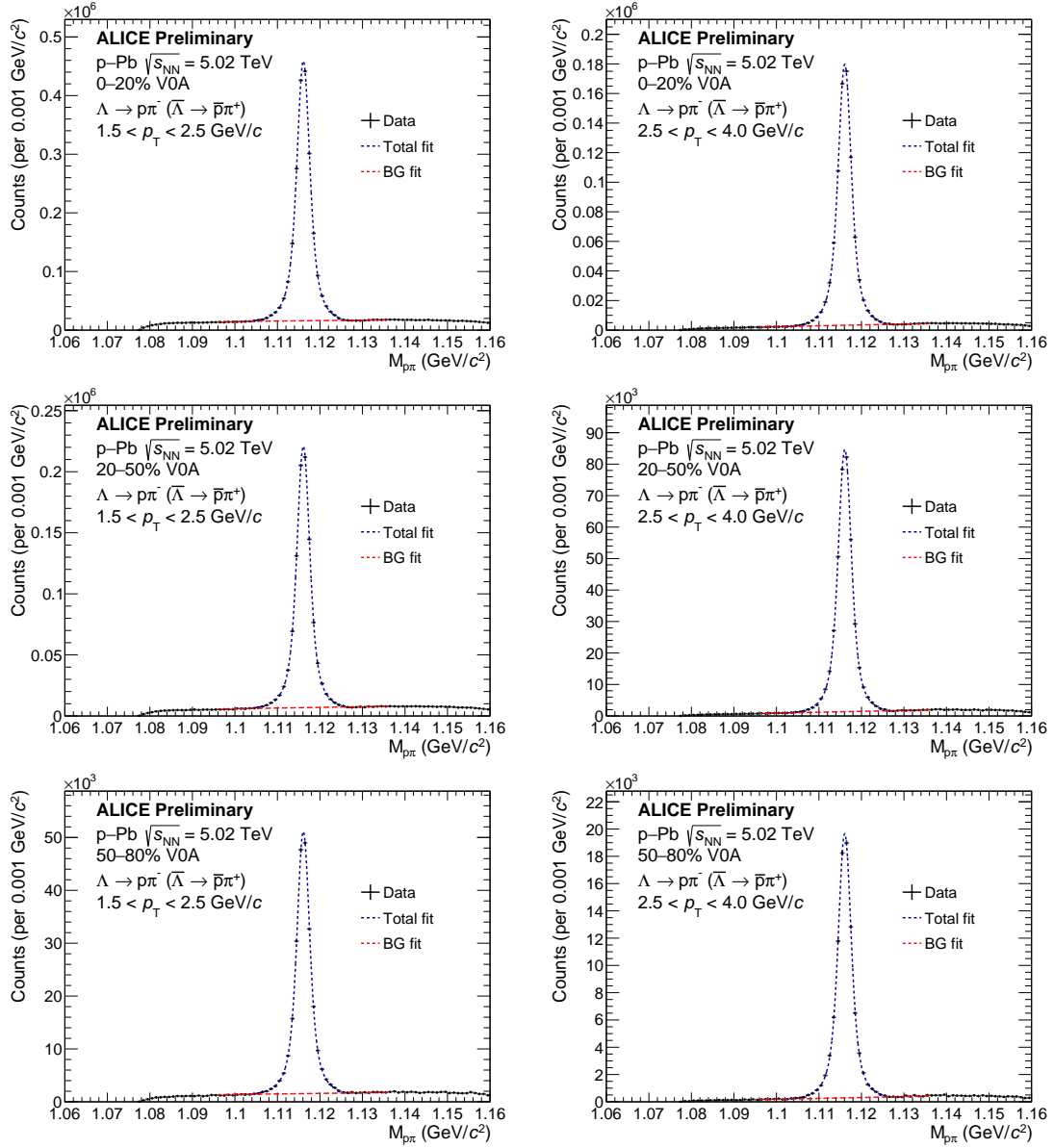


Figure 4.7: Invariant mass distributions in the 0-20% (top), 20-50% (middle), and 50-80% (bottom) multiplicity bins for the  $\Lambda$  candidates which pass the selection criteria with  $1.5 < p_T < 2.5 \text{ GeV}/c$  (left) and  $2.5 < p_T < 4.0 \text{ GeV}/c$  (right). A Voigtian signal + straight-line background fit to the data is shown in blue, with just the background fit shown in red. For these plots, the  $\Lambda$ s were only reconstructed in events with a trigger hadron.

2105 **4.4 Reconstruction efficiency**

2106 In an ideal world, the number of reconstructed particles of interest would be equal  
2107 to the number of particles produced in the collision. Unfortunately this is not the  
2108 case, as there are a number of detector effects which can cause particles to be “lost”  
2109 during reconstruction. To correct for these effects, the reconstruction efficiency

$$\epsilon(x_1, x_2, \dots, x_n) \equiv P(f(x_1, x_2, \dots, x_n) | g(x_1, x_2, \dots, x_n)), \quad (4.2)$$

2110 is used. Here  $x_i$  are the kinematic variables of the particle of interest (e.g.  $p_T$ ,  
2111  $\eta$ ,  $\varphi$ ),  $f(x_1, x_2, \dots, x_n)$  is the probability that a particle is reconstructed (“found”)  
2112 with kinematic variables  $x_i$ , and  $g(x_1, x_2, \dots, x_n)$  is the probability that a particle is  
2113 produced (“generated”) with the same variables. While the distributions  $f$  and  $g$  are  
2114 inaccessible within a given event, the efficiency can be calculated using Monte Carlo  
2115 simulation techniques via the equation

$$\epsilon(x_1, x_2, \dots, x_n) = \frac{N_{\text{reco.}}(x_1, x_2, \dots, x_n)}{N_{\text{gen.}}(x_1, x_2, \dots, x_n)}, \quad (4.3)$$

2116 where  $N_{\text{reco.}}$  and  $N_{\text{gen.}}$  are the reconstructed and generated particle distributions,  
2117 respectively, usually taken across a large number of simulated events. In this analy-  
2118 sis, these distributions are calculated as a function of  $p_T$  and  $\eta$  for each multiplicity  
2119 class using 30 million events generated by the Monte Carlo event generator DPM-  
2120 JET [101] with particle propagation through the ALICE detector performed by the  
2121 GEANT3 [147] detector simulation software. These efficiency distributions are then  
2122 used to correct the h- $\Lambda$  and h-h correlation distributions using the procedure described  
2123 in Section 4.5.

2124 **4.4.1 Charged hadron reconstruction efficiency**

2125 The trigger and associated hadron track reconstruction efficiencies are calculated  
2126 using Equation 4.3, where the trigger and associated hadrons from  $N_{\text{reco.}}$  are subject  
2127 to the following:

- 2128 • The track passes the quality cuts outlined in Tables 4.2 (trigger) or 4.3 (asso-  
2129 ciated)
- 2130 • The track has a corresponding generated particle

2131     • That generated particle is either a pion, proton, kaon, electron, or muon  
 2132     •  $|\eta_{\text{track}}| \leq 0.8$ ,  
 2133 and the trigger and associated hadrons from  $N_{\text{gen}}$ . are subject to:  
 2134     •  $|\eta_{\text{track}}| \leq 0.8$   
 2135     • The particle is either a pion, proton, kaon, electron, or muon  
 2136     • The particle is primary (i.e. did not originate from a weak decay)  
 2137 The trigger and associated track reconstruction efficiencies are shown for each multi-  
 2138 plicity class as a function of  $p_T$  in Figure 4.8. While these efficiencies exhibit relatively  
 2139 flat behavior as a function of  $p_T$  and multiplicity, they are still treated as  $p_T$  and mul-  
 2140 tiplicity dependent during the correction procedure.

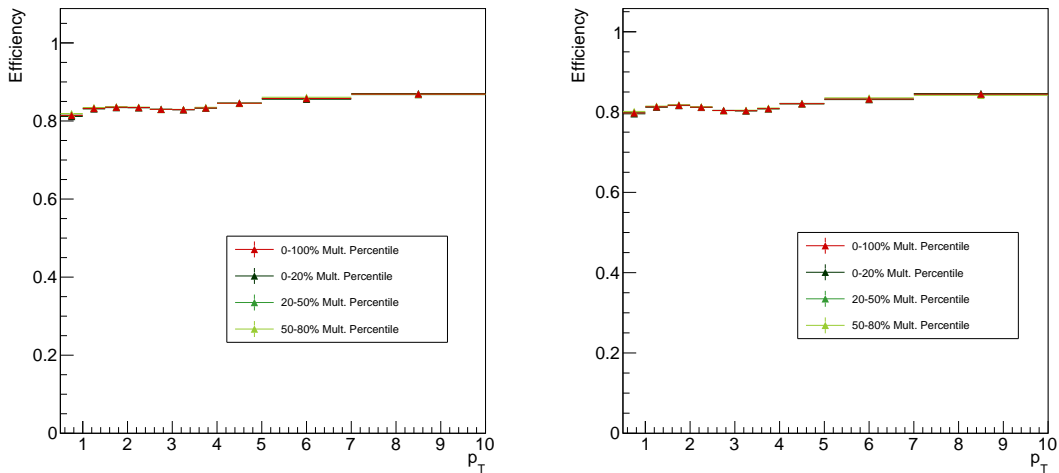


Figure 4.8: Efficiency vs.  $p_T$  for trigger (left) and associated (right) hadrons. While they may look identical, the associated hadron efficiency is slightly lower due to the stricter selection criteria.

#### 2141 4.4.2 $\Lambda$ reconstruction efficiency

2142 The  $\Lambda$  reconstruction efficiency is calculated as a function of  $p_T$  and  $\eta$  using Equa-  
 2143 tion 4.3, where the  $\Lambda$ s from  $N_{\text{reco}}$ . are subject to the following:

- They pass the topological selection criteria from Table 4.5
- The reconstructed daughter  $p, \pi$  tracks pass the quality cuts from Table 4.4
- The daughter  $p, \pi$  tracks have corresponding generated  $p, \pi$  particles
- Those generated  $p, \pi$  daughters come from the same mother  $\Lambda$
- $|\eta_\Lambda| \leq 0.8$ ,

and the  $\Lambda$ s from  $N_{\text{gen.}}$  are subject to:

- $|\eta_\Lambda| \leq 0.8$
- The  $\Lambda$  decays to  $p\pi$ .

The requirement that the generated  $\Lambda$ s decay into  $p\pi$  means the branching ratio is not included in the efficiency calculation as it is corrected for separately (see Section 4.5). The  $\Lambda$  reconstruction efficiency can be seen for each multiplicity class as a function of  $p_T$  and  $\eta$  in Figure 4.9. Note that the efficiency is no longer flat as a function of  $\eta$  due to the  $|\eta| < 0.8$  requirement for the daughter tracks, which kinematically restricts the  $\Lambda$  reconstruction to a smaller  $\eta$  range.

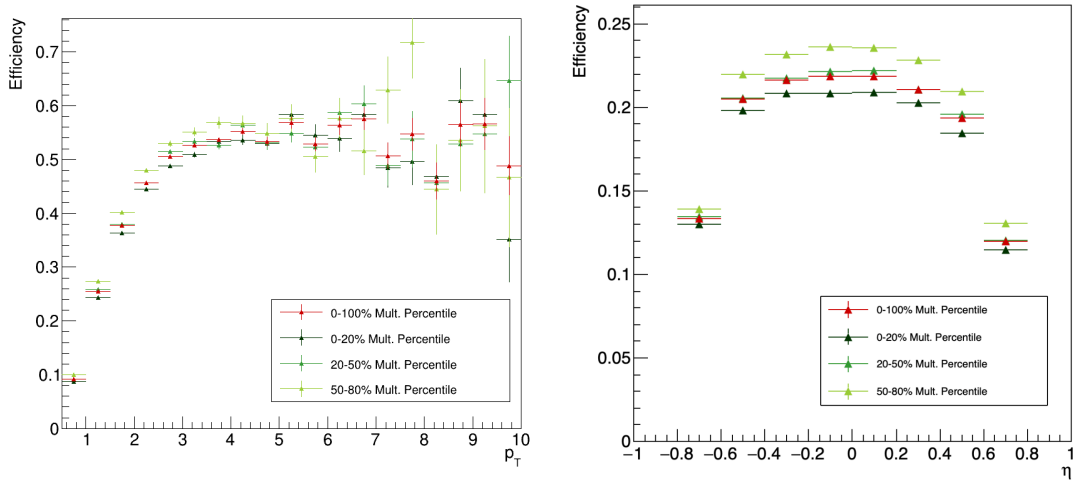


Figure 4.9: Efficiency vs.  $p_T$  (left) and  $\eta$  (right) for  $\Lambda$  reconstruction in each multiplicity bin, along with an integrated 0-100% point in red.

## 2158 4.5 Corrections to the correlation distributions

2159 Once the trigger and associated particles are selected, the two-particle h- $\Lambda$  and h-h  
2160 correlation distributions are generated. As mentioned in the previous chapter, the  
2161 corrected two-particle correlation function is given by

$$\frac{1}{N_{trig}} \frac{d^2 N_{pair}}{d\Delta\varphi d\Delta\eta} = \frac{1}{N_{trig}^{corr}} \frac{1}{\epsilon_{trig} \times \epsilon_{assoc}} B(0, 0) \frac{S(\Delta\varphi, \Delta\eta)}{B(\Delta\varphi, \Delta\eta)}. \quad (4.4)$$

2162 which contains a number of explicit correction terms (in the form of  $\epsilon$ s) along with  
2163 some implicit corrections. These corrections are described in this section, and are  
2164 presented in the order in which they are applied to the data.

### 2165 4.5.1 Single-particle efficiency corrections

2166 As both the trigger and the associated particles have their own independent recon-  
2167 struction efficiencies, the trigger-associated pair reconstruction efficiency should be

$$\epsilon_{trig,assoc} = \epsilon_{trig} \times \epsilon_{assoc}, \quad (4.5)$$

2168 meaning the single-particle efficiency distributions from Section 4.4 can be used to  
2169 calculate the weight  $1/(\epsilon_{trig} \times \epsilon_{assoc})$ . This weight is applied for each h- $\Lambda$  and h-h  
2170 pair in the two-dimensional correlation distribution. However, the assumption that  
2171 the reconstruction efficiencies are independent is slightly incorrect in the case of the  
2172 h- $\Lambda$  distributions due to track merging effects, thus an additional  $\epsilon_{pair}$  correction is  
2173 required (discussed in detail in Section 4.5.3).

2174 The trigger efficiency weight  $1/\epsilon_{trig}$  is also applied to the single-particle trigger  
2175 hadron distribution in data to obtain  $N_{trig}^{corr}$ .

### 2176 4.5.2 Mixed-event acceptance correction

2177 As mentioned in Section 3.2.3.1, the  $B(0, 0)/B(\Delta\varphi, \Delta\eta)$  term in Equation 3.2 cor-  
2178 rects for the finite acceptance along  $\eta$  as both our trigger and associated particles  
2179 are required to be within  $|\eta| < 0.8$ . The mixed-event distribution  $B(\Delta\varphi, \Delta\eta)$  shown  
2180 in Figure 3.5 has a characteristic triangular shape along  $\Delta\eta$ , which is purely due to  
2181 detector geometry as no physical correlations are present. When scaled by  $1/B(0, 0)$ ,  
2182 the mixed event distribution becomes the probability that a particle pair is found

given that the trigger particle is within  $|\eta| < 0.8$ , which is unity at  $\Delta\varphi, \Delta\eta = 0, 0$ . Thus correcting the same-event distribution  $S(\Delta\varphi, \Delta\eta)$  by  $B(0, 0)/B(\Delta\varphi, \Delta\eta)$  removes this acceptance effect and allows for a more accurate determination of the pair-wise yields.

While the generation of the mixed event distribution  $B(\Delta\varphi, \Delta\eta)$  was discussed briefly in Section 3.2.3.1, the specific details are as follows. First, in order to ensure that the mixed-event pairs are coming from similar events, the events in the mixing pool are separated by both multiplicity percentile and  $Z_{\text{vtx}}$  position. The categorizing of events based off of  $Z_{\text{vtx}}$  position is an integral part of the acceptance correction: events with a  $Z_{\text{vtx}}$  at one edge of the detector have a completely different (and nearly inverted)  $\eta$  acceptance than those on the opposite edge. The multiplicity bins are the same as they are for the same-event distributions (namely 0-20%, 20-50% and 50-80%), and the ten  $Z_{\text{vtx}}$  bins are split evenly from -10 cm to 10 cm. For each multiplicity and  $Z_{\text{vtx}}$  bin, the acceptance correction

$$S_{\text{corr.}}(\Delta\varphi, \Delta\eta) = \frac{S(\Delta\varphi, \Delta\eta)}{B(\Delta\varphi, \Delta\eta)/B(0, 0)} \quad (4.6)$$

is performed, and the results for each multiplicity bin are then merged across all  $Z_{\text{vtx}}$  bins. The same-event distributions are also split into  $Z_{\text{vtx}}$  bins during this correction procedure. The uncorrected distributions  $S(\Delta\varphi, \Delta\eta)$  and the mixed-event distributions  $B(\Delta\varphi, \Delta\eta)$  are shown for both the h- $\Lambda$  and h-h cases for all multiplicity and associated momentum bins in Figures 4.10 through 4.13.

This mixed-event correction is the final correction applied to the h-h distributions. However, the h- $\Lambda$  distributions require additional corrections that are not present in the dihadron case.

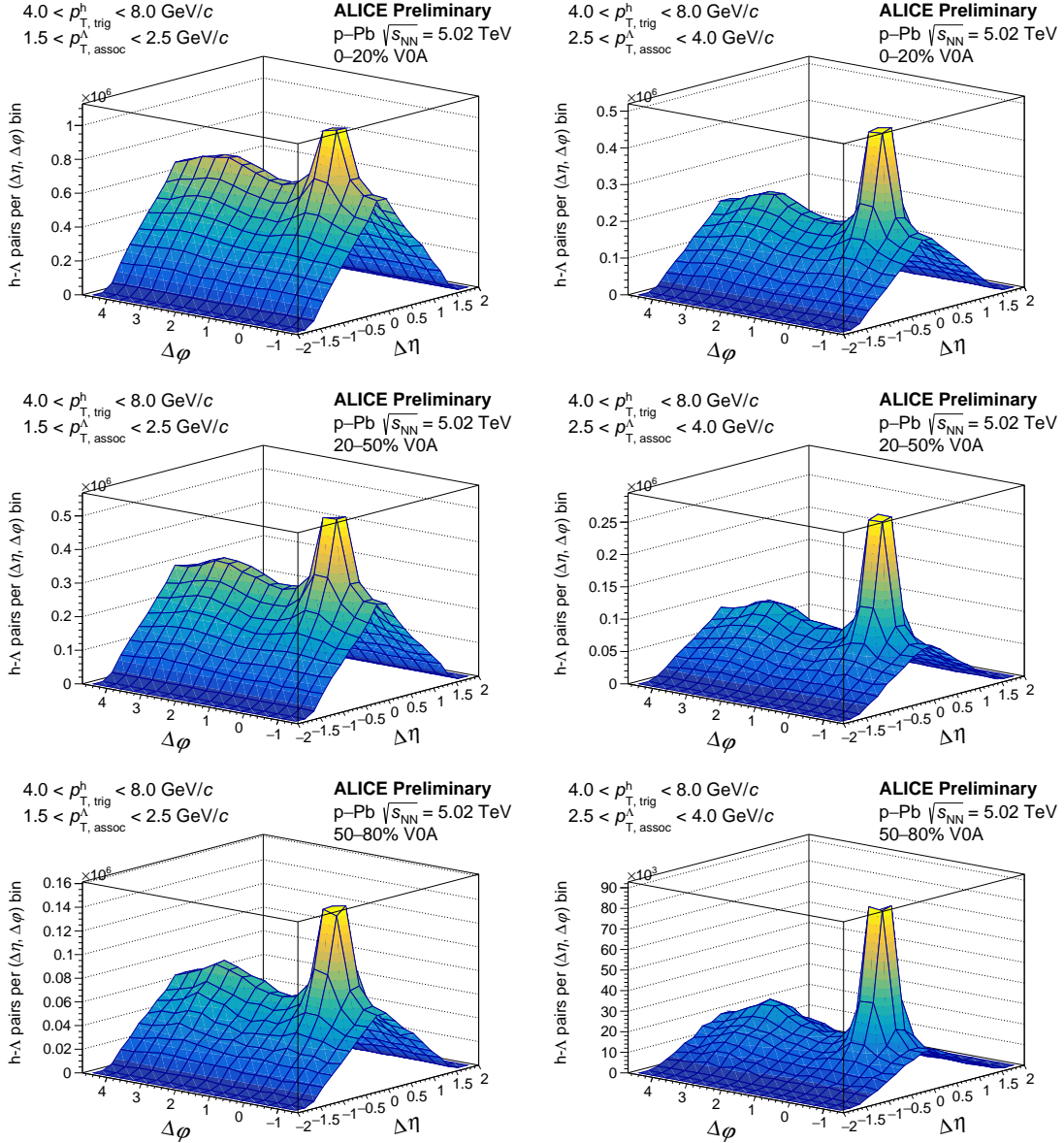


Figure 4.10: 2-D non-acceptance corrected  $h\bar{\Lambda}$  angular correlations for the 0-20% (top), 20-50% (middle), and 50-80% (bottom) multiplicity bins for  $1.5 < p_T < 2.5 \text{ GeV}/c$  (left) and  $2.5 < p_T < 4.0 \text{ GeV}/c$  (right).

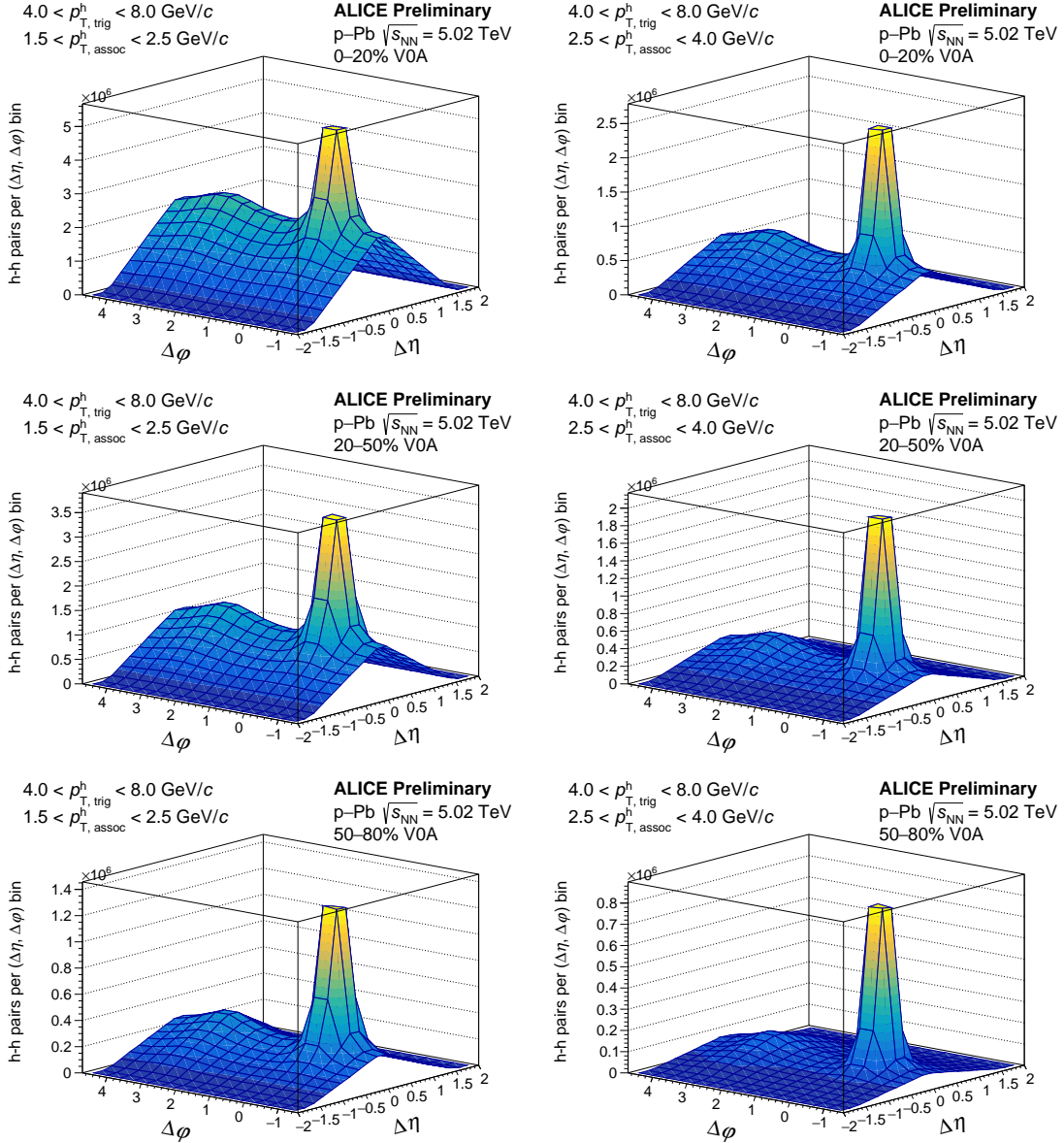


Figure 4.11: 2-D non-acceptance corrected h-h angular correlations for the 0-20% (top), 20-50% (middle), and 50-80% (bottom) multiplicity bins for  $1.5 < p_T < 2.5 \text{ GeV}/c$  (left) and  $2.5 < p_T < 4.0 \text{ GeV}/c$  (right).

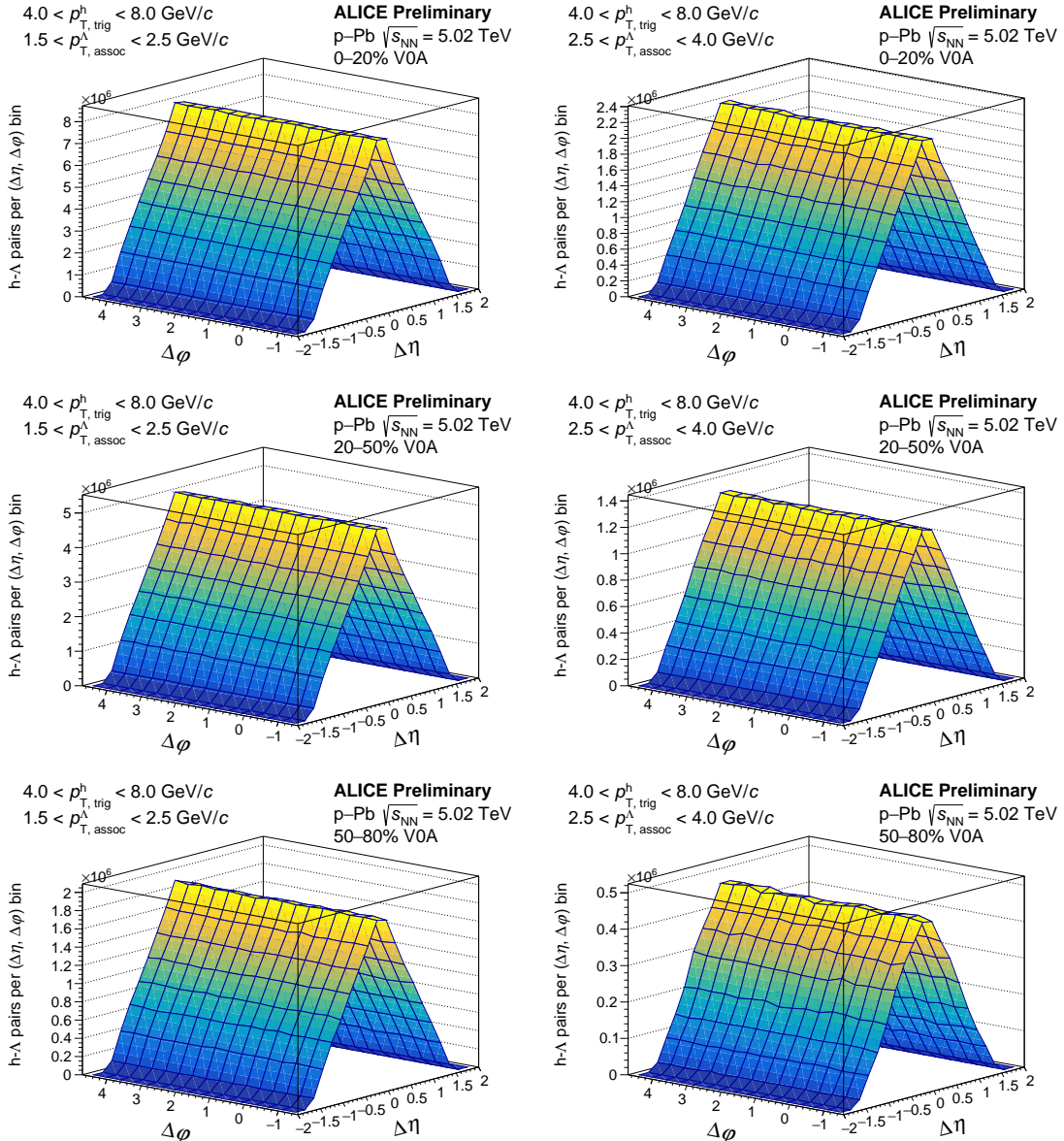


Figure 4.12: 2-D mixed-event h- $\Lambda$  angular correlations for the 0-20% (top), 20-50% (middle), and 50-80% (bottom) multiplicity bins for  $1.5 < p_T < 2.5 \text{ GeV}/c$  (left) and  $2.5 < p_T < 4.0 \text{ GeV}/c$  (right). The  $Z_{\text{vtx.}}$  bins are merged together for these plots.

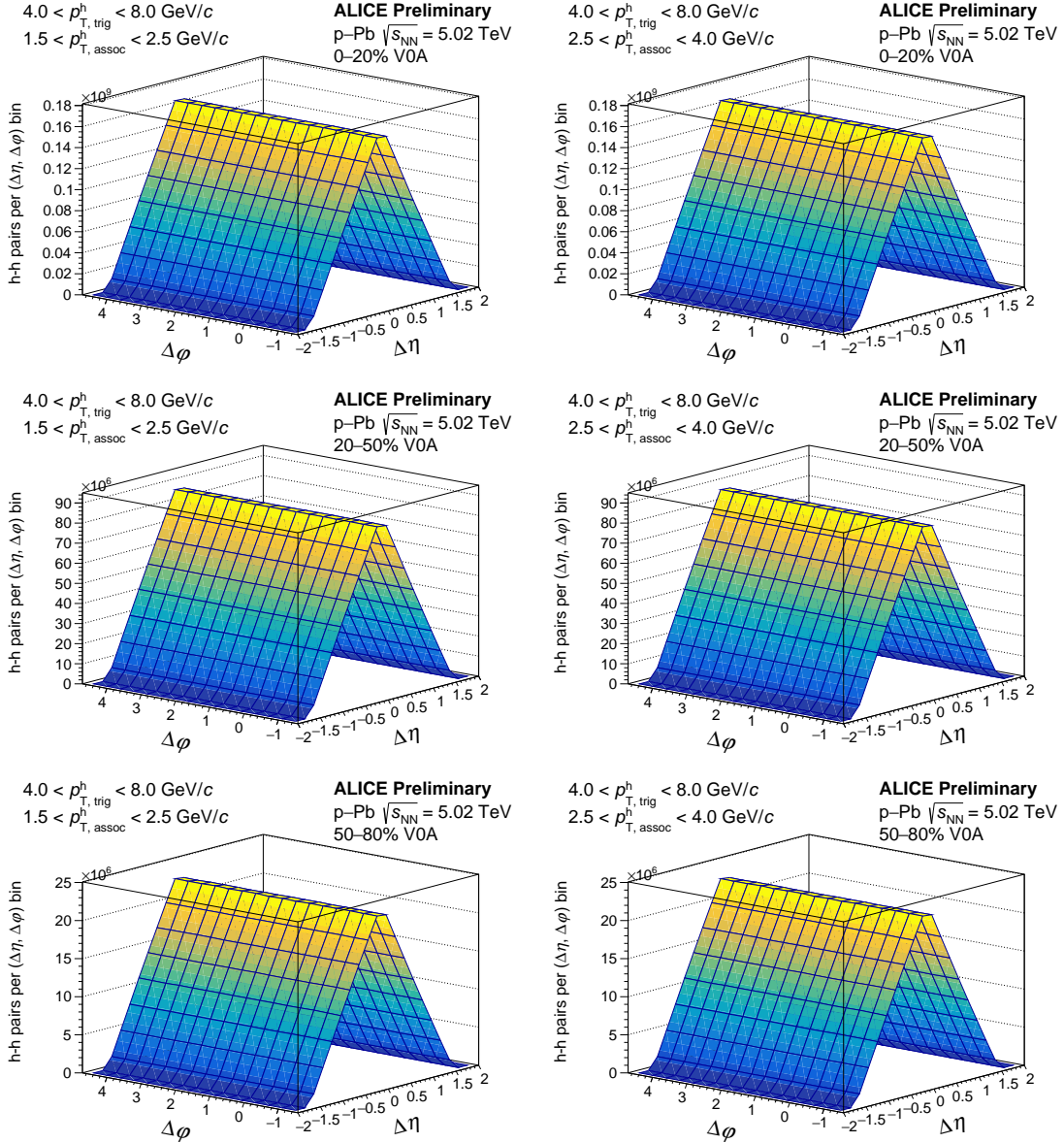


Figure 4.13: 2-D mixed-event h-h angular correlations for the 0-20% (top), 20-50% (middle), and 50-80% (bottom) multiplicity bins for  $1.5 < p_T < 2.5 \text{ GeV}/c$  (left) and  $2.5 < p_T < 4.0 \text{ GeV}/c$  (right). The  $Z_{\text{vtx}}$  bins are merged together for these plots.

2205 **4.5.3 Additional corrections for the h- $\Lambda$  distributions**

While the corrected correlation function from Equation 3.2 is generally true for two-particle correlations, there are a few additional corrections that must be applied to the h- $\Lambda$  distributions due to the  $\Lambda$  reconstruction procedure and the presence of track merging effects. To formalize this, the corrected h- $\Lambda$  correlation function can be written as

$$C_{\text{corr.}}^{\text{h-}\Lambda}(\Delta\varphi, \Delta\eta) = \frac{r_{\text{signal}} \times r_{\text{branch}}}{\epsilon_{\text{pair}}(\Delta\varphi, \Delta\eta)} \left( C_{\text{signal}}^{\text{h-p}\pi}(\Delta\varphi, \Delta\eta) - r_{\text{comb.}} \times C_{\text{sideband}}^{\text{h-p}\pi}(\Delta\varphi, \Delta\eta) \right), \quad (4.7)$$

2206 where  $C_{\text{corr.}}^{\text{h-}\Lambda}$  is the final corrected h- $\Lambda$  distribution. Each term on the RHS of the  
 2207 equation will be described in detail in the following sections, and they are presented  
 2208 in the order in which they are applied to the distributions.

2209 **4.5.3.1 Combinatorial background removal**

2210 The term

$$C_{\text{signal}}^{\text{h-p}\pi}(\Delta\varphi, \Delta\eta) - r_{\text{comb.}} \times C_{\text{SB, norm.}}^{\text{h-p}\pi}(\Delta\varphi, \Delta\eta) \quad (4.8)$$

2211 describes the removal of the combinatorial background resulting from the  $\Lambda$  recon-  
 2212 struction procedure from Section 4.3 using the **sideband subtraction** technique.  
 2213 The  $C_{\text{signal}}^{\text{h-p}\pi}$  distribution corresponds to  $\Lambda$  candidates where the invariant mass of the  
 2214 p $\pi$  pair falls within the range specified in Table 4.5, and the self-normalized  $C_{\text{SB, norm.}}^{\text{h-p}\pi}$   
 2215 distribution corresponds to candidates where the mass of the p $\pi$  pair falls within  
 2216 the so-called “sideband” region. An invariant mass plot highlighting these different  
 2217 regions can be seen in Figure 4.14. Both of the  $C_{\text{signal}}$  and  $C_{\text{sideband}}$  distributions are  
 2218 corrected for acceptance and efficiency using the techniques described in the previous  
 2219 sections. The sideband region is chosen such that it is far enough away from the sig-  
 2220 nal region to be free of any  $\Lambda$  signal, but close enough to ensure that the background  
 2221 p $\pi$  pairs in the signal region are kinematically similar to the pairs in the sideband  
 2222 region as to not introduce any biases in the correlations. The underlying assumption  
 2223 of this technique is that the correlation shape of h-p $\pi$  pairs from the sideband region  
 2224 is the same as the shape from the background h-p $\pi$  pairs in the signal region. For  
 2225 this analysis, the nominal sideband region was chosen to be  $1.135 < M_{p\pi} < 1.150$

2226  $\text{GeV}/c^2$ , but the effects of varying this region are studied in detail in the next chapter.  
2227 The  $r_{\text{comb.}}$  is the integral of the combinatorial background in the  $C_{\text{signal}}^{\text{h-p}\pi}$  distribution,  
2228 obtained by

$$r_{\text{Comb}} \equiv \frac{B}{S + B} \int \int C_{\text{signal}}^{\text{h-p}\pi}(\Delta\varphi, \Delta\eta) d\Delta\varphi d\Delta\eta, \quad (4.9)$$

2229 where  $S$  and  $B$  are the signal and background obtained from the fits to the  $\Lambda$  invariant  
2230 mass distributions in Figure 4.7. As the  $S/B$  ratio is the same for the  $\Lambda$  invariant mass  
2231 distributions in events with a trigger hadron as it is for the h- $\Lambda$  distributions, the scale  
2232  $B/(S + B)$  can be used to give only the background contribution from the integral  
2233  $\int \int C_{\text{signal}}^{\text{h-p}\pi}(\Delta\varphi, \Delta\eta) d\Delta\varphi d\Delta\eta$ . The self-normalized  $C_{\text{SB, norm.}}^{\text{h-p}\pi}$  distribution is then scaled  
2234 by  $r_{\text{comb.}}$  and subtracted from  $C_{\text{signal}}^{\text{h-p}\pi}$  to remove the combinatorial background.

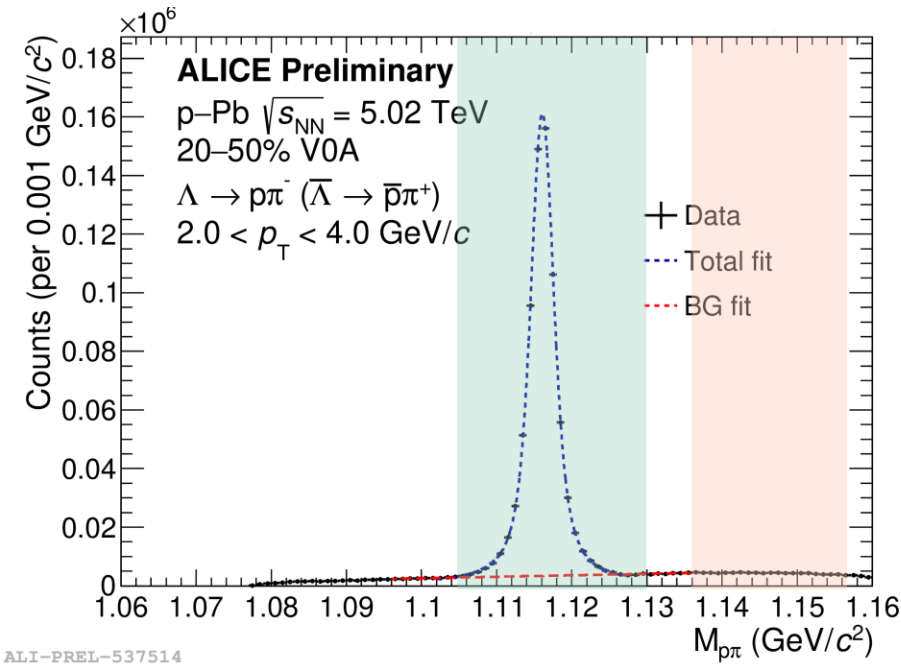


Figure 4.14: Invariant mass distribution of  $p\pi$  pairs in the 20-50% multiplicity class. The signal region is shown in light green, and the sideband region is shown in light pink. The correlation distribution in the sideband region is used to remove the combinatorial background from the signal region.

2235 While the above procedure describes the background removal in a more technical  
2236 manner, it can be condensed into the following steps:

- 2237 1. Generate the correlation distribution using  $\Lambda$  candidates in the signal invariant  
2238 mass region

- 2239     2. Do the same thing for  $\Lambda$  candidates in the sideband invariant mass region  
 2240     3. Scale the sideband distribution to match the background in the signal region  
 2241     4. Subtract the sideband distribution from the signal distribution  
 2242 Examples of the signal and sideband distributions  $C_{\text{signal}}^{\text{h-p}\pi}$  and  $C_{\text{SB}}^{\text{h-p}\pi}$  are shown for the  
 2243 0-20% multiplicity bin in Figure 4.15.

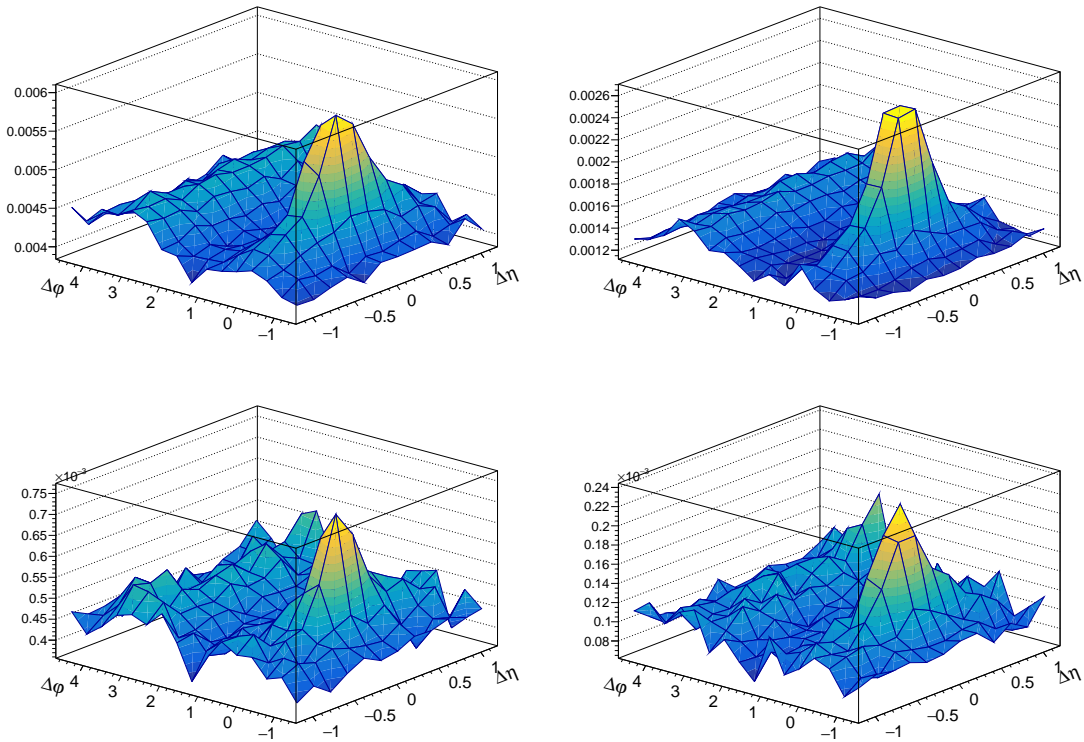


Figure 4.15: The signal (top) and sideband (bottom) distributions  $C_{\text{signal}}^{\text{h-p}\pi}$  and  $C_{\text{SB}}^{\text{h-p}\pi}$  for the lower (left) and higher (right) associated  $p_T$  bins. All plots were generated in the 0-20% multiplicity class.

2244 **4.5.3.2 Signal scaling**

- 2245 As the  $\Lambda$  candidate invariant mass signal region is finite, the fraction of the  $\Lambda$  signal  
 2246 that is missed in the tails of the invariant mass distribution must be corrected for.

2247 This is handled by the  $r_{\text{signal}}$  term in Equation 4.7, which is calculated by

$$r_{\text{signal}} \equiv \left( \frac{\text{Integral of residual in signal region}}{\text{Integral of residual between 1.098 and 1.134}} \right)^{-1} \quad (4.10)$$

2248 where “residual” refers to the invariant mass distributions from Figure 4.7 after sub-  
2249 tracting the straight-line background fit. 1.098 and 1.134 are the points in which  
2250 there is effectively zero signal, verified in Monte Carlo. Due to the width of the signal  
2251 region,  $r_{\text{signal}}$  is usually near unity. However, to study the effects of narrowing the  
2252 signal region, this term must be included in the analysis.

#### 2253 4.5.3.3 Branching ratio correction

2254 The most simple correction from Equation 4.7 comes from the branching ratio term,  
2255 namely

$$r_{\text{branch}} \equiv \frac{1}{BR(\Lambda \rightarrow p\pi)} = \frac{1}{0.639}. \quad (4.11)$$

2256 As not all  $\Lambda$ s decay into  $p\pi$  pairs, this term corrects for the fraction of  $\Lambda$ s that  
2257 decided to decay into something else. In many analyses, this term is not required, as  
2258 it is already included in the efficiency computation  $\epsilon_{\text{assoc.}}$ . As the  $\Lambda$  reconstruction  
2259 efficiency from this analysis is calculated using only  $\Lambda$ s that decay into  $p\pi$  pairs, this  
2260 term must be included separately.

#### 2261 4.5.3.4 Pair efficiency correction

2262 The  $\epsilon_{\text{pair}}$  term in Equation 4.7 is the h- $\Lambda$  “pair” efficiency, which is used to correct  
2263 for track merging effects. Many correlation studies are susceptible to track merging  
2264 inefficiencies [148], [149], whereby either the trigger or associated particle gets merged  
2265 over by the other during the track reconstruction. This results in a dip at small angles  
2266 in the angular correlation distribution when compared to a similar distribution with  
2267 no instances of track merging. As this effect cannot be seen directly in data due to  
2268 the missing reconstructed tracks, it is investigated using the Monte Carlo sample,  
2269 where the reconstructed tracks are compared to the MC-generated particles they  
2270 were reconstructed from. While this effect is usually negligible and only relevant at  
2271 extremely small angles ( $\Delta\varphi < 0.01, \Delta\eta < 0.1$ ), in this analysis this effect is more  
2272 severe and occurs at larger angles ( $\Delta\varphi < 1, \Delta\eta < 0.6$ ), shown in Figure 4.16.

2273 The severity of this effect for the h- $\Lambda$  distributions is likely due to two factors:

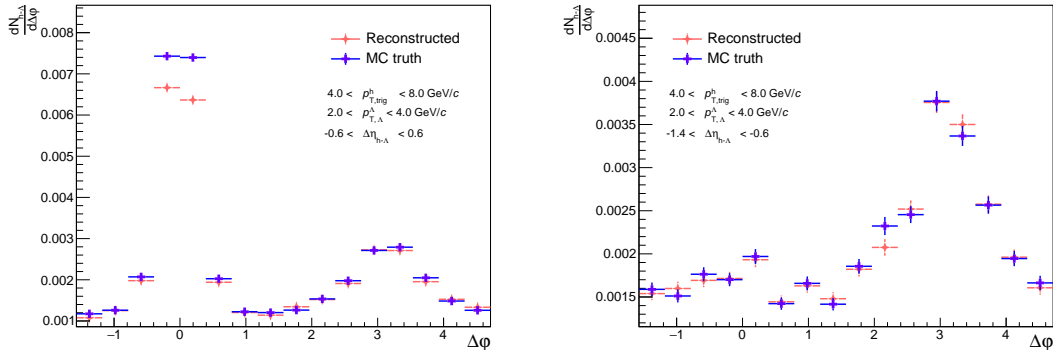


Figure 4.16: Demonstration of the track merging effect for h- $\Lambda$  pairs, whereby we see a dip in the reconstructed distribution at small  $\Delta\varphi$  and  $\Delta\eta$  when compared to the MC ground truth (left). This dip is not present at large  $\Delta\eta$  (right), but we also lose nearly the entirety of our near-side peak.

2274 • The  $\Lambda$  decay length is large ( $c\tau \approx 10 \text{ cm}$ ), meaning the daughter particles will  
2275 have less hits in the detector than the trigger particle (which is produced at  
2276 the primary vertex). As Kalman filtering [150] (track reconstruction) favors  
2277 the track with more hits, the  $\Lambda$  daughter track is “merged” over by the trigger  
2278 track.

2279 • The  $\Lambda$  decay is asymmetric ( $m_p/m_\pi \approx 7$ ), so the  $\Lambda$  and daughter proton end  
2280 up with similar momenta (and thus  $\varphi$  and  $\eta$ ). This means that whenever a  
2281 proton from a  $\Lambda$  decay is “merged” over by a trigger track, a h- $\Lambda$  pair with  
2282 small  $\Delta\varphi, \Delta\eta$  is lost.

2283 To see how the decay length can affect the track merging, the (reconstructed)/(MC  
2284 ground-truth)  $C(\Delta\varphi, \Delta\eta)$  distribution ratio for h-pion pairs in our MonteCarlo sam-  
2285 ple where the pion is **secondary**—meaning it came from a weak decay with decay  
2286 length  $> 2\text{cm}$ —is measured. Pions are chosen for this demonstration as they are  
2287 more abundantly produced than protons, and charged track reconstruction is par-  
2288 ticle species agnostic. Any “dips” from unity present in this ratio are indicative of  
2289 pairs being lost during reconstruction. This is then compared to the same ratio for  
2290 *h*—pion pairs where the pion is **primary**, and the results are shown in Figure 4.17.  
2291 All reconstructed triggers and pions pass the trigger hadron and  $\Lambda$  daughter cuts  
2292 from Tables 4.2 and 4.4, respectively. Furthermore, all distributions have been fully

2293 corrected for single-particle efficiencies and detector acceptance using the procedures  
 2294 from Sections 4.5.1 and 4.5.2, respectively. A large suppression at small  $(\Delta\varphi, \Delta\eta)$  is  
 2295 observed for the h-secondary pion case, but the h-primary pion case exhibits no such  
 2296 suppression. As such, it stands to reason that this suppression is at least in part due  
 2297 to the decay length of the  $\Lambda$ , as all particles that come from  $\Lambda$ s are secondaries (by  
 2298 a long shot).

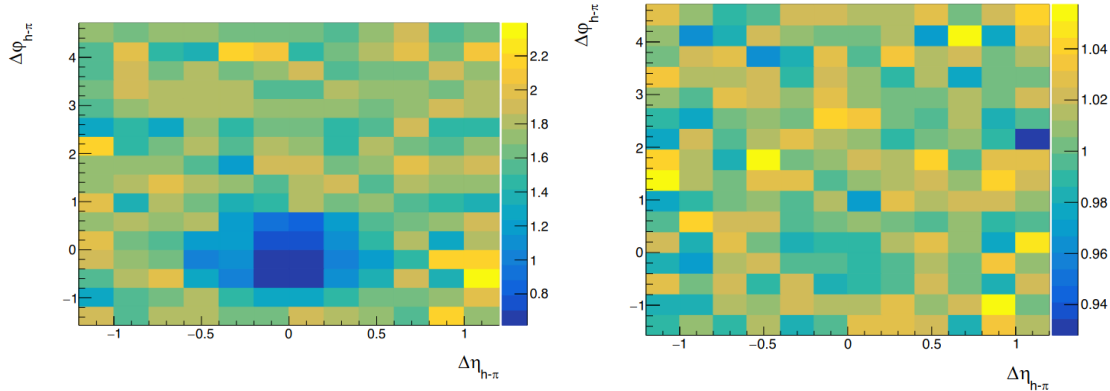


Figure 4.17: The reconstructed/ground truth ratios of the 2D  $C(\Delta\varphi, \Delta\eta)$  distributions for h-(secondary pions) (left) and h-(primary pions) (right). The suppression at smaller  $\Delta\varphi, \Delta\eta$  is clearly seen in the secondary case, but is not observable in the primary case, indicating a decay-length dependence.

2299 The  $p_T$  dependence of this effect can also be studied by measuring the recon-  
 2300 structed and ground truth  $h$ -(secondary pion)  $\Delta\varphi$  distributions at low ( $1.0 < p_T <$   
 2301  $2.0 \text{ GeV}/c$ ) and high ( $2.0 < p_T < 4.0 \text{ GeV}/c$ ) associated momentum. The result  
 2302 is shown in Figure 4.18. Note that the distributions were projected onto  $\Delta\varphi$  with  
 2303  $|\Delta\eta| < 1.2$ . A suppression relative to MC ground-truth is observed in the near-side of  
 2304 the reconstructed distribution in the higher  $p_T$  range, which is not seen in the low  $p_T$   
 2305 bin. This is also consistent with the decay length dependence shown in the previous  
 2306 figures, as decay length is roughly proportional to  $p_T$ .

2307 The  $p_T$  dependence of this inefficiency demonstrates why this effect is so severe  
 2308 in the h- $\Lambda$  case: due to the asymmetry of the  $\Lambda$  decay ( $m_p/m_\pi \approx 7$ ), the daughter  
 2309 proton receives most of the momentum. Therefore when investigating h- $\Lambda$  correlations  
 2310 within a given associated  $p_T$  range, any inefficiencies present in the corresponding h-  
 2311 (daughter proton) distribution with the same associated momentum would also be  
 2312 present in our final h- $\Lambda$  distribution within a similar  $\Delta\varphi, \Delta\eta$  range. As demonstrated

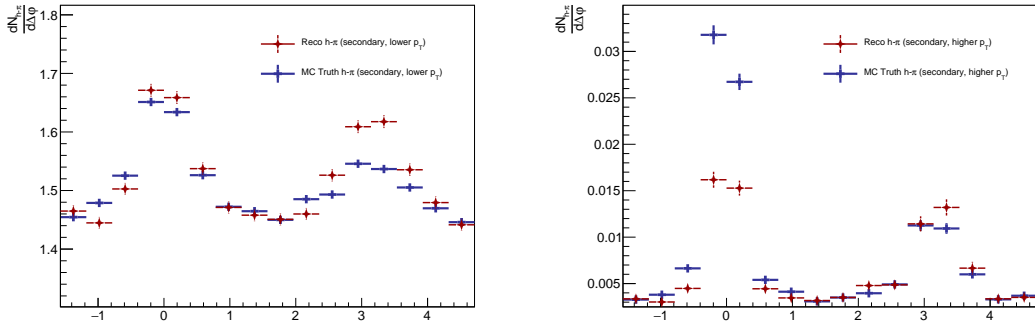


Figure 4.18: The reconstructed and ground truth  $\Delta\varphi$  distributions in the  $-1.2 < \Delta\eta < 1.2$  region for h-(secondary pions) with  $0.15 < p_T < 2$  (left) and  $2 < p_T < 4$  (right). The suppression at smaller  $\Delta\eta, \Delta\varphi$  is clearly seen in the higher momentum bin, but not present in the lower one.

in Figure 4.18, secondary charged particles with  $2 < p_T < 4$  GeV/c see a large inefficiency, and therefore we would expect a similar inefficiency to be present in our h- $\Lambda$  distribution (which was shown in Figure 4.16). In similar analyses using the  $K_S^0$  in leiu if the  $\Lambda$  [151], such an effect is not as present, both because the decay length is much shorter (2 cm vs 10 cm), and the  $K_S^0$  decay is symmetric, meaning the daughter pions will have momenta that are no longer similar to the mother kaon.

The following techniques have been investigated to correct for this effect:

- Applying a  $\Delta\varphi^*$  correction, which accounts for the helical nature of the tracks in the detector, as described in [152]: While  $\Delta\varphi$  and  $\Delta\varphi^*$  are different, they are correlated enough that in order to remove this effect, a  $|\Delta\varphi^*| < 0.7$  cut is required, which removes a significant amount of the near-side yield in the corresponding  $\Delta\varphi$  distribution.
- Applying a cut on the minimum distance between the fully reconstructed helices of the trigger and  $\Lambda$  daughter proton (varied between 0.1 cm and 10 cm): Again, this cut removes roughly the same amount of near-side yield as the  $\Delta\varphi^*$  cut, as this minimum distance is also highly correlated with  $\Delta\varphi$ .
- Using the resonance technique for  $\Lambda$  reconstruction (more details in Section 4.7.5): This moderately reduces the severity of this effect, but the statistical

fluctuations introduced by the smaller S/B ratio make it difficult to gauge how effective this correction is.

- Only correlating h- $\Lambda$  pairs where the charge of the  $\Lambda$  daughter proton (or antiproton) is opposite to the trigger, as oppositely charged tracks bend in opposite directions in the detector magnet: This reduces the effect by a considerable amount, but reduces our overall correlation statistics by a factor of 2.
- Selecting “lower quality” trigger tracks by loosening the cuts from Table 4.2 so they are less likely to be merged over the low-quality daughter tracks: This reduces the effect, but introduces a large amount of secondary contamination. Furthermore, we would like this analysis to be directly compared with other analyses, and therefore want to maintain the same cuts on the trigger hadron.
- Selecting “higher quality”  $\Lambda$  daughter tracks by tightening the cuts from Table 4.4 (and adding additional selection criteria): This again reduces the effect but heavily cuts into the  $\Lambda$  signal

As each of these techniques reduces the statistics of the h- $\Lambda$  correlation distribution beyond the realm of acceptability, the two-track inefficiencies are instead corrected for using a MC-generated template method, similar to the one used in [149]. For this method, the pair efficiency is given by

$$\epsilon_{pair}(\Delta\varphi, \Delta\eta) \equiv \frac{C_{\text{reco}}^{\text{tag}}(\Delta\varphi, \Delta\eta)}{C_{\text{gen}}(\Delta\varphi, \Delta\eta)}, \quad (4.12)$$

where  $C_{\text{reco}}^{\text{tag}}$  is the efficiency-corrected correlation distribution calculated in MC using reconstructed trigger hadrons and  $\Lambda$  candidates with the same selection criteria as described in Section 4.2, with the additional requirement that the  $\Lambda$  candidate has a corresponding generated  $\Lambda$  which is used for all calculations involving kinematic quantities. This removes the need to perform any of the additional corrections from the previous sections (e.g. background subtraction, signal scaling) as the invariant mass of generated lambdas is exact.  $C_{\text{gen}}$  is the correlation distribution calculated in MC using only generated trigger hadrons and  $\Lambda$  candidates. The template  $\epsilon_{pair}(\Delta\varphi, \Delta\eta)$  is applied for each associated  $p_T$  bin in this analysis, but it is independent of multiplicity and event generator. The templates for each associated  $p_T$  bin are shown in Figure 4.19. This correction is applied to the h- $\Lambda$  distributions after side-band subtraction, signal scaling, and the branching ratio correction.

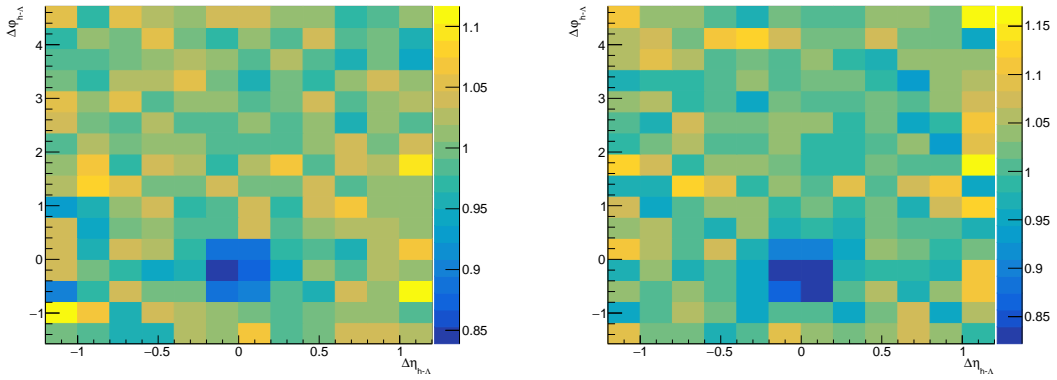


Figure 4.19: The  $\epsilon_{\text{pair}}(\Delta\varphi, \Delta\eta)$  templates for the track merging correction in the lower ( $1.5 < p_T < 2.5$  GeV/ $c$ , left) and higher ( $2.5 < p_T < 4.0$  GeV/ $c$ , right) associated momentum bins. While it may be difficult to observe, the lower  $p_T$  bin has a minimum dip of around 0.84, whereas the higher  $p_T$  bin has a minimum dip of around 0.81, reflecting the  $p_T$  dependence discussed in this section.

2361 After these corrections, both the h- $\Lambda$  and h-h 2D distributions are finalized and  
 2362 ready for projection onto  $\Delta\varphi$  to extract the yields and widths of interest from the  
 2363 previous chapter. These fully corrected distributions can be seen in Figures 4.20 (h-  
 2364  $\Lambda$ ) and 4.21 (h-h). However, there are still a number of systematic uncertainties to  
 2365 investigate and cross-checks required to ensure the validity of the final results.

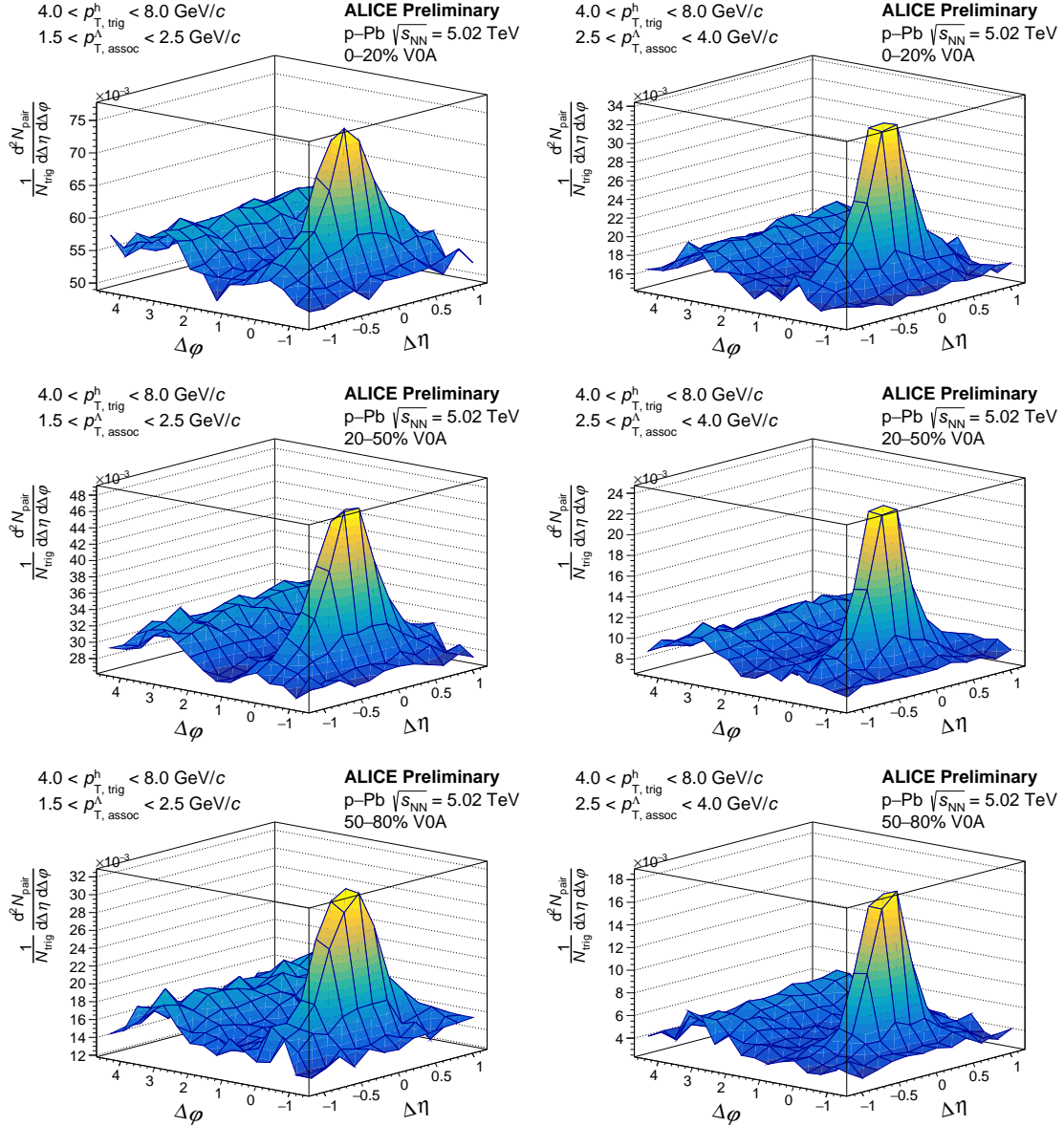


Figure 4.20: 2-D fully-corrected h- $\Lambda$  angular correlations for the 0-20% (top), 20-50% (middle), and 50-80% (bottom) multiplicity bins for  $1.5 < p_T < 2.5 \text{ GeV}/c$  (left) and  $2.5 < p_T < 4.0 \text{ GeV}/c$  (right).

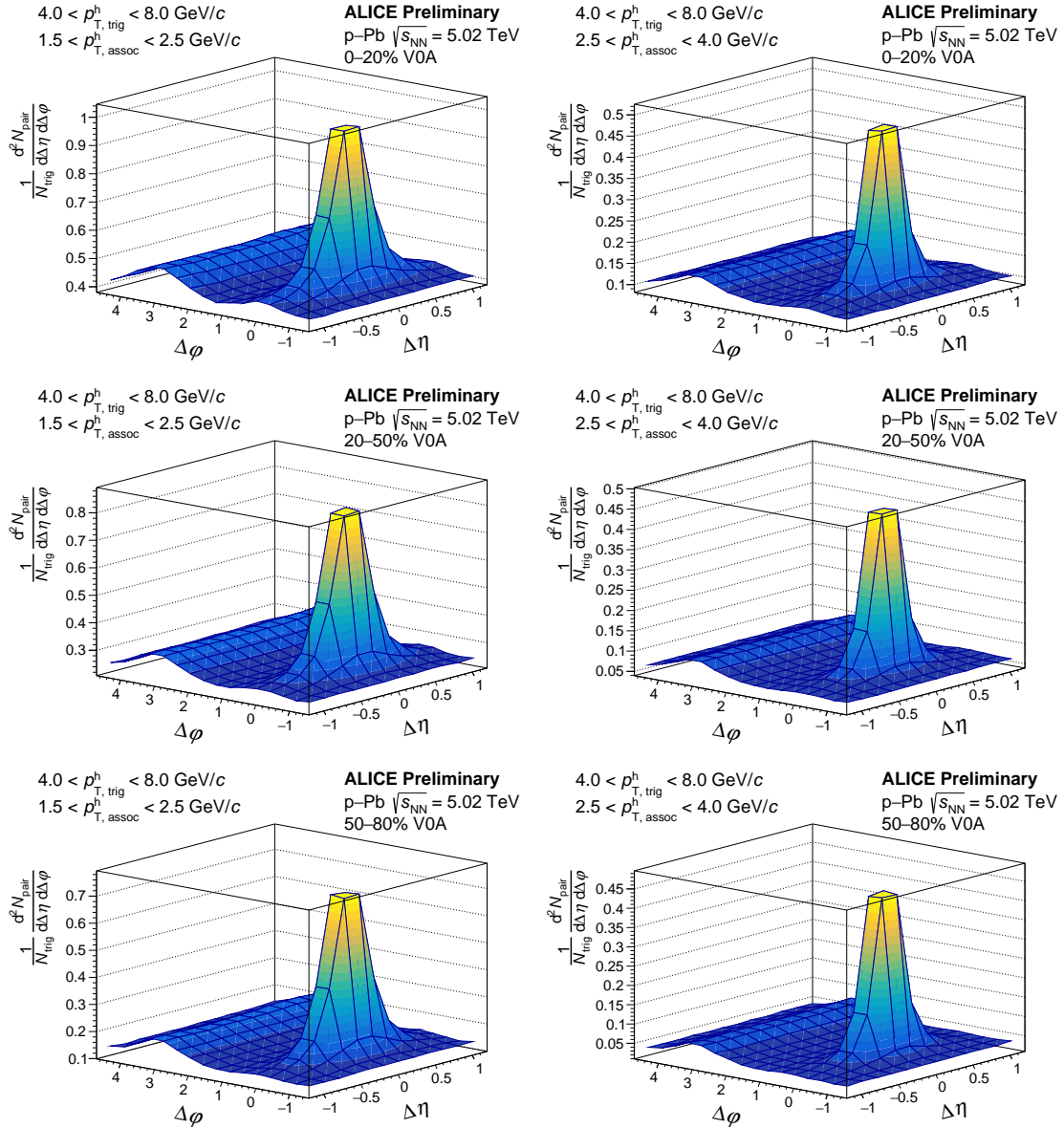


Figure 4.21: 2-D fully-corrected h-h angular correlations for the 0-20% (top), 20-50% (middle), and 50-80% (bottom) multiplicity bins for  $1.5 < p_T < 2.5 \text{ GeV}/c$  (left) and  $2.5 < p_T < 4.0 \text{ GeV}/c$  (right).

2366 chapterSystematic Uncertainties and Cross-checks While it would be nice to pro-  
2367 duce exact results for the measurements presented in this thesis, uncertainties are  
2368 inevitable. These uncertainties are usually grouped into two categories: **statistical**  
2369 **uncertainties** and **systematic uncertainties**. Statistical uncertainties are those  
2370 which arise from things like detector imprecisions or even the inherent statistical nature  
2371 of the measurement itself. Calculating these uncertainties is *usually* straightforward,  
2372 though it often involves well-motivated assumptions about the underlying probability  
2373 distributions of the data. Determining systematic uncertainties, on the other hand, is  
2374 a much more complicated process. To that end, the first section of this chapter goes  
2375 into a large amount of detail about the calculation of systematic uncertainties for this  
2376 analysis, starting with clearly defining what “systematic uncertainty” means and how  
2377 it is quantified in the context of this thesis, followed by comprehensive ingestigations  
2378 into each of the sources of uncertainty considered in this research, and ending with a  
2379 summary of the final systematic uncertainties for each observable.

2380 The second section of this chapter is dedicated to the cross-checks performed to  
2381 ensure the validity of the analysis procedure. There are a variety of such checks,  
2382 ranging from a general Monte Carlo closure test to more specific checks into physical  
2383 biases that may be introduced by the analysis procedure.

## 2384 4.6 Systematic uncertainties

2385 “*The treatment of systematic errors is often mishandled. This is due to*  
2386 *lack of understanding and education, based on a fundamental ambiguity*  
2387 *as to what is meant by the term*”

2388 —Roger Barlow, *Systematic Errors: Facts and Fictions* [153]

2389 In every experimental analysis, choices must be made. These choices can be as  
2390 simple as the selection of a particular data set, or as complex as choosing a fit function  
2391 of fifteen parameters instead of three. In either case, these choices can have an effect  
2392 on the final results, which is usually quantified by the **systematic uncertainty**.  
2393 Broadly speaking, the systematic uncertainty is a measure of the sensitivity of the  
2394 final results to the choices made during the analysis procedure.

2395 In this analysis, the procedure for estimating the systematic uncertainty from a  
2396 certain choice is as follows:

1. Vary the choice in a way that is reasonable and justifiable
2. Measure the observable of interest after the variation
3. Quantify the effect of the variation on the observable by calculating the percent change from the original value of the observable
4. Vary the choice in a slightly different way, and repeat steps 2 and 3
5. Repeat steps 2 through 4 until all reasonable variations have been considered
6. Calculate the systematic uncertainty as the root mean square (RMS) of the percentages from step 3.

Note the usage of the words “reasonable” and “justifiable”, which seem to indicate that the systematic uncertainty is a subjective quantity. Indeed the process of obtaining the systematic uncertainty involves even more choices, like the choice of which choices to consider, the choices of how to vary the choices, and even the choice on how to quantify the uncertainty itself. In this sense, systematic uncertainty calculations are an art form, where the artist (analyzer) must use their creativity and best judgement to determine which choices are indeed reasonable. To that end, the list of sources of systematic uncertainties considered for this analysis is not exhaustive, but it is the best attempt at a comprehensive list of reasonable choices that affect the final results.

To provide more structure to this section, the analysis procedure is broken into the following components:

1. The generation of the  $h-\Lambda$  and  $h-h$   $\Delta\varphi$  distributions,
2. The extraction of the pairwise yields from the  $\Delta\varphi$  distributions, and
3. The extraction of the near- and away-side widths from the fits of the  $\Delta\varphi$  distributions,

which are used to separate this section into three subsections, one for each of these components. In each section, the sources of systematic uncertainties are described, followed by a Barlow analysis [153] to ensure the variations result in a statistically significant deviation from the nominal values. Finally, a summary of the final systematic uncertainties is provided.

Table 4.6: The systematic uncertainties for the  $\Delta\varphi$  distributions which are not directly calculated in this thesis, instead taken from previous analyses using the same particle species and collision system [151], [154]–[156]. Each source of uncertainty is verified to be independent of multiplicity, but the  $\Lambda$  material budget and topological selection uncertainties exhibit a small dependence on  $p_T$ .

Source name	Lower $p_T$ %	Higher $p_T$ %
$\Lambda$ topological selection	3.2%	3.0%
$\Lambda$ material budget	1.1%	0.6%
Charged h tracking efficiency	3.5%	3.5%
Charged h material budget	negl.	negl.

#### 2426 4.6.1 $\Delta\varphi$ distribution generation

2427 The sources of systematic uncertainties that affect the  $\Delta\varphi$  distribution considered for  
 2428 this analysis are the following, in order of decreasing magnitude:

- 2429 •  $\Lambda$  topological selection (h- $\Lambda$  distribution only)
- 2430 • Material budget
- 2431 • Tracking efficiency
- 2432 •  $\Lambda$  daughter PID cuts (h- $\Lambda$  distribution only)
- 2433 •  $\Lambda$  invariant mass signal region selection (h- $\Lambda$  distribution only)
- 2434 •  $\Lambda$  invariant mass sideband region selection (h- $\Lambda$  distribution only)

2435 As the  $\Lambda$  topological selection, material budget, and tracking efficiencies have been  
 2436 studied in detail in previous analyses using the same particle species and collision  
 2437 system [151], [154], [155], the systematic uncertainty associated with these sources  
 2438 is taken directly from these analyses and presented in Table 4.6. The uncertainties  
 2439 from these sources exhibit no multiplicity dependence, and a very small dependence  
 2440 on  $p_T$ . These uncertainties are also assumed to be independent of  $\Delta\varphi$ , although this  
 2441 is studied more thoroughly in Section 4.6.3.

2442 Each of the other sources of systematic uncertainty is described in detail in the  
 2443 following sections.

2444 **4.6.1.1 Signal region selection**

2445 The nominal signal region for the  $\Lambda$  invariant mass is fairly wide, accounting for  
2446 nearly 97% of the total  $\Lambda$  signal. However, the final result should not be heavily  
2447 influenced by the choice of signal region so long as it is centered about the true  $\Lambda$   
2448 mass. Furthermore, altering the signal region tests the validity of the signal scaling  
2449 procedure outlined in Section 4.5. To investigate this, the signal region is varied in the  
2450 ways presented in Table 4.7. The resulting  $\Delta\varphi$  distributions and ratios to the nominal  
2451 distribution for each signal region variation in each multiplicity and associated  $p_T$  bin  
2452 are shown in Figures 4.22 (lower  $p_T$ ) and 4.23 (higher  $p_T$ ). The average deviation  
2453 from the nominal distribution is around 2%, with no individual variation exceeding  
2454 5%. As no significant dependence on  $\Delta\varphi$  is observed, the systematic uncertainty is  
2455 calculated as the RMS of the percent change from each variation across the entire  
2456  $\Delta\varphi$  range as opposed to calculating the RMS in each bin.

Table 4.7: The variations of the  $\Lambda$  invariant mass signal region considered for this analysis.

Variation name	Signal range ( $\text{GeV}/c^2$ )
Narrow	$1.108 < M_{p\pi} < 1.124$
Narrower	$1.112 < M_{p\pi} < 1.120$
Wide	$1.100 < M_{p\pi} < 1.132$
Wider	$1.096 < M_{p\pi} < 1.136$

2457 **4.6.1.2 Sideband region selection**

2458 The choice of sideband region also leaves a lot of room for reasonable variation: all  
2459 that is required is that the region is 1) large enough to produce a smooth  $h\text{-}p\pi$  distri-  
2460 bution with minimal statistical fluctuations and 2) close enough to the signal region  
2461 that the  $p\pi$  pairs are kinematically similar to those in the background of the signal  
2462 region. As long as these requirements are met, the final result should not be very  
2463 dependent on the choice of sideband region. To investigate the effects of changing the  
2464 sideband region, the variations presented in Table 4.8 are considered. The measured  
2465  $\Delta\varphi$  distributions and variation/nominal ratios for each sideband region variation in  
2466 each multiplicity and associated  $p_T$  bin are shown in Figures 4.24 (lower  $p_T$ ) and 4.25  
2467 (higher  $p_T$ ). The result is even less deviation from the nominal distribution than the

2468 signal region variations, with the average deviation being closer to 1%. Again, no  
2469 significant dependence is observed on  $\Delta\varphi$ , so the systematic uncertainty is calculated  
2470 as the RMS of the percent change from each variation across every  $\Delta\varphi$  bin.

Table 4.8: The variations of the  $\Lambda$  invariant mass sideband region considered for this analysis. Note that the “shifted left” sideband falls on the opposite (left) side of the signal region.

Variation name	Sideband range ( $\text{GeV}/c^2$ )
Narrow	$1.135 < M_{p\pi} < 1.145$
Wide	$1.135 < M_{p\pi} < 1.16$
Shifted left	$1.086 < M_{p\pi} < 1.098$
Shifted right	$1.14 < M_{p\pi} < 1.155$

2471 **4.6.1.3  $\Lambda$  daughter particle identification**

2472 The  $\Lambda$  daughter particle identification (PID) cuts are chosen to be wide enough to  
2473 ensure a high efficiency, but narrow enough to ensure a high purity. As the require-  
2474 ment for a higher purity should be offset by the subtraction of the combinatorial  
2475 background, altering the PID cuts should only minimally affect the final  $\Delta\varphi$  distri-  
2476 butions. To study this, the PID cuts are varied in the ways presented in Table 4.9.  
2477 The final  $\Delta\varphi$  distributions and ratios to the nominal distribution for each PID cut  
2478 variation in each multiplicity and associated  $p_T$  bin are shown in Figures 4.26 (lower  
2479  $p_T$ ) and 4.27 (higher  $p_T$ ). Requiring a signal in the TOF detector drastically reduces  
2480 the  $\Lambda$  signal as the daughter pions are often heavily deflected by the magnetic field  
2481 due to their lower  $p_T$  (again,  $m_p/m_\pi \approx 7$ , so most of the mother momentum belongs  
2482 to the proton). This causes a large amount of statistical fluctuations in the corre-  
2483 sponding  $\Delta\varphi$  distribution, which is why the “require TOF” variation is inevitably  
2484 excluded after the Barlow check presented in Section 4.6.1.4. The other variations  
2485 result in only around a 2% deviation from the nominal  $\Delta\varphi$  distribution, on average.

Table 4.9: The variations of the  $\Lambda$  daughter PID cuts considered for this analysis. The “require TOF” variation requires a TOF hit for both the proton and pion, but maintains the nominal values for  $|n\sigma_{\text{TPC, TOF}}|$ .

Variation name	$ n\sigma_{\text{TPC, TOF}}^\pi $	$ n\sigma_{\text{TPC, TOF}}^p $
Narrow	< 1.8	< 1.2
Wide	< 4.2	< 2.8
Require TOF	< 3.0	< 2.0

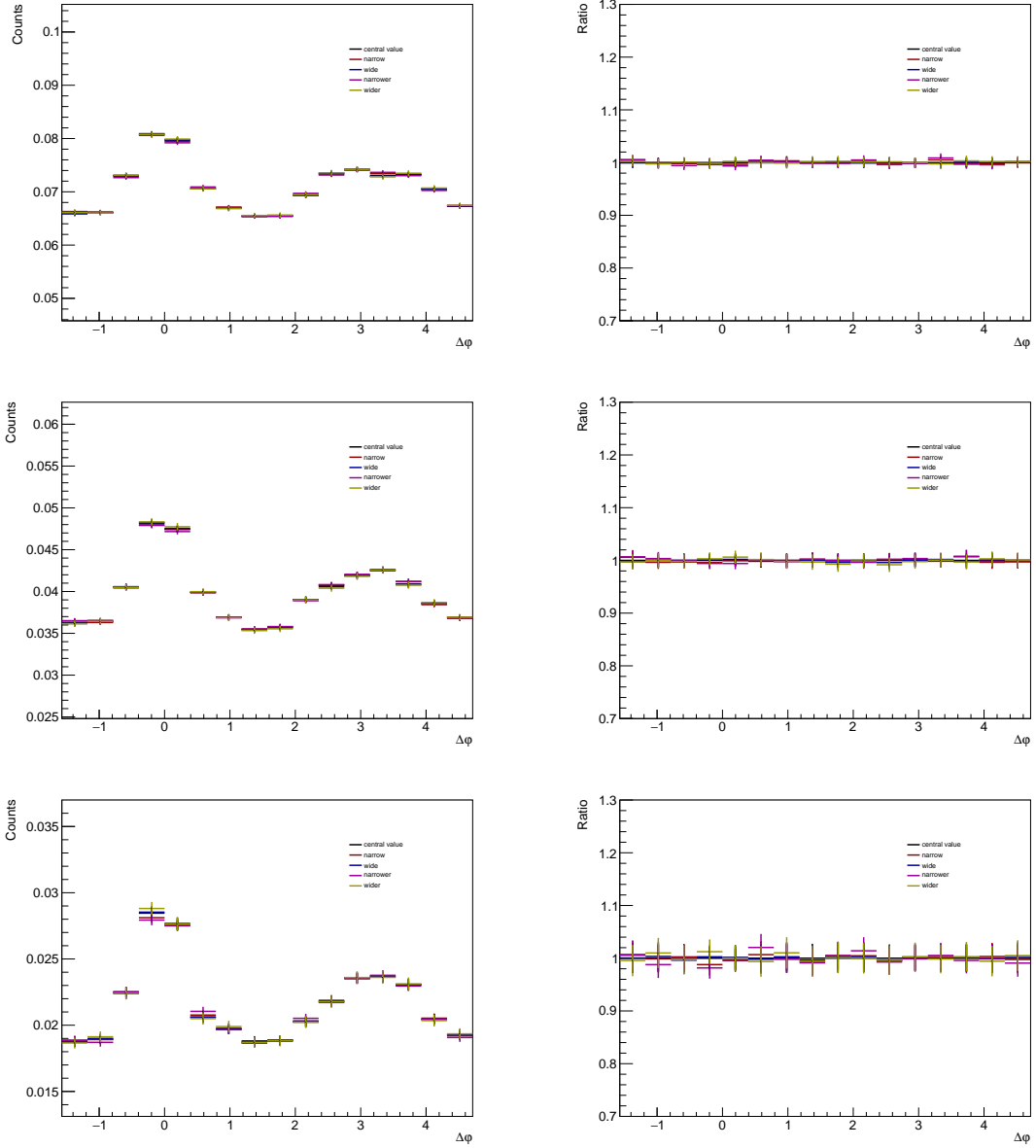


Figure 4.22: The  $h-\Lambda$   $\Delta\varphi$  distributions within the 0-20% (top), 20-50% (middle), and 50-80% (bottom) multiplicity bins in the lower associated  $p_T$  bin for each of the signal region variations (left) with the ratios to the nominal distribution (right).

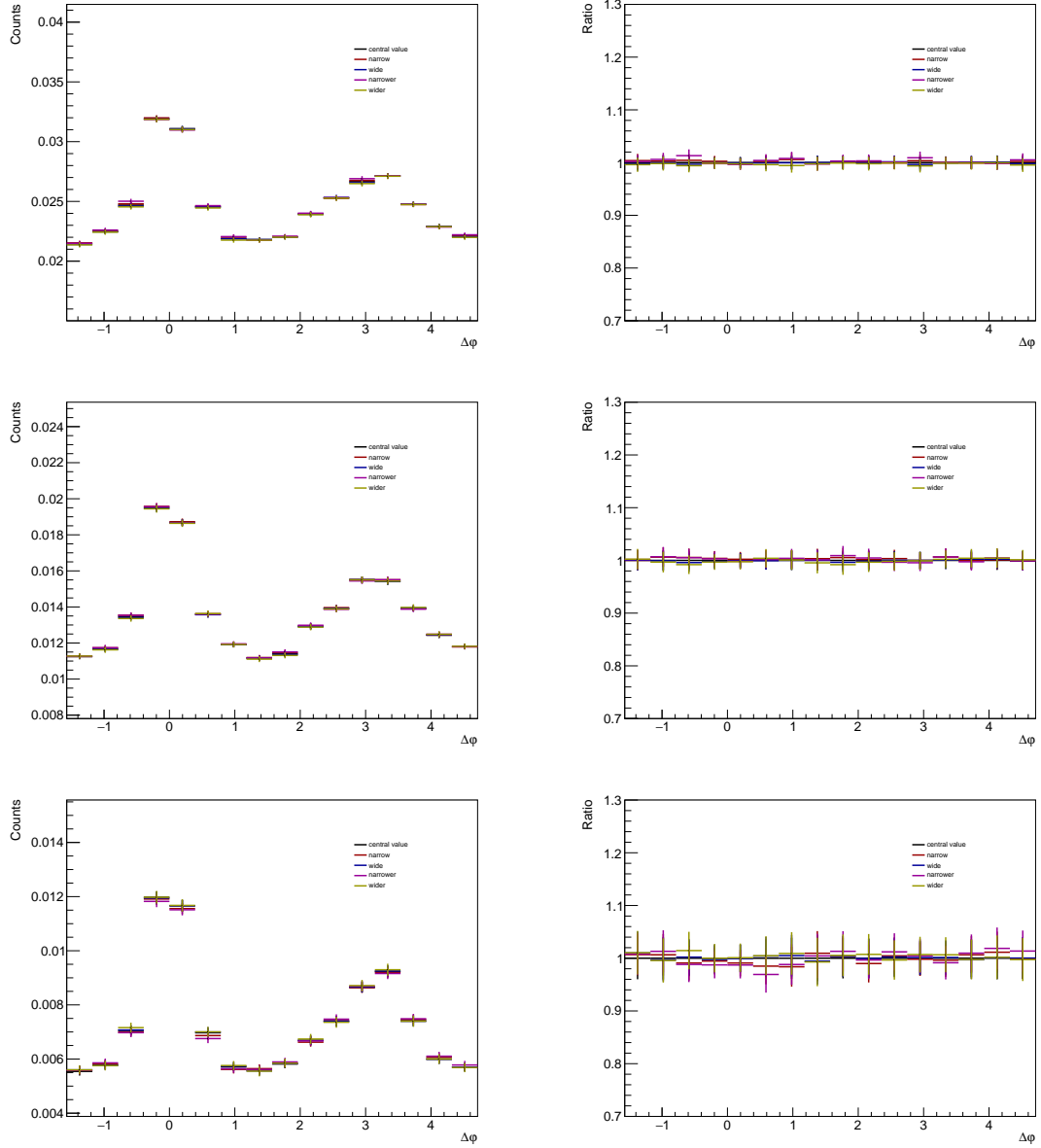


Figure 4.23: The  $h-\Lambda$   $\Delta\varphi$  distributions within the 0-20% (top), 20-50% (middle), and 50-80% (bottom) multiplicity bins in the higher associated  $p_T$  bin for each of the signal region variations (left) with the ratios to the nominal distribution (right).

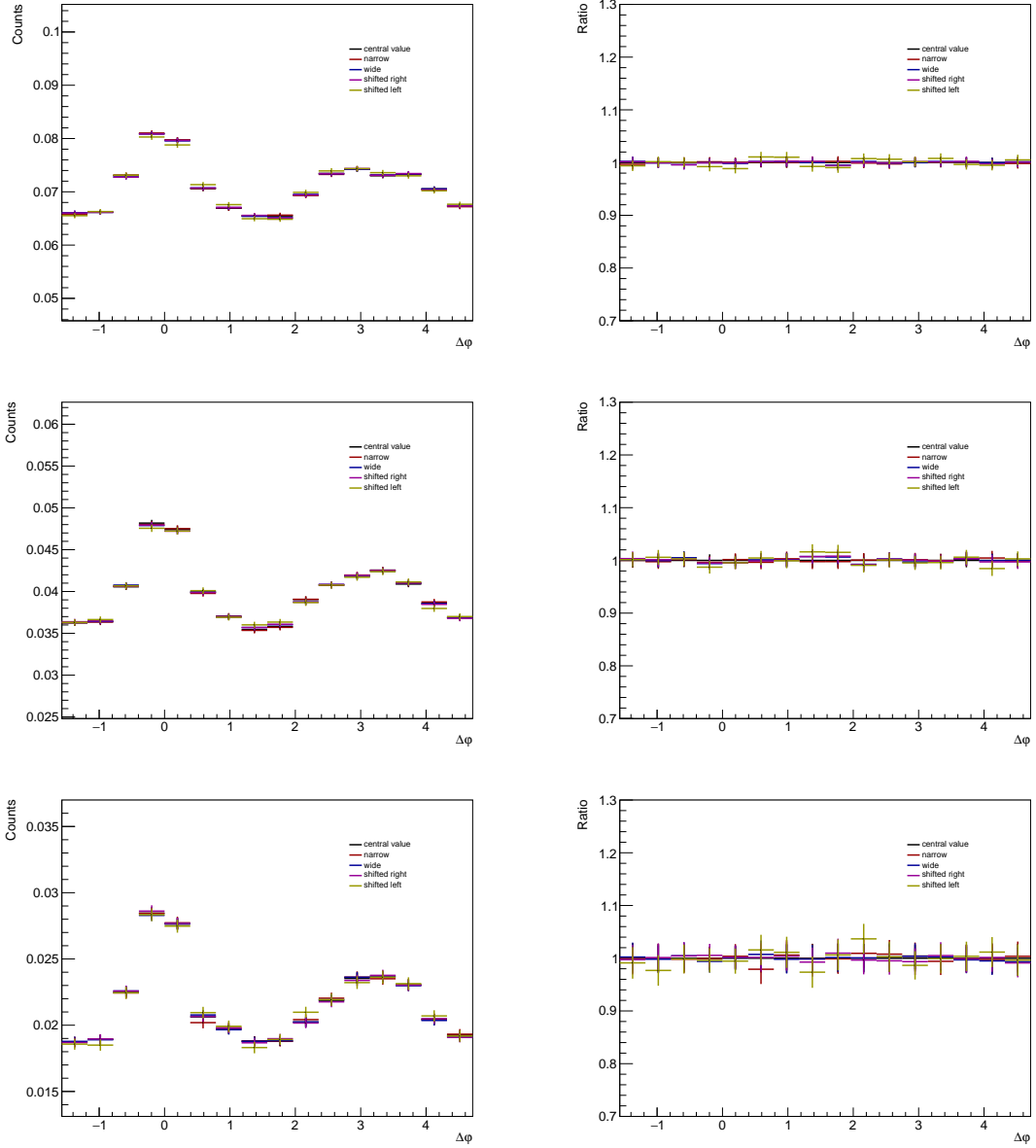


Figure 4.24: The  $h-\Lambda$   $\Delta\varphi$  distributions within the 0-20% (top), 20-50% (middle), and 50-80% (bottom) multiplicity bins in the lower associated  $p_T$  bin for each of the sideband region variations (left) with the ratios to the nominal distribution (right).

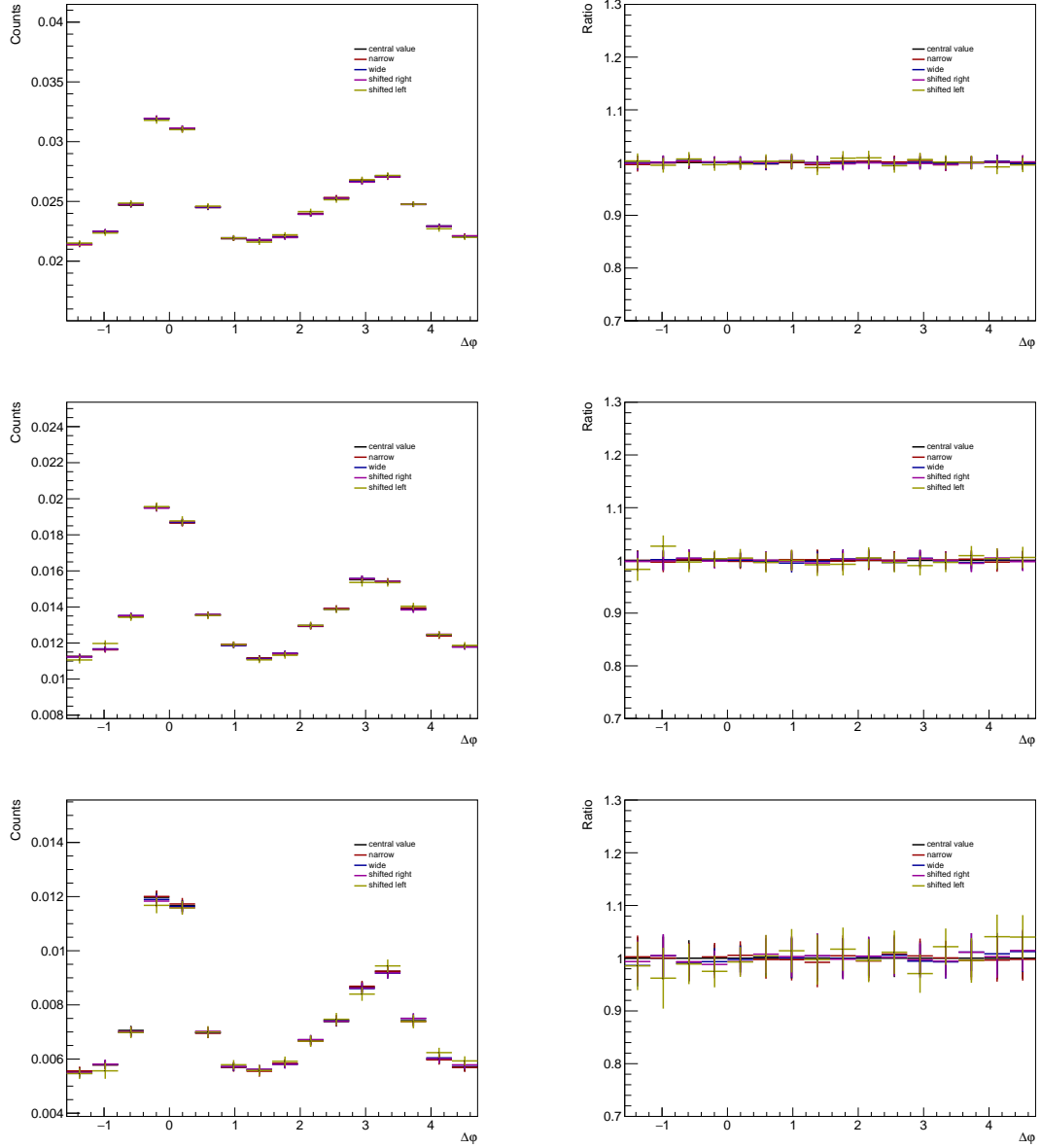


Figure 4.25: The  $h-\Lambda$   $\Delta\varphi$  distributions within the 0-20% (top), 20-50% (middle), and 50-80% (bottom) multiplicity bins in the higher associated  $p_T$  bin for each of the sideband region variations (left) with the ratios to the nominal distribution (right).

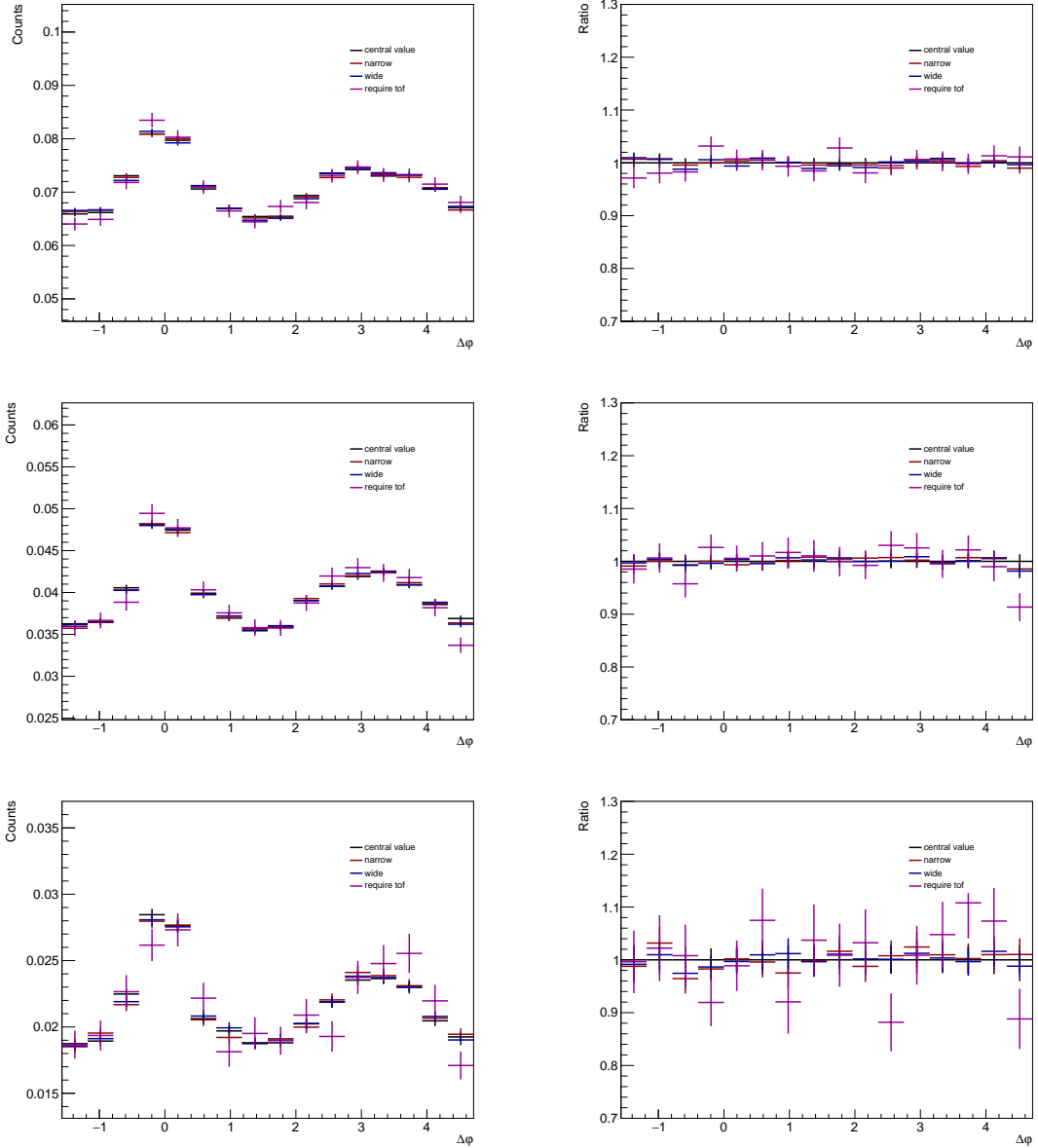


Figure 4.26: The  $h\text{-}\Lambda$   $\Delta\varphi$  distributions within the 0-20% (top), 20-50% (middle), and 50-80% (bottom) multiplicity bins in the lower associated  $p_T$  bin for each of the PID cut variations (left) with the ratios to the nominal distribution (right).

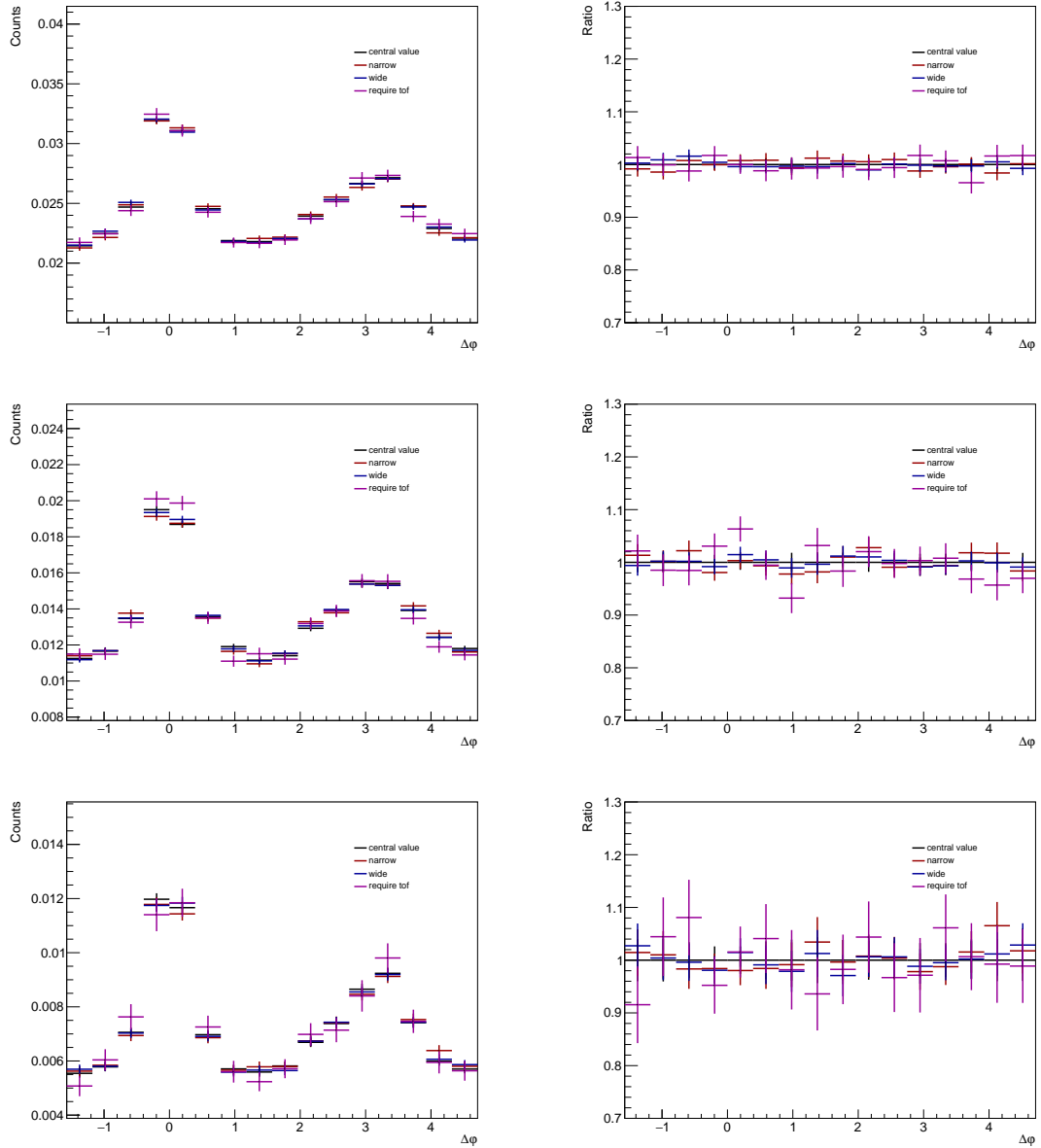


Figure 4.27: The  $h\text{-}\Lambda$   $\Delta\varphi$  distributions within the 0-20% (top), 20-50% (middle), and 50-80% (bottom) multiplicity bins in the higher associated  $p_T$  bin for each of the PID cut variations (left) with the ratios to the nominal distribution (right).

2486 4.6.1.4 Barlow check for  $\Delta\varphi$  distribution generation

2487 Due to statistical fluctuations, it may be the case that some variations result in a  
 2488 statistically insignificant deviation from the nominal  $\Delta\varphi$  distribution. In such cases,  
 2489 the variation should not be considered in the final systematic uncertainty calcula-  
 2490 tion. To determine which variations give statistically significant deviations, a Barlow  
 2491 check [153] is performed. For each  $\Delta\varphi$  bin, the following quantity is calculated:

$$N\sigma_{RB} := \frac{y_{\text{var.}} - y_{\text{nom.}}}{\sqrt{|\sigma_{\text{var.}}^2 - \sigma_{\text{nom.}}^2|}}, \quad (4.13)$$

2492 where  $y_{\text{var.}}$  and  $\sigma_{\text{var.}}$  are the measured yield and statistical uncertainty for the vari-  
 2493 ation, and  $y_{\text{nom.}}$  and  $\sigma_{\text{nom.}}$  are the yield and statistical uncertainty for the nominal  
 2494 value.

2495 To determine whether a given variation should be excluded, the number of  $\Delta\varphi$   
 2496 bins that have  $|N\sigma_{RB}| < 1$  is counted. If this is the majority of the bins (across all  
 2497 multiplicity and associated  $p_T$  ranges), the variation is excluded from the systematic  
 2498 calculation. Example plots of  $N\sigma_{RB}$  for each variation of the signal, sideband and  
 2499 PID cuts are shown in Figure 4.28. The red lines represent  $N\sigma_{RB} = \pm 1$ .

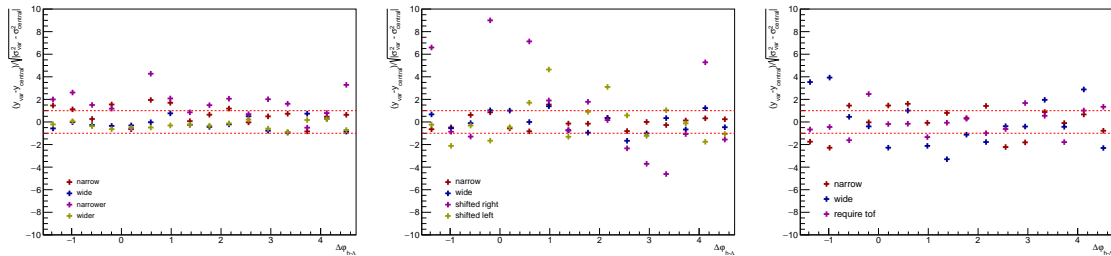


Figure 4.28: Barlow check for the signal (left), sideband (middle), and PID (right) variations in the 0-20% multiplicity bin. The red lines represent  $N\sigma_{RB} = \pm 1$ , and if the majority of the points fall within the red lines (across all  $\Delta\varphi$ , multiplicity and  $p_T$  bins), they are excluded from the systematic uncertainty calculation.

2500 As a result of the check, the following variations are excluded from the final  
 2501 systematic uncertainty calculation:

- 2502 • Signal: wide, wider  
 2503 • Sideband: wide, narrow

- 2504 • PID: require TOF

2505 These exclusions are not so surprising. As the nominal signal region is already fairly  
 2506 wide, making it wider does not significantly change the  $\Delta\varphi$  distribution. Similarly,  
 2507 the initial sideband region falls fairly close to the signal region. So long as there are  
 2508 enough statistics in the corresponding sideband  $h\text{-}\Lambda$  distribution, changing its width  
 2509 should not affect the  $\Delta\varphi$  distribution in a meaningful way. It also appears that re-  
 2510 quiring a TOF hit introduces large statistical errors, which dominate the denominator  
 2511 in Equation 4.13.

2512 **4.6.1.5  $\Delta\varphi$  distribution systematics, summarized**

2513 The final systematic errors (after the Barlow check) from the  $h\text{-}\Lambda$   $\Delta\varphi$  distribution  
 2514 generation for each multiplicity bin and  $p_T$  bin are shown in Table 4.10. The total  
 2515 systematic uncertainty is calculated by adding each systematic error in quadrature.  
 2516 This table is consolidated into plots showing the systematic errors for each multiplicity  
 2517 bin and  $p_T$  bin, which are presented in Figure 4.29. As the systematic uncertainties  
 2518 associated with the generation of the dihadron  $\Delta\varphi$  distributions are only from the  
 2519 tracking efficiency presented in Table 4.6, they are not plotted in this section.

Table 4.10: The final systematic uncertainties (in percentages) from the  $h\text{-}\Lambda$   $\Delta\varphi$   
 distribution generation for each multiplicity and associated  $p_T$  bin.

Mult. and $p_T$ bin	Sig.	Sideband	PID	Topo. sel.	Mat. bud.	Total
0-20%, low $p_T$	0.36	0.53	0.64	3.2	1.1	3.3
20-50%, low $p_T$	0.35	0.67	0.65	3.2	1.1	3.4
50-80%, low $p_T$	0.76	1.1	1.4	3.2	1.1	3.8
0-20%, high $p_T$	0.42	0.42	0.76	3.0	0.6	3.2
20-50%, high $p_T$	0.4	0.71	1.2	3.0	0.6	3.3
50-80%, high $p_T$	1.1	1.6	2.0	3.0	0.6	4.1

2520 The total systematic error is observed to be mostly  $p_T$ -independent. However,  
 2521 there appears to be a slight correlation between the systematic uncertainty and multi-  
 2522 plicity, with the 0-20% bin exhibiting lower uncertainties than the 50-80% bin across  
 2523 both  $p_T$  ranges. This can become problematic when investigating the multiplicity  
 2524 dependence of observables extracted from the  $\Delta\varphi$  distributions, as the fraction of  
 2525 the systematic uncertainty which is directly correlated with multiplicity should not  
 2526 be considered when measuring multiplicity-dependent trends like slopes and percent

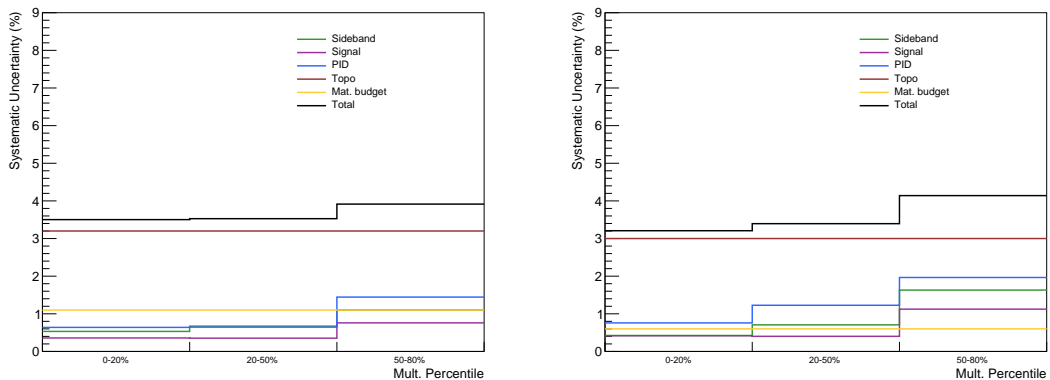


Figure 4.29: A visual depiction of the final systematic errors for the  $h\Lambda \Delta\varphi$  distributions for each multiplicity bin in the low (left) and high (right) associated  $p_T$  bins. The total systematic error is shown in black.

2527 changes. Because of this, the fraction of the systematic uncertainty which is uncor-  
2528 related with multiplicity is approximated using

$$\sigma_{\text{uncor},i}^2 = \sum_{\text{vars}} (R_{\text{var},i} - 1)^2, \quad (4.14)$$

2529 where

$$R_{\text{var},i} = \left( \frac{y_{\text{var},i}}{y_{\text{nom},i}} \right) / \left( \frac{y_{\text{var}}^{\text{MB}}}{y_{\text{nom}}^{\text{MB}}} \right), \quad (4.15)$$

2530 where “i” refers to the  $i$ th multiplicity bin, and “MB” refers to the min-bias (multiplicity-  
2531 integrated) results. The deviations of  $R_{\text{var},i}$  from unity quantify how the deviations  
2532 in multiplicity bin  $i$  differ from those in the MB sample.  $\sigma_{\text{uncor},i}$  is computed for each  
2533  $\Delta\varphi$  bin, then the RMS is taken across all  $\Delta\varphi$  bins to obtain the final multiplicity-  
2534 uncorrelated portion of the systematic errors. The results for each  $p_T$  bin are shown in  
2535 Figure 4.30. These systematic errors are only used when quantifying the multiplicity  
2536 dependence of an observable extracted from the  $\Delta\varphi$  distributions.

## 2537 4.6.2 Yield extraction

2538 One of the largest sources of systematic uncertainty of this analysis corresponds to  
2539 the different techniques that can be used to extract the yields in the near-side jet,  
2540 away-side jet, and underlying event from the  $\Delta\varphi$  distributions. As mentioned in

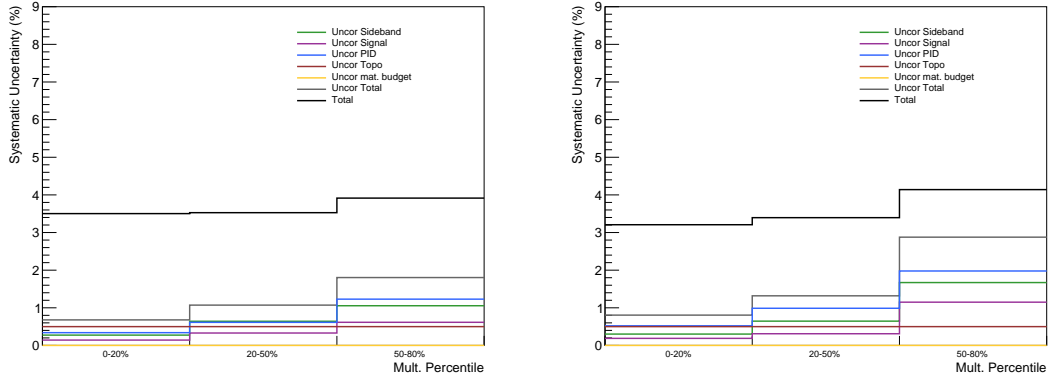


Figure 4.30: Visual depiction of the multiplicity-uncorrelated systematic errors for the  $h\Lambda \Delta\varphi$  distributions for each multiplicity bin in the low (left) and high (right) associated  $p_T$  bins, along with the total systematic error shown in black.

2541 Section 3.2.3.3, the equations for extracting these yields are

$$Y_{near} = \int_{-\pi/2}^{\pi/2} \left( \frac{dN}{d\Delta\varphi} - U(\Delta\varphi) \right) d\Delta\varphi, \quad Y_{away} = \int_{\pi/2}^{3\pi/2} \left( \frac{dN}{d\Delta\varphi} - U(\Delta\varphi) \right) d\Delta\varphi \quad (4.16)$$

$$Y_{UE} = \int_{-\pi/2}^{3\pi/2} U(\Delta\varphi) d\Delta\varphi, \quad (4.17)$$

2542 where  $\frac{dN}{d\Delta\varphi}$  is the  $\Delta\varphi$  distribution and  $U(\Delta\varphi)$  is the underlying event fit. As the  $\Delta\varphi$   
 2543 distribution is present in these equations, all of the previous variations concerning  
 2544 the generation of this distribution must be considered. However, these equations also  
 2545 naturally introduce two new categories of systematic uncertainty: those associated  
 2546 with the underlying event fit, and those associated with the integration of the  $\Delta\varphi$   
 2547 distribution. Both of these categories will be discussed in detail in the following  
 2548 sections.

#### 2549 4.6.2.1 Underlying event fit techniques

2550 As the underlying event term  $U(\Delta\varphi)$  is present in every yield extraction equation  
 2551 above, any changes in the underlying event fitting procedure will affect the final yield  
 2552 measurements. To maintain compatibility with previous analyses (specifically for  
 2553 the dihadron correlations), the nominal underlying event fit is a straight line to the  
 2554 average of the  $\Delta\varphi$  distribution in the ranges  $[-\frac{\pi}{2}, -\frac{\pi}{4}] \cup [\frac{\pi}{4}, \frac{5\pi}{8}] \cup [\frac{11\pi}{8}, \frac{3\pi}{2}]$ . These ranges  
 2555 were initially chosen as there is expected to be little-to-no contamination from the jet

2556 components in each range. However, to investigate the effect the UE fitting procedure  
2557 may have on the final yields, the following alternative methods were considered:

- 2558     1. Straight line fit in a more restricted range, specifically  $[-\frac{\pi}{2}, -\frac{3\pi}{8}) \cup [\frac{3\pi}{8}, \frac{5\pi}{8}) \cup$   
2559        $[\frac{11\pi}{8}, \frac{3\pi}{2})$
- 2560     2. Straight line fit using the Zero Yield At Minimum (ZYAM) technique, where  
2561       the underlying event line is set to the minimum of the  $\Delta\varphi$  distribution
- 2562     3. Sinusoidal fit which includes a non-zero  $v_2$  contribution

2563 The first two techniques are similar enough to the nominal technique that they will not  
2564 be explicitly shown in this section. Restricting the range of the flat fit region results  
2565 in deviations from the nominal procedure of around 2%, whereas the ZYAM tech-  
2566 nique gives much larger deviations at about 15%. Ultimately the ZYAM procedure  
2567 is not included in the final systematics calculation due to a physical incompatibility,  
2568 whereby the presence of  $v_2$  in the higher multiplicity  $\Delta\varphi$  distributions causes the  
2569 ZYAM procedure to massively underestimate the underlying event contribution.

2570 Including a non-zero  $v_2$  contribution is a much more involved procedure and re-  
2571 quires new machinery to be developed, so it will be described in detail in the next  
2572 section.

#### 2573 4.6.2.2 Including a non-zero $v_2$ contribution

2574 All of the “straight line” UE fitting techniques are based on the flatness assumption of  
2575 the non-jet part of the correlation in  $\Delta\varphi$ . This means that the dijet axis direction does  
2576 not affect the non-jet particle distribution’s overall shape within an event. However,  
2577 as mentioned in Section 1.5.2, previous Pb–Pb, p–Pb, and even pp collision studies  
2578 have shown that the QGP’s collective flow components ( $v_1$ ,  $v_2$ , etc.) influence the  
2579 phase-space distribution of particles within an event. Using Fourier decomposition,  
2580 the  $\Delta\varphi$  distributions on an event-by-event basis can be written as

$$\frac{dN}{d\Delta\varphi} = a_0 + \sum_{n=1}^{\infty} 2a_n \cos(n\Delta\varphi), \quad (4.18)$$

2581 where  $a_n$  are the Fourier coefficients. As mentioned in the introduction, these coeffi-  
2582 cients have been shown [80] to be related to the collective flow coefficients  $v_n$  via

$$v_n = \frac{a_n}{a_0}. \quad (4.19)$$

Table 4.11:  $v_2$  values used in this analysis for each associated  $p_T$  bin. The values were calculated as the weighted average of published  $p_T$ -differential  $v_2$  measurements with the published  $p_T$  spectra, taken across the entire associated  $p_T$  range.

$p_T^{\text{assoc.}}$	$v_2^{\text{trig.}}$	$v_2^{\text{assoc. h}}$	$v_2^{\text{assoc.}\Lambda}$
1.5 - 2.5	0.092	0.100	0.075
2.5 - 4.0	0.092	0.119	0.137

2583 This means that even without reconstructing the reaction plane within a specified  
 2584 event, the effects of collective flow are present in the  $\Delta\varphi$  distributions. This manifests  
 2585 in the correlation distributions as an underlying event which is not flat with respect  
 2586 to  $\Delta\varphi$ , but rather sinusoidal. While this is in direct conflict to the initial assumption  
 2587 of a flat underlying event, this nominal choice was made to maintain compatibility  
 2588 with previous measurements of dihadron yields using correlation techniques, which  
 2589 also assume a flat UE in  $\Delta\varphi$ .

2590 As the  $v_2$  or “elliptic flow” coefficient is the most dominant of the collective flow  
 2591 coefficients measured in p–Pb collisions [157] in the  $p_T$  ranges for this analysis, it  
 2592 is the only one considered. Furthermore, the  $v_2$  coefficients are exceedingly difficult  
 2593 to determine, with fully published papers solely dedicated to measuring the  $v_2$  for  
 2594 different particle species and collision systems. Luckily, these coefficients have been  
 2595 measured by ALICE in p–Pb collisions for both charged hadrons and  $\Lambda$  baryons across  
 2596 a wide range of  $p_T$  [158], [159]. As the  $p_T$  binning in this analysis is much wider, the  
 2597 weighted average

$$v_2^{\text{avg}} = \frac{\int_{p_{T,\min}}^{p_{T,\max}} v_2(p_T) \frac{dN}{dp_T} dp_T}{\int_{p_{T,\min}}^{p_{T,\max}} \frac{dN}{dp_T} dp_T}, \quad (4.20)$$

2598 is used, where  $p_{T,\min}$  and  $p_{T,\max}$  are the minimum and maximum values of  $p_T$  in the  
 2599 bins from this analysis (namely 1.5 – 2.5 and 2.5 – 4.0 GeV/c). The  $v_2(p_T)$  values  
 2600 for charged hadrons and  $\Lambda$  baryons are taken from [158], and  $dN/dp_T$  is taken from  
 2601 the published  $p_T$  spectra for charged hadrons and  $\Lambda$  baryons from [160], plots of  
 2602 which can be seen in Figures 4.31 ( $v_2$ ) and 4.32 ( $p_T$  spectra). The values of  $v_2^{\text{avg}}$  for  
 2603 each  $p_T$  bin are shown in Table 4.11. Note that the trigger  $v_2$  remains the same,  
 2604 as the trigger  $p_T$  range is fixed for this analysis. The  $\Lambda$   $v_2$  is markedly higher than  
 2605 the charged hadron  $v_2$ , which ultimately manifests itself as a larger deviation from  
 2606 the nominal UE fit when compared to the dihadron case. Unfortunately there are  
 2607 few multiplicity-dependent measurements of the  $v_2$  coefficients for identified particle

species. Because of this, the  $v_2$  values from Table 4.11 are used only in the 0-20% multiplicity bin, with the  $v_2$  values for the 20-50% and 50-80% multiplicity bins taken as 0.85 and 0.50 times the 0-20% value, respectively.

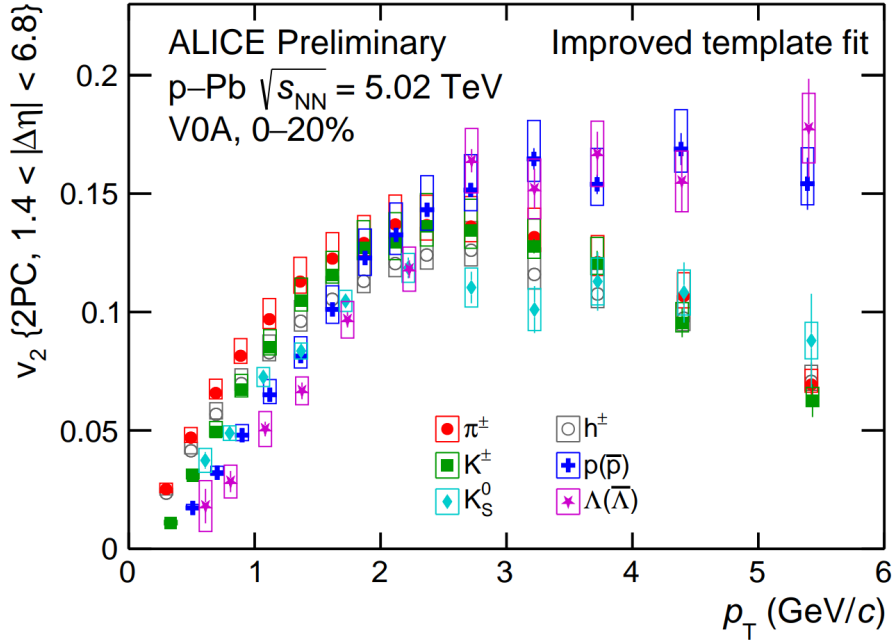


Figure 4.31: The  $v_2$  values for identified hadrons as a function of  $p_T$ , taken from [158].

Using these  $v_2$  values, the underlying event is estimated by fitting the function

$$U_{v_2}(\Delta\varphi) = A \times (1 + 2v_2^{\text{trig.}} v_2^{\text{assoc.}} \cos(2\Delta\varphi)) \quad (4.21)$$

in the ranges  $-\pi/2 < \Delta\varphi < -1$  and  $1 < \Delta\varphi < +\pi/2$ , where little jet contribution is expected. The underlying event **pedestal**  $A$  is allowed to vary during the fit, but the  $v_2$  values are fixed. Examples of h- $\Lambda$  and h-h  $\Delta\varphi$  distributions with the UE fit using this procedure are shown in Figure 4.33.

The validity of this procedure can be tested by examining the  $\Delta\varphi$  distributions at large  $\Delta\eta$ , where the near-side jet component is minimal, leaving just the UE at small  $\Delta\varphi$ <sup>2</sup>. In fact, this procedure is often used to determine the  $v_2$  coefficients in the first place. In this case, however, it will just be used to serve as a sanity check for both the fitting procedure and the fixed  $v_2$  coefficients from 4.11. If the UE fit

<sup>2</sup>At large  $\Delta\varphi$ , the away-side ridge is still present.

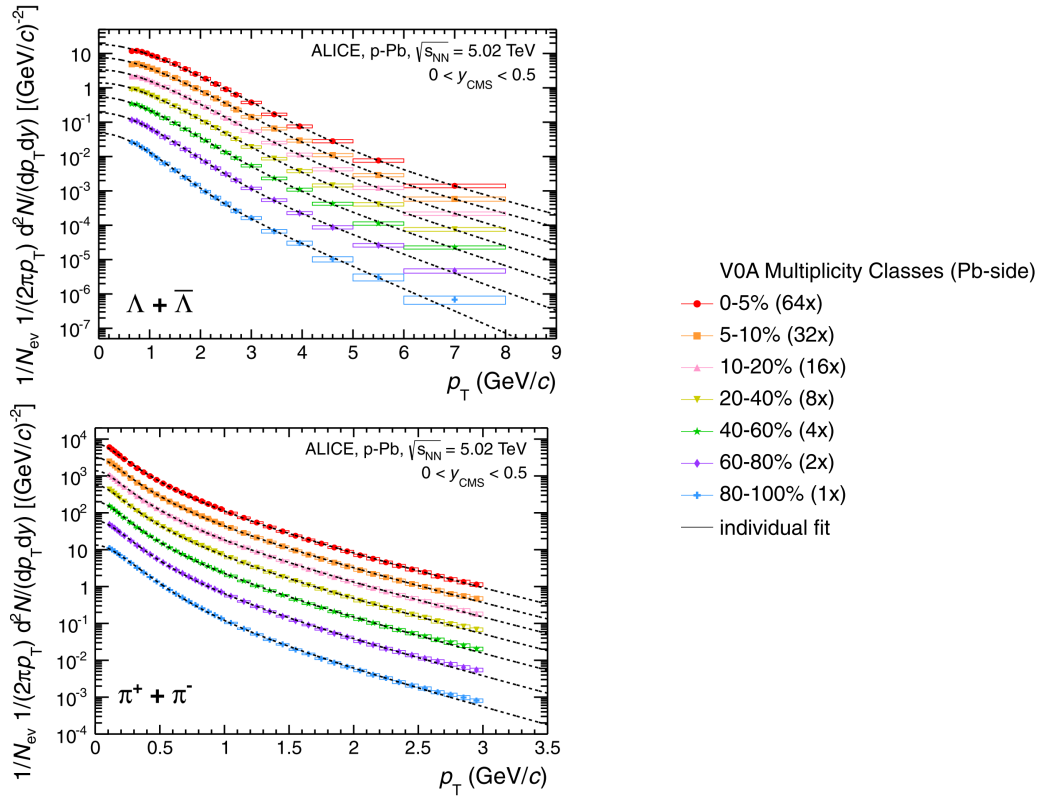


Figure 4.32: The published [155]  $p_T$  spectra for  $\Lambda$  baryons (top) and charged hadrons ( $\approx$  pions) (bottom), used to compute the weighted average of the  $v_2$  coefficients across the wide momentum bins used in this analysis.

2621 matches the near-side of the  $\Delta\varphi$  distribution at large  $\Delta\eta$ , then the  $v_2$  coefficients and  
 2622 fitting procedure are likely valid. Examples of the  $\Delta\varphi$  distributions with  $|\Delta\eta| > 1.4$   
 2623 and  $|\Delta\eta| < 1.2$  showing the  $v_2$ -based UE fit can be seen in Figure 4.34. These are  
 2624 generated in the highest multiplicity and momentum bins, where the effects of the  
 2625  $v_2$  contribution are maximal. Both the h- $\Lambda$  and h-h  $\Delta\varphi$  distributions show good  
 2626 agreement between the UE fit and the data at small  $\Delta\varphi$  and large  $\Delta\eta$ , where the  
 2627 near-side jet peak and away-side ridge are no longer present, pointing to the validity  
 2628 of the  $v_2$ -based UE fitting procedure.

2629 The effects of including  $v_2$  on the extracted h- $\Lambda$  and h-h yields in each region is not  
 2630 obvious at first glance. For the most central collisions, the inclusion of  $v_2$  results in  
 2631 nearly a 5% decrease for the jet-like yields when compared to the nominal technique.  
 2632 This can mostly be seen in Figure 4.33, where the peaks of the sinusoidal fit achieve  
 2633 their maxima within the near- and away-side components of the jet, causing the

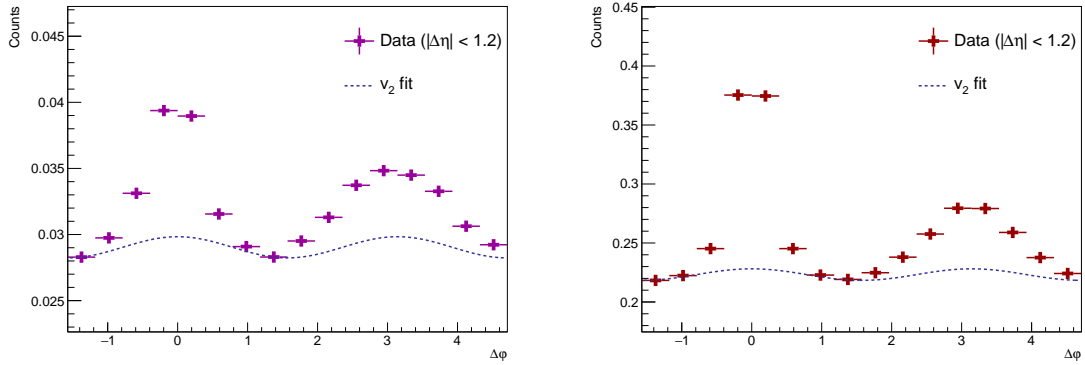


Figure 4.33: Examples of the underlying event fit using the  $v_2$ -based procedure for the h- $\Lambda$  (left) and h-h (right)  $\Delta\varphi$  distributions in the 0-20% multiplicity bin in the higher associated  $p_T$  bin.

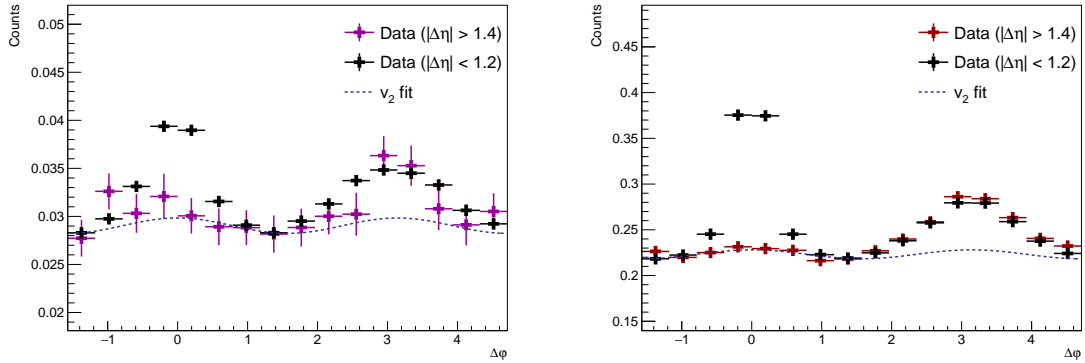


Figure 4.34: The h- $\Lambda$  (left) and h-h (right)  $\Delta\varphi$  distributions in the 0-20% multiplicity bin and higher  $p_T$  bin at small and large values of  $\Delta\eta$ , with the UE fit using the  $v_2$ -based procedure shown in blue. The fits are in good agreement with data in both cases.

2634 overall yields to be lower than those obtained by the flat UE assumption. However,  
 2635 at lower multiplicities (20-50%, 50-80%), the extracted h- $\Lambda$  and h-h jet-like yields  
 2636 actually exhibit a slight increase of around 5% in their extracted yields when compared  
 2637 to those measured using the nominal UE fit. This is due to the variation of the  
 2638 pedestal  $A$  in Equation 4.21 during the fit, which results in a smaller pedestal value  
 2639 than the nominal fit in these multiplicity ranges. The extracted underlying event  
 2640 yield never deviates by more than 3% from the yield obtained using the nominal

procedure for all multiplicity and momentum bins for both the h- $\Lambda$  and h-h cases.

#### 4.6.2.3 Integration procedures

The general yield-extraction equation

$$Y_{\Delta\varphi} = \int_{\Delta\varphi_1}^{\Delta\varphi_2} \left( \frac{dN}{d\Delta\varphi} - U(\Delta\varphi) \right) d\Delta\varphi \quad (4.22)$$

leaves some room for interpretation. Obviously the  $\Delta\varphi$  distributions shown thus far are in some way related to  $dN/d\Delta\varphi$ , but integrals prefer continuous integrands, which the  $\Delta\varphi$  distributions are clearly not as they have finitely many (16) bins. Furthermore, there is nothing explicitly preventing

$$\frac{dN}{d\Delta\varphi} < U(\Delta\varphi), \quad (4.23)$$

possibly resulting in a *negative* yield, which is clearly unphysical. There are a few ways to alleviate these issues, which are discussed in this section.

For all of the yield extraction procedures discussed thus far, the usage of the integration symbol in Equation 4.22 is *slightly* misleading: the yields are actually calculated by summing the bin contents of the  $\Delta\varphi$  distribution in the specified range, and subtracting off the value of  $U(\Delta\varphi)$  at the center of each bin. To be more explicit, the yields are calculated as

$$Y_{\Delta\varphi} = \sum_{i=L}^U \left( \frac{dN}{d\Delta\varphi_i} - U(\Delta\varphi_i) \right), \quad (4.24)$$

where  $L$  and  $U$  are the bin numbers of the Lower and Upper  $\Delta\varphi$  bins in the specified range,  $dN/d\Delta\varphi_i$  is the value of the correlation distribution in the  $i$ th  $\Delta\varphi$  bin, and  $U(\Delta\varphi)$  is the value of  $U$  in the center of the  $i$ th  $\Delta\varphi$  bin.

Equation 4.24 provides an easy way to deal with the negative yield issue: if the value of  $U(\Delta\varphi_i)$  is greater than the value of  $dN/d\Delta\varphi_i$  in a given bin, the yield in that bin is set to zero. While this is not done for the nominal yield extraction procedure in this analysis, it is a completely reasonable technique and is therefore explored in the systematic uncertainty analysis. Using the flat UE assumption with the UE average taken in the nominal range, the results are relatively unsurprising: the yields extracted using this procedure are strictly higher than those extracted using the main

procedure where negative contributions are allowed. However, the deviations never exceed more than 3.5%, with the average deviation being around 2% for both the h- $\Lambda$  and h-h cases.

Another way to address the lack of continuity in the  $\Delta\varphi$  distributions is to fit these distributions with continuous functions, then use the corresponding fit for the integration in Equation 4.22. This thesis considers two such functions, which are presented in the following two sections.

#### 4.6.2.4 The double Gaussian fit

There are a number of functions that may appear suitable to fit the  $\Delta\varphi$  distributions, but given the Gaussian-like appearance of the near- and away-side jet components, a double Gaussian fit is a natural choice. The double Gaussian fit function is given by

$$f(\Delta\varphi) = U + A_{\text{NS}} e^{\frac{(\Delta\varphi - \mu_{\text{NS}})^2}{2\sigma_{\text{NS}}^2}} + A_{\text{AS}} e^{\frac{(\Delta\varphi - \mu_{\text{AS}})^2}{2\sigma_{\text{AS}}^2}} + A_{\text{NS}}^{\text{mirror}} e^{\frac{(\Delta\varphi - \mu_{\text{NS}} + 2\pi)^2}{2\sigma_{\text{NS}}^2}} + A_{\text{AS}}^{\text{mirror}} e^{\frac{(\Delta\varphi - \mu_{\text{AS}} - 2\pi)^2}{2\sigma_{\text{AS}}^2}}, \quad (4.25)$$

where  $A$  and  $\mu$  are the amplitude and means of the Gaussian components, and the subscript “NS” (“AS”) refers to the near-side (away-side) jet component. The “mirror” terms are added to account for the  $2\pi$  periodicity of the  $\Delta\varphi$  distribution, and are required to obtain a convergent fit. The  $U$  term describes a flat underlying event, and is fixed to the average of the  $\Delta\varphi$  distribution in the regions  $[-\frac{\pi}{2}, -\frac{\pi}{4}) \cup [\frac{\pi}{4}, \frac{5\pi}{8}) \cup [\frac{11\pi}{8}, \frac{3\pi}{2}]$ , as is done for the nominal UE determination procedure. Furthermore, the mean in the near-side gaussian (and corresponding mirror term) is fixed to 0 ( $2\pi$ ) and the mean in the away-side guassian (and corresponding mirror term) is fixed to  $\pi$  ( $-\pi$ ), leaving only the amplitudes and widths to vary freely. The double Gaussian fits to both the h- $\Lambda$  and h-h correlation distributions for every multiplicity and momentum bin are shown in Figures 4.35 (h- $\Lambda$ ) and 4.36. The fits generally describe the data quite well, though an extreme amount of effort went in to ensuring the convergence of each fit due to an inordinate amount of instability.

The yields extracted using the double Gaussian fit are nearly identical to those extracted using the nominal bin-wise integration procedure, with deviations from the nominal procedure never exceeding 1% for either the h- $\Lambda$  or h-h cases. This indicates two things:

1. The fits describe the data quite well, and

2694     2. The differences between Equations 4.22 and 4.24 are mostly aesthetic, so long  
2695       as (1) holds and the choice of  $U(\Delta\varphi)$  is consistent.

2696 As the deviations are so small, this procedure ends up excluded from the final sys-  
2697 tematic uncertainty calculation after the Barlow check in Section 4.6.2.6, but the fits  
2698 are still used for the systematic studies involving the near- and away-side jet widths  
2699 discussed in Section 4.6.3.

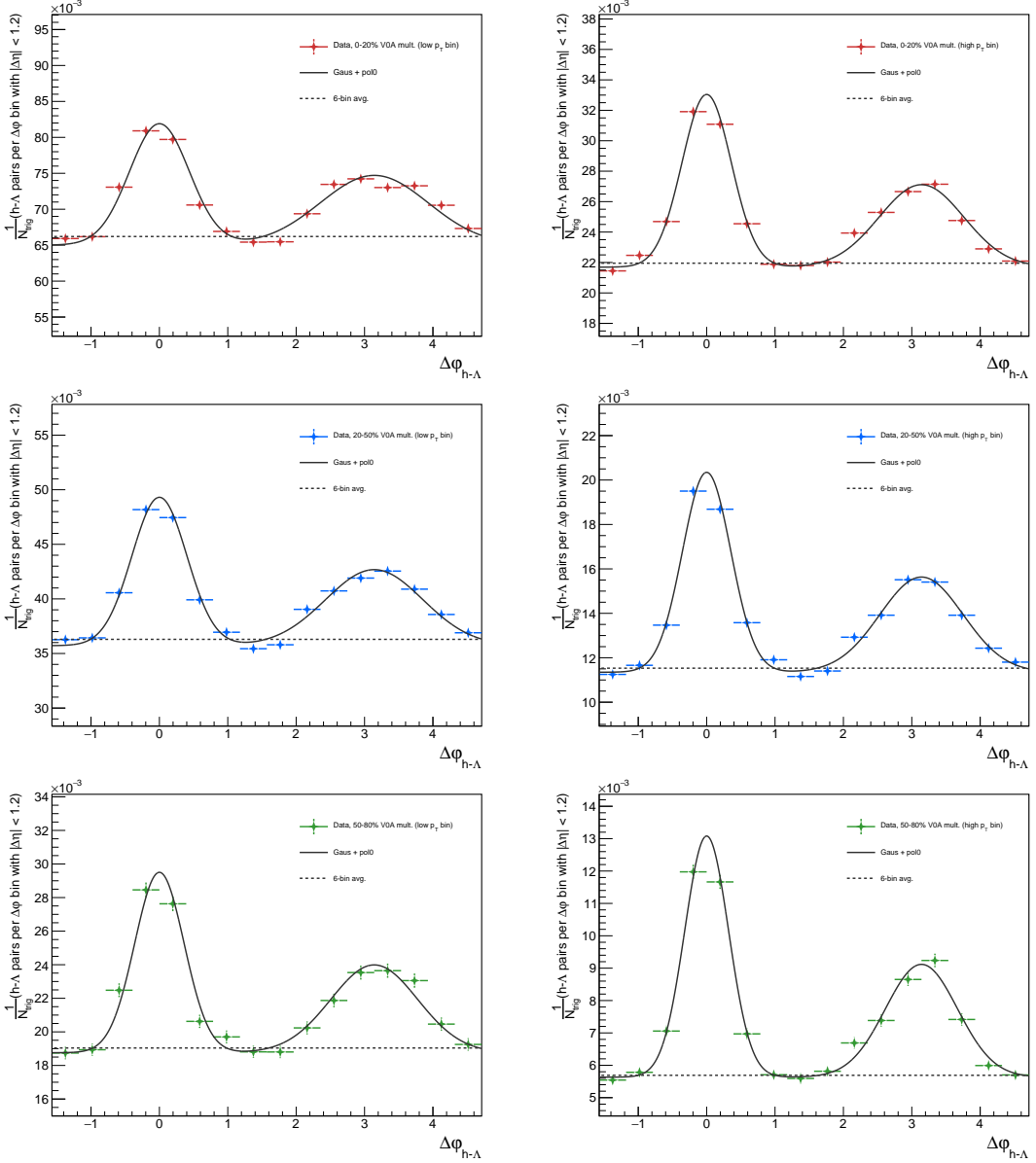


Figure 4.35: The final per-trigger h- $\Lambda$   $\Delta\varphi$  correlation distributions with the full double Gaussian fit for the 0-20% (top), 20-50% (middle), and 50-80% (bottom) multiplicity bins in the lower (left) and higher (right) associated  $p_T$  bins. The UE fit is also shown as a dashed line.

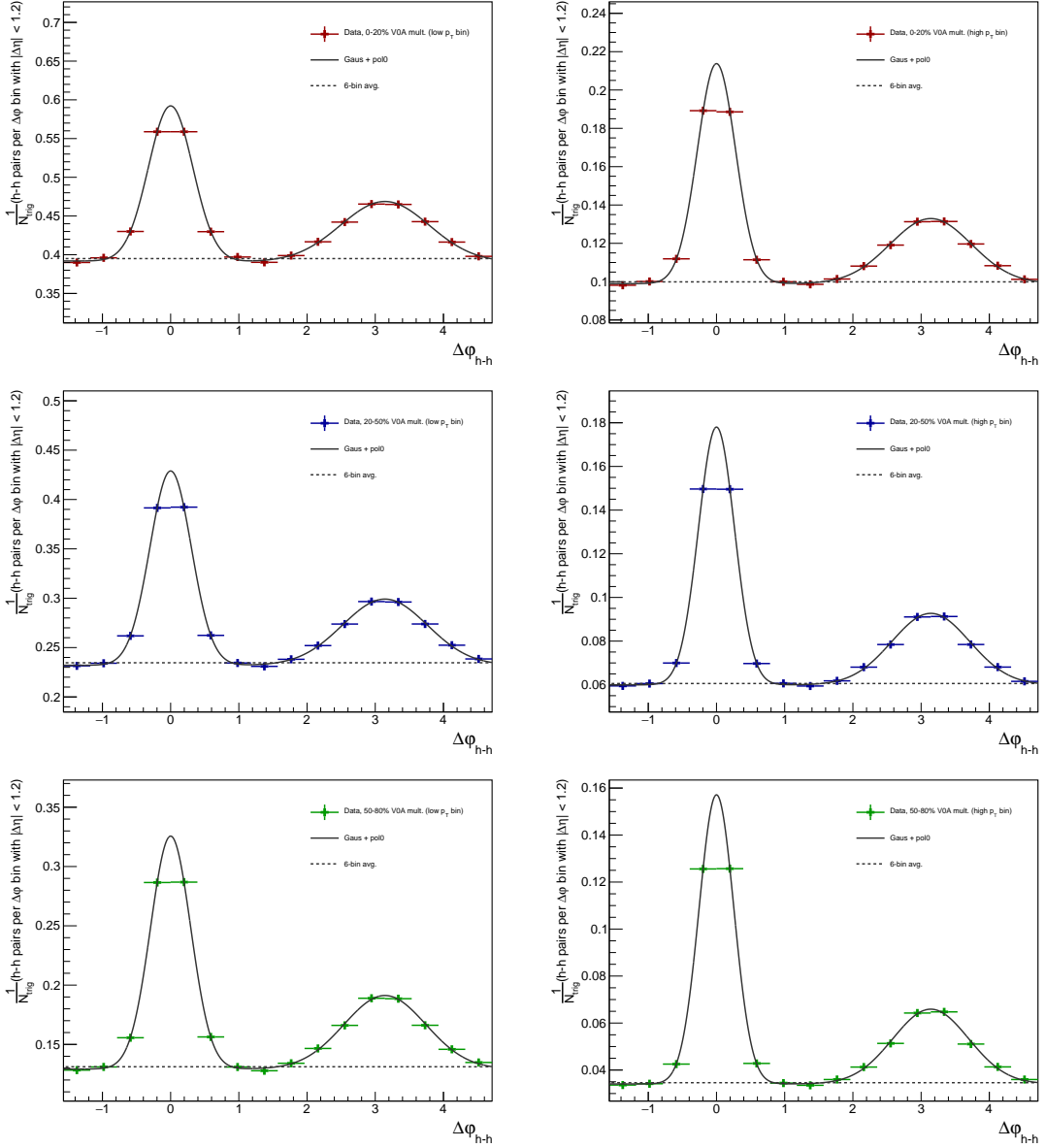


Figure 4.36: The final per-trigger h-h  $\Delta\phi$  correlation distributions with the full double Gaussian fit for the 0-20% (top), 20-50% (middle), and 50-80% (bottom) multiplicity bins in the lower (left) and higher (right) associated  $p_T$  bins. The UE fit is also shown as a dashed line.

2700 4.6.2.5 The von Mises fit

2701 While only briefly mentioned in Section 3.2.3.3 in the context of extracting the near-  
 2702 and away-side jet widths, the von Mises distribution is another natural choice for  
 2703 fitting the  $\Delta\varphi$  distributions due to its combined Gaussian-like behaviour while natu-  
 2704 rally exhibiting  $2\pi$ -periodicity (which was “forced” onto the double Gaussian fit via  
 2705 the mirror terms). As a reminder, the von Mises fit function is given by

$$f(\Delta\varphi) = U(\Delta\varphi) + \frac{A_{\text{NS}}}{2\pi I_0(k_{\text{NS}})} e^{k_{\text{NS}} \cos(\Delta\varphi - \mu_{\text{NS}})} + \frac{A_{\text{AS}}}{2\pi I_0(k_{\text{AS}})} e^{k_{\text{AS}} \cos(\Delta\varphi - \mu_{\text{AS}})}, \quad (4.26)$$

2706 where  $A$  and  $\mu$  are as they were in Equation 4.25, and  $k$  is a measure of the collimation  
 2707 of the distribution, which is inversely related to the width through

$$\sigma = \sqrt{-2 \ln \frac{I_1(\kappa)}{I_0(\kappa)}}. \quad (4.27)$$

2708 In these equations,  $I_n$  refers to the modified Bessel function of the  $n$ th kind. Note  
 2709 that the  $U(\Delta\varphi)$  has been given explicit  $\Delta\varphi$  dependence, as this fit function does not  
 2710 require the UE component to be flat with respect to  $\Delta\varphi$  in order to converge nicely.

2711 During the fitting procedure, the means  $\mu_{\text{NS}}$  and  $\mu_{\text{AS}}$  are again fixed to 0 and  $\pi$ ,  
 2712 respectively, and the  $U(\Delta\varphi)$  term is fixed to the function obtained by fitting the UE  
 2713 which includes a non-zero  $v_2$  contribution, as described in Section 4.6.2.2. While the  
 2714 fitting of this function is much more stable than the aforementioned double Gaussian  
 2715 function—possibly allowing for the variation of  $U$  during the fit—the term is ultimately  
 2716 fixed due to an interesting feature of the von Mises distribution, which is discussed  
 2717 in 4.6.3. The von Mises fits to both the h- $\Lambda$  and h-h correlation distributions for every  
 2718 multiplicity and momentum bin are shown in Figures 4.37 (h- $\Lambda$ ) and 4.38. Again,  
 2719 the fits describe the data very well. Furthermore, the fits are extremely stable, which  
 2720 is a welcome change from the double Gaussian fits and was the initial motivation for  
 2721 the width analysis presented in this thesis.

2722 Given these fits are taken with a different choice of  $U(\Delta\varphi, \Delta\eta)$ , the extracted  
 2723 yields from the von Mises function deviate from the nominal extraction procedure by  
 2724 a relatively large amount, with both the h- $\Lambda$  and h-h jet-like yields seeing a decrease  
 2725 of around 5%. This percentage is familiarly the same as the percent deviation seen in  
 2726 Section 4.6.2.2 from the h- $\Lambda$  and h-h yields when using the  $v_2$ -based UE fit while still  
 2727 using bin-wise summation to extract the yields. In fact, all of the yields extracted

2728 using the von Mises fitting procedure are nearly identical to the yields extracted using  
2729 the  $v_2$ -based UE fit with bin-wise summation, again indicating that the data are well  
2730 described by the fits. As these two procedures are nearly identical in their results,  
2731 the von Mises fitting procedure is also excluded from the final systematic uncertainty  
2732 calculation for the yield extraction after the Barlow check in Section 4.6.2.6. However,  
2733 the fits are so incredibly well-behaved that they spawned the initial investigation into  
2734 the near- and away-side jet widths, which eventually became a major topic of interest  
2735 in this thesis<sup>3</sup>.

2736 **4.6.2.6 Barlow check for yield extraction**

2737 Following the same procedure as outlined in Section 4.6.1.4, a Barlow check is per-  
2738 formed for the different techniques for extracting the per-trigger yields from Equa-  
2739 tions 4.16 and 4.17. If the majority of the measured h- $\Lambda$  yields for a given variation  
2740 have  $|N\sigma_{RB}| < 1$ , that variation is excluded from the systematic uncertainty calcula-  
2741 tion. This majority is calculated across all kinematic regions (near-side jet, away-side  
2742 jet, underlying event), multiplicity bins, and associated momentum bins. While the  
2743 h-h yields were initially considered for this check, their statistical errors are so small  
2744 that the denominator in Equation 4.13 is close to zero, resulting in erratic  $N\sigma_{RB}$  val-  
2745 ues. Thus any technique which gets excluded for the h- $\Lambda$  yields will also be excluded  
2746 for the h-h yields. Examples of the Barlow check for the yield extraction are shown  
2747 in Figure 4.39.

2748 As a result of the Barlow check, the following variations are excluded from the  
2749 systematic uncertainty calculation:

- 2750     • The double Gaussian fit procedure  
2751     • The von Mises fit procedure

2752 These exclusions were foreshadowed in the previous sections, as the fits describe  
2753 the data well enough that there are no statistically significant differences between  
2754 the yields extracted using these fit functions and the yields extracted using bin-wise  
2755 summation.

---

<sup>3</sup>Systematic uncertainty calculations involving misbehaving fits are a nightmare.

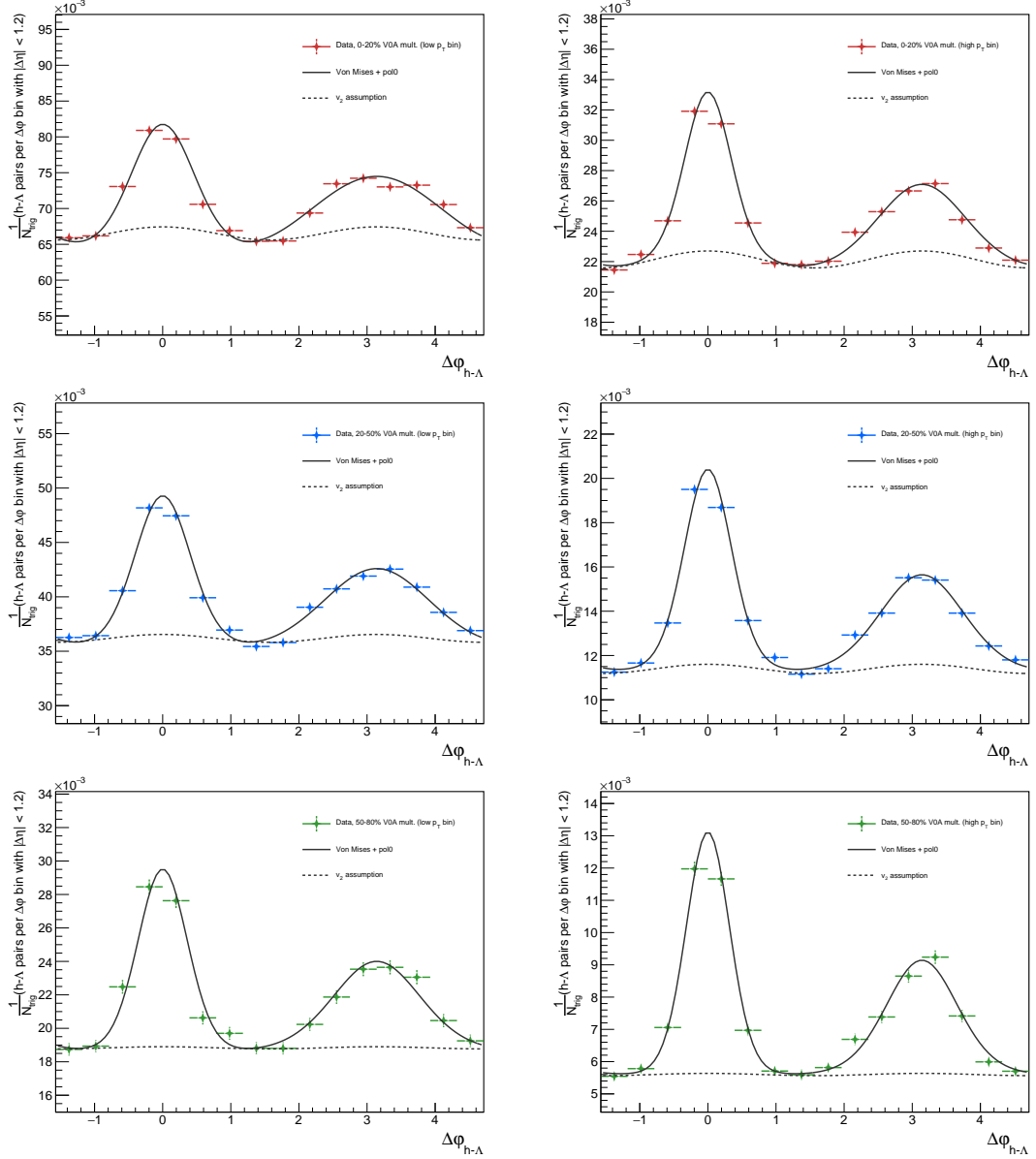


Figure 4.37: The final per-trigger h- $\Lambda$   $\Delta\phi$  correlation distributions with the von Mises fit for the 0-20% (top), 20-50% (middle), and 50-80% (bottom) multiplicity bins in the lower (left) and higher (right) associated  $p_T$  bins. The UE fit with  $v_2$  contribution is also shown as a dashed line.

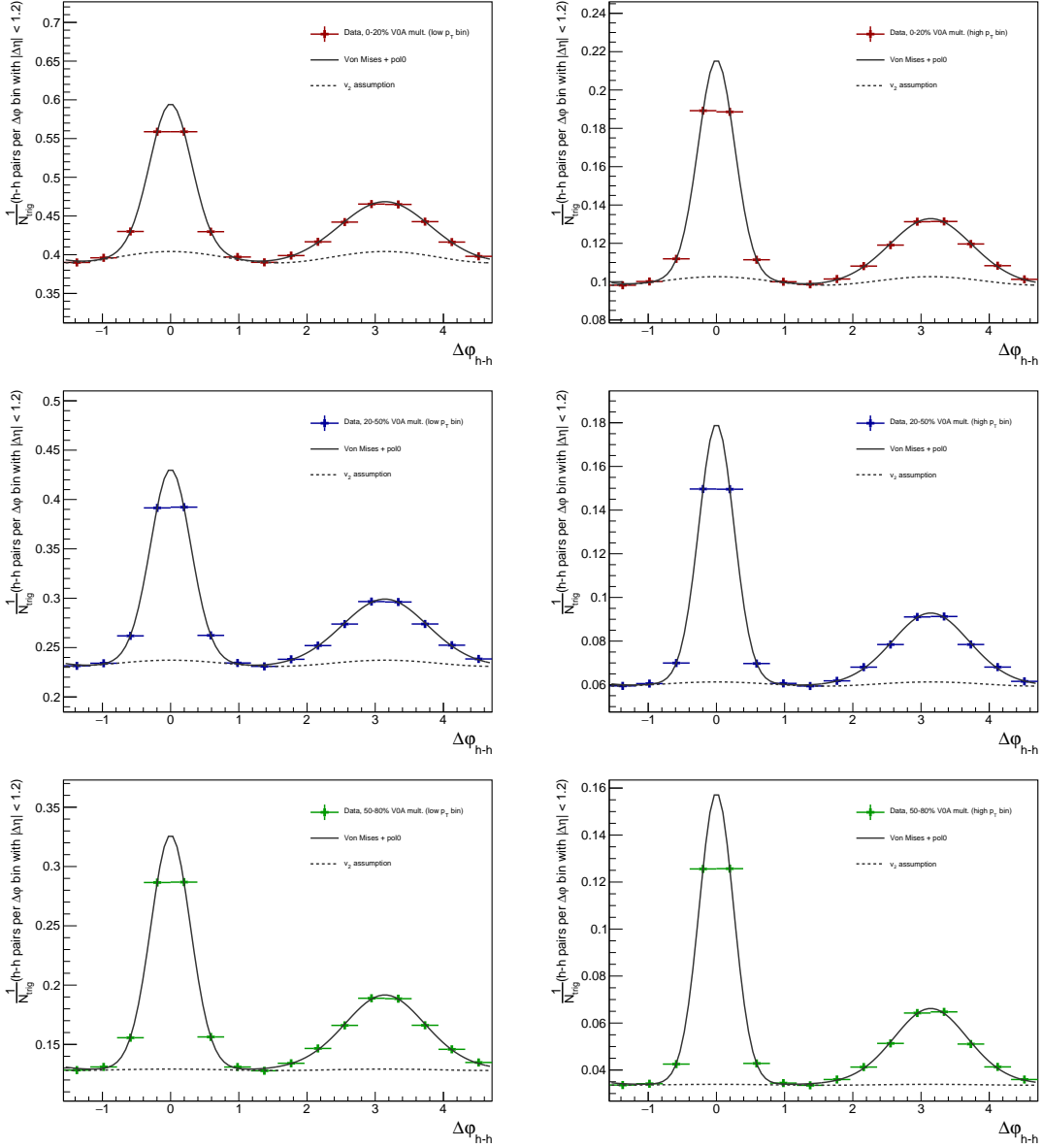


Figure 4.38: The final per-trigger h-h  $\Delta\phi$  correlation distributions with the von Mises fit for the 0-20% (top), 20-50% (middle), and 50-80% (bottom) multiplicity bins in the lower (left) and higher (right) associated  $p_T$  bins. The UE fit with  $v_2$  contribution is also shown as a dashed line.

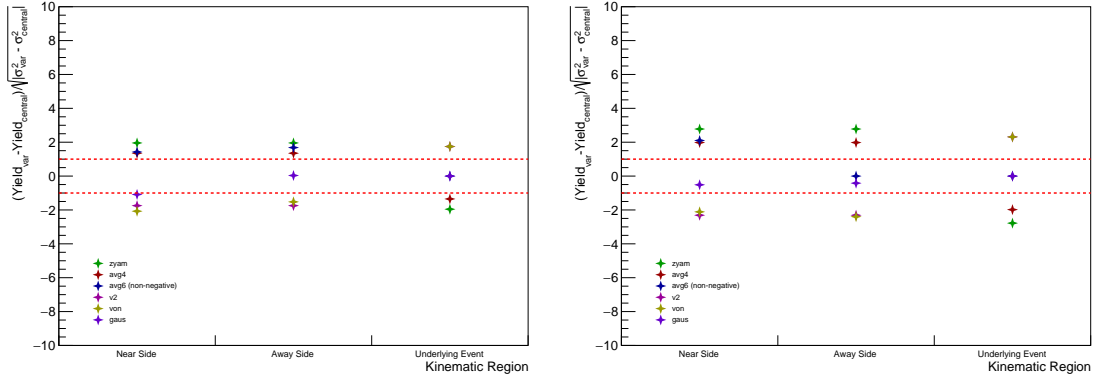


Figure 4.39: The Barlow check for the yield extraction procedure in the 0-20% multiplicity bin for the lower (left) and higher (right) associated  $p_T$  bins. The red lines represent  $N_{\sigma_{RB}} = \pm 1$ , and if the majority of the points from a given procedure fall within these lines (across all multiplicity and momentum bins), the procedure is excluded from the systematic uncertainty calculation.

#### 2756 4.6.2.7 Yield extraction systematics, summarized

2757 As most of the main results of this thesis involve the h- $\Lambda$  and h-h per-trigger yields  
 2758 in the various kinematic regions, the systematic uncertainties associated with the ex-  
 2759 traction of these yields deserve to be consolidated to concise tables and plots from the  
 2760 overly detailed descriptions of the previous sections. To that end, plots demonstrat-  
 2761 ing the resulting yield deviations from the nominal technique for each of the afore-  
 2762 mentioned yield extraction procedure variations (post Barlow check) can be seen in  
 2763 Figures 4.40 (h- $\Lambda$ ) and 4.41 (h-h). Furthermore, tables containing the final systematic  
 2764 uncertainties for both the h- $\Lambda$  and h-h per-trigger yields in each kinematic region for  
 2765 every multiplicity and associated  $p_T$  bin can be seen in Tables 4.12 (h- $\Lambda$ ) and 4.13  
 2766 (h-h). Note that included in these systematic uncertainties are both the technique  
 2767 variations associated with the yield extraction procedure, as well as the variations in  
 2768 the yields due to the variations in the  $\Delta\varphi$  distributions themselves (after the Barlow  
 2769 check), as discussed in Section 4.6.1. The UE yield systematic uncertainties are gen-  
 2770 erally much lower than the jet-like yields, averaging around 3.5% for both the h- $\Lambda$   
 2771 and h-h cases. The larger uncertainties for the jet-like yields (4-7%) are primarily due  
 2772 to the fact that the jet-like yield extraction techniques rely both on the integration  
 2773 procedure and the choice of  $U(\Delta\varphi)$ , where both including  $v_2$  and excluding negative

yield contributions can have a large effect on these extracted yields. Both of those choices have little effect (or no effect in the case of the non-negative yield requirement) on the integral of the  $U(\Delta\varphi)$  across the entire azimuthal range (i.e. the UE yield).

As was the case in Section 4.6.1.5, the portion of systematic uncertainty which is uncorrelated with multiplicity is computed using Equations 4.14 and 4.15 and presented in Tables 4.14 (h- $\Lambda$ ) and 4.15. Whenever the trends of these yields with respect to multiplicity are measured (either by taking slopes or looking at percent differences), the errors are always calculated using these multiplicity-uncorrelated systematic uncertainties.

Table 4.12: Final systematic errors (in %) for the per-trigger h- $\Lambda$  yields in each kinematic region, multiplicity, and momentum bin.

Mult. and $p_T$ bin	Near-side (jet)	Away-side (jet)	UE
0-20%, low	5.50e+00	5.57e+00	3.12e+00
20-50%, low	4.94e+00	5.24e+00	3.22e+00
50-80%, low	6.34e+00	7.19e+00	3.68e+00
0-20%, high	5.47e+00	6.10e+00	3.15e+00
20-50%, high	5.88e+00	6.54e+00	3.33e+00
50-80%, high	4.75e+00	5.25e+00	3.72e+00

Table 4.13: Final systematic errors (in %) for the h-h per-trigger yields in each kinematic region, multiplicity, and momentum bin.

Mult. and $p_T$ bin	Near-side (jet)	Away-side (jet)	UE
0-20%, low	4.46e+00	4.75e+00	3.51e+00
20-50%, low	3.75e+00	3.63e+00	3.50e+00
50-80%, low	4.94e+00	6.35e+00	3.67e+00
0-20%, high	3.80e+00	4.00e+00	3.51e+00
20-50%, high	3.61e+00	3.63e+00	3.51e+00
50-80%, high	4.17e+00	5.16e+00	3.81e+00

Table 4.14: Final multiplicity-uncorrelated systematic errors (in %) for the per-trigger h- $\Lambda$  yields in each kinematic region, multiplicity, and momentum bin, used for calculating errors associated with quantities describing trends versus multiplicity (slopes and percent changes).

Mult. and $p_T$ bin	Near-side (jet)	Away-side (jet)	UE
0-20%, low	2.73e+00	2.83e+00	6.66e-01
20-50%, low	3.09e+00	3.57e+00	1.00e+00
50-80%, low	5.80e+00	6.95e+00	2.23e+00
0-20%, high	2.91e+00	3.65e+00	7.40e-01
20-50%, high	4.32e+00	5.41e+00	1.28e+00
50-80%, high	4.47e+00	5.45e+00	2.35e+00

Table 4.15: Final multiplicity-uncorrelated systematic errors (in %) for the h-h per-trigger yields in each kinematic region, multiplicity and momentum bin, used for calculated errors associated with quantities describing trends versus multiplicity (slopes and percent changes).

Mult. and $p_T$ bin	Near-side (jet)	Away-side (jet)	UE
0-20%, low	1.72e+00	2.31e+00	1.86e-01
20-50%, low	1.31e+00	1.92e+00	2.29e-01
50-80%, low	3.95e+00	6.23e+00	1.21e+00
0-20%, high	1.03e+00	1.68e+00	2.42e-01
20-50%, high	7.24e-01	1.22e+00	2.76e-01
50-80%, high	2.28e+00	4.08e+00	1.54e+00

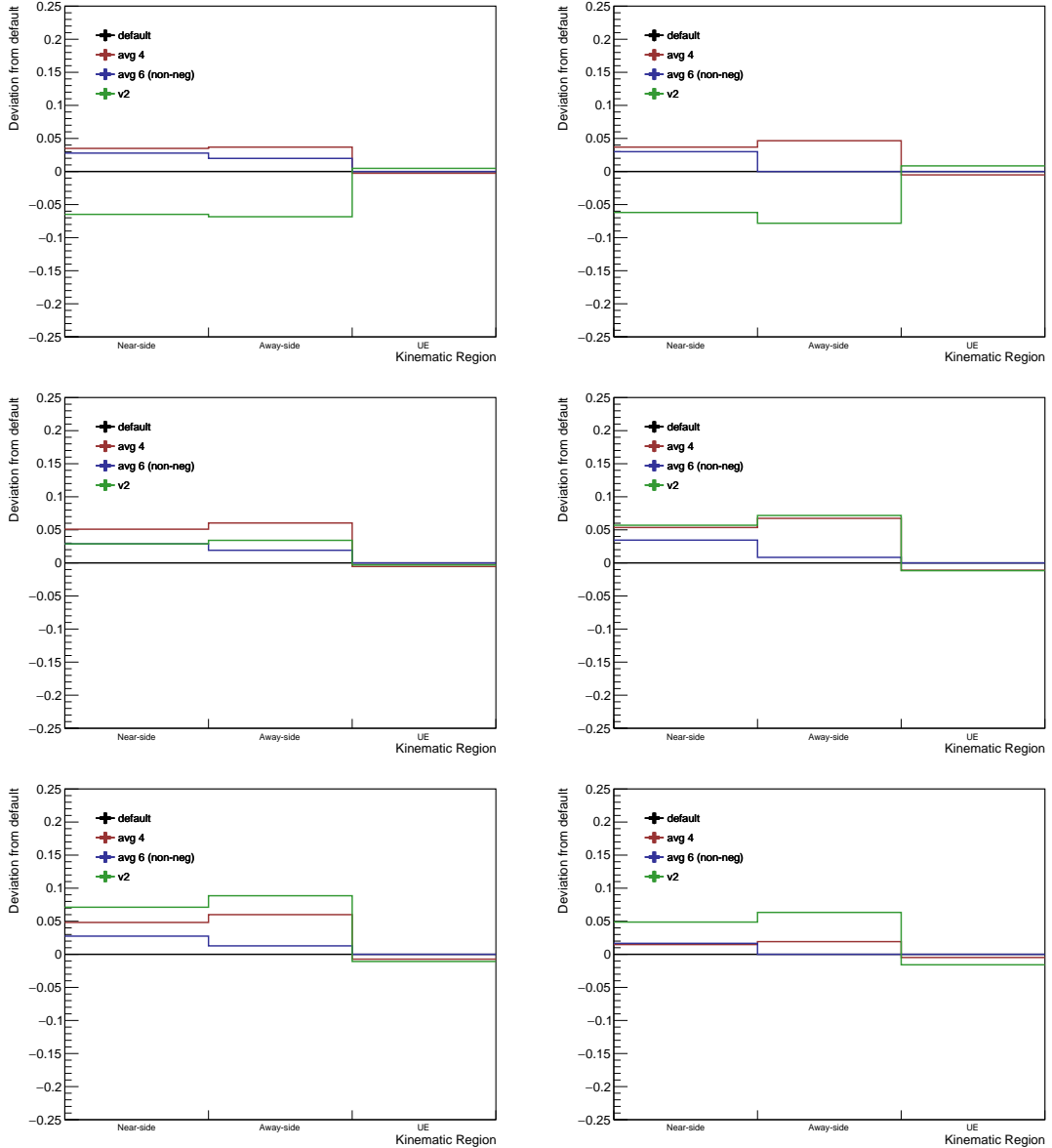


Figure 4.40: The deviation from the nominal  $h\text{-}\Lambda$  per-trigger yields for each yield extraction procedure variation (post Barlow check) in each kinematic region for the 0-20% (top), 20-50% (middle), and 50-80% (bottom) multiplicity bins in the lower (left) and higher (right) associated  $p_T$  bins. The systematic uncertainty for the yield extraction procedure is calculated by taking the RMS of these deviations for each kinematic region.

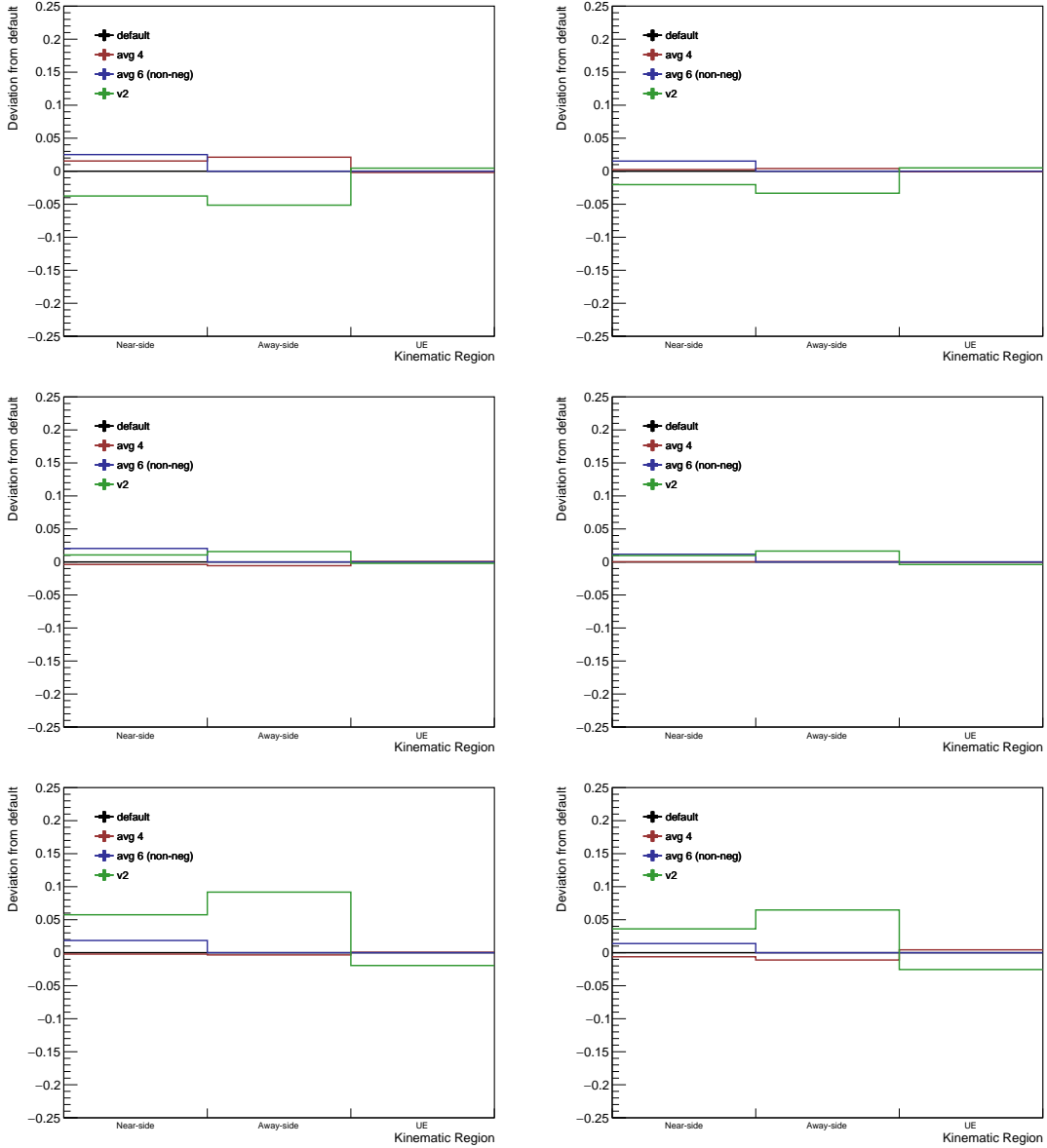


Figure 4.41: The deviation from the nominal h-h per-trigger yields for each yield extraction procedure variation (post Barlow check) in each kinematic region for the 0-20% (top), 20-50% (middle), and 50-80% (bottom) multiplicity bins in the lower (left) and higher (right) associated  $p_T$  bins. The systematic uncertainty for the yield extraction procedure is calculated by taking the RMS of these deviations for each kinematic region.

2784 **4.6.3 Near- and away-side width extraction**

2785 The extracted widths of the near- and away-side jet components from the  $\Delta\varphi$  dis-  
 2786 tributions are also subject to a fair amount of systematic uncertainty, both from the  
 2787 variations of the  $\Delta\varphi$  distributions themselves as well as the techniques used to ex-  
 2788 tract said widths. None of the  $\Delta\varphi$  distributions variations are “new”, in that they  
 2789 have been discussed in some way within the previous sections. However, the effects  
 2790 of these variations on the extracted widths are not as straightforward as the effects  
 2791 on the yields, and thus deserve their own section. Furthermore, the fitting techniques  
 2792 used to extract the widths are different enough than the fitting techniques for yield  
 2793 extraction (Sections 4.6.2.4 and 4.6.2.5) that they should be discussed separately.

2794 As a brief reminder, the nominal procedure for extracting the jet widths is by  
 2795 fitting the  $\Delta\varphi$  distribution to the von Mises-based fit function,

$$f(\Delta\varphi) = U(\Delta\varphi) + \frac{A_{\text{NS}}}{2\pi I_0(k_{\text{NS}})} e^{k_{\text{NS}} \cos(\Delta\varphi - \mu_{\text{NS}})} + \frac{A_{\text{AS}}}{2\pi I_0(k_{\text{AS}})} e^{k_{\text{AS}} \cos(\Delta\varphi - \mu_{\text{AS}})}, \quad (4.28)$$

2796 where  $A$  and  $\mu$  are the amplitudes and means of the von Mises components, and  $k$   
 2797 is a measure of the collimation of the distribution, which is inversely related to the  
 2798 width through

$$\sigma = \sqrt{-2 \ln \frac{I_1(\kappa)}{I_0(\kappa)}}. \quad (4.29)$$

2799 In these equations,  $I_n$  refers to the modified Bessel function of the nth kind. During  
 2800 the fitting procedure, the means  $\mu_{\text{NS}}$  and  $\mu_{\text{AS}}$  are again fixed to 0 and  $\pi$ , respectively,  
 2801 and the  $U(\Delta\varphi)$  term is fixed to the function obtained by fitting the UE which includes  
 2802 a non-zero  $v_2$  contribution, as described in Section 4.6.2.2.

2803 The reason for fixing the  $U$  component during fitting is subtle, as the von Mises  
 2804 distributions describe the data extremely well and generally allow for the variation of  
 2805 this component while still obtaining a convergent fit. However, the form of the Von  
 2806 Mises function,

$$f(x) = e^{k \cos(x)}, \quad (4.30)$$

2807 presents a unique issue: if the width is sufficiently large, meaning  $k$  is sufficiently  
 2808 small ( $\approx 1$ ), there is an “offset” from the  $U$  term that never tapers off. This is  
 2809 fundamentally different than a Gaussian, which will always converge to zero (or  $U$   
 2810 in this case) at large enough  $x$ . A visual depiction of this effect can be seen in  
 2811 Figure 4.42. In most cases, this never presents an issue as the widths are usually

such that  $k > 2$ . However, in the lowest momentum bin for the more central  $h\text{-}\Lambda \Delta\varphi$  distributions, allowing the  $U$  term to vary during the fitting procedure has a very large effect on the corresponding  $k$  value, as the fitting software tries to “absorb” this offset into  $U$ . Because of this, the  $U$  term is fixed during all fitting procedures, and instead the techniques for determining  $U$  are varied.

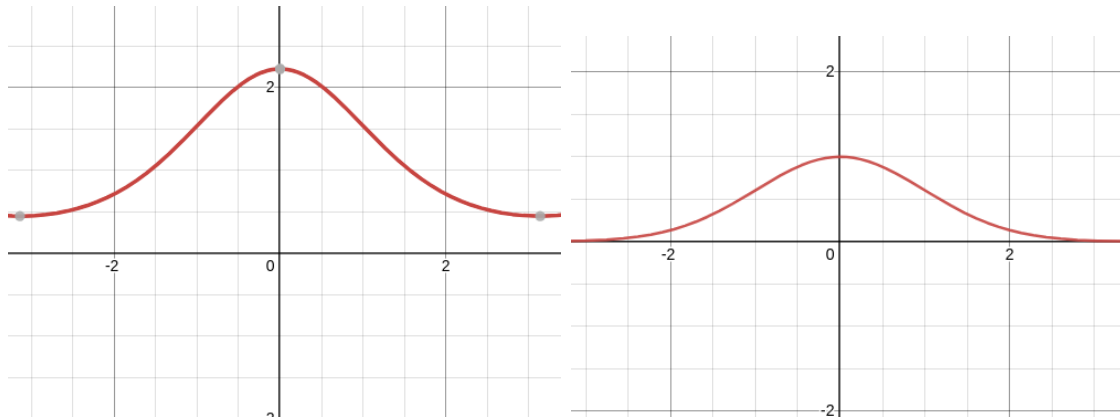


Figure 4.42: The Von Mises (left) and Gaussian (right) dist with  $\kappa = 1$  and  $\sigma = 1$ . Note that the von Mises distribution does not approach zero at large  $x$ , while the Gaussian does.

#### 4.6.3.1 Signal, sideband, and PID cut variations

Each of the signal, sideband, and PID cut variations that affect the  $\Delta\varphi$  distributions (from Section 4.6.1) can also affect the corresponding extracted widths. To that end, the  $h\text{-}\Lambda \Delta\varphi$  von Mises-based fits and extracted widths for each of these variations for all multiplicity and momentum bins can be seen in Figure 4.44. Note that these widths were extracted using the nominal procedure described at the beginning of this section. Deviations from the nominal near-side widths never exceed 3.5% in most cases, whereas the away-side width deviations are much larger, with some variations resulting in over a 10% change from the nominal value, even after removing statistically insignificant variations via the Barlow procedure in Section 4.6.3.3.

Again, problematic behavior arises from the PID cut variation which requires a TOF hit for both of the  $\Lambda$  daughters, with both the near- and away-side widths being particularly sensitive to this cut. As the lower momentum daughter pions are usually deflected by the detector’s magnetic field before reaching the TOF, in cases when the

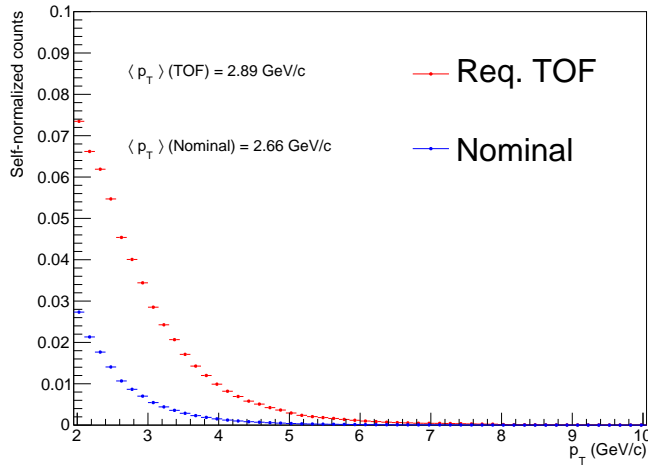


Figure 4.43: The  $p_T$  distributions of  $\Lambda$  candidates with and without the TOF signal requirement. The mean  $p_T$  of the  $\Lambda$  candidates with daughters that generate a TOF signal is nearly 10% higher than those without this requirement, which indicates that requiring a TOF signal for the  $\Lambda$  daughters introduces a physical bias.

2831 pion actually generates a TOF signal, its corresponding momentum is likely higher  
 2832 than usual. This would result in a higher-than-usual  $\Lambda$  momentum, which in turn  
 2833 would give lower-than-usual jet widths in the corresponding h- $\Lambda$  correlations as jets  
 2834 become less collimated as their constituent momentum decreases. To test this, the  
 2835  $p_T$  distributions of  $\Lambda$  candidates with and without the TOF signal are compared in  
 2836 Figure 4.43. The mean  $p_T$  of the  $\Lambda$  candidates with daughters that generate a TOF  
 2837 signal is around 10% higher than those without this requirement, which indicates that  
 2838 the TOF signal requirement introduces a physical bias into the h- $\Lambda$   $\Delta\varphi$  distributions,  
 2839 manifesting as unusually low jet widths. Luckily, this requirement also happens to  
 2840 reduce the overall yield of  $\Lambda$  candidates by a huge margin, causing a large amount  
 2841 of statistical fluctuations in the corresponding h- $\Lambda$  correlation distributions. Because  
 2842 of this, the TOF signal requirement ends up being excluded after the Barlow check.  
 2843 However, it is important to distinguish between excluding variations because they  
 2844 are statistically insignificant and excluding them because they introduce *physical*  
 2845 biases into the data. Had the data sample been larger, the TOF signal requirement  
 2846 would have likely survived the Barlow check, leaving no choice but to rely on the  
 2847 aforementioned argument.

## 2848 4.6.3.2 Fitting procedure variations

2849 Both of the fitting functions discussed in this thesis are of the form

$$f(\Delta\varphi) = U(\Delta\varphi) + f_{\text{NS}}(\Delta\varphi) + f_{\text{AS}}(\Delta\varphi), \quad (4.31)$$

2850 where  $U$  is the underlying event function, and  $f_{\text{NS}}$  ( $f_{\text{AS}}$ ) is the distribution that  
 2851 describes the near-side (away-side) jet. To estimate the systematic uncertainty asso-  
 2852 ciated with the fitting procedure, the following variations are considered:

2853 1. **Varying  $U(\Delta\varphi)$ :** The  $U(\Delta\varphi)$  term is varied by replacing the nominal  $v_2$ -based  
 2854 UE function with a flat line equal to the average of the  $\Delta\varphi$  distribution in the  
 2855 ranges  $[-\frac{\pi}{2}, -\frac{\pi}{4}] \cup [\frac{\pi}{4}, \frac{5\pi}{8}] \cup [\frac{11\pi}{8}, \frac{3\pi}{2}]$  and  $[-\frac{\pi}{2}, -\frac{3\pi}{8}] \cup [\frac{3\pi}{8}, \frac{5\pi}{8}] \cup [\frac{11\pi}{8}, \frac{3\pi}{2}]$  (i.e. the  
 2856 nominal and restricted-range UE variations from the yield extraction procedure)

2857 2. **Varying the  $f_{\text{NS}}$  and  $f_{\text{AS}}$  functions:** The  $f_{\text{NS}}$  and  $f_{\text{AS}}$  functions are varied  
 2858 by replacing the nominal von Mises distributions with the Gaussian ones, as  
 2859 described in Section 4.6.2.4, and the  $U$  term is fixed to the average of the  $\Delta\varphi$   
 2860 distribution in the ranges  $[-\frac{\pi}{2}, -\frac{\pi}{4}] \cup [\frac{\pi}{4}, \frac{5\pi}{8}] \cup [\frac{11\pi}{8}, \frac{3\pi}{2}]$  (again, the nominal UE  
 2861 determination technique from the yield extraction procedure)

2862 More variations were initially considered—namely using the  $v_2$ -based UE with the  
 2863 Gaussian functions from Equation 4.25 and trying generalized Gaussians [161] to  
 2864 describe the jet components—but they were discarded as many of the fits did not  
 2865 converge for all multiplicity and momentum ranges<sup>4</sup> despite a large amount of effort.

2866 The choice of making the  $v_2$ -based UE determination procedure the nominal one  
 2867 was not made lightly, as it breaks the symmetry with the nominal yield extraction  
 2868 technique. In the presence of non-zero elliptic flow (as is likely the case at higher  
 2869 multiplicities), the  $v_2$ -based UE determination procedure is the most physically mo-  
 2870 tivated, as it is the only one that takes into account the underlying event’s azimuthal  
 2871 anisotropy. The only reason this procedure was not chosen as the nominal technique  
 2872 for yield extraction is extremely specific to this analysis: at the time of writing this  
 2873 thesis, the only available  $h\text{-}\phi(1020)$  correlation results in p–Pb at  $\sqrt{s_{\text{NN}}} = 5.02$  TeV  
 2874 come in the form of the  $h\text{-}\phi/h\text{-}h$  per-trigger yield ratios, where the yields are extracted  
 2875 assuming a flat UE. As mentioned in the abstract, one of the topics of this analysis

---

<sup>4</sup>This is a strict requirement, there are twelve fits in total, each with at least four free parameters, and the fitting software is not particularly robust.

2876 involves investigating open versus hidden strangeness in the form of the h- $\Lambda$ /h- $\phi$  per-  
2877 trigger yield ratios in the different kinematic regions. This is done by taking a ratio  
2878 of ratios, namely

$$\frac{(h-\Lambda)}{(h-h)_1} / \frac{(h-\phi)}{(h-h)_2} \quad (4.32)$$

2879 where the subscripts 1 and 2 are used to differentiate between this research and the  
2880  $\phi$  analysis, respectively. This only reduces to the h- $\Lambda$ /h- $\phi$  ratios if two conditions  
2881 are met: the first is that the h-h distributions are the same (which is investigated  
2882 more thoroughly in Section 4.7.4), and the second is that the yields are extracted  
2883 from these dihadron distributions using the exact same procedure. While this is not  
2884 required in the case of the h- $\Lambda$  yields, the same procedure is applied for the sake of  
2885 consistency.

2886 The resulting fits and extracted widths for each of the variations listed above in  
2887 all multiplicity and momentum ranges for both the h- $\Lambda$  and h-h cases can be seen in  
2888 Figure 4.45. Again, only small deviations from the central values are observed in the  
2889 near-side widths across all variations, with the largest percent difference being around  
2890 3% across all multiplicity and momentum bins for both the h- $\Lambda$  and h-h distributions.  
2891 Interestingly, the away-side widths appear to be much more sensitive to the inclusion  
2892 of  $v_2$ , as all variations from the nominal technique—again, each variation assumes a  
2893 flat UE—result in widths which are systematically lower than the central values by  
2894 around 5-10%. This is a strange result, as the  $v_2$ -based UE is completely symmetric  
2895 about  $\Delta\varphi = \pi/2$ , and thus should affect the near-side widths in the same way as  
2896 the away-side. As mentioned above, including  $v_2$  in the UE is the more *physically*  
2897 motivated choice, and therefore is chosen to be nominal despite these large deviations.  
2898 Note that the Gaussian and von Mises widths are more similar in the cases where the  
2899 flat UE is used, indicating that the observed deviations are not due to the choice of  
2900 fitting function.

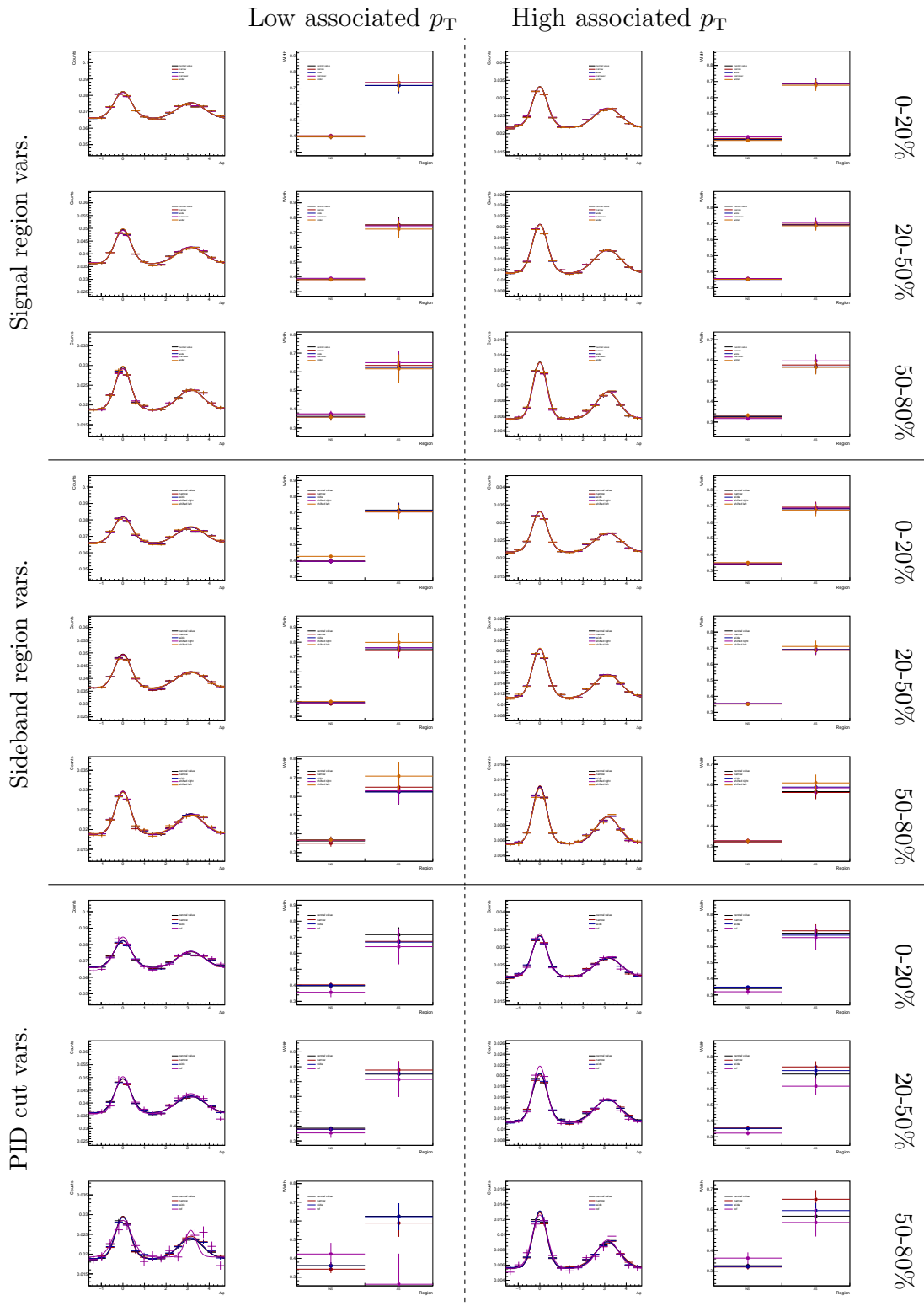


Figure 4.44: The resulting von Mises fits and extracted jet widths after the signal, sideband and PID cut variations are applied to the  $h-\Lambda \Delta\varphi$  distributions.

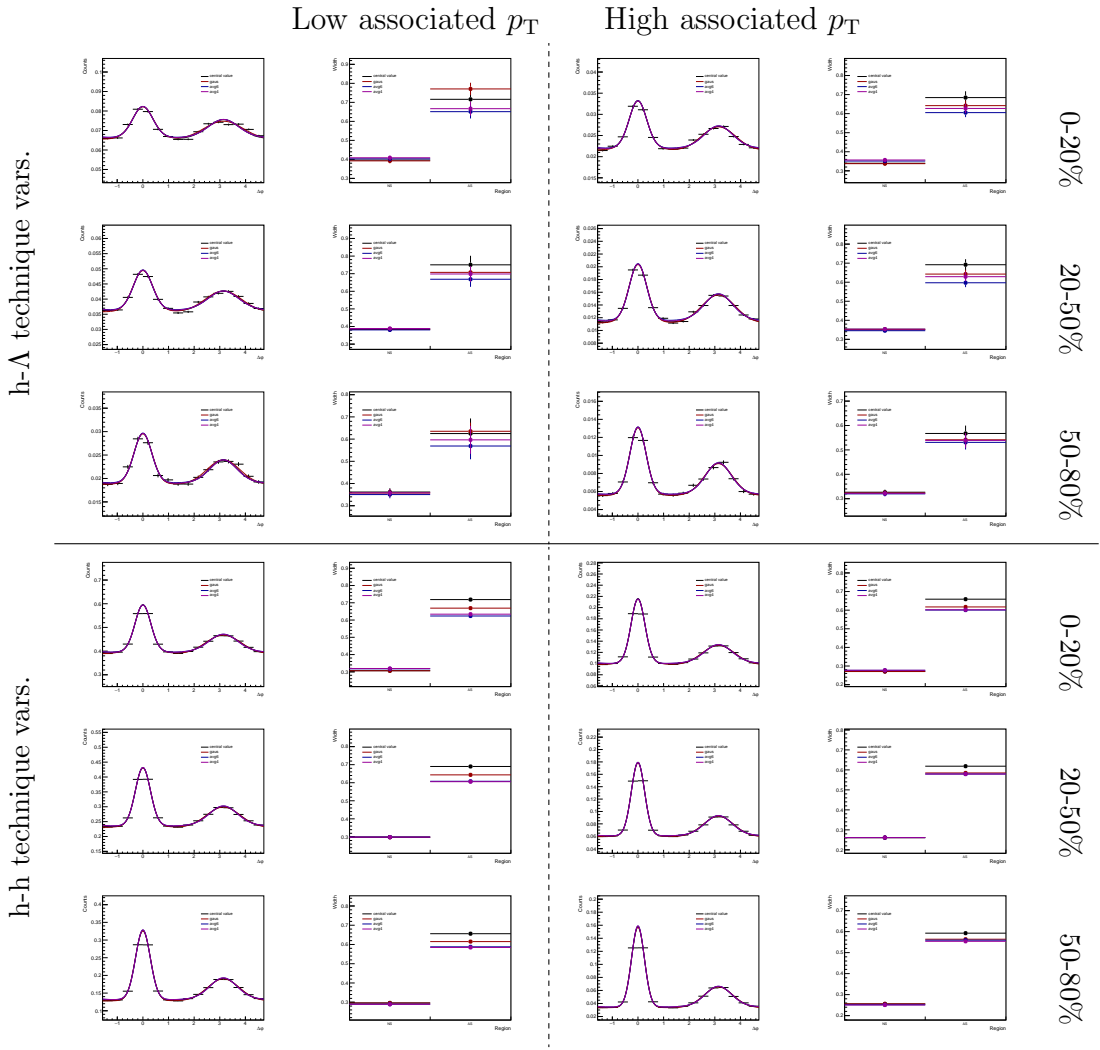


Figure 4.45: The resulting  $h\text{-}\Lambda$  (top) and  $h\text{-}h$  (bottom) von Mises fits and extracted jet widths in each multiplicity and momentum bin after each variation of the fitting procedure.

2901 **4.6.3.3 Barlow check for width extraction**

2902 Again, following the same techniques as outlined in Sections 4.6.1.4 and 4.6.2.6, a  
2903 Barlow check is performed for the variations presented in this section that affect the  
2904 extracted near- and away-side widths. As was before, if the majority of the extracted  
2905  $h\text{-}\Lambda$  widths for a given variation have  $|N\sigma_{RB}| < 1$ , that variation is excluded from the  
2906 systematic uncertainty calculation. This majority is calculated using both the near-  
2907 and away-side jet components across all multiplicity bins and associated momentum  
2908 bins. Again, the dihadron widths are not considered for this procedure<sup>5</sup>, and any  
2909 fitting technique variation that is excluded from the uncertainty calculation as the  
2910 result of this check for the  $h\text{-}\Lambda$  widths will also be excluded for the  $h\text{-}h$  case. Visual  
2911 depictions of the Barlow procedure can be seen in Figure 4.46.

2912 As a result of the check, the following variations were excluded from the systematic  
2913 uncertainty calculation for the jet widths:

2914 • Signal: Wide, Wider

2915 • Sideband: Wide, Narrow

2916 • PID: Require TOF

2917 Curiously, these are the same variations that were excluded for the  $\Delta\varphi$  distributions,  
2918 which is *mostly*<sup>6</sup> a coincidence.

2919 **4.6.3.4 Width extraction systematics, summarized**

2920 The systematic uncertainties associated with the  $h\text{-}\Lambda$  and  $h\text{-}h$  jet width extraction  
2921 for each multiplicity and associated momentum bin can be seen in Tables 4.16 ( $h\text{-}\Lambda$ )  
2922 and 4.17 ( $h\text{-}h$ ), with visual depictions shown in Figures 4.47 ( $h\text{-}\Lambda$ ) and 4.48. The  
2923 total systematic uncertainties are obtained by adding the individual uncertainties  
2924 in quadrature. Note that the away-side width uncertainties are much larger than  
2925 the near-side, indicating that constraining the away-side jet width is a much more

---

<sup>5</sup>Due to extremely small statistical errors, see Section 4.6.2.6

<sup>6</sup>There is obviously some correlation between variations in the individual  $\Delta\varphi$  bins and the widths. Consider a hypothetical variation that causes an unusually large spike in a  $\Delta\varphi$  bin near zero: this would certainly cause the near-side width to be considerably smaller than normal. This is an extreme example, however, and generally these variations affect the individual  $\Delta\varphi$  bins in similar ways.

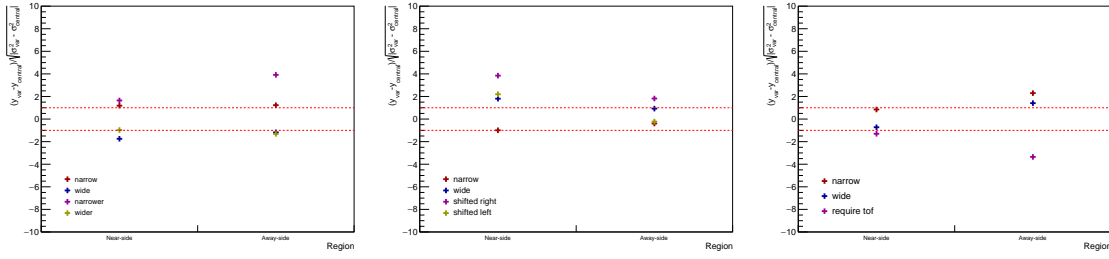


Figure 4.46: Barlow check for the width extraction procedure for the signal (left), sideband (middle), and PID (right) variations in the 20-50% multiplicity bin. The red lines represent  $N\sigma_{RB} = \pm 1$ , and if the majority of the points fall within the red lines (across all  $p_T$  and multiplicity bins), they are excluded from the width systematic uncertainty calculation.

2926 difficult procedure, especially in the presence of non-zero elliptic flow (as discussed  
 2927 in Section 4.6.3.2). As the width uncertainties do not exhibit any significant multi-  
 2928 plicity dependence, the multiplicity-uncorrelated portion of these uncertainties is not  
 2929 reported.

2930 Both the topological selection and associated hadron efficiency uncertainties are  
 2931 given in the tables and figures, which were obtained by randomly varying the  $\Delta\varphi$  dis-  
 2932 tributions within their respective systematic uncertainties (Table 4.6) and extracting  
 2933 the widths using the nominal procedure. As the topological selection and track-  
 2934 ing efficiency uncertainties were not directly calculated in this analysis, these results  
 2935 serve as a “best guess” for how the widths would be affected by variations in the  
 2936 corresponding selection criteria. The results of this procedure for the h- $\Lambda$  and h-h  
 2937 distributions in the 20-50% multiplicity bin for both associated momentum ranges  
 2938 can be seen in Figure 4.49.

Mult.	$p_T$	Peak	Signal	Sideband	PID	Fit proc.	Topo.	Total
0-20%	low	NS	1.19	5.41	1.19	2.09	3.40	6.93
20-50%	low	NS	1.13	2.70	1.74	0.93	3.40	4.90
50-80%	low	NS	3.20	1.19	3.82	2.05	3.40	6.48
0-20%	low	AS	2.53	1.64	6.21	7.91	2.40	10.77
20-50%	low	AS	0.57	4.68	2.62	8.16	2.40	10.07
50-80%	low	AS	2.88	9.43	4.11	5.88	2.40	12.43
0-20%	high	NS	3.44	1.66	2.19	3.51	3.10	6.43
20-50%	high	NS	1.10	0.48	1.09	1.35	3.10	3.75
50-80%	high	NS	2.46	0.56	1.68	1.54	3.10	4.60
0-20%	high	AS	0.51	1.00	1.99	8.95	6.10	11.07
20-50%	high	AS	1.56	1.93	5.02	10.33	6.10	13.24
50-80%	high	AS	3.93	5.74	10.80	5.40	6.10	15.21

Table 4.16: The final systematic errors from the h- $\Lambda$   $\Delta\varphi$  near-side (NS) and away-side (AS) width extraction for each multiplicity bin in the lower (top) and higher (bottom) associated  $p_T$  bins. The total systematic error is calculated by adding each systematic error in quadrature.

Mult.	$p_T$	Peak	Fit proc.	Trk. eff.	Total
0-20%	low	NS	2.21	1.00	2.42
20-50%	low	NS	0.21	1.00	1.02
50-80%	low	NS	1.74	1.00	2.01
0-20%	low	AS	8.75	1.50	8.87
20-50%	low	AS	6.66	1.50	6.82
50-80%	low	AS	6.91	1.50	7.07
0-20%	high	NS	1.86	1.00	2.11
20-50%	high	NS	0.12	1.00	1.01
50-80%	high	NS	1.47	1.00	1.78
0-20%	high	AS	8.02	1.50	8.16
20-50%	high	AS	6.06	1.50	6.24
50-80%	high	AS	5.73	1.50	5.93

Table 4.17: The final systematic errors from the h-h  $\Delta\varphi$  near-side (NS) and away-side (AS) width extraction for each multiplicity bin in the lower (top) and higher (bottom) associated  $p_T$  bins. The total systematic error is calculated by adding each systematic error in quadrature.

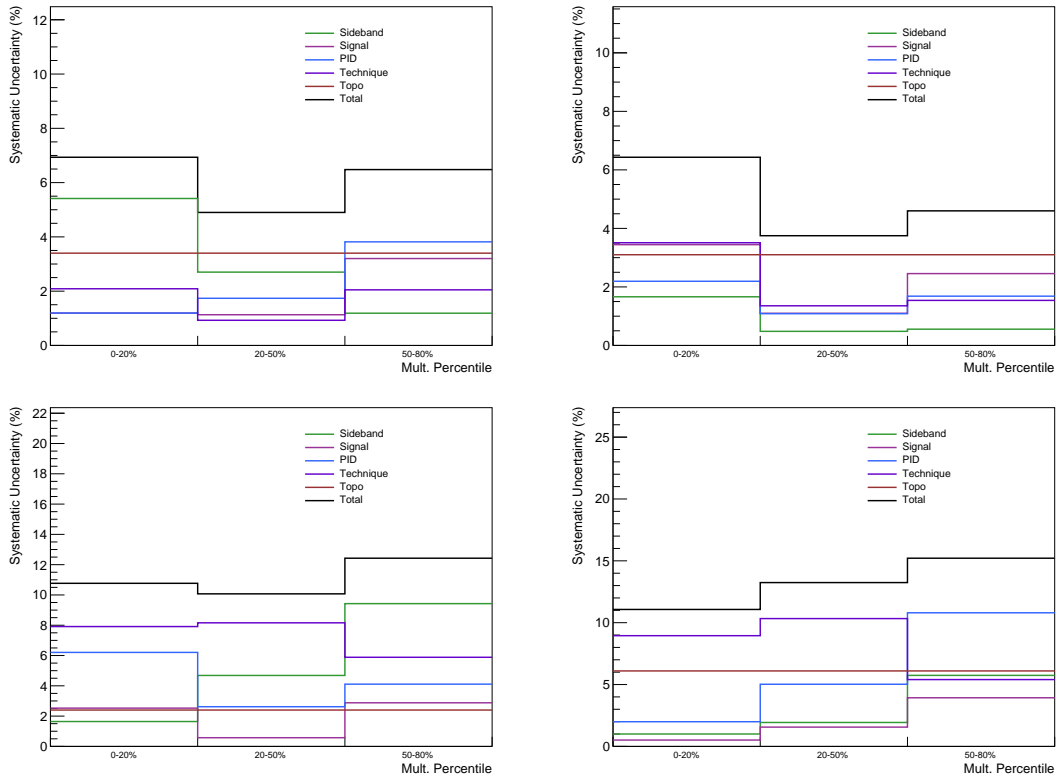


Figure 4.47: Final systematic errors for the  $h\Lambda \Delta\varphi$  near-side (top) and away-side (bottom) width extraction for each multiplicity bin in the lower (left) and higher (right) associated  $p_T$  bins.

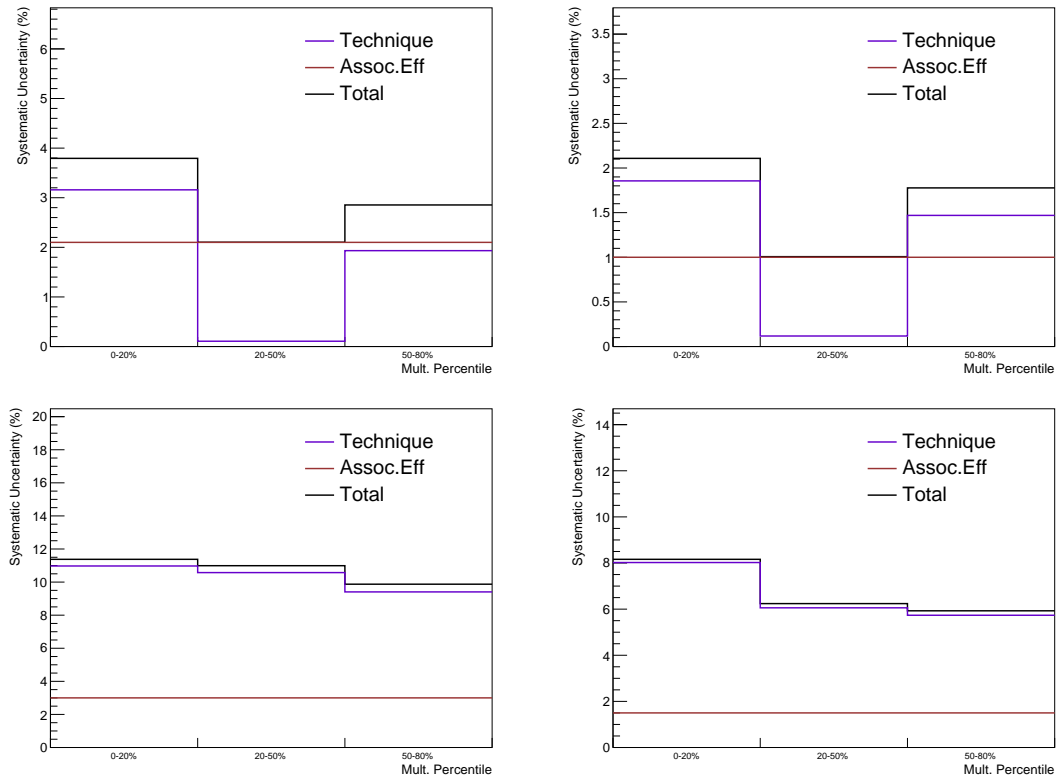


Figure 4.48: Final systematic errors for the h-h  $\Delta\varphi$  near-side (top) and away-side (bottom) width extraction for each multiplicity bin in the lower (left) and higher (right) associated  $p_T$  bins.

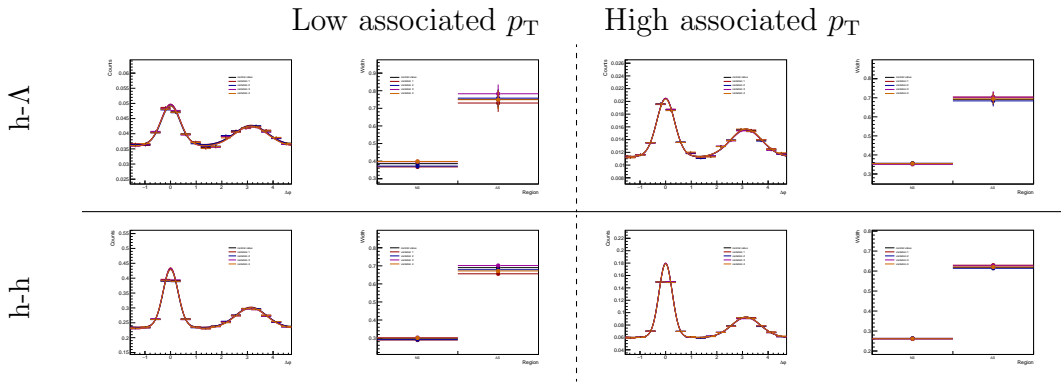


Figure 4.49: The resulting h- $\Lambda$  (top) and h-h (bottom) von Mises fits and extracted jet widths in the 20-50% multiplicity bin for each momentum bin after random variations of the individual  $\Delta\varphi$  bins within the topological selection (h- $\Lambda$ ) and tracking efficiency (h-h) uncertainties from Table 4.6.

## 2939 4.6.4 Final systematics tables

2940 For ease of reference, all of the final systematic uncertainties discussed in the previous  
 2941 sections have been consolidated into Tables 4.18 (h- $\Lambda$ ) and 4.19 (h-h).

Table 4.18: The final systematic uncertainties for the h- $\Lambda$   $\Delta\varphi$  distributions, the per-trigger jet and UE yields, and the jet widths in all multiplicity and associated momentum bins. The fraction of the systematic uncertainty which is uncorrelated with multiplicity is reported separately in parentheses for the extracted yields. The low (high) momentum bin is such that  $1.5 < p_T^{\text{assoc.}} < 2.5 \text{ GeV}/c$  ( $2.5 < p_T^{\text{assoc.}} < 4.0 \text{ GeV}/c$ ).

Mult. and $p_T$ bin	$\Delta\varphi$ dist.	$Y_{\text{near}}$	$Y_{\text{away}}$	$Y_{\text{UE}}$	$\sigma_{NS}$	$\sigma_{\text{away}}$
0-20%, low	3.3%	5.5(2.7)%	5.6(2.8)%	3.1(0.7)%	6.9%	10.8%
20-50%, low	3.4%	4.9(3.1)%	5.2(3.6)%	3.2(1.0)%	4.9%	10.1%
50-80%, low	3.8%	6.3(5.8)%	7.2(7.0)%	3.7(2.2)%	6.5%	12.4%
0-20%, high	3.2%	5.5(2.9)%	6.1(3.7)%	3.2(0.7)%	6.4%	11.1%
20-50%, high	3.3%	5.9(4.3)%	6.5(5.4)%	3.3(1.3)%	3.8%	13.2%
50-80%, high	4.1%	4.8(4.5)%	5.3(5.5)%	3.7(2.4)%	4.6%	15.2%

Table 4.19: The final systematic uncertainties for the h-h  $\Delta\varphi$  distributions, the per-trigger jet and UE yields, and the jet widths in all multiplicity and associated momentum bins. The fraction of the systematic uncertainty which is uncorrelated with multiplicity is reported separately in parentheses for the extracted yields. The low (high) momentum bin is such that  $1.5 < p_T^{\text{assoc.}} < 2.5 \text{ GeV}/c$  ( $2.5 < p_T^{\text{assoc.}} < 4.0 \text{ GeV}/c$ ).

Mult. and $p_T$ bin	$\Delta\varphi$ dist.	$Y_{\text{near}}$	$Y_{\text{away}}$	$Y_{\text{UE}}$	$\sigma_{NS}$	$\sigma_{\text{away}}$
0-20%, low	3.5%	4.5(1.7)%	4.8(2.3)%	3.5(0.2)%	2.4%	8.9%
20-50%, low	3.5%	3.8(1.3)%	3.6(1.9)%	3.5(0.2)%	1.0%	6.8%
50-80%, low	3.5%	4.9(3.9)%	6.4(6.2)%	3.7(1.2)%	2.0%	7.1%
0-20%, high	3.5%	3.8(1.0)%	4.0(1.7)%	3.5(0.2)%	2.1%	8.2%
20-50%, high	3.5%	3.6(0.7)%	3.6(1.2)%	3.5(0.3)%	1.0%	6.2%
50-80%, high	3.5%	4.2(2.3)%	5.2(4.1)%	3.8(1.5)%	1.8%	5.9%

2942 **4.7 Cross-checks**

2943 As mentioned in the introduction to this chapter, this section presents a number of  
2944 cross-checks that were performed to verify the validity and robustness of the analysis  
2945 procedure.

2946 **4.7.1 Monte Carlo closure tests**

2947 One of the most common procedures for verifying the validity of an experimental  
2948 analysis comes in the form of a **Monte Carlo closure test** [162]. The basic steps  
2949 of any MC closure test are as follows:

- 2950     1. Generate a large sample of simulated events using a Monte Carlo generator,  
2951       which models both the physics of the collision and the detector response
- 2952     2. Apply the same analysis method and selection criteria to the detector-simulated  
2953       events as to the experimental data to obtain a **reconstructed** observable
- 2954     3. Compare the reconstructed observable with the **ground-truth** observable, which  
2955       is obtained directly from the generator-level particles

2956 Generally the third step is done by taking a ratio of the reconstructed observable to  
2957 the ground-truth observable, which should be consistent with unity if the analysis  
2958 procedure is valid. Significant deviations from unity would indicate that the experi-  
2959 mental procedure introduces a non-physical bias to the measurement, which should  
2960 be addressed.

2961 For the Monte Carlo closure tests presented in this section, the p–Pb collision  
2962 events are simulated using the DPMJet generator [91], with the ALICE detector  
2963 response to the simulated particles handled by the GEANT [147] software package.  
2964 The reconstructed h– $\Lambda$  and h–h 2D correlation distributions are generated using the  
2965 same procedure as described in 4. In particular, this means that:

- 2966     • Both the reconstructed trigger and associated  $\Lambda$  (h) pass the track cuts de-  
2967       scribed in Tables 4.2 and 4.5 (4.3), respectively

2968 • To avoid issues with PID using GEANT<sup>7</sup>, the  $\Lambda$  daughter tracks are verified to  
2969 be from a proton/pion by checking their corresponding generator-level particles

2970 • The efficiency and acceptance corrections are applied to the h-h and h- $\Lambda$  distri-  
2971 butions in the same was as described in Section 4.5

2972 • The additional corrections (sideband subtraction, signal scaling, and two-track  
2973 template) are applied to the h- $\Lambda$  distributions as they are in Section 4.5.3

2974 For the ground-truth distributions, the trigger and associated  $\Lambda$  (h) are taken directly  
2975 from the generator-level particles. The same kinematic cuts are also applied, namely  
2976 the trigger is required to have momentum  $4.0 < p_T < 8.0 \text{ GeV}/c$ , the associated  
2977  $\Lambda$  (h) have the same momentum ranges as the reconstructed case, and all particles  
2978 are required to fall within  $|\eta| < 0.8$ . Applying these pseudorapidity cuts on the  
2979 trigger and associated particles ensures that the underlying physics<sup>8</sup> is the same as  
2980 the reconstructed case. Unfortunately this requirement also introduces the same  
2981 triangular shape along  $\Delta\eta$  in the correlation distributions as seen in data, which is  
2982 corrected for using the mixed-event technique described in Section 4.5.

2983 Both the reconstructed and ground-truth 2D correlation distributions are pro-  
2984 jected onto  $\Delta\varphi$  in the range  $|\Delta\eta| < 1.2$ , and the results for the h- $\Lambda$  and h-h  $\Delta\varphi$   
2985 distributions are shown for each associated  $p_T$  bin in Figures 4.50 (h- $\Lambda$ ) and 4.51  
2986 (h-h), along with the corresponding (reconstructed)/(ground-truth) distribution ra-  
2987 tios. A fit to the ratio is also shown, which is consistent with unity in all cases.  
2988 This indicates that the analysis procedure is valid, and that the corrections applied  
2989 to the h- $\Lambda$  and h-h distributions are not introducing any non-physical biases to the  
2990  $\Delta\varphi$  distribution measurements. As all of the observables are derived directly from  
2991 these distributions, it is safe to assume the reconstructed and ground-truth versions  
2992 of these observables are also consistent with each other.

2993 While the MC closure tests provide a general framework for checking the validity  
2994 of an experimental analysis, there are a few more specific checks that are performed  
2995 to ensure the robustness of this analysis, which are described in the following sections.

---

<sup>7</sup>The  $n\sigma_{\text{TPC,TOF}}$  values predicted by GEANT differ from experimental data by a large margin, so using GEANT for PID is generally avoided whenever possible.

<sup>8</sup>Particle production is rapidity-dependent, so choosing particles in a different rapidity range could alter the spectrum.

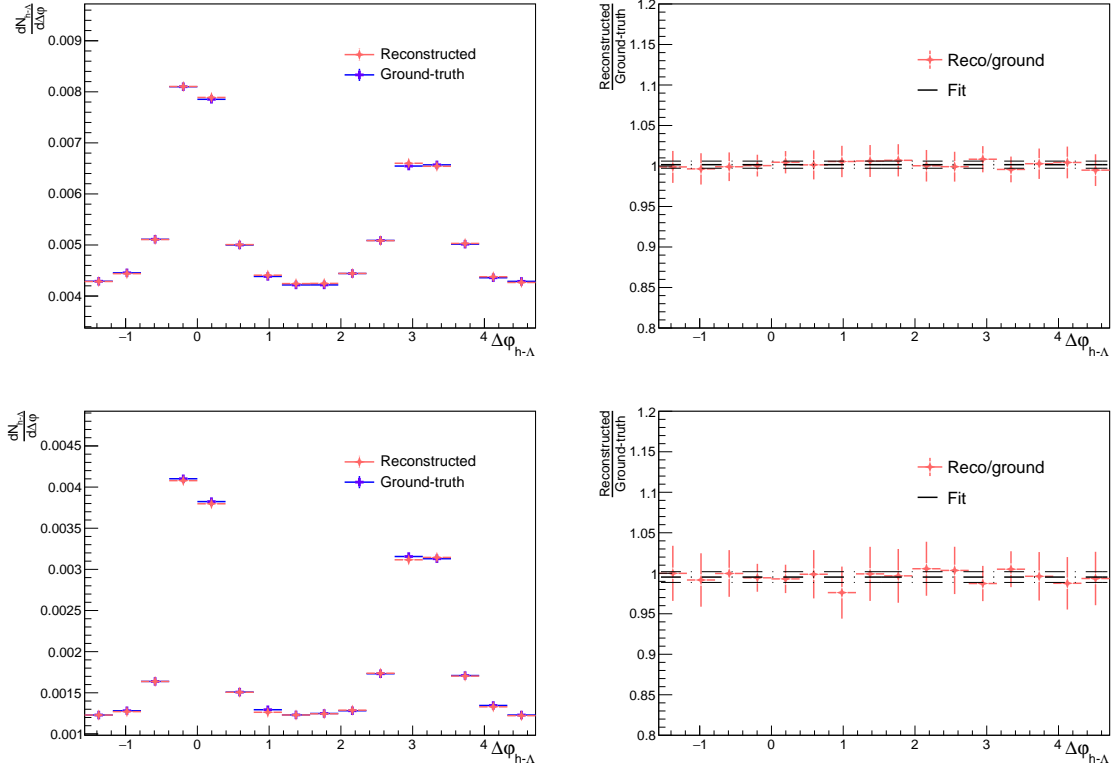


Figure 4.50: The reconstructed (pink) and ground-truth (blue)  $h\text{-}\Lambda$   $\Delta\varphi$  distributions in the lower (top) and higher (bottom) associated  $p_T$  bins, along with a (reconstructed)/(ground-truth) ratio and straight-line fit with errors shown as dashed lines. The ratio is consistent with unity, and thus the corrections applied to the  $h\text{-}\Lambda$  distributions are valid.

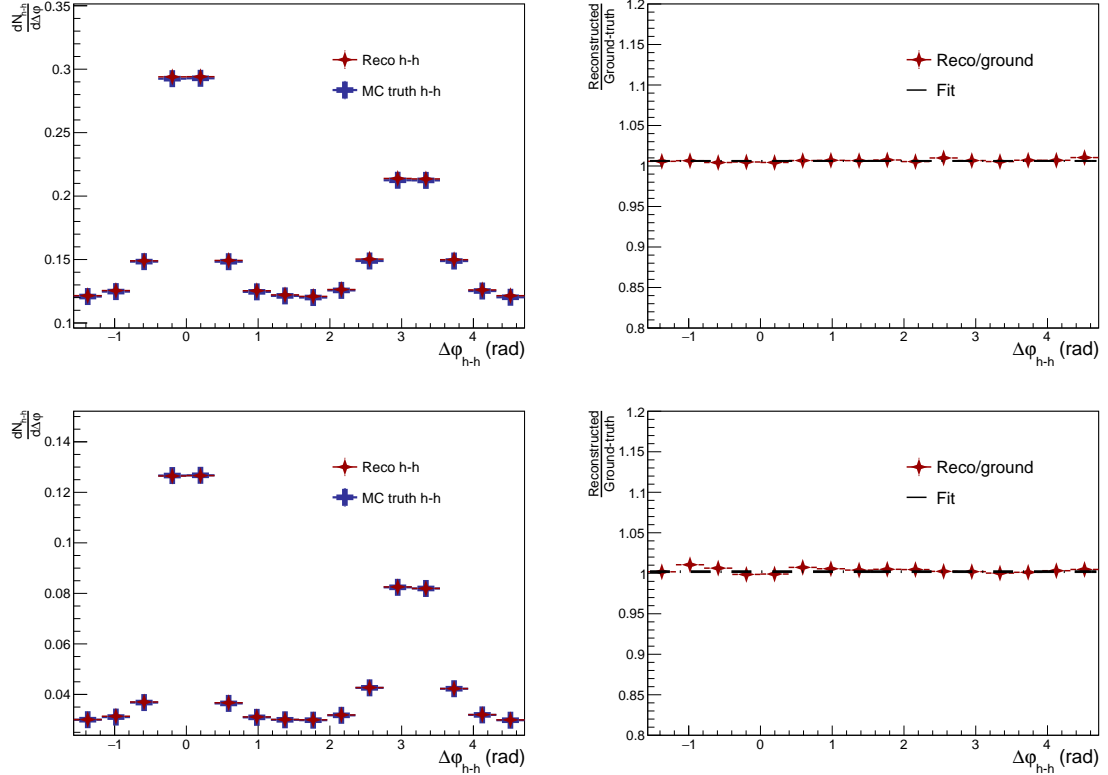


Figure 4.51: The reconstructed (pink) and ground-truth (blue) h-h  $\Delta\varphi$  distributions in the lower (top) and higher (bottom) associated  $p_T$  bins, along with a (reconstructed)/(ground-truth) ratio and straight-line fit with errors shown as dashed lines. Again, the ratio is consistent with unity, and thus the corrections applied to the h-h distributions are valid.

2996 **4.7.2 Investigating radial flow effects**

2997 Any multiplicity-differential analysis involving a sample of particles within a fixed  
2998  $p_T$  momentum window will be subject to **radial flow** effects. Radial (or directed)  
2999 flow [79] can be characterized by the increase of the average transverse momentum  
3000  $\langle p_T \rangle$  with increasing event multiplicity for a given particle species. This could result  
3001 in an increased yield integrated within a fixed  $p_T$  window, and that increase may be  
3002 different for different particle species. As this thesis presents many results concerning  
3003 the  $\Lambda/h(\pi)$  ratio as a function of multiplicity within fixed  $p_T$  ranges, it is important  
3004 to investigate the effect radial flow may have on the final results.

3005 Luckily, the effects of radial flow have *already* been thoroughly investigated for the  
3006  $\phi(1020)/\pi$  ratio, where it was found that radial flow causes a larger increase in the  $\pi$   
3007 yield than the  $\phi$  yield within the  $2 < p_T < 4$  GeV/ $c$  momentum window. This would  
3008 result in a *decrease* in the  $\phi/\pi$  ratio with increasing multiplicity. Thus any observation  
3009 of an *increase* in the  $\phi/\pi$  ratio with increasing multiplicity can not be attributed to  
3010 radial flow effects. Importantly, the  $\Lambda$  baryon shares a similar mass (1.115 vs. 1.020  
3011 GeV/ $c^2$ ) and  $p_T$  spectrum shape (shown in Figure 4.52) to the  $\phi$  meson. As such, any  
3012 conclusion regarding the radial flow effects (which are determined using these two  
3013 observables) on the  $\Lambda/\pi$  results can be inferred from the  $\phi/\pi$  study. A brief summary  
3014 of the  $\phi/\pi$  radial flow study is presented below.

3015 **4.7.2.1 Radial flow effects on the  $\phi/\pi$  ratio**

3016 First, the mean  $p_T$  of both the  $\phi$  and  $\pi$  were taken from published p–Pb data in the  
3017 0-5% and 60-80% multiplicity percentiles. Then, the momentum spectra of the  $\phi$  and  
3018  $\pi$  were fit to the simplified Boltzman function,

$$B(p_T) = \frac{C}{T(m + T)} p_T e^{-(m_T - m)/T}, \quad (4.33)$$

3019 where  $m$  is the particle mass,  $m_T$  is the particle's transverse mass ( $= \sqrt{p_T^2 + m^2}$ ),  $T$   
3020 is the temperature, and  $C$  is a normalization constant. The temperature  $T$  was found  
3021 such that the mean  $p_T$  of the fit function matched the published mean  $p_T$  values. The  
3022 resulting fits are shown for the  $\phi$  and the  $\pi$  in both multiplicity bins in Figure 4.53.  
3023 The  $2 < p_T < 4$  GeV/ $c$  momentum window is also highlighted.

3024 The ratio of the yields in the higher multiplicity bin to the lower multiplicity bin  
3025 within the momentum window was then calculated for both the  $\phi$  and the  $\pi$ , which

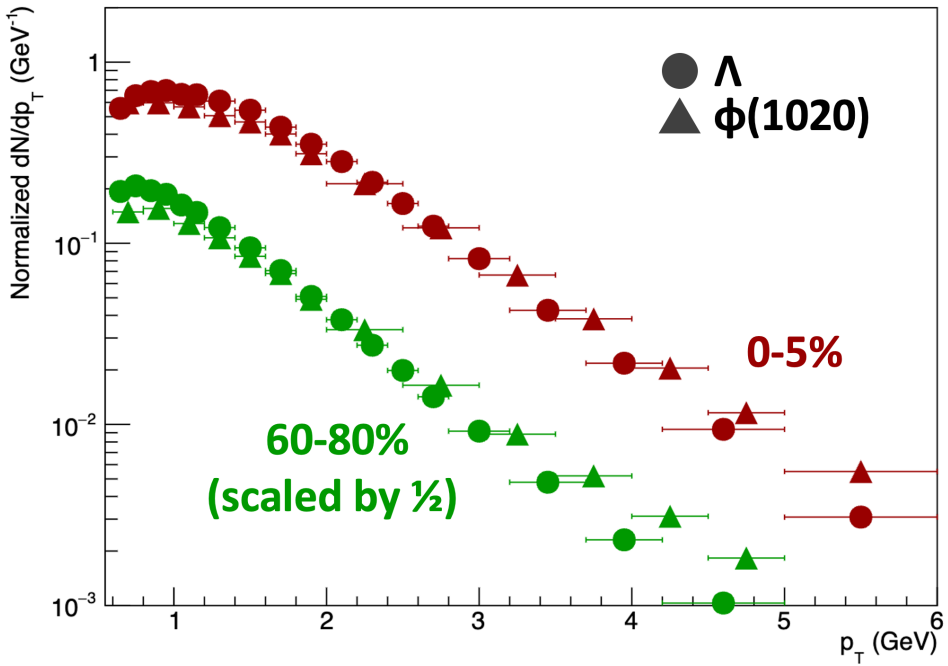


Figure 4.52: The  $p_T$  spectra shape of the  $\phi$  (triangles) and  $\Lambda$  (squares) in p–Pb collisions at  $\sqrt{s_{NN}} = 5.02$  TeV in the 0–5% (red) and 60–80% (green) multiplicity bins. Both spectra in the 0–5% have been normalized to unity, whereas the 60–80% spectra has been normalized to 0.5 for visibility. The  $\Lambda$  and  $\phi$  spectra shapes are very similar in both multiplicity bins.

3026 revealed that the  $\phi$  yield increases by around 30%, whereas the  $\pi$  yield increases by  
 3027 nearly 200%.

### 3028 4.7.3 Correlations with a single trigger

3029 A central feature of this analysis relies on the assumption that the per-trigger pair-  
 3030 wise yields from the h- $\Lambda$  or h-h distributions are roughly equal to the per-trigger  
 3031 associated yields for  $\Lambda$  baryons or charged hadrons in events that have a trigger  
 3032 hadron, so that the (h- $\Lambda$ )/(h-h) yield results can be interpreted as the  $\Lambda/h$  ratio in  
 3033 each region. This is only true if there is only a single trigger hadron in each event,  
 3034 which is obviously not the case across a large event sample. To see why this is required,  
 3035 consider two events: the first has a single trigger with three associated particles, while  
 3036 the second has two triggers with three associated particles. In the first event, there are

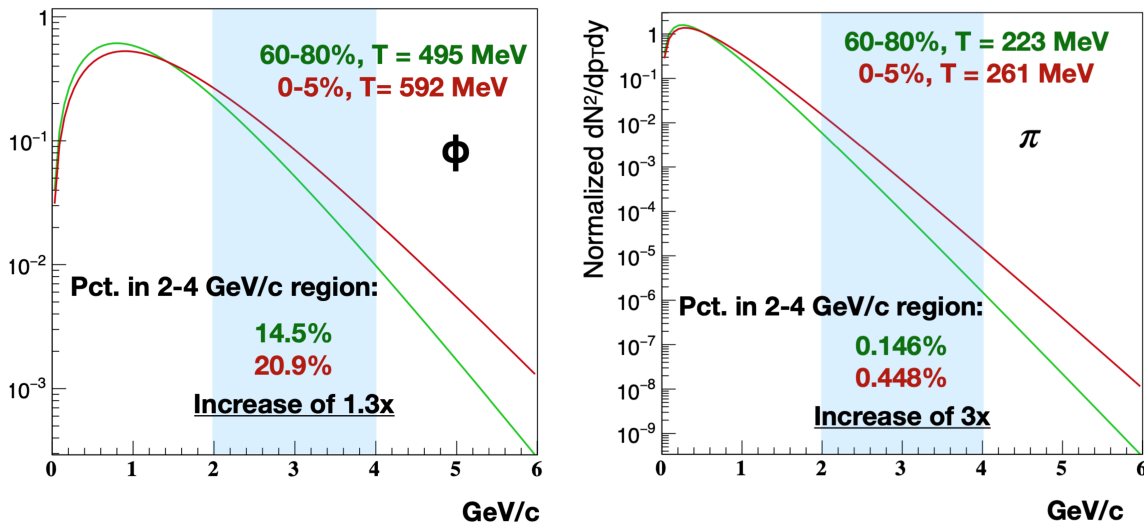


Figure 4.53: The fits to the momentum spectra of the  $\phi$  (left) and  $\pi$  (right) in the 0-5% (red) and 60-80% (green) multiplicity bins, with fit function given by Equation 4.33. The  $2 < p_T < 4 \text{ GeV}/c$  momentum window is highlighted in blue.

3037 three trigger-associated pairs, which corresponds exactly to the number of associated  
 3038 particles in the event. In the second, there are twice as many pairs as there are  
 3039 associated particles, meaning that the pair-wise yield “double counts” the associated  
 3040 particles. A diagram of this effect is shown in Figure 4.54. This effect scales with  
 3041 the number of triggers: if there are  $N$  triggers in an event, there would be  $N$  times  
 3042 as many pairs as associated particles. This diagram also introduces another subtle  
 3043 effect of multiple triggers: if triggers  $t_1$  and  $t_2$  belong to separate jets within a single  
 3044 event, then the associated particles that fall into the jet-like regions when correlated  
 3045 with  $t_1$  could be mistakenly placed in the “underlying event” when correlated with  
 3046  $t_2$ , artificially inflating the UE yields.

3047 Luckily, less than 1% of all events have more than a single trigger, as shown in  
 3048 Figure 4.55. Even still, the effect of multiple triggers on the per-trigger pair-wise  
 3049 yield is investigated by repeating the same analysis procedure as described in the  
 3050 previous chapter, with one change:

- 3051     • If an event has more than one trigger, only the trigger with the highest momen-  
 3052       tum within the  $4.0 < p_T < 8.0 \text{ GeV}/c$  range is used

3053 This guarantees that no associated particles will be counted more than once, at the

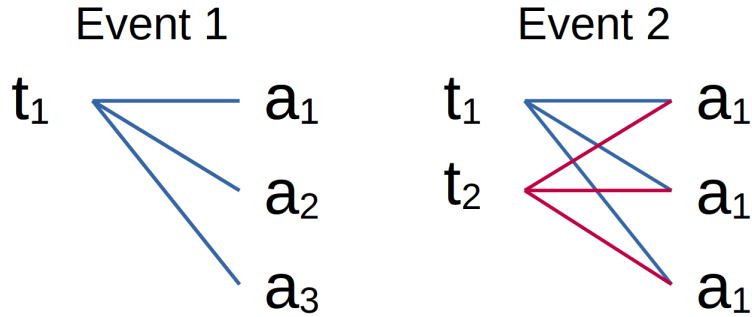


Figure 4.54: A diagram showing the effect of multiple triggers on the per-trigger pair-wise yield. In the first event, there is a single trigger with three associated particles, so the pair-wise yield is equal to the number of associated particles. In the second event, there are two triggers with three associated particles, so the pair-wise yield is twice the number of associated particles.

3054 expense of a slightly modified trigger  $p_T$  spectrum<sup>9</sup>. The final single trigger h- $\Lambda$  and  
 3055 h-h  $\Delta\varphi$  distributions for each multiplicity bin are compared with the original method  
 3056 (all trigger) distributions in Figure 4.56. A flat deviation of around 5% is observed  
 3057 for both the h- $\Lambda$  and h-h cases, which is consistent across all multiplicity bins.

3058 As the (single trigger)/(all trigger) distribution ratios are mostly flat for both  
 3059 the h- $\Lambda$  and h-h distributions across all multiplicity bins, the effect on the final yield  
 3060 measurements would only be a  $\approx 5\%$  change of scale along the y-axis, and the ratio  
 3061 measurements would remain unchanged. Furthermore, this scale factor is the same  
 3062 across all multiplicity bins, indicating that using the standard per-trigger correlation  
 3063 method accurately captures the multiplicity-dependent behaviour of the  $\Lambda/h$  ratios  
 3064 in events with a trigger. Because the conclusions drawn from the results of this thesis  
 3065 only rely on the relative y-axis behavior of the measured observables, the effect of  
 3066 multiple triggers on the final distributions is negligible.

---

<sup>9</sup>Selecting the highest  $p_T$  trigger in the 4-8 GeV/ $c$  range usually still amounts to selecting a  $\approx 4$  GeV/ $c$  particle.

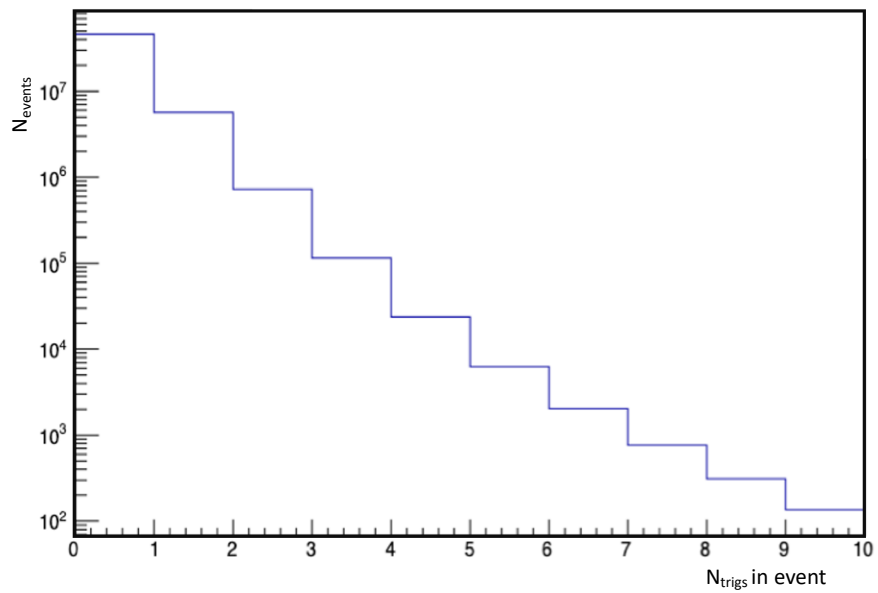


Figure 4.55: A log-plot showing the number of triggers per event across the entire data sample. Only a small fraction of events have at least a single trigger, and of those events, only a small fraction have more than one trigger.

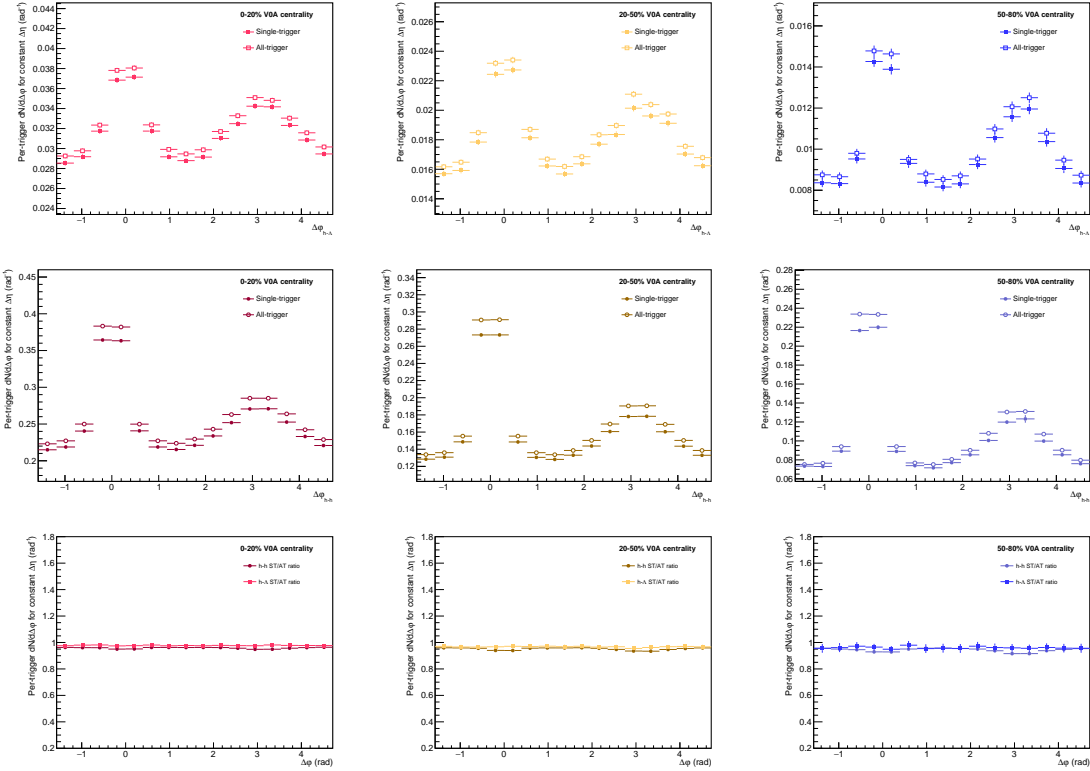


Figure 4.56: The per-trigger  $h\text{-}\Lambda$  (top) and  $h\text{-}h$  (middle)  $\Delta\varphi$  distribution comparison between using a single trigger (closed points) and all triggers (open points) in a given event, along with the (single trigger)/(all trigger) distribution ratio (bottom), for the 0-20% (left), 20-50% (center), and 50-80% (bottom) multiplicity bins in the associated momentum range  $2.0 < p_T < 4.0 \text{ GeV}/c$ . The distributions are nearly identical up to a  $\approx 0.95$  scale factor, which is constant as a function of multiplicity.

3067 **4.7.4 Dihadron comparison with  $\phi$  analysis**

3068 As mentioned in Section 4.6.3.2, the differences between open and hidden strangeness  
3069 are investigated by taking the  $\Lambda/\phi(1020)$  per-trigger yield ratios in the different kine-  
3070 matic regions (e.g. near-side jet, away-side jet, and underlying event). This is done  
3071 by taking a ratio of ratios, namely

$$\frac{(h-\Lambda)}{(h-h)_1} / \frac{(h-\phi)}{(h-h)_2}, \quad (4.34)$$

3072 where the  $(h-\phi)/(h-h)_2$  ratio in the denominator is taken from previously published  
3073 results in p–Pb collisions at  $\sqrt{s_{NN}} = 5.02$  TeV which use the same angular correlation  
3074 techniques to extract the per-trigger yields in the different regions [142]. This only  
3075 reduces to the per-trigger  $(h-\Lambda)/(h-\phi) \approx \Lambda/\phi$  yield ratios if two conditions are met:

- 3076 1. The  $(h-h)_1$  and  $(h-h)_2$  yields are identical  
3077 2. The yields are extracted using the same procedure

3078 Condition 2 has been met by design, as both analyses assume a flat UE taken as the  
3079 average of the correlation distributions in the same  $\Delta\varphi$  regions, and they both use  
3080 bin-wise summation to extract the per-trigger yields. Condition 1, however, needs to  
3081 be checked more thoroughly. While all of the selection criteria is the same between  
3082 the two, the analyses were performed by two different humans with vastly different  
3083 coding styles.

3084 To this end, a direct comparison between the dihadron per-trigger  $\Delta\varphi$  distribu-  
3085 tions from this analysis and the  $\phi$  analysis is shown in Figure 4.57. The distributions  
3086 are nearly identical across all multiplicity bins, which is indicated by the ratios at the  
3087 bottom of the figure never deviating unity. As such, the cancellation of the  $(h-h)_1$   
3088 and  $(h-h)_2$  yields in Equation 4.34 is valid.

3089 **4.7.5 Resonance technique for  $\Lambda$  reconstruction**

3090 The  $\Lambda$  baryons used in this analysis are reconstructed by exploiting their characteristic  
3091  $V^0$  decay topology, as discussed in Section 4.3. However, this method introduces a  
3092 small physical bias in the  $\Lambda$  sample: only  $\Lambda$ s which decay far enough from the primary  
3093 vertex to be reconstructed as  $V^0$ s (i.e. they have a detector-resolvable secondary  
3094 vertex) are considered. While the average decay length of the  $\Lambda$  is quite large ( $c\tau \approx$

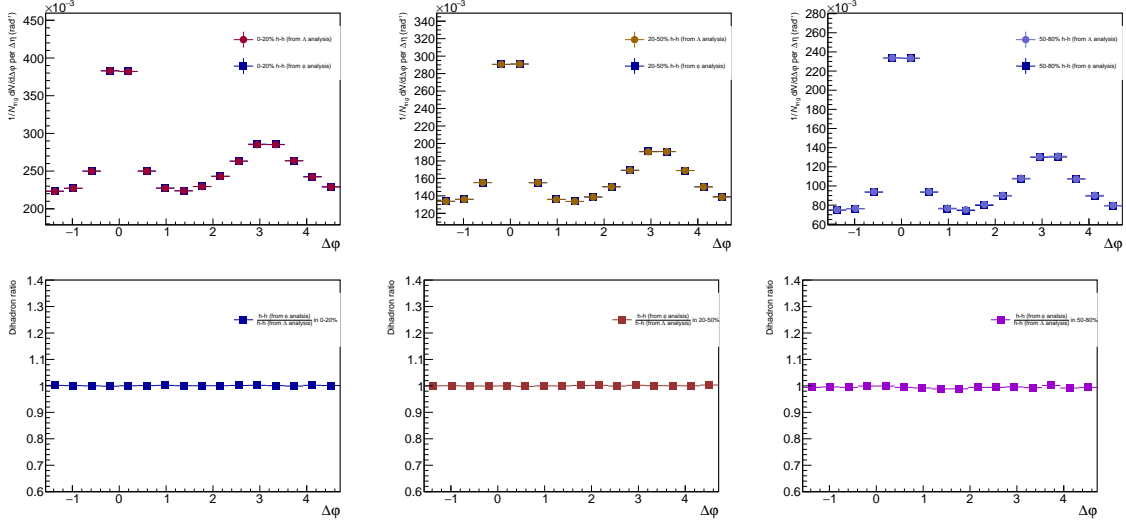


Figure 4.57: Comparison of the dihadron  $\Delta\varphi$  correlations between the  $\phi$  and  $\Lambda$  analyses for the 0-20% (left), 20-50% (middle), and 50-80% (right) multiplicity bins, taken in the  $2.0 < p_T < 4.0$  GeV/ $c$  associated momentum range. They are functionally identical for all multiplicity bins.

7.89 cm where  $\tau$  is the average lifetime), decay length distributions are exponentials of the form  $e^{-t/\tau}$ . This means that there is a small fraction of  $\Lambda$ s that decay too quickly to be resolved using their  $V^0$  topology, and thus are not included in the analysis. While the single particle  $\Lambda$  efficiency is used to correct for the overall  $\Lambda$  yield, it may be possible that the  $h-\Lambda$  correlation shape is influenced by the exclusion of these short-lived  $\Lambda$  baryons.

To investigate this possible bias, a new set of  $h-\Lambda$  distributions are produced, where the associated  $\Lambda$ s are reconstructed using the **resonance technique**: all oppositely charged proton-pion pairs from the event are combined to form  $\Lambda$  candidates. This is the only way to reconstruct extremely short-lived particles—like resonances—as they will never have a resolvable secondary vertex. This technique gives access to all  $\Lambda$  baryons that *can* be reconstructed in the event, regardless of their decay length. However, the large combinatorial background associated with the resonance technique presents many difficulties, which are discussed thoroughly in Appendix A. Even still, it is possible to repeat the same analysis procedure from the previous chapter with  $\Lambda$ s reconstructed using this technique, and the resulting  $h-\Lambda$   $\Delta\varphi$  distributions are shown in Figure 4.58, along with the original distributions for comparison. It should

be noted that neither of the distributions are corrected for the two-track inefficiency or the branching ratio, as this investigation was performed prior to those tools being developed in this analysis. However, the comparison should be mostly<sup>10</sup> unaffected by these corrections, as they are the same in both cases.

The distributions are very similar across all multiplicity bins, although the resonance technique distributions exhibit much larger statistical fluctuations due to the subtraction of the large combinatorial background using the sideband procedure. This provides solid evidence that the V<sup>0</sup> reconstruction technique is not introducing a significant bias in the shape of the h- $\Lambda$   $\Delta\varphi$  distributions, and that the exclusion of short-lived  $\Lambda$  baryons has little effect on the final results.

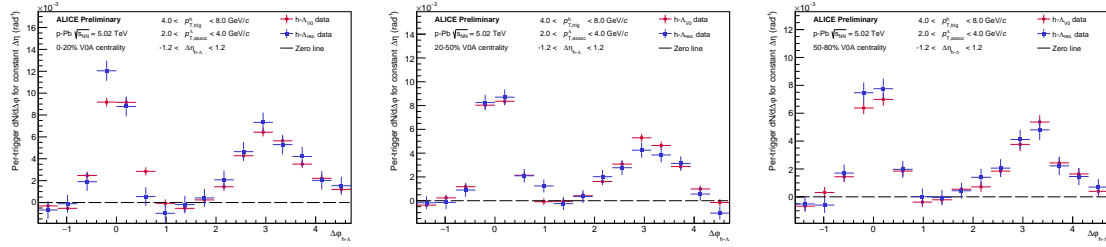


Figure 4.58: The final per-trigger h- $\Lambda$   $\Delta\varphi$  correlations for  $\Lambda$ s reconstructed using the resonance technique (blue) and the V<sup>0</sup>-based technique (red) in the 0-20% (left), 20-50% (middle), and 50-80% (right) multiplicity bins, taken in the associated momentum range  $2.0 < p_T < 4.0$  GeV/c, after the subtraction of the UE. The distributions show good agreement across all multiplicity bins, indicating that the V<sup>0</sup>-based reconstruction technique is not introducing a bias in the correlation shape.

After calculating the systematic uncertainties and performing the various cross-checks described in this chapter, the final results of this thesis are ready to be presented.

<sup>10</sup>The two-track inefficiency is actually very slightly less for the resonance technique as the shorter-lived  $\Lambda$ s usually have daughter tracks with higher quality track parameters due to more hits in the detector, making them less likely to be merged with the trigger.

3125

## Chapter Five: Results and Discussion

3126 The time has come to present the final results of this thesis. As there are quite a few  
3127 exciting measurements to be presented, the structure of this chapter is as follows. In  
3128 the first section, a brief reminder of the motivation and methodology for this analysis  
3129 are given to help with the digestion of the observables to be presented. The next  
3130 section presents the final results as they are, with lengthy discussions about the trends  
3131 for each observable. The final sections will compare these results to theoretical models  
3132 and previous measurements, and will discuss the implications of these measurements  
3133 on the current understanding of strangeness production in heavy-ion collisions.

3134 **5.1 Quick recap: motivation and methodology**

3135 This section serves as a *brief* recap of the “how” and “why” for this thesis. For more  
3136 details, please refer to Chapter 3.

3137 The goal of this thesis is to measure the production of strangeness ( $\Lambda$  baryons)  
3138 both in and out-of jets in p–Pb collisions. By separating the production of  $\Lambda$ s in  
3139 these regions, the underlying processes responsible for strangeness enhancement may  
3140 be brought to light.

3141 To perform this separation, **two-particle h- $\Lambda$  angular correlations** are used.  
3142 Using these angular correlations with a high momentum trigger hadron, the produc-  
3143 tion of  $\Lambda$ s can be separated into three regions: the near-side region (corresponding  
3144 to unmodified jet-like production), the away-side region (corresponding to jet-like  
3145 production with medium modification), and the underlying event or UE region (as-  
3146 sociated with soft production in the QGP medium). A diagram highlighting these  
3147 regions can be seen in Figure 5.1.

3148 The yields and widths presented in this section are extracted from these correlation  
3149 distributions, and studied as a function of multiplicity and  $\Lambda$  momentum. The same  
3150 procedure is performed for charged hadrons (h-h), and the results are compared.  
3151 These observables are also compared to multiple theoretical model predictions, as  
3152 well as to similar results from the  $\phi(1020)$  meson.

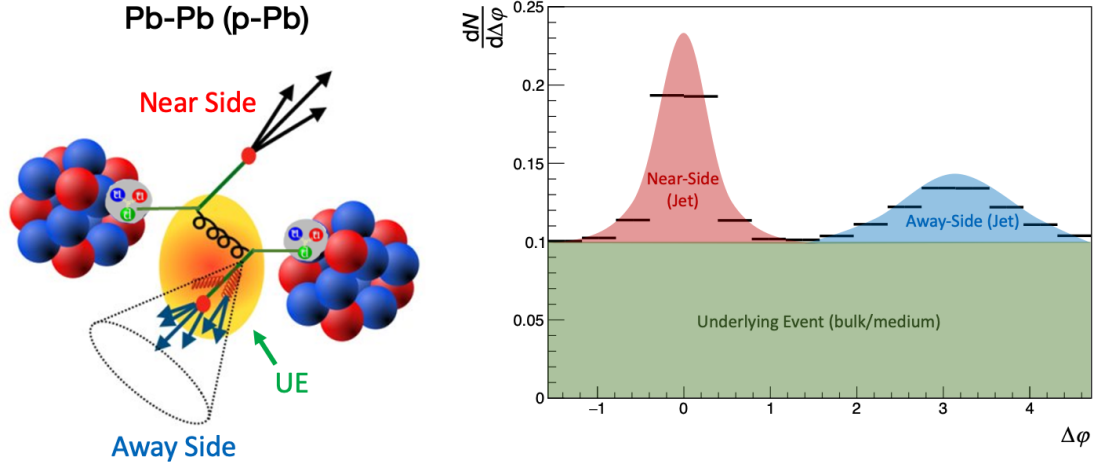


Figure 5.1: A cartoon of a  $\text{Pb-Pb}$  ( $\text{p-Pb}$ ) collision that produces particles in the near- and away-side jets, along with the UE. The the corresponding regions in the  $\Delta\varphi$  distribution are highlighted on the right.

## 3153 5.2 Per-trigger $\Delta\varphi$ distributions

3154 The per-trigger h-h and h- $\Lambda$   $\Delta\varphi$  distributions for all multiplicity and associated  $p_{\text{T}}$   
 3155 bins can be seen in Figure 5.2 (h- $\Lambda$ ) and Figure 5.3 (h-h). Summarizing plots that  
 3156 contain both the h- $\Lambda$  and h-h distributions together for each multiplicity class for  
 3157 the lower ( $1.5 < p_{\text{T}} < 2.5 \text{ GeV}/c$ ) and higher ( $2.5 < p_{\text{T}} < 4.0 \text{ GeV}/c$ ) associated  $p_{\text{T}}$   
 3158 bins can be seen in Figures 5.4 and 5.5, respectively. In the summarizing plots, the  
 3159 entire range along the y-axis is shown to emphasize the relative contribution to each  
 3160 distribution from the UE.

3161 In the lower associated momentum range, the UE baseline for both the h- $\Lambda$  and  
 3162 h-h distributions is found to increase by around a factor of three from the lowest  
 3163 to highest multiplicity class (0.05 to 0.17 in the h- $\Lambda$  case, 0.35 to 1 in the dihadron  
 3164 case). The higher associated momentum range exhibits a similar increase in the UE  
 3165 baseline with increasing multiplicity, but the h- $\Lambda$  baseline increases by a factor of four  
 3166 instead of three. The UE baseline is also found to be higher in the lower associated  
 3167  $p_{\text{T}}$  range than in the higher range by around a factor of three in the h- $\Lambda$  case and four  
 3168 in the h-h case for each multiplicity class. These observations suggest that associated  
 3169 production in the UE region truly is “softer” than production in the near- and away-  
 3170 side regions, supporting the idea that the production in the UE is heavily linked to

3171 the QGP.

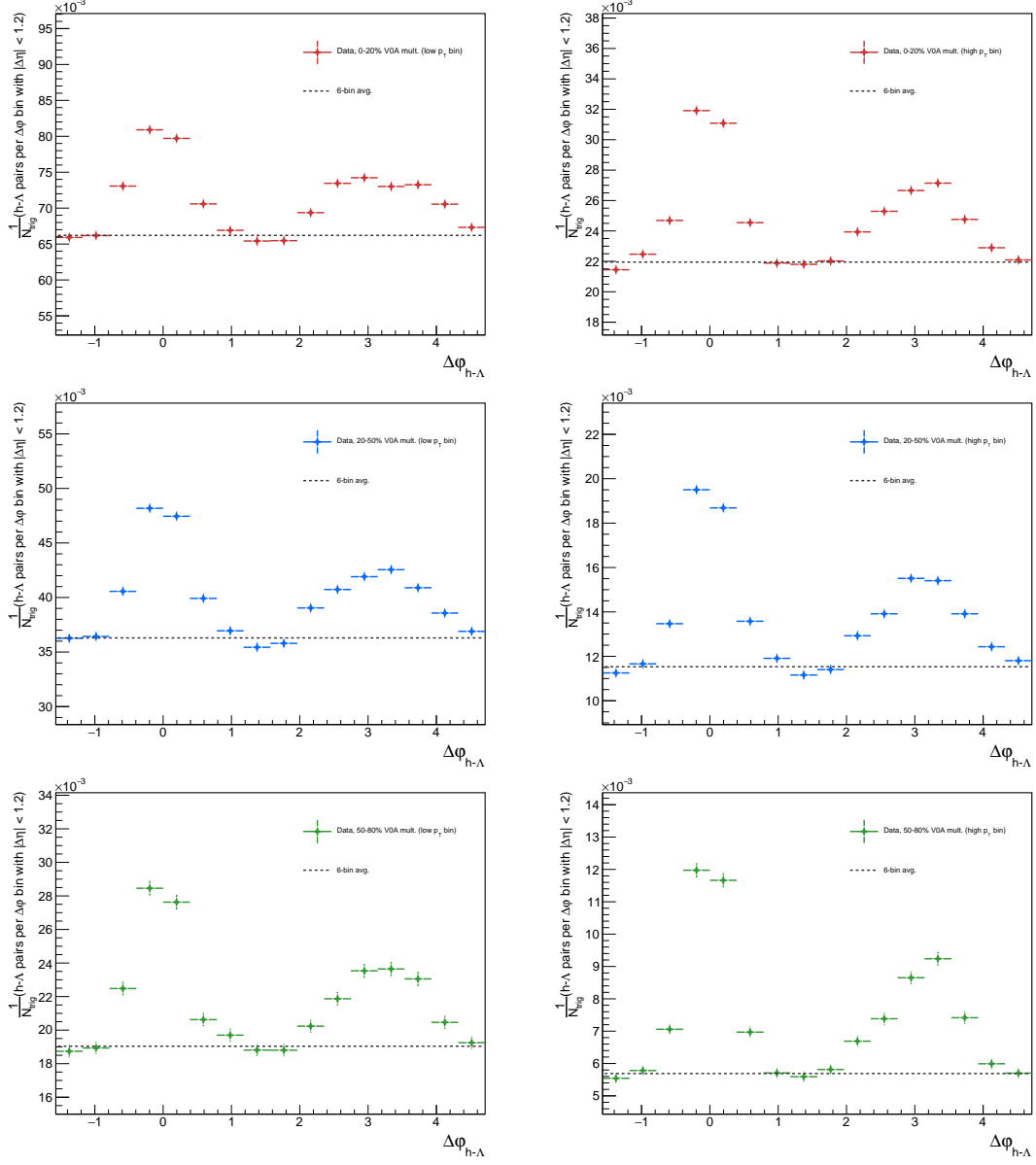


Figure 5.2: The final per-trigger h- $\Lambda$   $\Delta\varphi$  distributions for the 0-20% (top), 20-50% (middle), and 50-80% (bottom) multiplicity bins for  $1.5 < p_T < 2.5 \text{ GeV}/c$  (left) and  $2.5 < p_T < 4.0 \text{ GeV}/c$  (right).

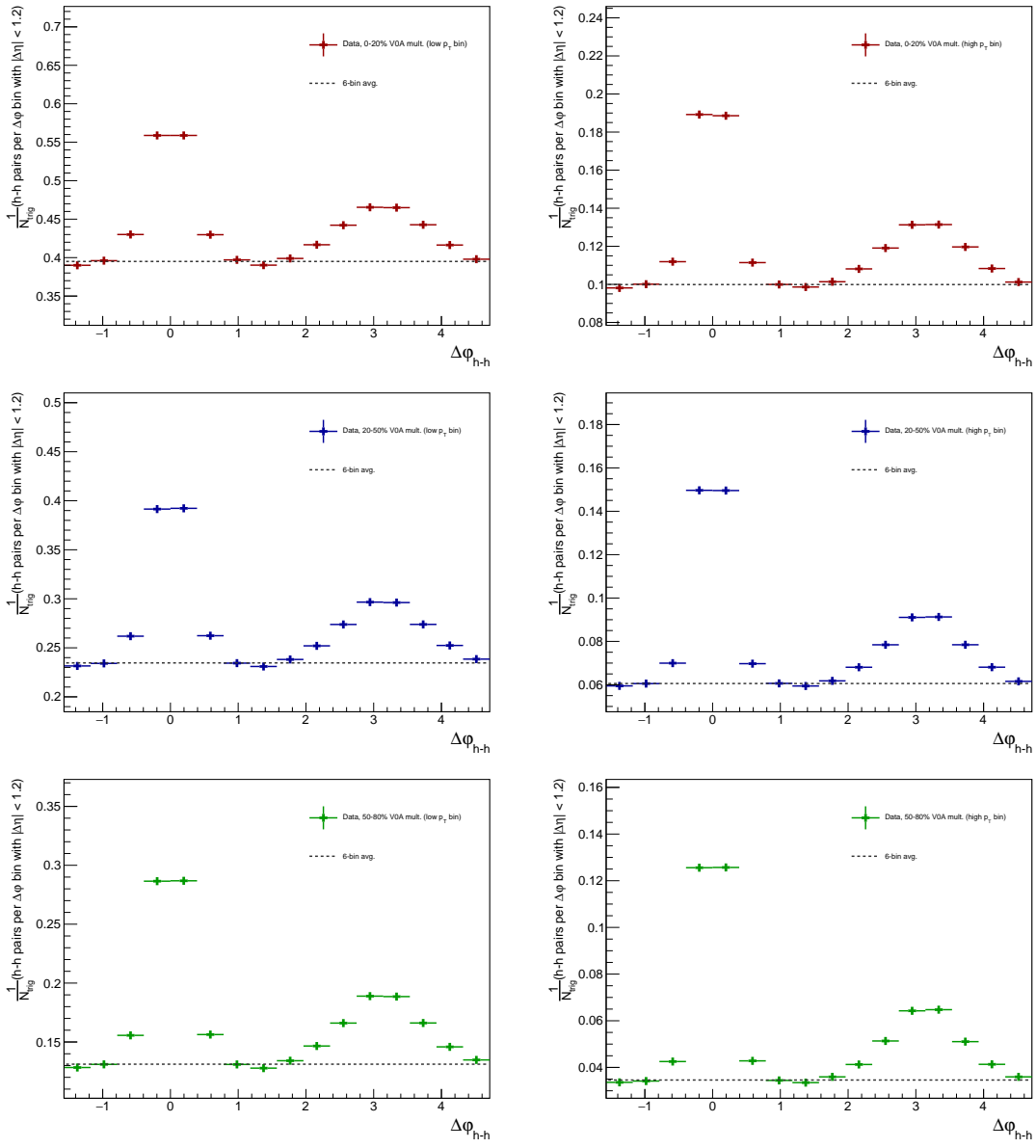


Figure 5.3: The final per-trigger h-h  $\Delta\varphi$  distributions for the 0-20% (top), 20-50% (middle), and 50-80% (bottom) multiplicity bins for  $1.5 < p_T < 2.5 \text{ GeV}/c$  (left) and  $2.5 < p_T < 4.0 \text{ GeV}/c$  (right).

### 3172 5.3 Per-trigger jet-like yields and jet widths

3173 The per-trigger yields in the near- and away-side regions of the  $\Delta\varphi$  distributions  
 3174 ( $Y_{\text{near}}$ ,  $Y_{\text{away}}$ ) are shown in each associated  $p_T$  range as a function of multiplicity  
 3175 percentile for both the h- $\Lambda$  and dihadron correlations in Figure 5.6.

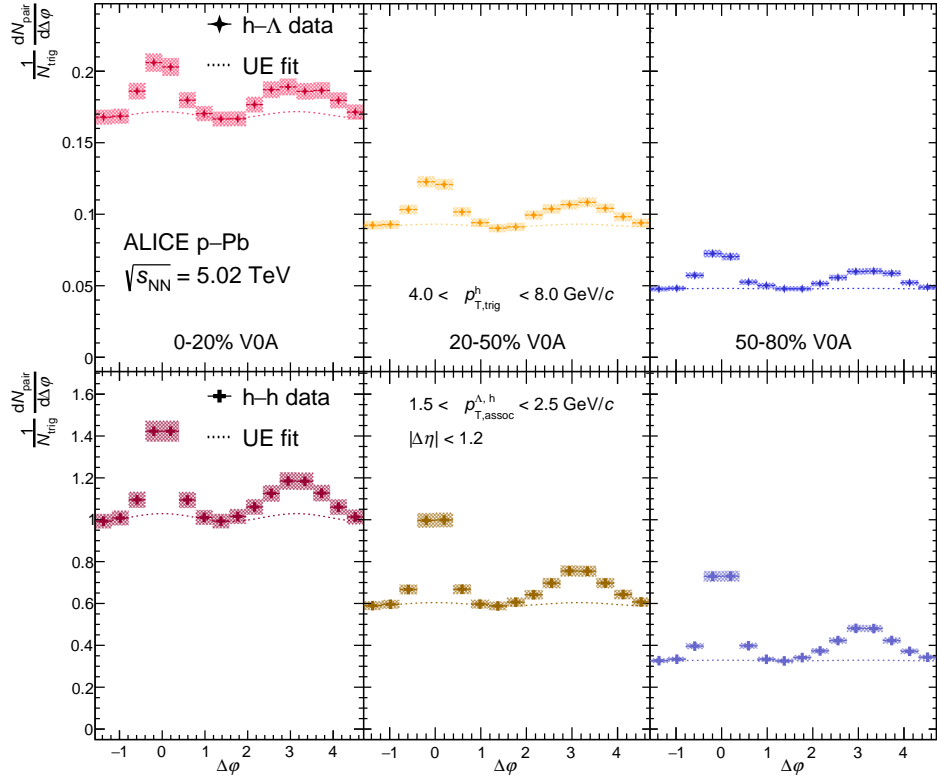


Figure 5.4: The h- $\Lambda$  (top) and h-h (bottom)  $\Delta\varphi$  distributions for each multiplicity class with  $1.5 < p_{T,\text{assoc}} < 2.5 \text{ GeV}/c$ , with statistical (systematic) uncertainties shown as vertical lines (shaded boxes). The multiplicity classes are plotted from most central (left) to least central (right). The UE estimate is shown as a dashed line, and is taken as the average of the distribution in the regions  $[-\frac{\pi}{2}, -\frac{\pi}{4}) \cup [\frac{\pi}{4}, \frac{5\pi}{8}) \cup [\frac{11\pi}{8}, \frac{3\pi}{2})$ .

3176 Across both associated  $p_T$  ranges, the h- $\Lambda$  yields see a substantial increase with  
 3177 respect to multiplicity for both the near- and away-side regions. This is in stark  
 3178 contrast to the dihadron yields, which see no significant increase as a function of mul-  
 3179 tiplicity in both associated  $p_T$  ranges. The increase can be quantified by calculating  
 3180 the percent change in the per-trigger yields from the lowest to highest multiplicity  
 3181 class, which is shown for each momentum range in Table 5.1. The errors reported are  
 3182 calculated using both the systematic and statistical uncertainties summed in quadra-  
 3183 ture, and the significance is obtained by calculating the deviation in the percent  
 3184 change from zero in terms of the total error. The significance obtained from the h- $\Lambda$   
 3185 yields across both regions and  $p_T$  ranges are all  $> 2\sigma$ , indicating that the increase is

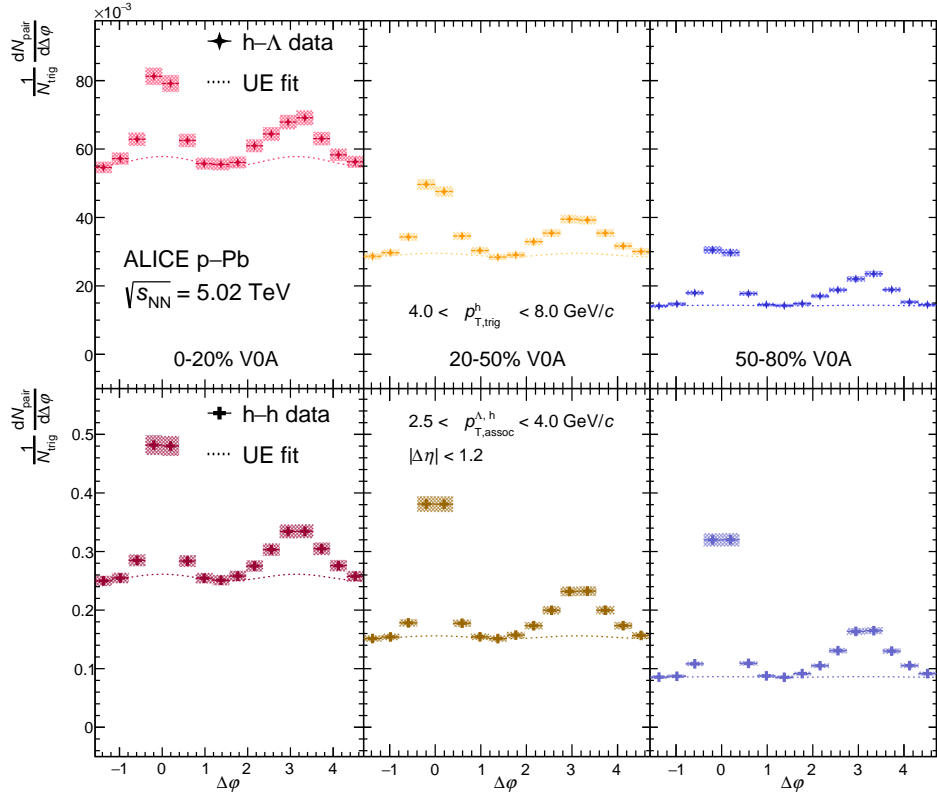


Figure 5.5: The h- $\Lambda$  (top) and h-h (bottom)  $\Delta\varphi$  distributions for each multiplicity class with  $2.5 < p_{T,\text{assoc}} < 4.0 \text{ GeV}/c$ , with statistical (systematic) uncertainties shown as vertical lines (shaded boxes). The multiplicity classes are plotted from most central (left) to least central (right). The UE estimate is shown as a dashed line, and is taken as the average of the distribution in the regions  $[-\frac{\pi}{2}, -\frac{\pi}{4}) \cup [\frac{\pi}{4}, \frac{5\pi}{8}) \cup [\frac{11\pi}{8}, \frac{3\pi}{2})$ .

statistically significant. However, the dihadron yields see no statistically significant increase in both regions across both momentum ranges. In the h- $\Lambda$  and h-h cases, the percent changes in the away-side yields are systematically higher than the changes in the near-side yields. These differences between the near- and away-side yields' behavior as a function of multiplicity hint at a possible modification of the away-side jet production due to interactions between the jet and the QGP medium.

To gain more insight to the underlying mechanisms responsible for strangeness production in jets, the widths of the near- and away-side peak regions are extracted from the h- $\Lambda$  and h-h  $\Delta\varphi$  distributions using Equations 3.5 and 3.6. Plots of these widths as a function of multiplicity for both associated momentum ranges are shown

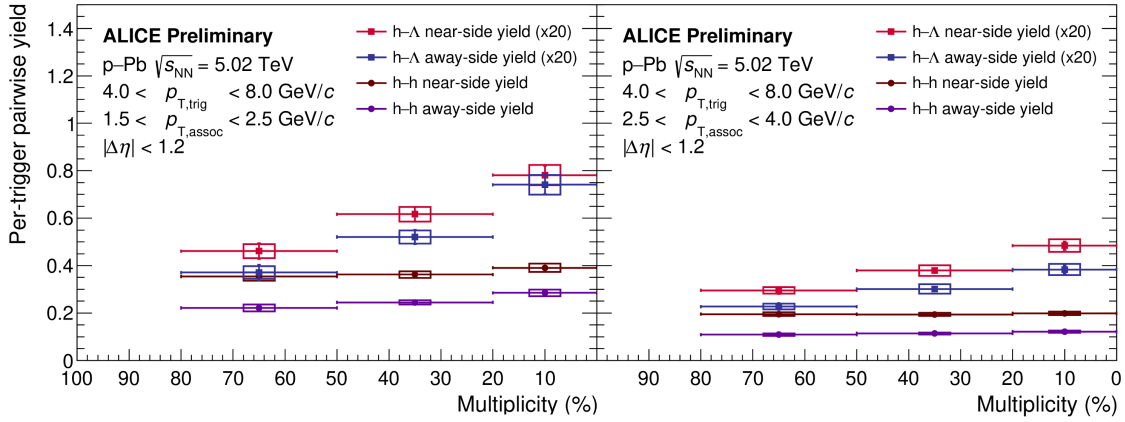


Figure 5.6: The per-trigger pair-wise yields  $Y_{\text{near}}$ ,  $Y_{\text{away}}$  as a function of multiplicity percentile for the h- $\Lambda$  (square markers) and h-h (circle markers) azimuthal correlations in the lower (left) and higher (right) associated  $p_{\text{T}}$  ranges. The statistical (systematic) uncertainties are shown as vertical lines (boxes).

Table 5.1: The percent change in the per-trigger yields from the lowest to highest multiplicity class in the lower and higher associated momentum ranges. The errors reported are obtained using the systematic and statistical uncertainties summed in quadrature. The reported significance is the number of standard deviations away from zero percent change.

Region	% change for lower (higher) $p_{\text{T, assoc}}^{\text{h},\Lambda}$	Lower (higher) $p_{\text{T, assoc}}^{\text{h},\Lambda}$	sig.
h- $\Lambda$ near-side	$47.9 \pm 16.8$ ( $46.6 \pm 14.6$ )		$2.9\sigma$ ( $3.2\sigma$ )
h- $\Lambda$ away-side	$71.0 \pm 22.5$ ( $46.2 \pm 17.9$ )		$3.2\sigma$ ( $2.6\sigma$ )
h-h near-side	$0.4 \pm 7.5$ ( $-3.9 \pm 4.3$ )		$0.1\sigma$ ( $-0.9\sigma$ )
h-h away-side	$11.7 \pm 12.3$ ( $1.0 \pm 7.0$ )		$0.9\sigma$ ( $0.1\sigma$ )

in Figure 5.7.

Expectedly, the near-side widths exhibit a significant decrease ( $>15\%$ ) from the lower momentum range to the higher for both the h- $\Lambda$  and h-h cases, indicating that higher momentum associated particles are more collimated along the jet axis. An interesting result comes from comparing the h- $\Lambda$  and h-h away-side peak widths in data, which are found to be the same within systematic uncertainties across all multiplicity and momentum ranges, although the uncertainties are very large. This contrasts with the h- $\Lambda$  near-side widths, which are around 40% ( $2\sigma$ ) larger than the h-h widths across the entire multiplicity range for both momentum ranges. This indicates that the  $\Lambda$  baryons are more readily produced in the periphery of the jet

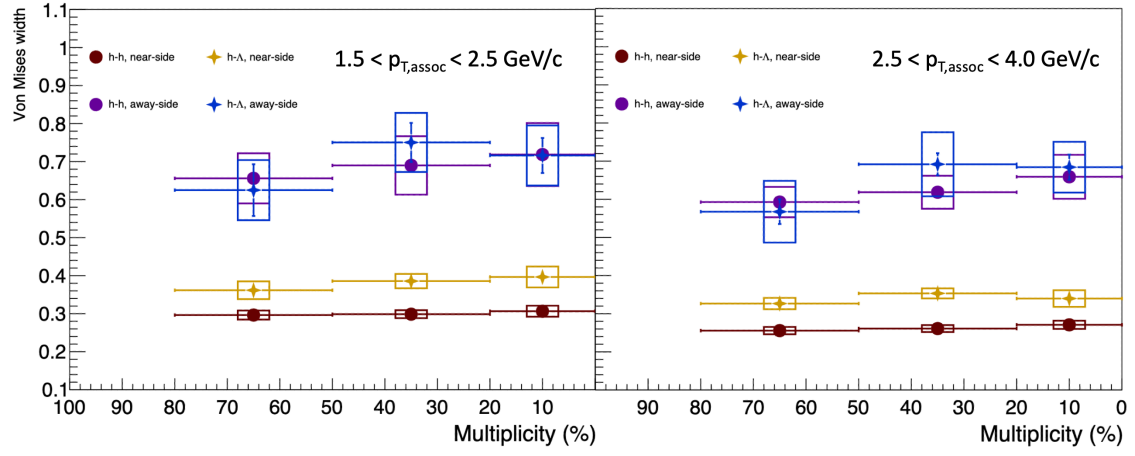


Figure 5.7: The  $h\text{-}\Lambda$  and  $h\text{-}h$  near- and away-side peak widths shown as a function of multiplicity for both associated momentum ranges. The statistical (systematic) uncertainties are shown as vertical lines (boxes).

cone, which is unexpected. Due to conservation of fourmomentum, particles with higher mass tend to be produced closer to the jet axis. As these results indicate that  $\Lambda$  baryons are being produced farther away from the jet axis than the less massive charged hadrons (pions, kaons and protons), this hints at a different underlying jet-fragmentation mechanism for  $\Lambda$  baryons than for charged hadrons. The away-side widths also exhibit a hint of broadening with increasing multiplicity, though the systematic errors are too large to exclude flat behavior.

### 5.3.1 Per-trigger yield ratios

To better understand the differences between  $\Lambda$  and charged hadron production both in and out-of jets, the per-trigger yield ratios  $R_i^{\Lambda/h} \equiv Y_i^{h-\Lambda}/Y_i^{h-h}$  ( $i = \text{near-side, away-side, UE}$ ) are measured as a function of multiplicity in both associated momentum ranges. These ratios serve as a proxy for the  $\Lambda/\pi$  ratio in each region, and are shown in Figure 5.8. Straight line fits to the data are shown as dashed lines, with slopes and corresponding errors reported in Table 5.2. To improve comparability with previous results [160], [163], the multiplicity classes have been converted to charged particle multiplicity by computing  $\langle dN_{\text{ch}}/d\eta \rangle$  in each multiplicity class in events with a trigger hadron for all charged hadrons with  $|\eta| < 0.5$  and  $p_T > 0.15 \text{ GeV}/c$ . The values of  $\langle dN_{\text{ch}}/d\eta \rangle$  for each multiplicity class in non-triggered and triggered events can be

3224 seen in Table 5.3.

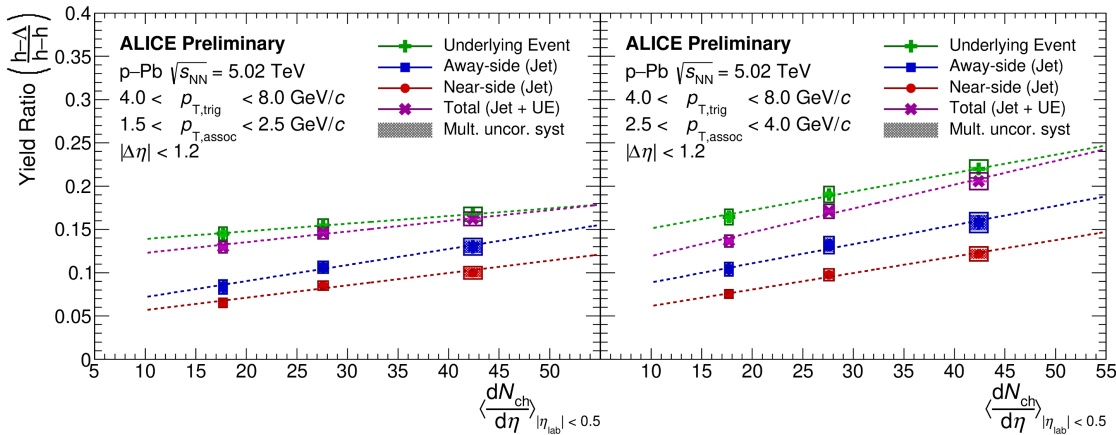


Figure 5.8: The per-trigger yield ratios  $R_i^{\Lambda/h} \equiv Y_i^{h-\Lambda}/Y_i^{h-h}$  ( $i = \text{near-side, away-side, UE}$ ) as a function of charged particle multiplicity for the lower (left) and higher (right) associated  $p_T$  ranges. The statistical (systematic) uncertainties are shown as vertical lines (boxes), and a first order polynomial fit to the data is shown as a dashed line.

3225 One surprising feature of these results is the clear separation between the ratios in  
 3226 each region across the entire multiplicity range in both momentum ranges, with the  
 3227 UE ratio being the largest, followed by the away-side ratio, and finally the near-side.  
 3228 This indicates that most of the relative  $\Lambda$  production is occurring in the UE, which  
 3229 is consistent with the idea that  $s$ -quark production is maximal in the QGP medium.  
 3230 This is further supported by the fact that the away-side ratio is larger than the  
 3231 near-side, as  $\Lambda$  production on the away-side is likely due to both the fragmentation  
 3232 of the away-side jet coupled with the possible production of strange quarks due to  
 3233 jet-medium interactions.

3234 The near- and away-side slopes reported in Table 5.2 are all more than  $2\sigma$  greater  
 3235 than zero, indicating that there is an enhancement of relative  $\Lambda$  production in jets  
 3236 as a function of multiplicity. This result is consistent with previous measurements  
 3237 of the  $\phi(1020)$  meson in jets [142], where a similar enhancement of the  $\phi/h$  ratio  
 3238 is observed in the near- and away-side regions. This provides further evidence that  
 3239 the production of strange quarks is enhanced in jets, which was thought to only be  
 3240 a feature of the QGP. The away-side slopes are also systematically larger than the  
 3241 near-side slopes in both momentum ranges, again hinting at possible modification

Table 5.2: The slopes obtained from the straight-line fits to the per-trigger pair-wise  $(h-\Lambda)/(h-h)$  yield ratios as a function of multiplicity in both associated momentum ranges. The fits are made using the statistical and systematic errors summed in quadrature. All fits are such that  $\chi^2/\text{ndf} < 1$ .

Region	Lower $p_{T, \text{assoc}}^{\text{h},\Lambda}$ slope ( $\times 10^{-3}$ )	Higher $p_{T, \text{assoc}}^{\text{h},\Lambda}$ slope ( $\times 10^{-3}$ )
Near-side	$1.1 \pm 0.4$	$1.6 \pm 0.4$
Away-side	$1.6 \pm 0.6$	$1.8 \pm 0.7$
UE	$0.9 \pm 0.1$	$2.2 \pm 0.2$

Table 5.3: The values of  $\langle dN_{\text{ch}}/d\eta \rangle_{|\eta_{\text{lab}}|<0.5}$  for each multiplicity class in min bias events (non-triggered) and events with a trigger hadron (triggered events).

Mult. class	$\langle dN_{\text{ch}}/d\eta \rangle$ (non-triggered)	$\langle dN_{\text{ch}}/d\eta \rangle$ (triggered)
0-20%	$35.6 \pm 0.9$	$42.4 \pm 0.9$
20-50%	$21.5 \pm 0.5$	$27.6 \pm 0.5$
50-80%	$12.0 \pm 0.3$	$17.7 \pm 0.4$

of the away-side  $s$ -quark production due to jet-medium interactions. Similarly, the UE slopes are not compatible with zero, but the value is smaller than the near- and away-side slopes by about  $1\sigma$  in the lower momentum range. However, the larger values of the UE ratios overall still suggest that a significant portion of the observed enhancement in the  $\Lambda/\pi$  ratio is due to softer production from the within the UE (QGP).

## 5.4 Model comparisons

This section details how the results of this analysis compare to some of the best p–Pb model predictions. The models included in these comparisons are the ones detailed in Section 1.6, namely PHSD, EPOS and DPMJET.

For each of these comparisons, the same techniques and cuts are applied as they were in data (if applicable). None of the corrections used in data (namely those in Equation 3.2) are applied to the models, with the exception of the mixed-event acceptance correction procedure. As both the trigger and associated particles have  $|\eta| < 0.8$ , this procedure corrects for the artificial triangular shape in the  $\Delta\eta$  correlation (see Section 4.5.2 for more details).

3258 **5.4.1 Per-trigger 2D  $\Delta\varphi\Delta\eta$  distributions**

3259 The multiplicity-integrated per-trigger  $h - \Lambda$  and  $h - h$  2D  $\Delta\eta\Delta\varphi$  distributions in  
3260 data and for each model can be seen in Figures 5.10 (h- $\Lambda$ ) and 5.9 (h-h). These  
3261 distributions were generated in the lower associated momentum bin ( $1.5 < p_T < 2.5$   
3262 GeV/ $c$ ) to maximize the statistics across all models. The h-h distributions for each  
3263 model exhibit some unique characteristics. For DPMJET, the correlation shape in  
3264 both the near- and away-side regions matches the data moderately well, though the  
3265 away-side width along  $\Delta\varphi$  appears more collimated. Furthermore, DPMJET exhibits  
3266 no elliptic flow (seen as a sinusoidal pattern at large  $\Delta\eta$ ), whereas the data has  
3267 a visible flow component. This is not unexpected. As mentioned in Section 1.6,  
3268 DPMJET does not have an explicit QGP phase, and therefore any collective flow  
3269 effects should not be present.

3270 EPOS-LHC, on the other hand, has a very large flow component, well beyond  
3271 that of the data. Additionally, the away-side jet region in EPOS-LHC appears to be  
3272 completely washed-out. This is likely due to the hydrodynamic core of EPOS-LHC,  
3273 which produces this collective flow at the expense of a loss of information from the  
3274 initial hard-scatterings that produce the jets. As the Lund string density is greater  
3275 on the away-side than the near-side, it is more likely for the strings in the away-side  
3276 to form the core. This core, once formed, loses all of its correlations from the initial  
3277 partonic scatterings, and thus the away-side jet correlation is destroyed.

3278 The yields and shape of the dihadron distribution from PHSD appears to match  
3279 the data the best, with well-defined near- and away-side peaks, as well as a flow com-  
3280 ponent that is similar to the data. The presence of this flow component is surprising,  
3281 as PHSD is a microscopic transport model, where all of the constituent particles (par-  
3282 tons, hadrons and strings) are treated as individual particles that interact with each  
3283 other. For such a fundamental model to produce this collective behavior is a refresh-  
3284 ing deviation from models that “force” this behavior through hydrodynamic means.  
3285 However, the near-side peak appears to be lower in PHSD than in data, indicating  
3286 that the description of jets within PHSD is not perfect.

3287 For the h- $\Lambda$  distributions, the story is a bit different. DPMJET still overestimates  
3288 the jet peaks and exhibits no flow, but the overall h- $\Lambda$  yield is now substantially  
3289 lower than it is in data. The distribution from EPOS-LHC now shows very little  
3290 signs of a near-side jet region, indicating that the production of  $\Lambda$  baryons is coming

3291 almost *entirely* from the hydrodynamic core. Still, the h- $\Lambda$  yields from EPOS are  
3292 the closest to data, indicating that this core does a good job of making  $\Lambda$  baryons  
3293 (but a bad job at telling them where to go). The PHSD distribution is the most  
3294 interesting, as it appears to be dominated by statistical fluctuations. As the PHSD  
3295 yields are generated across 1.2 billion events (over twice as much as data and the other  
3296 event generators), the conclusion is quite simple: PHSD does not produce enough  $\Lambda$   
3297 baryons in events that have a trigger. This was investigated more thoroughly, and it  
3298 was found that PHSD produces a factor of 10 less events with both a trigger hadron  
3299 and a  $\Lambda$  baryon than in data, shown in Figure 5.11. In data, around 2% of the event  
3300 sample has both a trigger hadron and a  $\Lambda$  baryon, whereas in PHSD this number is  
3301 around 0.2%. In order to generate the same number of h- $\Lambda$  pairs as seen in data, over  
3302 4 billion PHSD events would need to be generated, requiring a significant amount of  
3303 computing resources.

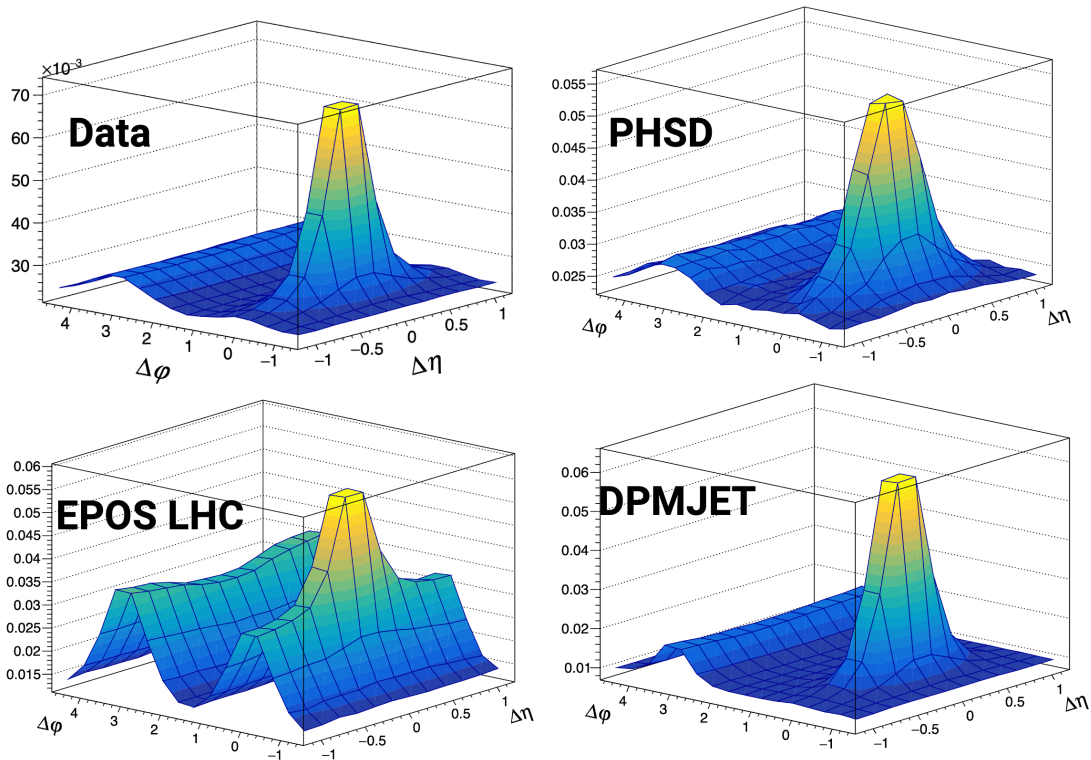


Figure 5.9: The multiplicity-integrated per-trigger h-h 2D  $\Delta\varphi\Delta\eta$  distributions in data and for each model within the  $1.5 < p_T < 2.5$  GeV/ $c$  associated momentum bin.

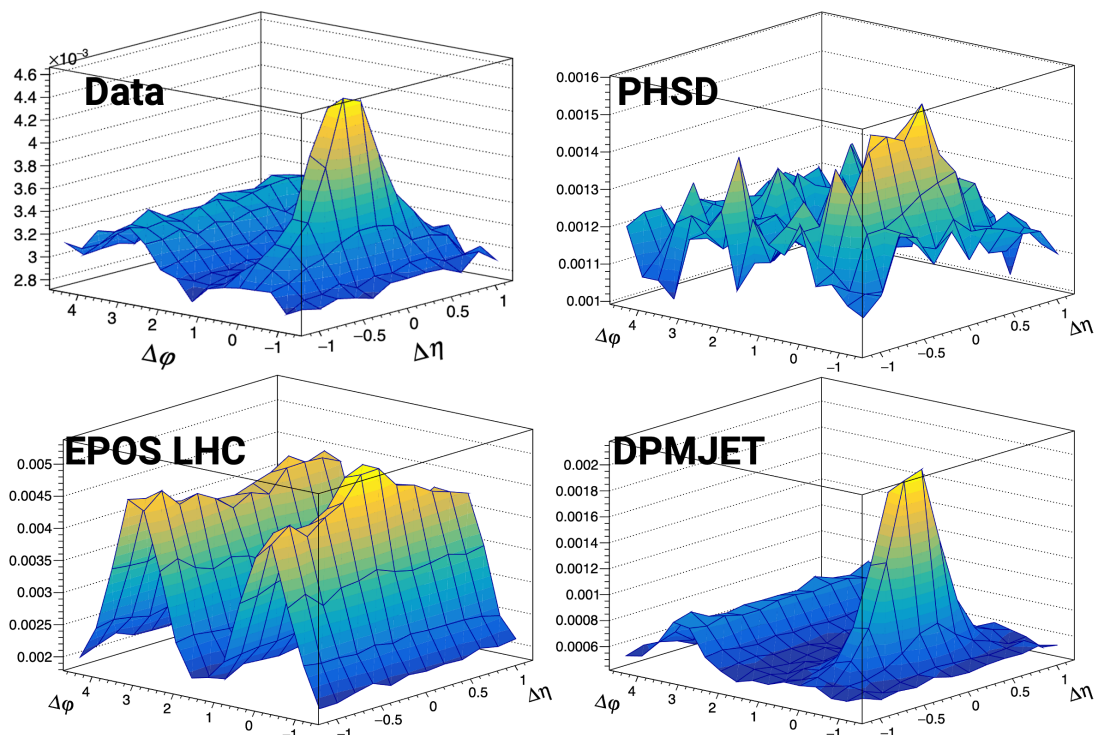


Figure 5.10: The multiplicity-integrated per-trigger h- $\Lambda$  2D  $\Delta\varphi\Delta\eta$  distributions in data and for each model within the  $1.5 < p_T < 2.5$  GeV/ $c$  associated momentum bin.

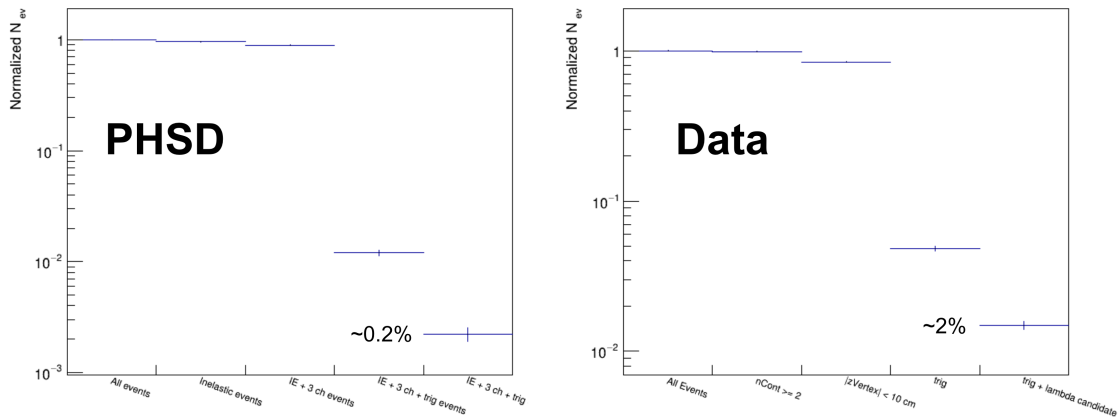


Figure 5.11: The fraction of events that pass various selection criteria for PHSD (left) and data (right). The right-most bin in both distributions represents the fraction of events that contribute to the h- $\Lambda$  yield, which is 10 times lower in PHSD than it is in data.

### 3304 5.4.2 Per-trigger $\Delta\varphi$ distributions

3305 The  $\Delta\varphi$  distributions generated by projecting the previous 2D distributions (Figures 5.9 and 5.10) in the  $|\Delta\eta| < 1.2$  range can be seen in Figures 5.13 (h- $\Lambda$ ) and 5.12  
 3306 (h-h). While most of the distinct features for each model have already been addressed  
 3307 in terms of the 2D distributions, projecting onto  $\Delta\varphi$  reveals a few more interesting  
 3308 properties.

3310 For the dihadron case, the shape of the  $\Delta\varphi$  distribution in PHSD looks nearly  
 3311 *identical* to the data. Even the yields are mostly correct, though the jet-like regions  
 3312 are slightly underestimated. The EPOS-LHC distribution is the perfect example  
 3313 of why it is important to first look at the 2D distribution *before* projecting: there  
 3314 appears to be an away-side peak of comparable size to the near-side, but the 2D  
 3315 distribution reveals that this is entirely due to flow. Projecting onto  $\Delta\varphi$  also makes  
 3316 it more clear that DPMJET does not accurately predict the UE contribution, which  
 3317 is nearly three times less than it is in data (0.12 vs. 0.29). The same can be said  
 3318 about the h- $\Lambda$  distributions, with the exception of PHSD. While the near-side peak  
 3319 is clearly visible, and its shape is somewhat similar to that in data, the away-side  
 3320 jet appears to have inexplicably vanished. Unfortunately the explanation for this is

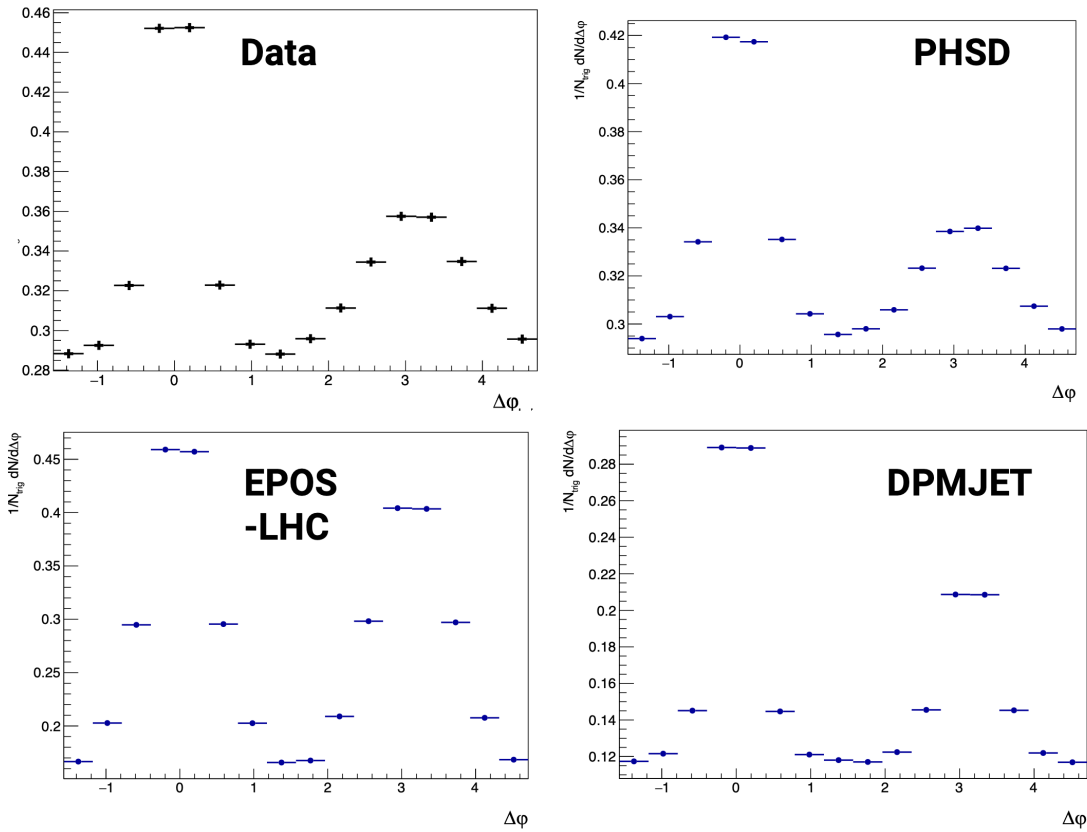


Figure 5.12: The multiplicity-integrated per-trigger h-h  $\Delta\varphi$  distributions in data and for each model within the  $1.5 < p_T < 2.5$  GeV/c associated momentum bin.

3321 not as cut-and-dry as it was for EPOS-LHC, as PHSD has no hydrodynamic core.  
 3322 The investigation into this effect is still ongoing, and may be addressed in a future  
 3323 publication.

3324 Do to a lack of away-side jet peak in both EPOS-LHC and PHSD (and the over-  
 3325 whelming flow contribution to the  $\Delta\varphi$  distribution in the case of EPOS-LHC), these  
 3326 models are excluded from the rest of the analysis. It is worth mentioning again,  
 3327 however, that PHSD shows promising initial results for dihadron correlation anal-  
 3328 yses. If the issues with the h- $\Lambda$  distributions can be resolved, PHSD looks like an  
 3329 excellent theoretical framework for these studies. The remainder of this section will  
 3330 focus on DPMJET, which, while clearly lacking in some areas, consistently exhibits  
 3331 a well-defined near- and away-side jet peak with a quantifiable UE contribution.

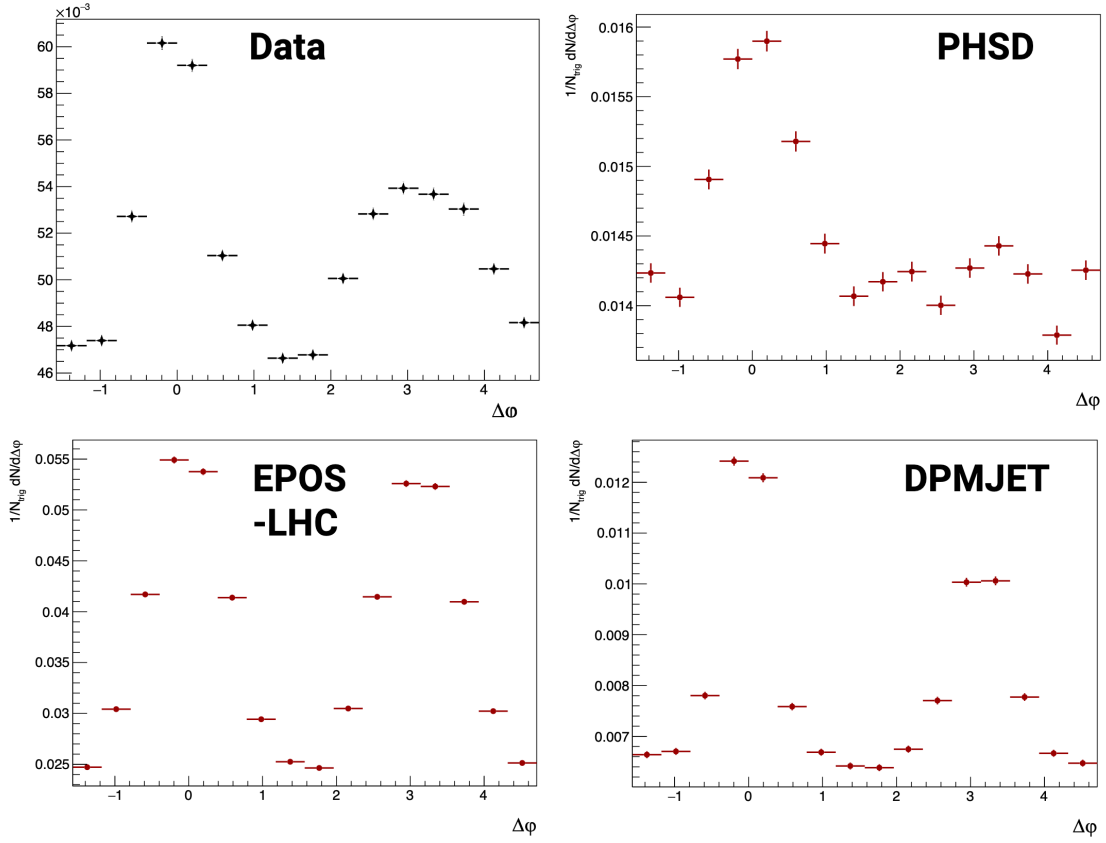


Figure 5.13: The multiplicity-integrated per-trigger h- $\Lambda$   $\Delta\varphi$  distributions in data and for each model within the  $1.5 < p_T < 2.5$  GeV/ $c$  associated momentum bin.

### 3332 5.4.2.1 Systematic uncertainties for DPMJET

3333 While most of the systematic variations considered for this analysis are not relevant  
 3334 for model predictions, both the yield extraction procedure and width extraction pro-  
 3335 cedure have systematic uncertainties that should be taken into account. As such,  
 3336 a table of the systematic uncertainties for the DPMJET model predictions in each  
 3337 multiplicity bin is provided in Tables 5.4 (h- $\Lambda$ ) and 5.5 (h-h). As these uncertainties  
 3338 are independent of associated  $p_T$ , only the 1.5 - 2.5 GeV/ $c$  associated momentum bin  
 3339 are given.

Mult. Bin	NS width	AS width	NS yield	AS yield	UE yield
0-20%	1.0	0.9	0.6	0.9	0.8
20-50%	1.0	1.6	0.7	0.8	0.9
50-80%	0.4	1.0	0.6	0.8	0.6

Table 5.4: The total systematic uncertainties associated with the various width and yield extraction procedures in DPMJet for the h- $\Lambda$  distributions.

Mult. Bin	NS width	AS width	NS yield	AS yield	UE yield	
0-20%	0.9	1.2	1.0	0.7	0.9	0.0
20-50%	0.7	1.2	1.0	0.7	0.7	0.0
50-80%	0.3	1.3	0.6	0.7	0.6	0.0

Table 5.5: The total systematic uncertainties associated with the various width and yield extraction procedures in DPMJet for the h-h distributions.

### 5.4.3 Per-trigger jet-like yields and jet widths

A comparison between the per-trigger jet-like yields in data and the same yields predicted by DPMJET for each associated  $p_T$  range as a function of multiplicity can be seen in Figure 5.14. Straight line fits of the data are shown as dashed lines. The same yields obtained using DPMJET shown as bands representing their systematic uncertainty, with a ratio to the data presented in the bottom panel. A dashed line at unity is drawn to help better visualize the deviations between data and the model.

The per-trigger near- and away-side yields predicted by DPMJET are mostly consistent with data in the dihadron case. This can be seen in the model/data ratio, with both the near- and away-side ratios remaining close to unity across the entire multiplicity range. The h- $\Lambda$  yields, however, are not well described by the model. Both the near- and away-side h- $\Lambda$  yields predicted by DPMJET are lower than data by around a factor of two across the entire multiplicity range in both momentum ranges, and there is no significant increase in these yields as a function of multiplicity. This is not unexpected: as mentioned in the previous section, DPMJET does not appear to exhibit *any* medium effects, and thus any possible enhancement in the production of  $\Lambda$  baryons due to the formation of a QGP is not present.

A comparison between DPMJET and data for the near- and away-side jet widths for each associated  $p_T$  range as a function of multiplicity is also presented in Figure 5.15. Again, straight line fits of the data are shown as dashed lines, and the widths

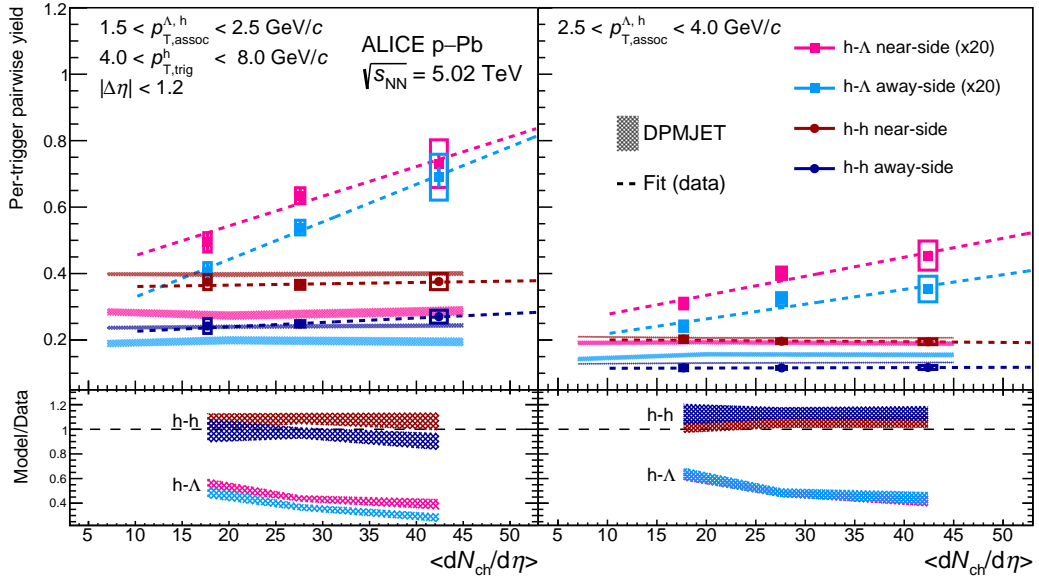


Figure 5.14: The per-trigger pair-wise yields  $Y_{\text{near}}$ ,  $Y_{\text{away}}$  as a function of charged particle multiplicity for the h- $\Lambda$  (square markers) and h-h (circle markers) correlations in the lower (left) and higher (right) associated  $p_{\text{T}}$  ranges. The statistical (systematic) uncertainties are shown as vertical lines (boxes), and a first order polynomial fit to the data is shown as a dashed line. The same yields predicted by DPMJET are also shown as shaded bands, with the width of the band representing the systematic uncertainty on the model. The ratio of the model to the data is shown in the bottom panel, along with a dashed line drawn at unity.

3360 obtained using DPMJET are shown as bands representing their systematic uncer-  
 3361 tainty. A model/data ratio is also given in the bottom panel, with a dashed line  
 3362 drawn at unity.

3363 For the h-h near-side widths, DPMJET describes the data well across both mo-  
 3364 mentum ranges, with a  $< 5(10)\%$  deviation from data seen in the lower (higher)  
 3365 momentum range. DPMJET also predicts the h- $\Lambda$  near-side width to be larger than  
 3366 the h-h width, though the values of the h- $\Lambda$  widths are much lower than they are in  
 3367 data. An alternative explanation to the one given in Section 5.3 for these differences  
 3368 between the near-side widths is that they could be due to the presence of gluon jets,  
 3369 which are generally more wide than quark jets [164] and exhibit an increased pro-  
 3370 duction of  $\Lambda$  baryons [165]. As DPMJET includes both quark and gluon jets, it is  
 3371 possible that the predicted differences between the h- $\Lambda$  and h-h near- and away-side  
 3372 peak widths are due to this effect. DPMJET also under-predicts both the h- $\Lambda$  and

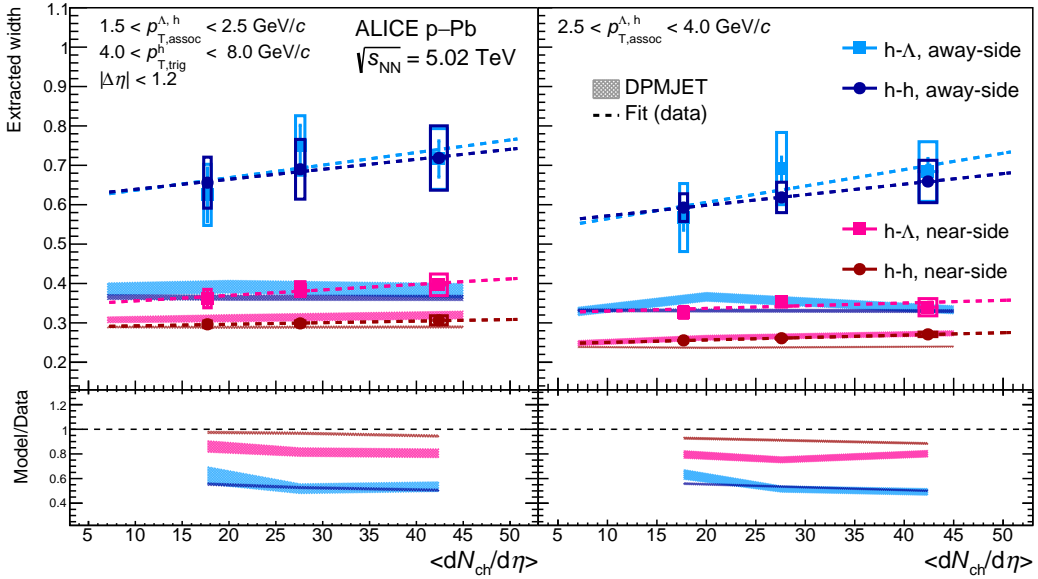


Figure 5.15: The h- $\Lambda$  and h-h near- and away-side peak widths shown as a function of multiplicity for both associated momentum ranges, along with a straight-line fit to the data. The statistical (systematic) uncertainties are shown as vertical lines (boxes). The ratios predicted by DPMJET are also presented as shaded bands, with the width of the band representing the systematic uncertainty on the model. The ratio of the model to the data is presented in the bottom panel, along with a dashed line drawn at unity.

3373 h-h away-side widths by around 40% across both momentum ranges. As the DP-  
 3374 MJET model does not include any medium effects, this suggests that the away-side  
 3375 peak widths in data are possibly “broadened” by jet-medium interactions. However,  
 3376 the larger uncertainties on the away-side widths prevent the exclusion of flat behav-  
 3377 ior with respect to multiplicity (i.e. increasing medium size), as the slopes are all  
 3378 consistent with zero within uncertainties.

### 3379 5.4.4 Per-trigger yield ratios

3380 A comparison between the per-trigger yield ratios in data and using DPMJET for each  
 3381  $p_T$  bin as a function of multiplicity are shown in Figure 5.16. As before, straight line  
 3382 fits of the data are shown as dashed lines, and the widths obtained using DPMJET  
 3383 are shown as bands representing their systematic uncertainty. A model/data ratio is  
 3384 also presented in the bottom panel, with a dashed line drawn at unity.

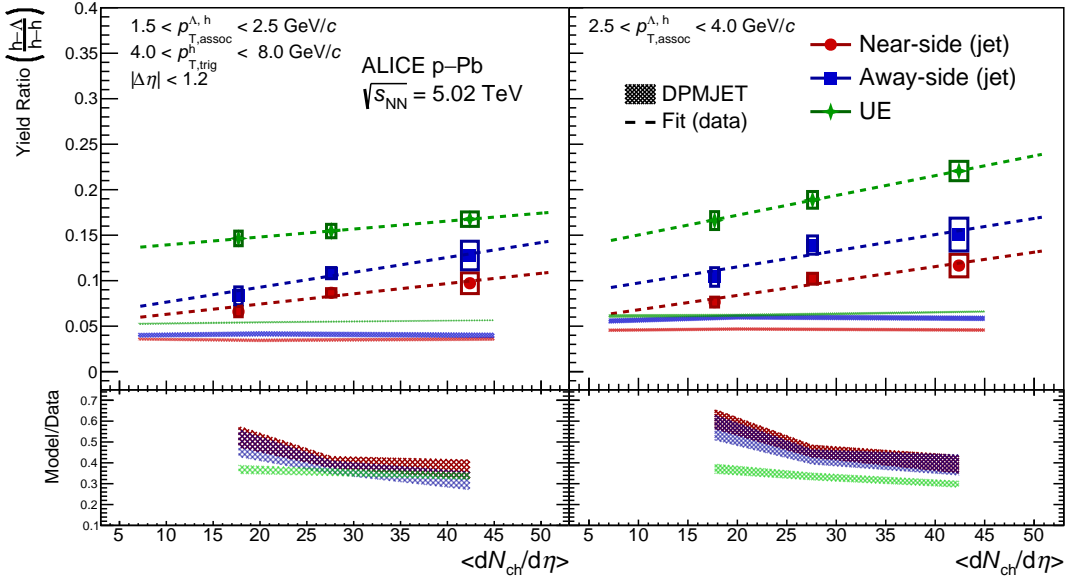


Figure 5.16: The per-trigger pair-wise yield ratios  $R_i^{\Lambda/h} \equiv Y_i^{h-\Lambda}/Y_i^{h-h}$  ( $i = \text{near-side, away-side, UE}$ ) as a function of multiplicity in the lower (left) and higher (right) associated momentum ranges. The statistical (systematic) uncertainties are shown as vertical lines (boxes). The ratios predicted by DPMJET are also presented as shaded bands, with the width of the band representing the systematic uncertainty on the model. The ratio of the model to the data is presented in the bottom panel.

3385     Unsurprisingly (given the discussions in Section 5.4.2), DPMJET underpredicts  
 3386     these ratios across the entire multiplicity range for both  $p_T$  bins. However, the straight  
 3387     line fits to the data appear like they may converge to DPMJET at sufficiently low  
 3388     multiplicities, indicating that DPMJET may be able to describe the magnitudes of  
 3389     these ratios in lower multiplicity pp collisions. This is not unexpected, as these  
 3390     lower multiplicity collisions are mostly described by the Lund string component of  
 3391     DPMJET, which is notorious for describing many features of these smaller collision  
 3392     systems [90]. While DPMJET is not able to predict any of the multiplicity-dependent  
 3393     behavior seen in data, it is able to produce the observed ordering in the ratios (UE  $i$   
 3394     away-side  $\not\sim$  near-side), which indicates that the dominating production mechanisms  
 3395     for  $\Lambda$  baryons within DPMJET come from the softer, less-correlated DPM processes.

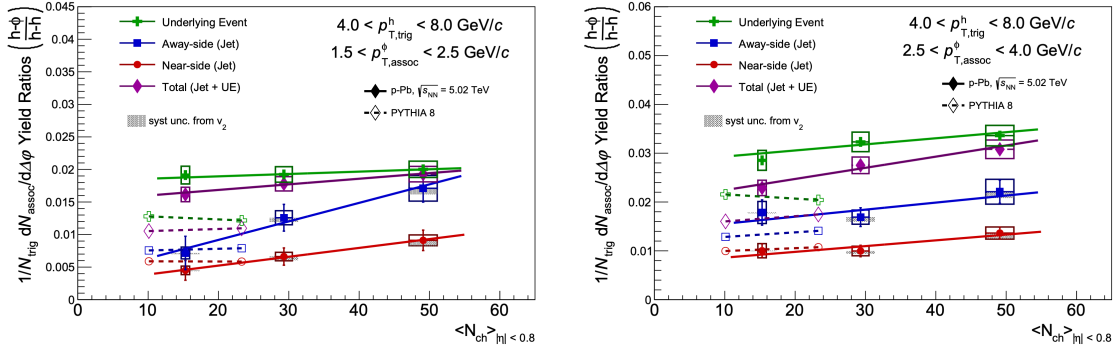


Figure 5.17: Previously published results for the per-trigger pair-wise yield ratios  $R_i^{\phi/h} \equiv Y_i^{h-\phi}/Y_i^{h-h}$  ( $i = \text{near-side, away-side, UE, total}$ ) as a function of charged particle multiplicity for lower (left) and higher (right) associated  $p_T$  ranges.

## 3396 5.5 Comparison with the $\phi(1020)$

3397 The  $\phi(1020)$  meson's net strangeness  $|S|$  is equal to zero. Despite this, it has been  
 3398 observed to exhibit a similar enhancement in production as a function of multiplicity  
 3399 as other hadrons with non-zero strangeness [166]. Due to their similar masses ( $\Delta M <$   
 3400  $100 \text{ MeV}/c^2$ ), the  $\phi(1020)$  is an excellent candidate to compare directly with the  $\Lambda$   
 3401 in order to better understand the differences between open ( $|S| \neq 0$ ) and hidden  
 3402 ( $|S| = 0$ ) strange hadron production. Using previously published results on  $\phi(1020)$   
 3403 production in and out-of jets in p–Pb collisions at  $\sqrt{s_{\text{NN}}} = 5.02 \text{ TeV}$  [142] (shown  
 3404 in Figure 5.17), the per-trigger pair-wise yield ratios  $R_i^{\Lambda/\phi} \equiv Y_i^{h-\Lambda}/Y_i^{h-\phi}$  ( $i = \text{near-}$   
 3405  $\text{side, away-side, UE}$ ) can be measured as a function of multiplicity. These ratios  
 3406 are presented in Figure 5.18 for both the lower and higher associated  $p_T$  ranges.  
 3407 Again, straight line fits to the data are shown as a dashed lines, with the slopes and  
 3408 corresponding errors reported in Table 5.6. The same ratios predicted by DPMJET  
 3409 are also presented, with a ratio to the data presented in the bottom panel.

3410 Interestingly,  $\Lambda/\phi$  near-side ratios are systematically higher than the ratios in all  
 3411 other regions across the entire multiplicity range and both momentum ranges. This  
 3412 indicates relative enhancement (suppression) of  $\Lambda$  ( $\phi$ ) production along the jet axis.  
 3413 As strangeness is always produced in the form of  $s\bar{s}$  pairs, one possible explanation  
 3414 of this effect is that when these pairs are produced from jet fragmentation, the  $s$  and  
 3415  $\bar{s}$  are less likely to hadronize into the same  $\phi$  due to their separation in phase-space.

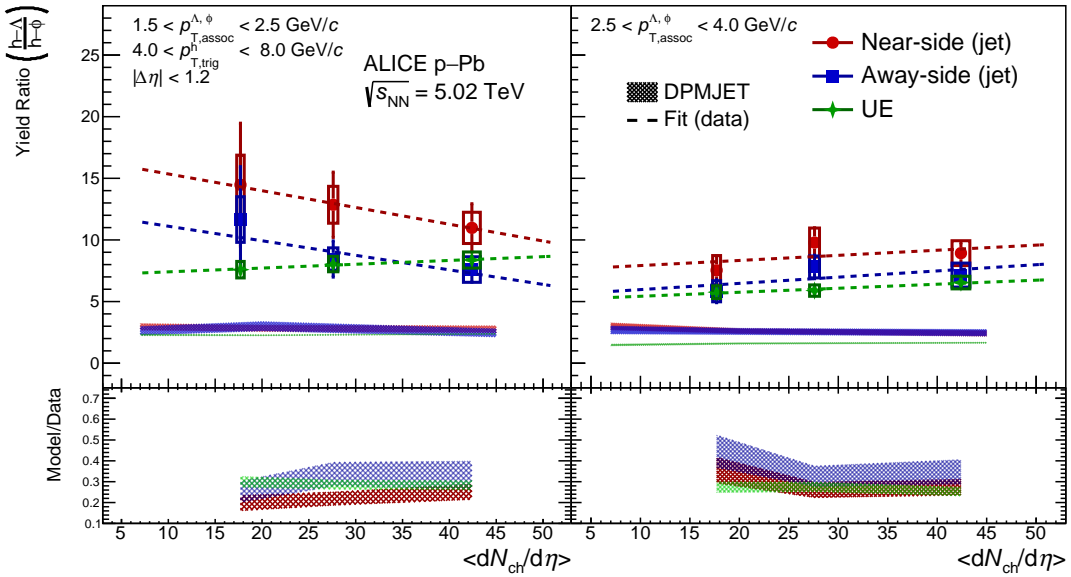


Figure 5.18: The per-trigger pair-wise yield ratios  $R_i^{\Lambda/\phi} \equiv Y_i^{h-\Lambda}/Y_i^{h-\phi}$  ( $i = \text{near-side, away-side, UE}$ ) as a function of multiplicity in the lower (left) and higher (right) associated momentum ranges. The statistical (systematic) uncertainties are shown as vertical lines (boxes). The ratios predicted by DPMJET are also presented as shaded bands, with the width of the band representing the systematic uncertainty on the model. The ratio of the model to the data is presented in the bottom panel.

3416 The away-side ratios are higher than the UE ratios on average, but the difference is  
 3417 not as pronounced as in the near-side. The ratios predicted by DPMJET provide  
 3418 further evidence for this explanation, as the model shows the near- and away-side  
 3419 ratios are systematically higher than the UE ratios across the entire multiplicity  
 3420 range. However, DPMJET predicts no differences between the near- and away-side  
 3421  $\Lambda/\phi$  ratios, possibly due to the missing medium effects in the model. While the  
 3422 central values of the near- and away-side ratios in the lower associated momentum  
 3423 range decrease with increasing multiplicity, the uncertainties are very large. All of  
 3424 the slopes presented in Table 5.6 are compatible with zero, indicating no dependence  
 3425 on multiplicity for the  $\Lambda/\phi$  ratios.

3426 The near- and away-side slopes reported in Table 5.2 are all more than  $2\sigma$  greater  
 3427 than zero, indicating that there is an enhancement of relative  $\Lambda$  production in jets as  
 3428 a function of multiplicity. This result is consistent with previous measurements of the  
 3429  $\phi(1020)$  meson in jets [142], where a similar enhancement of the  $\phi/h$  ratio is observed

Table 5.6: The slopes obtained from the straight-line fits to the per-trigger pair-wise  $(h-\Lambda)/(h-\phi)$  yield ratios as a function of multiplicity in both associated momentum ranges. The fits are made using the statistical and systematic errors summed in quadrature. All fits are such that  $\chi^2/\text{ndf} < 1$ .

Region	Lower $p_{T, \text{assoc}}^{\Lambda,\phi}$ slope ( $\times 10^{-1}$ )	Higher $p_{T, \text{assoc}}^{\Lambda,\phi}$ slope ( $\times 10^{-1}$ )
Near-side	$-1.6 \pm 2.0$	$0.2 \pm 0.9$
Away-side	$-1.1 \pm 1.4$	$0.3 \pm 0.7$
UE	$0.3 \pm 0.4$	$0.3 \pm 0.3$

in the near- and away-side regions. This provides further evidence that the production of strange quarks is enhanced in jets. The away-side slopes are also systematically larger than the near-side slopes in both momentum ranges, again hinting at possible modification of the away-side  $s$ -quark production due to jet-medium interactions. Similarly, the UE slopes are not compatible with zero, but the value is smaller than the near- and away-side slopes by about  $1\sigma$  in the lower momentum range. However, the larger values of the UE ratios overall still suggest that a significant portion of the observed enhancement in the  $\Lambda/\pi$  ratio is due to softer production from the UE. The slopes calculated using the ratios obtained from DPMJET are all nearly exactly zero, and are thus not shown in the table.

## Chapter Six: Summary and outlook

3441 Quantum chromodynamics (QCD) is the theory that describes how the protons and  
3442 neutrons, which compose almost all ordinary matter, are bound to one another within  
3443 the nucleus of an atom. In this theory, the fundamental constituents of matter are  
3444 *not* protons and neutrons, but rather quarks and gluons. These quarks and gluons  
3445 bind together through their color charge, creating the color neutral hadrons observed  
3446 in nature. One of the most interesting predictions of QCD is that, at extreme temper-  
3447 atures and densities, these hadrons dissolve into their constituent quarks and gluons,  
3448 forming a new state of matter known as the Quark-Gluon Plasma (QGP). Under-  
3449 standing the QGP, which is thought to be the state of the universe shortly after the  
3450 Big Bang, can help answer questions about the nature of everyday matter and the  
3451 evolution of the universe.

3452 Studying the QGP requires recreating the extreme conditions of the early uni-  
3453 verse, which can only be achieved through high energy particle collisions. In such  
3454 collisions, however, the QGP is only produced for a very short time, after which it  
3455 expands and cools into the hadrons that are observed in the detector. Thus the QGP  
3456 cannot be studied directly, and its formation and properties must be inferred from  
3457 the information that is accessible to experiment. One of the first predicted exper-  
3458 imental signatures for the formation of this plasma is the enhancement of strange  
3459 hadron production, relative to non-strange pion production. While this enhancement  
3460 was thought to be unique to heavy-ion collisions, experimental data from ALICE  
3461 indicates that even high multiplicity pp and p–Pb collisions exhibit an onset of this  
3462 enhanced production. This enhancement can only be described using statistical mod-  
3463 els, as its microscopic origin is not yet understood.

3464 One way to study the strange particles that are produced in these high energy  
3465 collisions is through jets, which are sprays of hadrons that come from a hard inter-  
3466 action of the partons inside the nuclei. By looking at how a high-momentum hadron  
3467 (that represents a jet direction) and a lower momentum strange hadron are aligned  
3468 in azimuthal angle, it is possible to separate the processes that create strangeness  
3469 between hard (jet-related) and soft (QGP-related) ones. This angular correlation  
3470 method can be used to further the understanding of how strangeness production de-

3471 pends on the multiplicity in these different regimes, thus providing insight to the  
3472 onset of strangeness enhancement in smaller collision systems.

3473 This thesis presents the first results using angular correlations to measure jet and  
3474 non-jet  $\Lambda$  and charged hadron production in p–Pb collisions at  $\sqrt{s_{\text{NN}}} = 5.02$  TeV. By  
3475 using the technique of two-particle angular correlations, the production of  $\Lambda$  baryons  
3476 can be separated into different kinematic regions: the near-side region (associated  
3477 with jet-like strangeness production without QGP modification) away-side region  
3478 (associated with jet-like production in the presence of the QGP), and the underlying  
3479 event (tied to the uncorrelated strangeness production in the QGP). Both the yields  
3480 and the jet widths on the near- and away-side regions are extracted from the azimuthal  
3481 correlation functions and studied as a function of associated momentum and event  
3482 multiplicity. A strong dependence on multiplicity is observed for both the near-  
3483 and away-side yields in the case of the  $\Lambda$ , whereas the charged hadron associated  
3484 yields exhibit a much smaller (nearly statistically insignificant) dependence. The  
3485 away-side yields also show a systematically larger increase with multiplicity than the  
3486 near-side yields for both cases, hinting at modification of the away-side production  
3487 due to jet-QGP interactions. The h- $\Lambda$  and h-h near-side jet widths reveal a large  
3488 dependence on  $p_{\text{T}}$ , becoming more collimated as momentum increases. The widths of  
3489 the away-side jets are found to be independent of both  $p_{\text{T}}$  and multiplicity, however  
3490 the larger systematic uncertainties introduce difficulties with excluding flat behavior.  
3491 Comparing width values of the h- $\Lambda$  and h-h correlations, the h- $\Lambda$  near-side widths  
3492 are found to be significantly ( $> 2\sigma$ ) larger than the dihadron widths, whereas the  
3493 away-side widths are consistent within uncertainties. This indicates that  $\Lambda$  baryons  
3494 are more readily produced in the peripheral regions of the jet cone, whereas charged  
3495 hadrons are produced closer to the jet axis. This hints at a modification of the jet  
3496 fragmentation process for strange hadrons, as more massive particles (like the  $\Lambda$ ) are  
3497 expected to be produced closer to the jet axis.

3498 The yield ratios  $R_i^{\Lambda/h}$  and  $R_i^{\Lambda/\phi}$  ( $i = \text{near-side jet, away-side jet, UE}$ ) are also  
3499 studied as a function of associated  $p_{\text{T}}$  and multiplicity. The  $\Lambda/h$  ratios exhibit a clear  
3500 ordering in each region for the entire multiplicity range in both  $p_{\text{T}}$  bins, with the  
3501 UE ratios being larger than the away-side ratios, which are larger than the near-side  
3502 ratios. This indicates that relative  $\Lambda$  production is larger in the UE (QGP) when  
3503 compared to the jet-like regions. The  $\Lambda/h$  ratios in each region also reveal a strong  
3504 dependence on multiplicity, with slopes that are greater than zero by nearly  $5\sigma$  for

3505 both momentum bins. This indicates that while the overall  $\Lambda$  production is mostly  
3506 concentrated in the UE, the observed enhancement of  $\Lambda$  production with increasing  
3507 multiplicity is *also* driven by the jet-like regions. Furthermore, the away-side slopes  
3508 are found to be systematically higher than the near-side slopes, indicating that the  
3509 away-side  $\Lambda$  production is more strongly enhanced than the near-side  $\Lambda$  production  
3510 with increasing multiplicity. Again, this suggests that the away-side jet strangeness  
3511 production is modified by medium interactions. The  $\Lambda/\phi$  ratios in the near-side jet  
3512 region are measured to be systematically higher than both the away-side and UE  
3513 ratios, hinting at a suppression of  $\phi$  mesons along the jet axis due to the lack of  
3514 available  $s$ -quarks in the unmodified jet. The slopes of these ratios in all kinematic  
3515 regions are consistent with zero, indicating that the ratio is independent of collision  
3516 centrality.

3517 The measurements in this thesis are compared with theoretical predictions from  
3518 the PHSD, EPOS and DPMJET models. PHSD is found to be in good agreement with  
3519 all dihadron measurements, but fails to describe the overall  $\Lambda$  yields. This is likely  
3520 due to the requirement of a high momentum trigger hadron, which are not readily  
3521 produced within the model. Even still, the shape of the near-side peak in the h- $\Lambda$   
3522 correlation distribution is well-described by PHSD. EPOS, on the otherhand, is able  
3523 to describe the  $\Lambda$  and hadron yields very well, but the correlation distributions are  
3524 dominated by elliptic flow, making it impossible to extract the jet-like components.  
3525 This flow contribution is much larger for the h- $\Lambda$  distributions, indicating that  $\Lambda$   
3526 baryons in EPOS are mostly produced within the hydronamic core. The predicted  
3527 near- and away-side yields from DPMJET are found to be in relatively good agreement  
3528 with data in the dihadron case, but the h- $\Lambda$  yield predictions deviate from data by a  
3529 large ( $> 40\%$ ) margin. DPMJET also fails to predict any of the observed multiplicity  
3530 dependence for both the h- $\Lambda$  and h-h jet yields. However, the model is able to closely  
3531 predict the near-side widths of the dihadron distributions across all multiplicity and  
3532 momentum ranges, although it underpredicts both the h- $\Lambda$  near-side widths and  
3533 the away-side widths for both ( $\Lambda$ , h) cases. The model also predicts a difference  
3534 between the h- $\Lambda$  and h-h near-side widths, which is observed in data as well. This  
3535 indicates that whatever process responsible for the production of strangeness in the  
3536 periphery of the jet cone is contained within DPMJET. The per-trigger  $\Lambda/h$  and  $\Lambda/\phi$   
3537 yield ratios are consistently underpredicted by DPMJET, and exhibit no multiplicity  
3538 dependence. Even still, DPMJET manages to predict the ordering of the  $\Lambda/h$  ratios

3539 in each region (UE > away-side jet > near-side jet) and the enhancement of the  
3540 jet-like  $\Lambda/\phi$  ratio when compared to the UE region. Thus the softer, uncorrelated  
3541 processes implemented in DPMJET are responsible for the majority of the relative  
3542 strangeness production.

3543 **6.1 Future outlook**

3544 The measurements presented in this thesis strongly indicate that, while the dom-  
3545 inating component for strangeness production comes from the QGP, the observed  
3546 *enhancement* of this production as a function of multiplicity has a large contribution  
3547 from the jet-like regions. More still, the away-side jet component appears to undergo  
3548 a larger enhancement than the near-side, hinting that the jet and medium are inter-  
3549 acting in such a way that strangeness is more readily produced. These observations  
3550 can be used to help fuel the theoretical models used to describe particle collisions, as  
3551 such models are currently incapable of describing these results in their entirety.

3552 The techniques presented in this thesis can be easily extended to other collision  
3553 systems, such as pp and Pb–Pb collisions, along with other particle species, such as  
3554 the  $K^0$ . With the advent of the Run 3 data-taking period at the LHC, the ALICE  
3555 detector will be able to collect more data than ever before, allowing for more precise  
3556 measurements of these observables across a wider range of particles and collision  
3557 systems. Such measurements will help further constrain the microscopic origins of  
3558 this strange enhancement, thus providing more insight into the nature of the QGP  
3559 and the universe as a whole.

3560            **Appendix A: Resonance technique for  $\Lambda$**   
3561            **reconstruction**

3562            **A.1 Introduction**

3563        This portion of the appendix is dedicated to describing the analysis procedure for  
3564        generating the  $h-\Lambda$  correlation distributions using lambdas which are reconstructed  
3565        using the **resonance technique**, where all proton-pion pairs in an event are com-  
3566        bined to form  $\Lambda$  candidates. All of the proton and pion daughter tracks meet the  
3567        same selection criteria as the tracks used in the  $V^0$  technique, described in Table 4.4.  
3568        All in all, the procedure is very similar to the one described in Chapter 4, but with  
3569        a few key differences that will be highlighted in the following sections.

3570            **A.2 Combinatorial background estimation**

3571        As  $\Lambda$  baryons reconstructed using the resonance technique will have a much larger  
3572        combinatorial background than those from the nominal procedure, the final correla-  
3573        tion will contain a higher fraction of  $h-(p\pi)$  pairs that need to be removed. While  
3574        the sideband subtraction technique provides a general procedure for removing these  
3575        pairs, the signal  $S$  and the background  $B$  of the  $\Lambda$  invariant mass distribution must be  
3576        well described. To estimate these quantities, the following techniques were explored:

- 3577        • **Like-sign  $p\pi$  pairs** - Reconstruct the invariant mass of like-sign (LS)  $p\pi$  pairs,  
3578        and scale the like-sign  $p\pi$  distribution to the unlike-sign (US)  $p\pi$  distribution  
3579        in a region outside of the  $\Lambda$  signal region.
- 3580        • **Rotated  $p\pi$  pairs** - Reconstruct the invariant mass of US  $p\pi$  pairs, but rotate  
3581        either the pion or proton around the z-axis by  $\pi$  radians, and scale the rotated  
3582         $p\pi$  distribution to the original US sign  $p\pi$  distribution in a region outside of  
3583        the  $\Lambda$  signal region.

- 3584 • **Voigtian + polynomial fit** - Perform a standard fitting procedure using a  
 3585      Voigtian distribution for the signal along with a second-order polynomial for  
 3586      the background.

3587 The last technique will be addressed first, as it fails to properly estimate the signal  
 3588 and background in data. To illustrate this, the best possible fits in data are found  
 3589 and the corresponding signal shape is extracted and compared with the signal shape  
 3590 in Monte Carlo using full track reconstruction via GEANT. This comparison is done  
 3591 for the 20-50% multiplicity bin in Figure A.1. Note that the background shown in the  
 3592 MC plot is the true combinatorial background, as the p $\pi$  pairs are accessed directly  
 3593 at the generator level to confirm they did not come from a  $\Lambda$  decay.

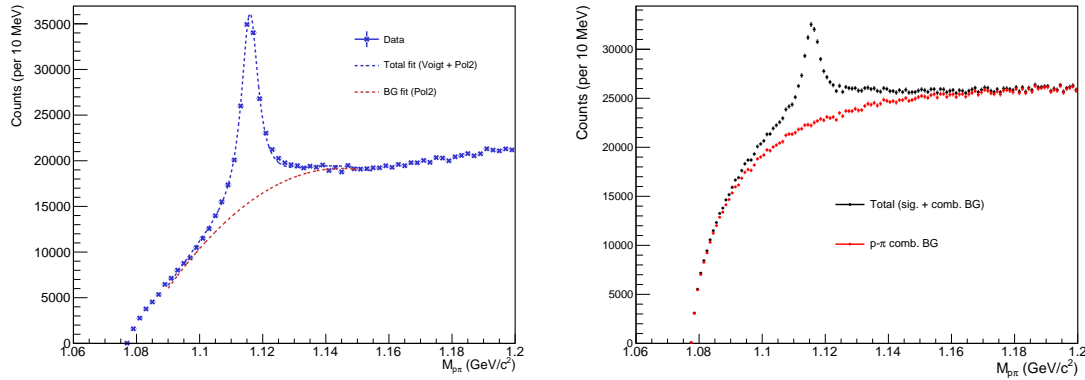


Figure A.1: Left: Invariant mass distribution with corresponding Voigt + Polynomial fit in the 20-50% multiplicity bin (data). Right: The signal and background shapes in MonteCarlo (MC). Note that even though MC appears to have a completely different S/B, the signal shapes should be similar. The fit in data appears to be massively underestimating the  $\Lambda$  signal, as the MC sample indicates there is  $\Lambda$  signal where the total data fit converges with the BG fit.

3594 This plot shows the main issue with reconstructing  $\Lambda$  baryons using the resonance  
 3595 technique: the tails of the signal distribution are much wider than the signal distri-  
 3596 bution obtained using the V $^0$  method. This is due to the fact that the kinematics  
 3597 of the corresponding daughter tracks are calculated assuming they originated from  
 3598 the primary vertex, which is only approximately true in the cases where the  $\Lambda$  is  
 3599 short-lived. This is different than the V $^0$  method, which calculates the kinematics for  
 3600 the daughter tracks assuming they originated from the secondary vertex. The wider  
 3601 tails of the distribution make it extremely difficult to describe using any common

3602 distribution, thus all techniques that rely on fitting the signal shape are not viable.  
 3603 Because of this, only the first two techniques (like-sign and rotated p $\pi$  pairs) will be  
 3604 considered for the rest of this analysis.

3605 To determine which of the two remaining techniques is more effective, the back-  
 3606 ground shape of the  $\Lambda$  invariant mass distribution for both techniques in MonteCarlo  
 3607 is compared to the ground-truth background shape. The resulting invariant mass  
 3608 distributions from like-sign and rotated p $\pi$  pairs are shown in Figure A.2, along with  
 3609 a comparison of the extracted signal shapes. The LS and rotated p $\pi$  distributions are  
 3610 scaled to match the US distribution in the sideband region, which will be discussed  
 3611 in the next section. The LS p $\pi$  pairs match the background shape of the  $\Lambda$  invariant  
 3612 mass distribution more closely than the rotated p $\pi$  pairs, so they are used to estimate  
 3613 the combinatorial background in the  $\Lambda$  invariant mass distribution in data.

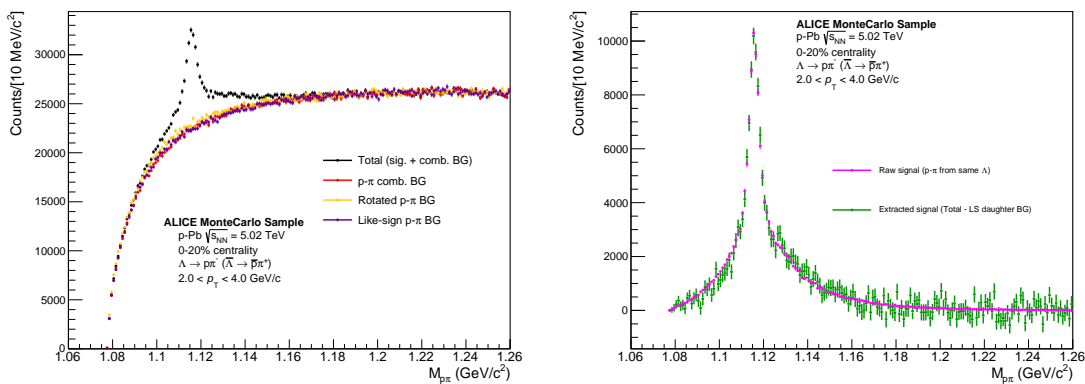


Figure A.2: Left: Invariant mass distribution for reconstructed unlike-sign p $\pi$  pairs (black) in the MonteCarlo sample. The like-sign p $\pi$  pair mass distribution (purple) and unlike-sign rotated p $\pi$  distributions are scaled to match the unlike-sign distribution outside of the  $\Lambda$  signal range. The true combinatorial background (red) matches most closely with the like-sign pairs. Right: The actual  $\Lambda$  signal (magenta) compared with the result of subtracting the like-sign from the total unlike-sign p $\pi$  distribution (green). The two distributions show good agreement.

### 3614 A.3 Signal and sideband regions

3615 As the invariant mass distributions from lambdas reconstructed using the resonance  
 3616 technique are very different from those reconstructed using the V<sup>0</sup> technique, so

too must the signal and sideband regions be different. The signal region was again chosen to maximize significance across all multiplicity bins, and is defined as the range  $1.014 < M_{p\pi} < 1.026 \text{ GeV}/c^2$ . Choosing the sideband region is a more complicated procedure, as there is no obvious region in the invariant mass distribution where the signal vanishes. Instead, the sideband region is chosen to minimize the difference between the extracted signal in data and the signal shape in MonteCarlo, which can be seen in Figure A.3. The resulting sideband region is  $1.160 < M_{p\pi} < 1.180 \text{ GeV}/c^2$ .

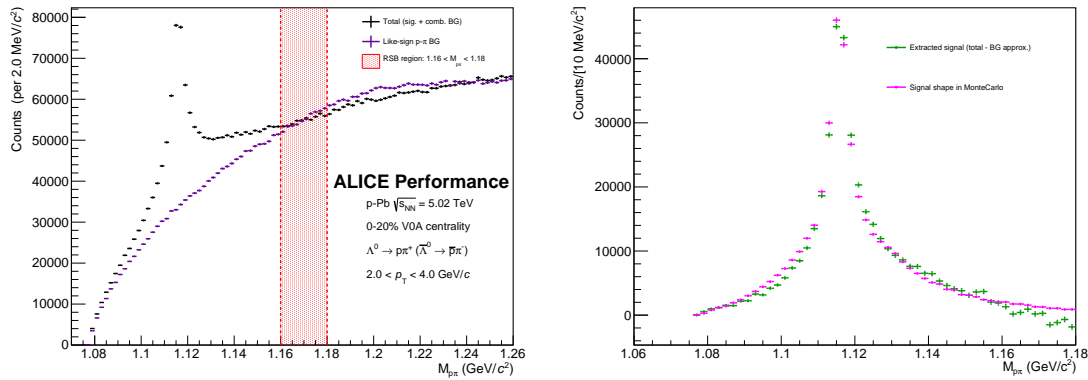


Figure A.3: Left: Invariant Mass distribution for unlike-sign  $p\pi$  pairs (black) along with the like-sign  $p\pi$  background (purple) and the sideband region (red) in the 0-20% multiplicity bin. Right: The extracted signal (green) compared with the resonance-technique reconstructed signal shape in MonteCarlo (magenta). The sideband region was chosen to minimize the differences between these distributions.

### 3624 A.3.1 Efficiency correction

3625 Again, the resonance technique-based  $\Lambda$  reconstruction efficiency is calculated in a  
3626 similar manner as the  $V^0$  technique, using the formula

$$\epsilon(x_1, x_2, \dots, x_n) = \frac{N_{\text{reco.}}(x_1, x_2, \dots, x_n)}{N_{\text{gen.}}(x_1, x_2, \dots, x_n)}, \quad (\text{A.1})$$

3627 where  $N_{\text{reco.}}$  and  $N_{\text{gen.}}$  are the reconstructed and generated particle distributions with  
3628 kinematic variables  $x_1, x_2, \dots, x_n$ . The main difference from the  $V^0$  efficiency computa-  
3629 tion comes from  $N_{\text{reco.}}$ , where each  $\Lambda$  candidate is generated using the following  
3630 procedure:

- 3631     • Find all protons and pions within the track list that pass the daughter selection  
3632       criteria

- 3633     • For each proton in the list, determine if it came from a  $\Lambda$  (at generator level)
- 3634     • If the proton came from a  $\Lambda$ , loop through the pion list until the pion that came  
3635       from the same  $\Lambda$  is found (again, verified at the generator level)
- 3636     • Reconstruct the  $\Lambda$  using the daughter tracks found in the previous two steps
- 3637     • Only keep the  $\Lambda$  if  $|\eta| < 0.8$
- 3638     The denominator  $N_{\text{gen.}}$  is calculated in the same way as the  $V^0$  technique. The  
3639     resulting efficiency is shown as a function of  $p_T$  for each multiplicity bin in Figure A.4.  
3640     As expected, the efficiency is higher than the  $V^0$  technique, as every  $\Lambda$  reconstructed  
3641     using the resonance technique would also be reconstructed using the  $V^0$  technique.

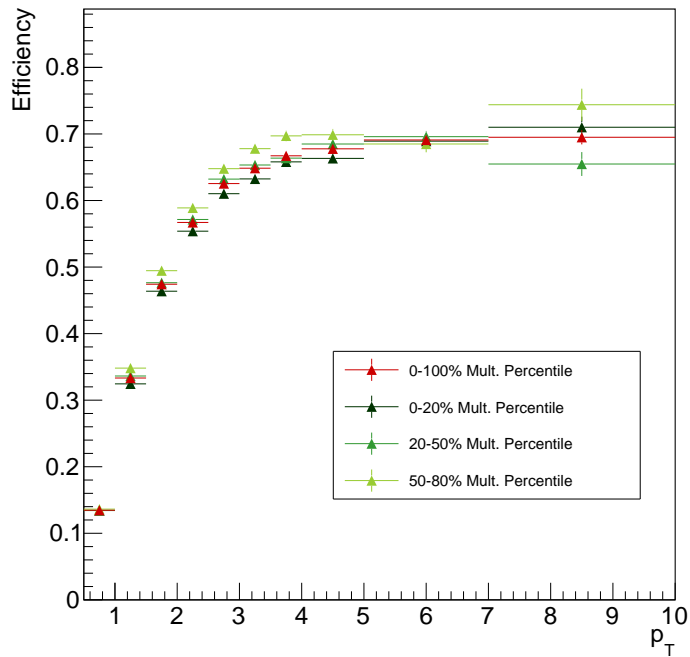


Figure A.4: Efficiency vs.  $p_T$  for  $\Lambda$  reconstruction using resonance technique for each multiplicity bin, along with an integrated 0-100% point in red. There does not appear to be any significant dependence on multiplicity. Also worth noting that the efficiency is higher for this technique when compared to the  $V^0$  technique, as expected (all AOD tracks from  $V^0$  finder daughters are also in total AOD track list).

## 3642 A.4 Corrections to the h- $\Lambda$ distributions

3643 All of the efficiency and acceptance corrections are applied to the resonance technique-based h- $\Lambda$  distribution in the same way as the V<sup>0</sup> technique. The only difference comes  
 3644 from the removal of the combinatorial background, as:

- 3646 1. The signal  $S$  and background  $B$  are calculated in a slightly different manner,  
 3647 and
- 3648 2. The sideband region is vastly different.

3649 For the first point, the signal and background are calculated via bin-wise summation  
 3650 of the invariant mass distribution using the LS p $\pi$  pairs as an estimate for the  
 3651 background, scaled to the US distribution in the sideband region.

3652 The second point is mostly inconsequential as the h-p $\pi$  distributions are very  
 3653 similar in a wide range of sideband regions, as shown in Figure A.5. The nominal  
 3654 sideband region was chosen to be  $1.160 < M_{\text{SSB}} < 1.180 \text{ GeV}/c^2$ , but any region with  
 3655 a lower bound greater than  $1.160 \text{ GeV}/c^2$  and upper bound less than  $1.22 \text{ GeV}/c^2$   
 3656 should produce similar results.

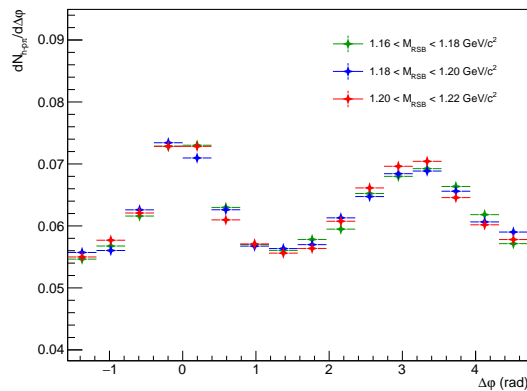


Figure A.5: The projected  $\Delta\varphi$  distributions for different choices of sideband, taken within the  $-1.2 < \Delta\eta < 1.2$  region. The correlation shapes are identical within the statistical errors.

3657 The signal scaling factor is calculated in the same way as it is in Equation 4.10, but  
 3658 with the residual now generated by subtracting the sideband-scaled LS p $\pi$  pairs from  
 3659 the US distribution. The two-track efficiency correction is not applied, as the tools

3660 used to calculate the  $\epsilon_{\text{pair}}(\Delta\varphi, \Delta\eta)$  template were not developed before the resonance  
 3661 technique-based analysis was completed.

## 3662 A.5 MC closure test

3663 An MC closure test was also performed for the resonance technique-based analysis,  
 3664 and the results are shown in Figure A.6. The ratio is consistent with unity, but the  
 3665 statistical fluctuations make it difficult to draw any meaningful conclusions.

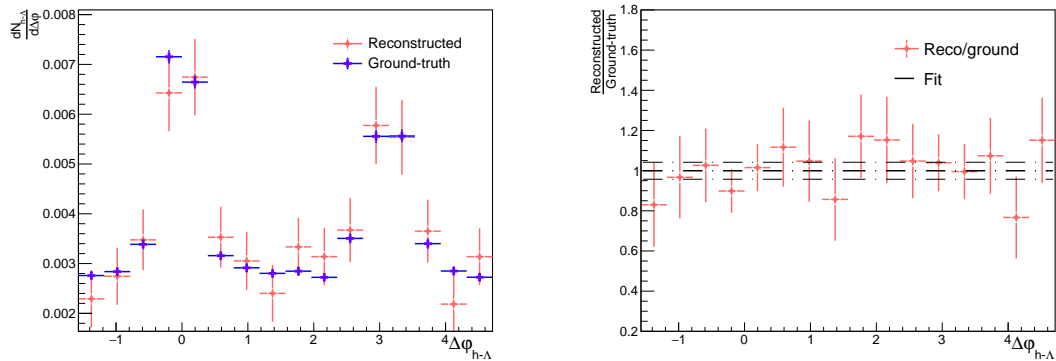


Figure A.6: The reconstructed (red) and ground-truth (blue)  $h\text{-}\Lambda_{\text{res}}$   $\Delta\varphi$  distributions along with a (reconstructed)/(ground-truth) ratio and straight-line fit. The fit is technically consistent with unity, but the statistical fluctuations are quite large.

3666 As the reconstructed distribution has not been corrected for the two-track merging  
 3667 effect, it is surprising that the ratio does not exhibit a significant deviation from unity  
 3668 at small  $\Delta\varphi$ . This is likely due to two factors:

- 3669 1. The resonance technique has a much lower S/B, and therefore the sideband  
 3670 subtraction introduces a large amount of statistical fluctuations making such  
 3671 deviations difficult to observe, and
- 3672 2. The reconstructed daughter tracks have a larger fraction of higher quality tracks  
 3673 when compared to the  $V^0$  technique, and those tracks are less likely to be merged  
 3674 over by the trigger during reconstruction.

3675 To elaborate on the second point, while the resonance and  $V^0$  techniques use the  
 3676 same loose quality cuts, the daughter tracks coming from the  $V^0$  technique must

3677 have a resolvable secondary vertex, which biases the corresponding  $\Lambda$  sample to those  
 3678 with a higher decay length. As discussed in 4.5.3.4, the two-track merging effect is  
 3679 more pronounced at larger decay lengths, thus the  $h\text{-}\Lambda$  distributions using the  $V^0$   
 3680 reconstruction technique will have a larger fraction of merged tracks when compared  
 3681 to the resonance technique-based distributions.

3682 To further investigate this surprising closure of the resonance technique-based  $h\text{-}\Lambda$   
 3683  $\Delta\varphi$  distributions, the same closure test is performed, but for the reconstructed  $h\text{-}\Lambda$   
 3684 distribution, the  $\Lambda$  candidate is required to have have a corresponding particle at the  
 3685 generator-level, making the combinatorial background exactly zero and removing the  
 3686 need for sideband subtraction. The results of this test are shown in Figure A.7. The  
 3687 ratio is no longer consistent with unity at small  $\Delta\varphi$ , as expected<sup>1</sup>

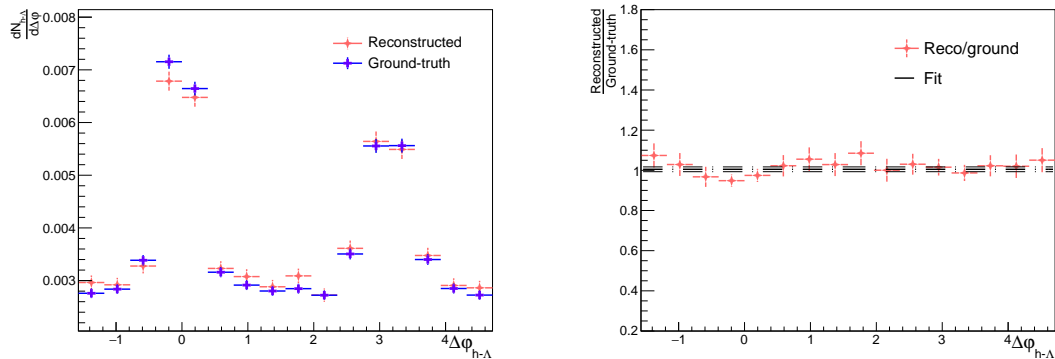


Figure A.7: The reconstructed (red) and ground-truth (blue)  $h\text{-}\Lambda_{\text{res}}$   $\Delta\varphi$  distributions along with a (reconstructed)/(ground-truth) ratio and straight-line fit, but instead requiring the reconstructed  $\Lambda$  to have a corresponding particle at the generator level to make sideband subtraction unnecessary. The result is no longer consistent with unity at small  $\Delta\varphi$  due to the track merging effect, but the non-closure is much smaller than the  $V^0$  technique.

## 3688 A.6 Some additional results

3689 A comparison of the final per-trigger  $h\text{-}\Lambda$   $\Delta\varphi$  correlation structure from the resonance  
 3690 and  $V^0$ -based techniques was shown in Chapter 4.5.3.4, but it can be seen again in

---

<sup>1</sup>It is strange to *want* non-closure, but it would be even stranger if the track merging effect were somehow not present in the resonance technique-based analysis.

3691 Figure A.8. As mentioned previously, the correlation shapes are nearly identical, with  
 3692 the resonance technique having slightly larger uncertainties due to the combinatorial  
 3693 background subtraction.

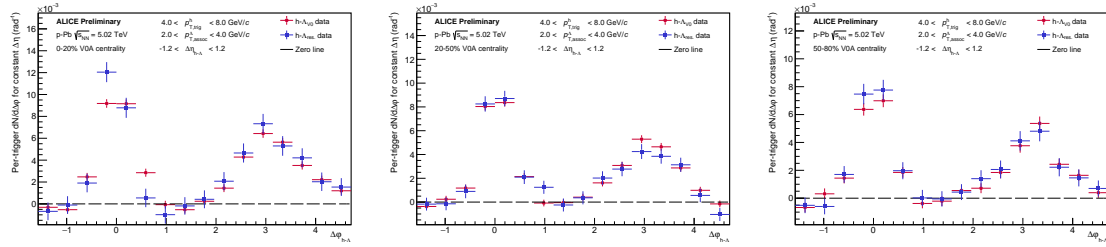


Figure A.8: The final per-trigger  $h\text{-}\Lambda$   $\Delta\varphi$  correlations for  $\Lambda$ s reconstructed using the resonance technique (blue) and the  $V^0$ -based technique (red) in the 0-20% (left), 20-50% (middle) and 50-80% (right) multiplicity bins, taken in the associated momentum range  $2.0 < p_T < 4.0 \text{ GeV}/c$ , after the subtraction of the UE. The distributions show good agreement across all multiplicity bins, indicating that the  $V^0$ -based reconstruction technique is not introducing a bias in the correlation shape.

3694 Additionally, the per-trigger near- and away-side pairwise yields and the  $(h\text{-}\Lambda)/(h\text{-}h)$   
 3695 ratios with  $\Lambda$ s reconstructed using the resonance technique are shown in Figure A.9.  
 3696 The results are qualitatively very similar to the nominal results, indicating that the  
 3697 resonance technique is a reasonably viable alternative to the  $V^0$  technique. How-  
 3698 ever, due to the larger combinatorial background (and likely very large systematic  
 3699 uncertainties), the  $V^0$  technique is still the preferred method for  $\Lambda$  reconstruction.

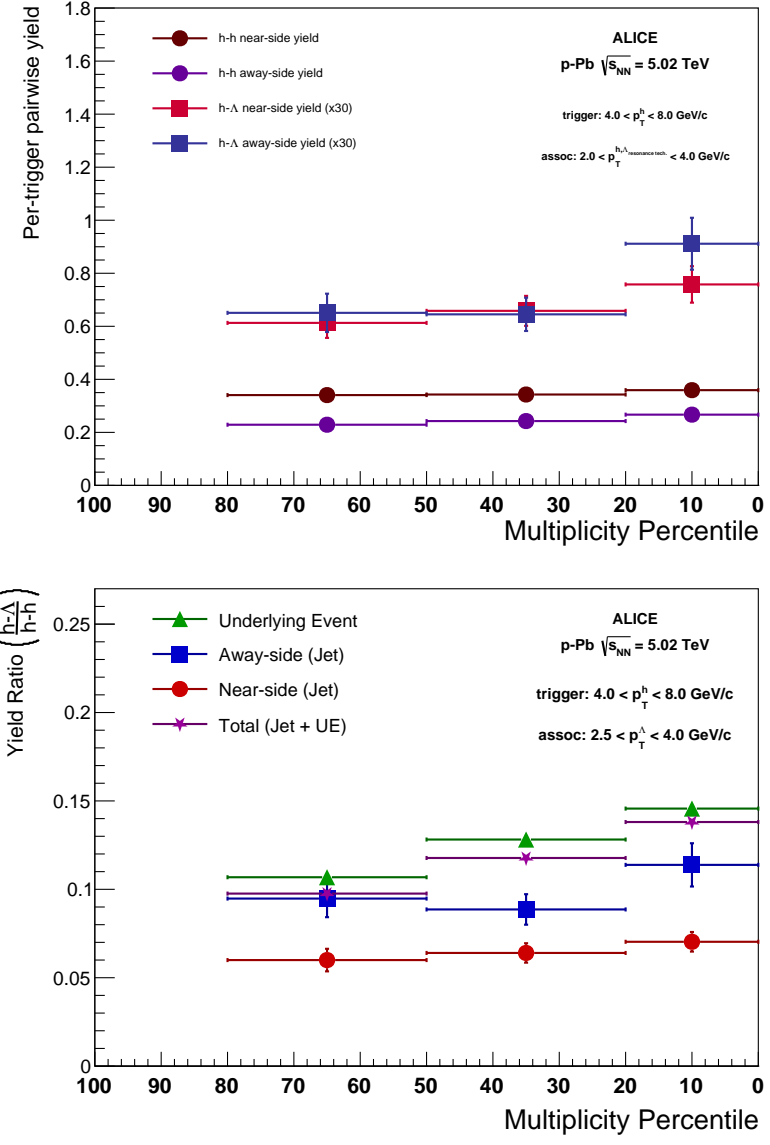


Figure A.9: The final  $h\text{-}\Lambda$  and  $h\text{-}h$  per-trigger pairwise jet yields (top) and  $(h\text{-}\Lambda)/(h\text{-}h)$  yield ratios (bottom) vs. multiplicity in the associated momentum range  $2.0 < p_T < 4.0 \text{ GeV}/c$  for  $\Lambda$ s reconstructed using the resonance technique. The general trends are similar to the nominal  $V^0$  technique-based procedure, with larger statistical uncertainties.

## Bibliography

- 3701 [1] B. Pullman, *The Atom in the History of Human Thought*. Oxford: Oxford  
3702 University Press, 1998, ISBN: 978-0-19-515040-7 (cit. on p. 2).
- 3703 [2] J. Dalton, “Experimental enquiry into the proportion of the several gases  
3704 or elastic fluids, constituting the atmosphere,” *Memoirs of the Literary and*  
3705 *Philosophical Society of Manchester*, vol. 1, pp. 244–258, 1805 (cit. on p. 2).
- 3706 [3] E. R. Scerri, *The Periodic Table: A Very Short Introduction*. Oxford University  
3707 Press, Jul. 2019, pp. 117–123, ISBN: 9780198842323. DOI: 10.1093/actrade/  
3708 9780198842323.001.0001. [Online]. Available: <https://doi.org/10.1093/actrade/9780198842323.001.0001> (cit. on p. 2).
- 3710 [4] D. Mendeleev, “The natural system of elements and its application to the  
3711 indication of the properties of undiscovered elements,” *Journal of the Russian*  
3712 *Chemical Society*, vol. 3, pp. 25–56, 1871 (cit. on p. 2).
- 3713 [5] I. Falconer, “J J Thomson and the discovery of the electron,” *Physics Edu-*  
3714 *cation*, vol. 32, no. 4, p. 226, 1997. DOI: 10.1088/0031-9120/32/4/015.  
3715 [Online]. Available: <https://dx.doi.org/10.1088/0031-9120/32/4/015>  
3716 (cit. on p. 3).
- 3717 [6] E. Rutherford, “The scattering of  $\alpha$  and  $\beta$  particles by matter and the structure  
3718 of the atom,” *Philosophical Magazine Series 6*, vol. 21, pp. 669–688, 1911 (cit.  
3719 on p. 3).
- 3720 [7] J. Chadwick, “Possible existence of a neutron,” *Nature*, vol. 129, p. 312, 1932  
3721 (cit. on p. 3).
- 3722 [8] C. D. Anderson, “The apparent existence of easily deflectable positives,” *Sci-*  
3723 *ence*, vol. 76, no. 1967, pp. 238–239, 1932. DOI: 10.1126/science.76.1967.  
3724 238. eprint: <https://www.science.org/doi/pdf/10.1126/science.76.1967.238>. [Online]. Available: <https://www.science.org/doi/abs/10.1126/science.76.1967.238> (cit. on p. 3).

- 3727 [9] S. H. Neddermeyer and C. D. Anderson, “Note on the nature of cosmic-ray  
3728 particles,” *Phys. Rev.*, vol. 51, pp. 884–886, 10 1937. DOI: 10.1103/PhysRev.  
3729 51.884. [Online]. Available: <https://link.aps.org/doi/10.1103/PhysRev.51.884> (cit. on p. 3).
- 3731 [10] R. Brown *et al.*, “Observations with Electron-Sensitive Plates Exposed to  
3732 Cosmic Radiation,” *Nature*, vol. 163, no. 4133, pp. 82–87, Jan. 1949. DOI:  
3733 10.1038/163082a0 (cit. on p. 3).
- 3734 [11] V. D. Hopper and S. Biswas, “Evidence concerning the existence of the new  
3735 unstable elementary neutral particle,” *Phys. Rev.*, vol. 80, pp. 1099–1100, 6  
3736 1950. DOI: 10.1103/PhysRev.80.1099. [Online]. Available: <https://link.aps.org/doi/10.1103/PhysRev.80.1099> (cit. on p. 3).
- 3738 [12] A. Barbaro-Galtieri *et al.*, “Apparent violation of the  $\Delta S = \Delta Q$  rule by lep-  
3739 tonic  $\Sigma^+$  decay,” *Phys. Rev. Lett.*, vol. 9, pp. 26–29, 1 1962. DOI: 10.1103/  
3740 PhysRevLett.9.26. [Online]. Available: <https://link.aps.org/doi/10.1103/PhysRevLett.9.26> (cit. on p. 3).
- 3742 [13] T. Nakano and K. Nishijima, “Charge Independence for V-particles,” *Progress  
3743 of Theoretical Physics*, vol. 10, no. 5, pp. 581–582, 1953. DOI: 10.1143/PTP.  
3744 10.581 (cit. on p. 3).
- 3745 [14] R. Serway, C. Moses, and C. Moyer, *Modern Physics*. Cengage Learning, 2004,  
3746 pp. 12–13, ISBN: 9780534493394. [Online]. Available: <https://books.google.com/books?id=Yfo3rnt3bkEC> (cit. on p. 3).
- 3748 [15] M. Gell-Mann, “The Eightfold Way: A theory of strong interaction symmetry,”  
3749 Mar. 1961. DOI: 10.2172/4008239. [Online]. Available: <https://www.osti.gov/biblio/4008239> (cit. on pp. 3, 4, 11).
- 3751 [16] Y. Ne’eman, “Derivation of strong interactions from a gauge invariance,” *Nu-  
3752 clear Physics*, vol. 26, no. 2, pp. 222–229, 1961. DOI: 10.1016/0029-5582(61)  
3753 90134-1 (cit. on p. 3).
- 3754 [17] W. Heisenberg, “Über den Bau der Atomkerne. I,” *Zeitschrift fur Physik*,  
3755 vol. 77, no. 1-2, pp. 1–11, Jan. 1932. DOI: 10.1007/BF01342433 (cit. on  
3756 p. 3).

- 3757 [18] M. Gell-Mann, “Isotopic Spin and New Unstable Particles,” *Physical Review*,  
3758 vol. 92, no. 3, pp. 833–834, Nov. 1953. DOI: 10.1103/PhysRev.92.833 (cit. on  
3759 pp. 3, 23, 28, 29).
- 3760 [19] T. Nakano and K. Nishijima, “Charge Independence for V-particles,” *Progress*  
3761 *of Theoretical Physics*, vol. 10, no. 5, pp. 581–582, Nov. 1953. DOI: 10.1143/  
3762 PTP.10.581 (cit. on p. 4).
- 3763 [20] M. Gell-Mann, “The interpretation of the new particles as displaced charge  
3764 multiplets,” *Il Nuovo Cimento*, vol. 4, no. S2, pp. 848–866, Apr. 1956. DOI:  
3765 10.1007/BF02748000 (cit. on p. 4).
- 3766 [21] M. Gell-Mann, “A schematic model of baryons and mesons,” *Physics Letters*,  
3767 vol. 8, no. 3, pp. 214–215, Feb. 1964. DOI: 10.1016/S0031-9163(64)92001-3  
3768 (cit. on p. 4).
- 3769 [22] A. Pickering, *Constructing quarks*. University of Chicago Press, 1999, pp. 114–  
3770 125. DOI: 10.7208/chicago/9780226667997.003.0007 (cit. on p. 5).
- 3771 [23] B. J. Bjørken and S. L. Glashow, “Elementary particles and SU(4),” *Physics*  
3772 *Letters*, vol. 11, no. 3, pp. 255–257, Aug. 1964. DOI: 10.1016/0031-9163(64)  
3773 90433-0 (cit. on p. 5).
- 3774 [24] S. Glashow, “The hunting of the atoms and their nuclei: Protons and neu-  
3775 trons,” *New York Times*, Jul. 1976. [Online]. Available: <https://www.nytimes.com/1976/07/18/archives/the-hunting-of-the-atoms-and-their-nuclei-protons-and-neutrons.html> (cit. on p. 5).
- 3776 [25] S. L. Glashow, J. Iliopoulos, and L. Maiani, “Weak Interactions with Lepton-  
3777 Hadron Symmetry,” *Phys Rev D*, vol. 2, no. 7, pp. 1285–1292, Oct. 1970. DOI:  
3778 10.1103/PhysRevD.2.1285 (cit. on p. 5).
- 3779 [26] H. Kendall, *Deep inelastic scattering: Experiments on the proton and the ob-  
3780 servation of scaling*, 1990. [Online]. Available: <https://www.nobelprize.org/uploads/2018/06/kendall-lecture.pdf> (visited on 08/21/2023) (cit.  
3781 on pp. 5, 6).
- 3782 [27] J. Friedman, *Deep inelastic scattering: Comparisons with the quark model*,  
3783 1990. [Online]. Available: <https://www.nobelprize.org/uploads/2018/06/friedman-lecture.pdf> (visited on 08/21/2023) (cit. on p. 5).

- 3788 [28] R. Taylor, *Deep inelastic scattering: The early years*, 1990. [Online]. Available:  
3789 <https://www.nobelprize.org/uploads/2018/06/taylor-lecture.pdf>  
3790 (visited on 08/21/2023) (cit. on p. 5).
- 3791 [29] E. D. Bloom *et al.*, “High-Energy Inelastic e-p Scattering at  $6^\circ$  and  $10^\circ$ ,”  
3792 *Physical Review Letters*, vol. 23, no. 16, pp. 930–934, Oct. 1969. DOI: 10 .  
3793 1103/PhysRevLett.23.930 (cit. on p. 5).
- 3794 [30] E. D. Bloom *et al.*, “High-Energy Inelastic e-p Scattering at  $6^\circ$  and  $10^\circ$ ,”  
3795 *Physical Review Letters*, vol. 23, no. 16, pp. 930–934, Oct. 1969. DOI: 10 .  
3796 1103/PhysRevLett.23.930 (cit. on p. 5).
- 3797 [31] J. Bjorken, “Current algebra at small distances,” Jun. 2018. [Online]. Available:  
3798 <https://www.osti.gov/biblio/1444446> (cit. on p. 6).
- 3799 [32] R. P. Feynman, “The behavior of hadron collisions at the uncertainties from  
3800 these sources exhibit no multiplicity dependence, and a very small depen-  
3801 dence on  $p_T$ . extreme energies,” in *Special Relativity and Quantum Theory:*  
3802 *A Collection of Papers on the Poincaré Group*, M. E. Noz and Y. S. Kim,  
3803 Eds. Dordrecht: Springer Netherlands, 1988, pp. 289–304, ISBN: 978-94-009-  
3804 3051-3. DOI: 10 .1007/978-94-009-3051-3\_25. [Online]. Available: [https://doi.org/10.1007/978-94-009-3051-3\\_25](https://doi.org/10.1007/978-94-009-3051-3_25) (cit. on p. 6).
- 3806 [33] J. Aubert *et al.*, “Experimental observation of a heavy particle  $J$ ,” *Physical*  
3807 *Review Letters*, vol. 33, Dec. 1974 (cit. on p. 6).
- 3808 [34] H. Fritzsch, M. Gell-Mann, and H. Leutwyler, “Advantages of the color octet  
3809 gluon picture,” *Physics Letters B*, vol. 47, no. 4, pp. 365–368, Nov. 1973. DOI:  
3810 10 .1016/0370-2693(73)90625-4 (cit. on p. 7).
- 3811 [35] D. J. Gross and F. Wilczek, “Ultraviolet Behavior of Non-Abelian Gauge The-  
3812 ories,” *Physical Review Letters*, vol. 30, no. 26, pp. 1343–1346, Jun. 1973. DOI:  
3813 10 .1103/PhysRevLett.30.1343 (cit. on p. 7).
- 3814 [36] H. D. Politzer, “Reliable Perturbative Results for Strong Interactions?” *Phys-*  
3815 *ical Review Letters*, vol. 30, no. 26, pp. 1346–1349, Jun. 1973. DOI: 10 .1103/  
3816 PhysRevLett.30.1346 (cit. on p. 7).
- 3817 [37] P. Söding, *Twenty-five years of gluons*, 2004. [Online]. Available: <https://cerncourier.com/a/twenty-five-years-of-gluons/> (cit. on pp. 7, 15).

- 3819 [38] P. Söding, “On the discovery of the gluon,” *European Physical Journal H*,  
3820 vol. 35, no. 1, pp. 3–28, Jul. 2010. DOI: 10.1140/epjh/e2010-00002-5 (cit.  
3821 on p. 7).
- 3822 [39] A. Salam and J. C. Ward, “Weak and electromagnetic interactions,” *Il Nuovo  
3823 Cimento*, vol. 11, no. 4, pp. 568–577, Feb. 1959. DOI: 10.1007/BF02726525  
3824 (cit. on p. 7).
- 3825 [40] S. Weinberg, “A Model of Leptons,” *Physical Review Letters*, vol. 19, no. 21,  
3826 pp. 1264–1266, Nov. 1967. DOI: 10.1103/PhysRevLett.19.1264 (cit. on p. 7).
- 3827 [41] P. W. Higgs, “Broken symmetries and the masses of gauge bosons,” *Phys. Rev.  
3828 Lett.*, vol. 13, pp. 508–509, 16 1964. DOI: 10.1103/PhysRevLett.13.508.  
3829 [Online]. Available: [https://link.aps.org/doi/10.1103/PhysRevLett.  
3830 13.508](https://link.aps.org/doi/10.1103/PhysRevLett.13.508) (cit. on pp. 7–9).
- 3831 [42] P. T. Smith, “Reporting New Evidence of Gravitons,” in *14th International  
3832 Symposium on Nuclei in the Cosmos (NIC2016)*, S. Kubono *et al.*, Eds., Jan.  
3833 2017, 020101, p. 020101. DOI: 10.7566/JPSCP.14.020101 (cit. on p. 8).
- 3834 [43] G. Jungman, M. Kamionkowski, and K. Griest, “Supersymmetric dark mat-  
3835 ter,” *Physics Reports*, vol. 267, no. 5, pp. 195–373, 1996, ISSN: 0370-1573.  
3836 DOI: [https://doi.org/10.1016/0370-1573\(95\)00058-5](https://doi.org/10.1016/0370-1573(95)00058-5). [Online].  
3837 Available: [https://www.sciencedirect.com/science/article/pii/  
3838 0370157395000585](https://www.sciencedirect.com/science/article/pii/0370157395000585) (cit. on p. 8).
- 3839 [44] G. Esposito, *An introduction to quantum gravity*, 2011. arXiv: 1108.3269  
3840 [hep-th] (cit. on p. 8).
- 3841 [45] G. Aad *et al.*, “Observation of a new particle in the search for the Standard  
3842 Model Higgs boson with the ATLAS detector at the LHC,” *Phys. Lett. B*,  
3843 vol. 716, pp. 1–29, 2012. DOI: 10.1016/j.physletb.2012.08.020. arXiv:  
3844 1207.7214 [hep-ex] (cit. on p. 9).
- 3845 [46] S. Chatrchyan *et al.*, “Observation of a New Boson at a Mass of 125 GeV  
3846 with the CMS Experiment at the LHC,” *Phys. Lett. B*, vol. 716, pp. 30–61,  
3847 2012. DOI: 10.1016/j.physletb.2012.08.021. arXiv: 1207.7235 [hep-ex]  
3848 (cit. on p. 9).

- 3849 [47] R. Shivni, *The deconstructed standard model equation*, Sep. 2023. [Online].  
3850 Available: [https://www.symmetrymagazine.org/article/the-deconstructed-](https://www.symmetrymagazine.org/article/the-deconstructed-standard-model-equation?language_content_entity=und)  
3851 [standard-model-equation?language\\_content\\_entity=und](#) (cit. on p. 10).
- 3852 [48] F. Gross *et al.*, “50 Years of Quantum Chromodynamics,” Dec. 2022. arXiv:  
3853 [2212.11107 \[hep-ph\]](https://arxiv.org/abs/2212.11107) (cit. on pp. 10, 11).
- 3854 [49] Wikipedia, *Structure constants — Wikipedia, the free encyclopedia*, <http://en.wikipedia.org/w/index.php?title=Structure%20constants&oldid=1160301276>, [Online; accessed 07-October-2023], 2023 (cit. on p. 11).
- 3855 [50] K. Chetyrkin and A. Rétey, “Renormalization and running of quark mass  
3856 and field in the regularization invariant and schemes at three and four loops,”  
3857 *Nuclear Physics B*, vol. 583, no. 1-2, pp. 3–34, Sep. 2000. DOI: [10.1016/s0550-3213\(00\)00331-x](https://doi.org/10.1016/s0550-3213(00)00331-x). [Online]. Available: <https://doi.org/10.1016/s0550-3213%2800%2900331-x> (cit. on p. 12).
- 3858 [51] S. Weinberg, “New Approach to the Renormalization Group,” *Phys. Rev. D*,  
3859 vol. 8, no. 10, pp. 3497–3509, Nov. 1973. DOI: [10.1103/PhysRevD.8.3497](https://doi.org/10.1103/PhysRevD.8.3497)  
3860 (cit. on p. 12).
- 3861 [52] C. G. Callan, R. F. Dashen, and D. J. Gross, “The structure of the gauge  
3862 theory vacuum,” *Physics Letters B*, vol. 63, no. 3, pp. 334–340, Aug. 1976.  
3863 DOI: [10.1016/0370-2693\(76\)90277-X](https://doi.org/10.1016/0370-2693(76)90277-X) (cit. on p. 12).
- 3864 [53] J. L. Rosner, “CP symmetry violation,” Sep. 2001. arXiv: [hep-ph/0109240](https://arxiv.org/abs/hep-ph/0109240)  
3865 (cit. on p. 12).
- 3866 [54] R. D. Peccei, “The Strong CP problem and axions,” *Lect. Notes Phys.*, vol. 741,  
3867 M. Kuster, G. Raffelt, and B. Beltran, Eds., pp. 3–17, 2008. DOI: [10.1007/978-3-540-73518-2\\_1](https://doi.org/10.1007/978-3-540-73518-2_1). arXiv: [hep-ph/0607268](https://arxiv.org/abs/hep-ph/0607268) (cit. on p. 12).
- 3868 [55] J. J. Lodder, “On gluon masses, color symmetry, and a possible massive ninth  
3869 gluon,” Jun. 1996. arXiv: [hep-ph/9606317](https://arxiv.org/abs/hep-ph/9606317) (cit. on p. 12).
- 3870 [56] ”. Griffiths”, *Introduction to Elementary Particles*, ”2nd”. ”Wiley-VCH”,  
3871 ”2008”, pp. 280–281, ISBN: ”978-3-527-40601-2” (cit. on p. 12).
- 3872 [57] T. Luthe, A. Maier, P. Marquard, and Y. Schroder, “Complete renormaliza-  
3873 tion of QCD at five loops,” *JHEP*, vol. 03, p. 020, 2017. DOI: [10.1007/JHEP03\(2017\)020](https://doi.org/10.1007/JHEP03(2017)020). arXiv: [1701.07068 \[hep-ph\]](https://arxiv.org/abs/1701.07068) (cit. on p. 13).

- 3880 [58] B. Andersson, G. Gustafson, G. Ingelman, and T. Sjöstrand, “Parton frag-  
3881 mentation and string dynamics,” *Phys. Rep.*, vol. 97, no. 2-3, pp. 31–145,  
3882 Jul. 1983. DOI: 10.1016/0370-1573(83)90080-7 (cit. on pp. 14, 37).
- 3883 [59] ”. Wilson and others”, “superconducting accelerator research and develop-  
3884 ment at slac”, *SLAC-PUB*, vol. ”749”, ”1970” (cit. on p. 15).
- 3885 [60] R. L. Workman *et al.*, “Review of Particle Physics,” *PTEP*, vol. 2022, p. 083C01,  
3886 2022. DOI: 10.1093/ptep/ptac097 (cit. on pp. 15, 18).
- 3887 [61] R. K. Ellis, W. J. Stirling, and B. R. Webber, *QCD and Collider Physics*  
3888 (Cambridge Monographs on Particle Physics, Nuclear Physics and Cosmol-  
3889 ogy). Cambridge University Press, 1996. DOI: 10.1017/CBO9780511628788  
3890 (cit. on p. 17).
- 3891 [62] U. W. Heinz, “The Strongly coupled quark-gluon plasma created at RHIC,”  
3892 *J. Phys. A*, vol. 42, D. Neilson and G. Senatore, Eds., p. 214 003, 2009. DOI:  
3893 10.1088/1751-8113/42/21/214003. arXiv: 0810.5529 [nucl-th] (cit. on  
3894 p. 16).
- 3895 [63] J. Letessier and J. Rafelski, *Hadrons and Quark-Gluon Plasma*. Oxford Uni-  
3896 versity Press, 2002, ISBN: 978-1-00-929075-3, 978-0-511-53499-7, 978-1-00-929070-  
3897 8, 978-1-00-929073-9. DOI: 10.1017/9781009290753 (cit. on p. 16).
- 3898 [64] A. Maire, “Phase diagram of QCD matter : Quark-Gluon Plasma,” General  
3899 Photo, 2015. [Online]. Available: <https://cds.cern.ch/record/2025215>  
3900 (cit. on p. 18).
- 3901 [65] J. Rafelski, “Connecting QGP-Heavy Ion Physics to the Early Universe,”  
3902 *Nucl. Phys. B Proc. Suppl.*, vol. 243-244, R. Battiston and S. Bertolucci, Eds.,  
3903 pp. 155–162, 2013. DOI: 10.1016/j.nuclphysbps.2013.09.017. arXiv:  
3904 1306.2471 [astro-ph.CO] (cit. on p. 17).
- 3905 [66] E. Annala *et al.*, “Evidence for quark-matter cores in massive neutron stars,”  
3906 *Nature Phys.*, vol. 16, no. 9, pp. 907–910, 2020. DOI: 10.1038/s41567-020-  
3907 0914-9. arXiv: 1903.09121 [astro-ph.HE] (cit. on p. 17).
- 3908 [67] F.-M. Liu and S.-X. Liu, “Quark-gluon plasma formation time and direct  
3909 photons from heavy ion collisions,” *Phys. Rev. C*, vol. 89, no. 3, p. 034 906,  
3910 2014. DOI: 10.1103/PhysRevC.89.034906. arXiv: 1212.6587 [nucl-th]  
3911 (cit. on p. 19).

- 3912 [68] Aug. 2021. [Online]. Available: <https://cerncourier.com/a/participants-and-spectators-at-the-heavy-ion-fireball/> (cit. on p. 21).
- 3913
- 3914 [69] B. Abelev *et al.*, “Centrality determination of Pb-Pb collisions at  $\sqrt{s_{NN}} =$   
3915 2.76 TeV with ALICE,” *Phys. Rev. C*, vol. 88, no. 4, p. 044909, 2013. DOI:  
3916 10.1103/PhysRevC.88.044909. arXiv: 1301.4361 [nucl-ex] (cit. on p. 22).
- 3917 [70] “Centrality determination in heavy ion collisions,” Aug. 2018 (cit. on pp. 22,  
3918 23).
- 3919 [71] M. L. Miller, K. Reygers, S. J. Sanders, and P. Steinberg, “Glauber modeling  
3920 in high energy nuclear collisions,” *Ann. Rev. Nucl. Part. Sci.*, vol. 57, pp. 205–  
3921 243, 2007. DOI: 10.1146/annurev.nucl.57.090506.123020. arXiv: nucl-  
3922 ex/0701025 (cit. on p. 22).
- 3923 [72] D. J. Gross and F. Wilczek, “Ultraviolet Behavior of Non-Abelian Gauge The-  
3924 ories,” *Phys. Rev. Lett.*, vol. 30, no. 26, pp. 1343–1346, Jun. 1973. DOI:  
3925 10.1103/PhysRevLett.30.1343 (cit. on p. 23).
- 3926 [73] H. Stoecker, “Collective flow signals the quark gluon plasma,” *Nucl. Phys. A*,  
3927 vol. 750, D. Rischke and G. Levin, Eds., pp. 121–147, 2005. DOI: 10.1016/j.  
3928 nuclphysa.2004.12.074. arXiv: nucl-th/0406018 (cit. on p. 23).
- 3929 [74] S. Cao and X.-N. Wang, “Jet quenching and medium response in high-energy  
3930 heavy-ion collisions: a review,” *Rept. Prog. Phys.*, vol. 84, no. 2, p. 024301,  
3931 2021. DOI: 10.1088/1361-6633/abc22b. arXiv: 2002.04028 [hep-ph] (cit.  
3932 on p. 24).
- 3933 [75] A. Collaboration, “ATLAS Feature: Looking inside trillion degree matter,”  
3934 General Photo, 2022. [Online]. Available: <https://cds.cern.ch/record/2809432> (cit. on p. 25).
- 3935
- 3936 [76] C. Adler *et al.*, “Disappearance of back-to-back high  $p_T$  hadron correlations  
3937 in central Au+Au collisions at  $\sqrt{s_{NN}} = 200\text{-GeV}$ ,” *Phys. Rev. Lett.*, vol. 90,  
3938 p. 082302, 2003. DOI: 10.1103/PhysRevLett.90.082302. arXiv: nucl-  
3939 ex/0210033 (cit. on pp. 24, 26).
- 3940 [77] K. Aamodt *et al.*, “Elliptic flow of charged particles in Pb-Pb collisions at 2.76  
3941 TeV,” *Phys. Rev. Lett.*, vol. 105, p. 252302, 2010. DOI: 10.1103/PhysRevLett.  
3942 105.252302. arXiv: 1011.3914 [nucl-ex] (cit. on pp. 25, 27).

- 3943 [78] P. Bo žek, “Splitting of proton-antiproton directed flow in relativistic heavy-  
3944 ion collisions,” *Phys. Rev. C*, vol. 106, p. L061901, 6 Dec. 2022. DOI: 10.1103/  
3945 PhysRevC.106.L061901. [Online]. Available: <https://link.aps.org/doi/10.1103/PhysRevC.106.L061901> (cit. on p. 26).
- 3947 [79] M. Luzum and J.-Y. Ollitrault, “Directed flow at midrapidity in heavy-ion col-  
3948 lisions,” *Phys. Rev. Lett.*, vol. 106, p. 102301, 2011. DOI: 10.1103/PhysRevLett.  
3949 106.102301. arXiv: 1011.6361 [nucl-ex] (cit. on pp. 26, 152).
- 3950 [80] A. M. Poskanzer and S. A. Voloshin, “Methods for analyzing anisotropic flow  
3951 in relativistic nuclear collisions,” *Phys. Rev. C*, vol. 58, pp. 1671–1678, 3 Sep.  
3952 1998. DOI: 10.1103/PhysRevC.58.1671. [Online]. Available: <https://link.aps.org/doi/10.1103/PhysRevC.58.1671> (cit. on pp. 27, 116).
- 3954 [81] J. Letessier and J. Rafelski, “Strangeness chemical equilibration in QGP at  
3955 RHIC and CERN LHC,” *Phys. Rev. C*, vol. 75, p. 014905, 2007. DOI: 10.  
3956 1103/PhysRevC.75.014905. arXiv: nucl-th/0602047 (cit. on p. 28).
- 3957 [82] I. Montvay and J. Zimanyi, “hadron chemistry in heavy ion collisions,” *Nu-  
3958 clear Physics*, 1978. [Online]. Available: [https://inis.iaea.org/collection/NCLCollectionStore/\\_Public/10/468/10468108.pdf](https://inis.iaea.org/collection/NCLCollectionStore/_Public/10/468/10468108.pdf) (cit. on p. 28).
- 3960 [83] J. Cleymans *et al.*, “Statistical model predictions for particle ratios at s(NN)\*\*(1/2)  
3961 = 5.5-TeV,” *Phys. Rev. C*, vol. 74, p. 034903, 2006. DOI: 10.1103/PhysRevC.  
3962 74.034903. arXiv: hep-ph/0604237 (cit. on pp. 28, 60).
- 3963 [84] A. Andronic, P. Braun-Munzinger, and J. Stachel, “Thermal hadron produc-  
3964 tion in relativistic nuclear collisions,” *Acta Phys. Polon. B*, vol. 40, pp. 1005–  
3965 1012, 2009. arXiv: 0901.2909 [nucl-th] (cit. on pp. 28, 60).
- 3966 [85] R. Hagedorn and J. Ranft, “Statistical thermodynamics of strong interactions  
3967 at high-energies. 2. Momentum spectra of particles produced in pp-collisions,”  
3968 *Nuovo Cim. Suppl.*, vol. 6, pp. 169–354, 1968 (cit. on pp. 28, 60).
- 3969 [86] F. Becattini and U. W. Heinz, “Thermal hadron production in p p and p anti-  
3970 p collisions,” *Z. Phys. C*, vol. 76, pp. 269–286, 1997, [Erratum: Z.Phys.C 76,  
3971 578 (1997)]. DOI: 10.1007/s002880050551. arXiv: hep-ph/9702274 (cit. on  
3972 pp. 28, 60).

- 3973 [87] J. Adam *et al.*, “Enhanced production of multi-strange hadrons in high-multiplicity  
3974 proton-proton collisions,” *Nature Phys.*, vol. 13, pp. 535–539, 2017. DOI: 10.  
3975 1038/nphys4111. arXiv: 1606.07424 [nucl-ex] (cit. on pp. 30, 61).
- 3976 [88] F. Becattini and J. Manninen, “Strangeness production from SPS to LHC,” *J.  
3977 Phys. G*, vol. 35, J.-e. Alam *et al.*, Eds., p. 104013, 2008. DOI: 10.1088/0954-  
3978 3899/35/10/104013. arXiv: 0805.0098 [nucl-th] (cit. on pp. 29, 60).
- 3979 [89] T. Pierog and K. Werner, “EPOS Model and Ultra High Energy Cosmic Rays,”  
3980 *Nucl. Phys. B Proc. Suppl.*, vol. 196, J.-N. Capdevielle, R. Engel, and B.  
3981 Pattison, Eds., pp. 102–105, 2009. DOI: 10.1016/j.nuclphysbps.2009.09.  
3982 017. arXiv: 0905.1198 [hep-ph] (cit. on p. 30).
- 3983 [90] C. Bierlich *et al.*, “A comprehensive guide to the physics and usage of PYTHIA  
3984 8.3,” Mar. 2022. DOI: 10.21468/SciPostPhysCodeb.8. arXiv: 2203.11601  
3985 [hep-ph] (cit. on pp. 30, 181).
- 3986 [91] S. Roesler, R. Engel, and J. Ranft, “The Monte Carlo event generator DPMJET-  
3987 III,” in *International Conference on Advanced Monte Carlo for Radiation  
3988 Physics, Particle Transport Simulation and Applications (MC 2000)*, Dec.  
3989 2000, pp. 1033–1038. DOI: 10.1007/978-3-642-18211-2\_166. arXiv: hep-  
3990 ph/0012252 (cit. on pp. 30, 148).
- 3991 [92] W. Cassing and E. L. Bratkovskaya, “Parton transport and hadronization from  
3992 the dynamical quasiparticle point of view,” *Phys. Rev. C*, vol. 78, p. 034919,  
3993 2008. DOI: 10.1103/PhysRevC.78.034919. arXiv: 0808.0022 [hep-ph] (cit.  
3994 on pp. 31, 34).
- 3995 [93] W. Cassing and E. L. Bratkovskaya, “Parton-Hadron-String Dynamics: an  
3996 off-shell transport approach for relativistic energies,” *Nucl. Phys. A*, vol. 831,  
3997 pp. 215–242, 2009. DOI: 10.1016/j.nuclphysa.2009.09.007. arXiv: 0907.  
3998 5331 [nucl-th] (cit. on pp. 31, 32).
- 3999 [94] W. Cassing, “From Kadanoff-Baym dynamics to off-shell parton transport,”  
4000 *Eur. Phys. J. ST*, vol. 168, R. Alkofer, H. Gies, and B.-J. Schaefer, Eds., pp. 3–  
4001 87, 2009. DOI: 10.1140/epjst/e2009-00959-x. arXiv: 0808.0715 [nucl-th]  
4002 (cit. on p. 31).

- 4003 [95] O. Soloveva, J. Aichelin, and E. Bratkovskaya, “Transport properties and  
4004 equation-of-state of hot and dense QGP matter near the critical endpoint in  
4005 the phenomenological dynamical quasiparticle model,” *Phys. Rev. D*, vol. 105,  
4006 no. 5, p. 054011, 2022. DOI: 10.1103/PhysRevD.105.054011. arXiv: 2108.  
4007 08561 [hep-ph] (cit. on p. 32).
- 4008 [96] T. Sjostrand, “PYTHIA 5.7 and JETSET 7.4: Physics and manual,” Feb. 1994.  
4009 arXiv: hep-ph/9508391 (cit. on p. 35).
- 4010 [97] W. Ehehalt and W. Cassing, “Relativistic transport approach for nucleus nu-  
4011 cleus collisions from SIS to SPS energies,” *Nucl. Phys. A*, vol. 602, pp. 449–  
4012 486, 1996. DOI: 10.1016/0375-9474(96)00097-8 (cit. on p. 35).
- 4013 [98] Y. Nambu and G. Jona-Lasinio, “Dynamical Model of Elementary Particles  
4014 Based on an Analogy with Superconductivity. I,” *Physical Review*, vol. 122,  
4015 no. 1, pp. 345–358, Apr. 1961. DOI: 10.1103/PhysRev.122.345 (cit. on p. 35).
- 4016 [99] T. Pierog *et al.*, “Epos lhc: Test of collective hadronization with data measured  
4017 at the cern large hadron collider,” *Phys. Rev. C*, vol. 92, p. 034906, 3 Sep.  
4018 2015. DOI: 10.1103/PhysRevC.92.034906. [Online]. Available: <https://link.aps.org/doi/10.1103/PhysRevC.92.034906> (cit. on pp. 36, 37).
- 4020 [100] Z. Wolff and D. Molnar, “Self-consistent Cooper-Frye freeze-out of a viscous  
4021 fluid to particles,” *J. Phys. Conf. Ser.*, vol. 535, p. 012020, 2014. DOI: 10.  
4022 1088/1742-6596/535/1/012020. arXiv: 1407.6413 [nucl-th] (cit. on p. 37).
- 4023 [101] S. Roesler, R. Engel, and J. Ranft, “The monte carlo event generator DPMJET-  
4024 III,” in *Advanced Monte Carlo for Radiation Physics, Particle Transport Sim-  
4025 ulation and Applications*, Springer Berlin Heidelberg, 2001. arXiv: 0012252  
4026 [hep-ph] (cit. on pp. 37, 71, 80).
- 4027 [102] A. Capella, U. Sukhatme, C.-I. Tan, and J. Tran Thanh Van, “Dual par-  
4028 ton model,” *Phys. Rept.*, vol. 236, pp. 225–329, 1994. DOI: 10.1016/0370-  
4029 1573(94)90064-7 (cit. on p. 37).
- 4030 [103] L. Evans, “The Large Hadron Collider,” *New Journal of Physics*, vol. 9, no. 9,  
4031 p. 335, 2007. DOI: 10.1088/1367-2630/9/9/335. [Online]. Available: <https://dx.doi.org/10.1088/1367-2630/9/9/335> (cit. on p. 39).
- 4033 [104] E. Keil, “The Large Hadron Collider LHC,” *eConf*, vol. C960625, OPS010,  
4034 1996 (cit. on p. 39).

- 4035 [105] K. Aamodt *et al.*, “The ALICE experiment at the CERN LHC,” *JINST*, vol. 3,  
4036 S08002, 2008. DOI: 10.1088/1748-0221/3/08/S08002 (cit. on p. 39).
- 4037 [106] G. Aad *et al.*, “The ATLAS Experiment at the CERN Large Hadron Collider,”  
4038 *JINST*, vol. 3, S08003, 2008. DOI: 10.1088/1748-0221/3/08/S08003 (cit. on  
4039 p. 39).
- 4040 [107] S. Chatrchyan *et al.*, “The CMS Experiment at the CERN LHC,” *JINST*,  
4041 vol. 3, S08004, 2008. DOI: 10.1088/1748-0221/3/08/S08004 (cit. on p. 39).
- 4042 [108] A. A. Alves Jr. *et al.*, “The LHCb Detector at the LHC,” *JINST*, vol. 3,  
4043 S08005, 2008. DOI: 10.1088/1748-0221/3/08/S08005 (cit. on p. 39).
- 4044 [109] J. Adam *et al.*, “Enhanced production of multi-strange hadrons in high-multiplicity  
4045 proton–proton collisions,” *Nature*, vol. 13, no. 6, pp. 535–539, 2017. DOI:  
4046 10.1038/nphys4111. [Online]. Available: <https://doi.org/10.1038%2Fnphys4111> (cit. on p. 39).
- 4048 [110] S. Acharya *et al.*, “Search for a common baryon source in high-multiplicity  
4049 pp collisions at the LHC,” *Physics Letters B*, vol. 811, p. 135849, 2020, ISSN:  
4050 0370-2693. DOI: <https://doi.org/10.1016/j.physletb.2020.135849>.  
4051 [Online]. Available: <https://www.sciencedirect.com/science/article/pii/S0370269320306523> (cit. on p. 39).
- 4053 [111] V. Khachatryan *et al.*, “Correlations between jets and charged particles in  
4054 PbPb and pp collisions at  $\sqrt{s_{\text{NN}}} = 2.76$  TeV,” *Journal of High Energy Physics*,  
4055 vol. 2016, no. 2, 2016. DOI: 10.1007/jhep02(2016)156. [Online]. Available:  
4056 <https://doi.org/10.1007%2Fjhep02%282016%29156> (cit. on p. 40).
- 4057 [112] G. Aad *et al.*, “Measurement of substructure-dependent jet suppression in  
4058 Pb+Pb collisions at 5.02 TeV with the ATLAS detector,” *Phys. Rev. C*,  
4059 vol. 107, no. 5, p. 054909, 2023. DOI: 10.1103/PhysRevC.107.054909. arXiv:  
4060 2211.11470 [nucl-ex] (cit. on p. 40).
- 4061 [113] J. Amos, *Large hadron collider can be “world’s biggest rain meter”*, 2016.  
4062 [Online]. Available: <https://www.bbc.com/news/science-environment-36094282> (cit. on p. 40).
- 4064 [114] A. Tauro, “ALICE Schematics,” General Photo, 2017. [Online]. Available:  
4065 <https://cds.cern.ch/record/2263642> (cit. on p. 41).

- 4066 [115] G. Dellacasa *et al.*, “ALICE technical design report of the inner tracking sys-  
4067 tem (ITS),” Jun. 1999 (cit. on p. 43).
- 4068 [116] A. collaboration, “Alignment of the ALICE Inner Tracking System with cosmic-  
4069 ray tracks,” *Journal of Instrumentation*, vol. 5, no. 03, P03003, 2010. DOI:  
4070 [10.1088/1748-0221/5/03/P03003](https://doi.org/10.1088/1748-0221/5/03/P03003). [Online]. Available: <https://dx.doi.org/10.1088/1748-0221/5/03/P03003> (cit. on p. 44).
- 4072 [117] F. Meddi, “The ALICE silicon pixel detector (SPD),” *Nucl. Instrum. Meth. A*,  
4073 vol. 465, L. Rossi, Ed., pp. 40–45, 2000. DOI: [10.1016/S0168-9002\(01\)00344-8](https://doi.org/10.1016/S0168-9002(01)00344-8) (cit. on p. 43).
- 4075 [118] S. Antinori *et al.*, *Design and construction of an ALICE SDD end-ladder proto-*  
4076 *type board*. 2004, vol. 3, 1669–1672 Vol. 3. DOI: [10.1109/NSSMIC.2004.1462561](https://doi.org/10.1109/NSSMIC.2004.1462561) (cit. on p. 44).
- 4078 [119] D. Nouais *et al.*, “Drift velocity monitoring of SDDs using MOS charge injec-  
4079 *tors*,” *Nuclear Instruments and Methods in Physics Research Section A: Accel-*  
4080 *erators, Spectrometers, Detectors and Associated Equipment*, vol. 450, no. 2,  
4081 pp. 338–342, 2000, ISSN: 0168-9002. DOI: [https://doi.org/10.1016/S0168-9002\(00\)00278-3](https://doi.org/10.1016/S0168-9002(00)00278-3). [Online]. Available: <https://www.sciencedirect.com/science/article/pii/S0168900200002783> (cit. on p. 45).
- 4084 [120] G. Contin, *The ALICE Silicon Strip Detector performance during the first*  
4085 *LHC data taking*, 2011. arXiv: [1101.2776](https://arxiv.org/abs/1101.2776) [physics.ins-det] (cit. on p. 45).
- 4086 [121] S. Fartoukh *et al.*, “LHC Configuration and Operational Scenario for Run 3,”  
4087 CERN, Geneva, Tech. Rep., 2021. [Online]. Available: <https://cds.cern.ch/record/2790409> (cit. on p. 45).
- 4089 [122] A. L. Gera, *Upgrade of the ALICE Time Projection Chamber for the LHC Run*  
4090 *3*, 2020. arXiv: [2004.10520](https://arxiv.org/abs/2004.10520) [physics.ins-det] (cit. on p. 45).
- 4091 [123] L. Terlizzi, *Upgrade and commissioning of the ALICE muon spectrometer*,  
4092 2022. arXiv: [2210.12431](https://arxiv.org/abs/2210.12431) [physics.ins-det] (cit. on p. 46).
- 4093 [124] “Upgrade of the ALICE ITS detector,” *Nuclear Instruments and Methods in*  
4094 *Physics Research Section A: Accelerators, Spectrometers, Detectors and Asso-*  
4095 *ciated Equipment*, vol. 1032, p. 166 632, 2022. DOI: [10.1016/j.nima.2022.166632](https://doi.org/10.1016/j.nima.2022.166632). [Online]. Available: <https://doi.org/10.1016%2Fj.nima.2022.166632> (cit. on p. 46).

- 4098 [125] M. Mager, “ALPIDE, the Monolithic Active Pixel Sensor for the ALICE ITS  
4099 upgrade,” *Nuclear Instruments and Methods in Physics Research Section A: Accelerators, Spectrometers, Detectors and Associated Equipment*, vol. 824,  
4100 pp. 434–438, 2016, ISSN: 0168-9002. DOI: <https://doi.org/10.1016/j.nima.2015.09.057>. [Online]. Available: <https://www.sciencedirect.com/science/article/pii/S0168900215011122> (cit. on p. 47).
- 4104 [126] G. Dellacasa *et al.*, “ALICE: Technical design report of the time projection  
4105 chamber,” Jan. 2000 (cit. on pp. 52, 54).
- 4106 [127] J. Alme *et al.*, “The ALICE TPC, a large 3-dimensional tracking device with  
4107 fast readout for ultra-high multiplicity events,” *Nuclear Instruments and Methods in Physics Research Section A: Accelerators, Spectrometers, Detectors and  
4108 Associated Equipment*, vol. 622, no. 1, pp. 316–367, 2010. DOI: [10.1016/j.nima.2010.04.042](https://doi.org/10.1016/j.nima.2010.04.042). [Online]. Available: <https://doi.org/10.1016%2Fj.nima.2010.04.042> (cit. on p. 52).
- 4112 [128] P. A. Zyla *et al.*, “Review of Particle Physics,” *Progress of Theoretical and Experimental Physics*, vol. 2020, no. 8, p. 083C01, Aug. 2020, ISSN: 2050-3911.  
4113 DOI: [10.1093/ptep/ptaa104](https://doi.org/10.1093/ptep/ptaa104). eprint: <https://academic.oup.com/ptep/article-pdf/2020/8/083C01/34673722/ptaa104.pdf>. [Online]. Available:  
4114 <https://doi.org/10.1093/ptep/ptaa104> (cit. on p. 53).
- 4117 [129] W. Yu, “Particle identification of the ALICE TPC via dE/dx,” *Nuclear Instruments and Methods in Physics Research Section A: Accelerators, Spectrometers, Detectors and Associated Equipment*, vol. 706, pp. 55–58, 2013, TRDs for  
4118 the Third Millenium, ISSN: 0168-9002. DOI: <https://doi.org/10.1016/j.nima.2012.05.022>. [Online]. Available: <https://www.sciencedirect.com/science/article/pii/S0168900212005098> (cit. on pp. 54, 55).
- 4123 [130] G. Dellacasa *et al.*, “ALICE technical design report of the time-of-flight system  
4124 (TOF),” Feb. 2000 (cit. on p. 56).
- 4125 [131] E. Cerron Zeballos *et al.*, “A New type of resistive plate chamber: The Multi-  
4126 gap RPC,” *Nucl. Instrum. Meth. A*, vol. 374, pp. 132–136, 1996. DOI: [10.1016/0168-9002\(96\)00158-1](https://doi.org/10.1016/0168-9002(96)00158-1) (cit. on p. 56).
- 4128 [132] N. Jacazio, *PID performance of the ALICE-TOF detector in Run 2*, 2018.  
4129 arXiv: 1809.00574 [physics.ins-det] (cit. on p. 57).

- 4130 [133] P. Cortese *et al.*, “ALICE electromagnetic calorimeter technical design report,”  
4131 Sep. 2008 (cit. on p. 57).
- 4132 [134] S. Acharya *et al.*, “Performance of the ALICE Electromagnetic Calorimeter,”  
4133 *JINST*, vol. 18, no. 08, P08007, 2023. DOI: 10.1088/1748-0221/18/08/  
4134 P08007. arXiv: 2209.04216 [physics.ins-det] (cit. on p. 57).
- 4135 [135] F. Ronchetti *et al.*, “The ALICE electromagnetic calorimeter project,” *Journal*  
4136 *of Physics: Conference Series*, vol. 160, no. 1, p. 012012, 2009. DOI: 10.1088/  
4137 1742-6596/160/1/012012. [Online]. Available: <https://dx.doi.org/10.1088/1742-6596/160/1/012012> (cit. on p. 58).
- 4139 [136] A. Fantoni *et al.*, “The ALICE Electromagnetic Calorimeter: EMCAL,” *Journal*  
4140 *of Physics: Conference Series*, vol. 293, no. 1, p. 012043, 2011. DOI: 10.1088/  
4141 1742-6596/293/1/012043. [Online]. Available: <https://dx.doi.org/10.1088/1742-6596/293/1/012043> (cit. on p. 58).
- 4143 [137] E. Abbas *et al.*, “Performance of the ALICE VZERO system,” *JINST*, vol. 8,  
4144 P10016, 2013. DOI: 10.1088/1748-0221/8/10/P10016. arXiv: 1306.3130  
4145 [nucl-ex] (cit. on p. 58).
- 4146 [138] K. Redlich and A. Tounsi, “Strangeness enhancement and energy dependence  
4147 in heavy ion collisions,” *Eur. Phys. J. C*, vol. 24, pp. 589–594, 2002. DOI:  
4148 10.1007/s10052-002-0983-1. arXiv: hep-ph/0111261 (cit. on p. 60).
- 4149 [139] Z. Li, W. Zha, and Z. Tang, “Rescattering effect on the measurement of  $K^{*0}$   
4150 spin alignment in heavy-ion collisions,” *Phys. Rev. C*, vol. 106, p. 064908, 6  
4151 Dec. 2022. DOI: 10.1103/PhysRevC.106.064908. [Online]. Available: <https://link.aps.org/doi/10.1103/PhysRevC.106.064908> (cit. on p. 62).
- 4153 [140] M. Cacciari, G. P. Salam, and G. Soyez, “The anti- $k_t$  jet clustering algorithm,”  
4154 *JHEP*, vol. 04, p. 063, 2008. DOI: 10.1088/1126-6708/2008/04/063. arXiv:  
4155 0802.1189 [hep-ph] (cit. on p. 65).
- 4156 [141] R. Singh, S. Khade, and A. Roy, “Jet fragmentation via azimuthal angular  
4157 correlations of heavy flavors in  $pp$  collisions at  $\sqrt{s} = 7$  tev,” *Phys. Rev. C*,  
4158 vol. 107, p. 025206, 2 Feb. 2023. DOI: 10.1103/PhysRevC.107.025206.  
4159 [Online]. Available: <https://link.aps.org/doi/10.1103/PhysRevC.107.025206> (cit. on pp. 65, 68).

- 4161 [142] J. Blair, “Investigating strangeness enhancement in jet and medium via  $\phi(1020)$   
4162 production,” 2023. arXiv: TBA [nuc-ex] (cit. on pp. 65, 158, 169, 182, 183).
- 4163 [143] S. Oh, A. Morsch, C. Loizides, and T. Schuster, “Correction methods for finite-  
4164 acceptance effects in two-particle correlation analyses,” *The European Phys.  
4165 Journal Plus*, vol. 131, no. 8, Aug. 2016. arXiv: 1604.05332 [nucl-th] (cit.  
4166 on p. 66).
- 4167 [144] D. J. Best and N. I. Fisher, “Efficient simulation of the von mises distribution,”  
4168 *Journal of the Royal Statistical Society. Series C (Applied Statistics)*, vol. 28,  
4169 no. 2, pp. 152–157, 1979, ISSN: 00359254, 14679876. [Online]. Available: <http://www.jstor.org/stable/2346732> (visited on 10/07/2023) (cit. on pp. 68,  
4170 69).
- 4172 [145] A. Kalweit, *Energy loss calibration of the ALICE TPC*, 2008 (cit. on p. 74).
- 4173 [146] S. Acharya *et al.*, “Production of  $K^*(892)^0$  and  $\phi(1020)$  in pp and p–Pb col-  
4174 lisions at  $\sqrt{s_{NN}} = 5.02$  tev,” *Phys. Rev.*, vol. C97, 2022. DOI: 10.1103/  
4175 physrevc.106.034907. [Online]. Available: <https://doi.org/10.1103/physrevc.106.034907> (cit. on p. 77).
- 4177 [147] R. Brun *et al.*, *GEANT: Detector Description and Simulation Tool; Oct 1994*  
4178 (CERN Program Library). Geneva: CERN, 1993, Long Writeup W5013. DOI:  
4179 10.17181/CERN.MUHF.DMJ1. [Online]. Available: <http://cds.cern.ch/record/1082634> (cit. on pp. 80, 148).
- 4181 [148] S. Acharya *et al.*, “Two-particle differential transverse momentum and number  
4182 density correlations in p–Pb and Pb–Pb at the LHC,” *Phys. Rev. C*, vol. C100,  
4183 no. 4, 2019. arXiv: 1805.04422 (cit. on p. 92).
- 4184 [149] S. Acharya *et al.*, “Longitudinal and azimuthal evolution of two-particle trans-  
4185 verse momentum correlations in Pb–Pb collisions at  $\sqrt{s_{NN}} = 2.76$  TeV,” *Phys.  
4186 Letters*, vol. B804, p. 135 375, 2020. arXiv: 1910.14393 (cit. on pp. 92, 96).
- 4187 [150] M. Ivanov *et al.*, “Track reconstruction in high density environment,” *Nuclear  
4188 Instruments and Methods in Physics Research Section A: Accelerators, Spec-  
4189 trometers, Detectors and Associated Equipment*, vol. 566, no. 1, pp. 70–74,  
4190 2006, TIME 2005, ISSN: 0168-9002. DOI: <https://doi.org/10.1016/j.nima.2006.05.029>. [Online]. Available: <https://www.sciencedirect.com/science/article/pii/S0168900206008126> (cit. on p. 93).

- 4193 [151] S. Acharya *et al.*, “ $K_S^0$ - and (anti-) $\Lambda$ -hadron correlations in pp collisions at  
 4194  $\sqrt{s_{NN}} = 13$  TeV,” *The European Phys. Journal*, vol. C81, no. 10, 2021. arXiv:  
 4195 2107.11209 [nucl-ex] (cit. on pp. 95, 102).
- 4196 [152] K. Aamodt *et al.*, “Two-pion Bose-Einstein correlations in central Pb-Pb col-  
 4197 lisions at  $\sqrt{s_{NN}} = 2.76$  TeV,” *Phys. Lett. B*, vol. 696, pp. 328–337, 2011. DOI:  
 4198 10.1016/j.physletb.2010.12.053. arXiv: 1012.4035 [nucl-ex] (cit. on  
 4199 p. 95).
- 4200 [153] R. Barlow, *Systematic errors: Facts and fictions*, 2002. arXiv: 0207026 [hep-ex]  
 4201 (cit. on pp. 100, 101, 112).
- 4202 [154] S. Acharya *et al.*, “Multiplicity dependence of light-flavor hadron production  
 4203 in pp collisions at  $\sqrt{s} = 7$  TeV,” *Phys. Rev.*, vol. C99, 2019. arXiv: 1807.11321  
 4204 [nucl-ex] (cit. on p. 102).
- 4205 [155] B. A. et al., “Multiplicity Dependence of Pion, Kaon, Proton and Lambda  
 4206 Production in p-Pb Collisions at  $\sqrt{s_{NN}} = 5.02$  TeV,” *Phys. Letters*, vol. B728,  
 4207 pp. 25–38, 2014. arXiv: 1307.6796 [nucl-ex] (cit. on pp. 102, 119).
- 4208 [156] B. Abelev *et al.*, “ $K_S^0$  and  $\Lambda$  production in Pb-Pb collisions at  $\sqrt{s_{NN}} = 2.76$   
 4209 tev,” *Phys. Rev. Lett.*, vol. 111, 2013. arXiv: 1307.5530 [nucl-ex] (cit. on  
 4210 p. 102).
- 4211 [157] Abelev *et al.*, “Long-range angular correlations of  $\pi$ , K and p in p-Pb collisions  
 4212 at  $\sqrt{s_{NN}} = 5.02$  TeV,” *Phys. Lett. B*, vol. 726, pp. 164–177, 2013. DOI: 10.  
 4213 1016 / j . physletb . 2013 . 08 . 024. arXiv: 1307 . 3237 [nucl-ex] (cit. on  
 4214 p. 117).
- 4215 [158] B. Abelev *et al.*, “Long-range angular correlations of  $\pi$ , K and p in p-Pb  
 4216 collisions at  $\sqrt{s_{NN}} = 5.02$  TeV,” *Phys. Lett.*, vol. B726, pp. 164–177, 2013.  
 4217 arXiv: 1307 . 3237 [nucl-ex] (cit. on pp. 117, 118).
- 4218 [159] B. Abelev *et al.*, “Observation of partonic flow in proton-proton and proton-  
 4219 nucleus collisions,” *Nature Phys.*, vol. TBA, TBA, 2023. arXiv: TBA [nucl-ex]  
 4220 (cit. on p. 117).
- 4221 [160] B. A. et al., “Multiplicity Dependence of Pion, Kaon, Proton and Lambda  
 4222 Production in p-Pb Collisions at  $\sqrt{s_{NN}} = 5.02$  TeV,” *Phys. Letters*, vol. B728,  
 4223 pp. 25–38, 2014. arXiv: 1307.6796 [nucl-ex] (cit. on pp. 117, 168).

- 4224 [161] A. K. Nandi and D. Mämpel, “An extension of the generalized gaussian distri-  
4225      bution to include asymmetry,” *Journal of the Franklin Institute*, vol. 332, no. 1,  
4226      pp. 67–75, 1995, ISSN: 0016-0032. DOI: [https://doi.org/10.1016/0016-0032\(95\)00029-W](https://doi.org/10.1016/0016-0032(95)00029-W). [Online]. Available: <https://www.sciencedirect.com/science/article/pii/001600329500029W> (cit. on p. 138).
- 4229 [162] V. D. Elvira, “Impact of Detector Simulation in Particle Physics Collider Ex-  
4230      periments,” *Phys. Rept.*, vol. 695, pp. 1–54, 2017. DOI: 10.1016/j.physrep.  
4231      2017.06.002. arXiv: 1706.04293 [hep-ex] (cit. on p. 148).
- 4232 [163] B. A. et al., “Enhanced production of multi-strange hadrons in high-multiplicity  
4233      proton-proton collisions,” *Nature Phys.*, vol. 13, pp. 535–539, 2017. arXiv:  
4234      1606.07424 [nucl-ex] (cit. on p. 168).
- 4235 [164] G. Abbiendi *et al.*, “Particle multiplicity of unbiased gluon jets from e+e-  
4236      three-jet events,” *The European Phys. Journal*, vol. C23, no. 4, pp. 597–613,  
4237      2002. arXiv: 0111013 [hep-ex] (cit. on p. 179).
- 4238 [165] K. Ackerstaff *et al.*, “Production of  $K_S^0$  and  $\Lambda$  in quark and gluon jets from  
4239       $Z^0$  decays,” *The European Phys. Journal*, vol. C8, no. 4, pp. 241–254, 1999.  
4240      arXiv: 9805025 [hep-ex] (cit. on p. 179).
- 4241 [166] S. Acharya *et al.*, *The ALICE experiment – a journey through QCD*, 2022.  
4242      arXiv: 2211.04384 [nucl-ex] (cit. on p. 182).